



THE HONG KONG
POLYTECHNIC UNIVERSITY

香港理工大學

Pao Yue-kong Library

包玉剛圖書館

Copyright Undertaking

This thesis is protected by copyright, with all rights reserved.

By reading and using the thesis, the reader understands and agrees to the following terms:

1. The reader will abide by the rules and legal ordinances governing copyright regarding the use of the thesis.
2. The reader will use the thesis for the purpose of research or private study only and not for distribution or further reproduction or any other purpose.
3. The reader agrees to indemnify and hold the University harmless from and against any loss, damage, cost, liability or expenses arising from copyright infringement or unauthorized usage.

IMPORTANT

If you have reasons to believe that any materials in this thesis are deemed not suitable to be distributed in this form, or a copyright owner having difficulty with the material being included in our database, please contact lbsys@polyu.edu.hk providing details. The Library will look into your claim and consider taking remedial action upon receipt of the written requests.

**NOVEL METAL/CORE-SHELL POLYMER COMPOSITE
PARTICLES: SYNTHESIS, CHARACTERIZATION AND
POTENTIAL APPLICATIONS**

TAN, NOEL PETER BENGZON

Ph.D

The Hong Kong Polytechnic University

2014

The Hong Kong Polytechnic University

Department of Applied Biology and Chemical Technology

**Novel metal/core-shell polymer composite particles: synthesis,
characterization and potential applications**

Tan, Noel Peter Bengzon

A thesis submitted in partial fulfillment of the requirements for
the degree of Doctor of Philosophy

(January 2014)

CERTIFICATE OF ORIGINALITY

I hereby declare that this thesis is my own work and that, to the best of my knowledge and belief, it reproduces no material previously published or written, nor material that has been accepted of any other degree or diploma, except where due acknowledgement has been made in the text.

TAN, NOEL PETER BENGZON

JANUARY 2014

Abstract

This thesis aims to develop metal/polymer composite particles through a simple, inexpensive and greener synthetic route using polymeric nanoparticles as both nanoreactors and templates, and explore potential application of the composite particles as smart catalysts in organic synthesis. Specifically, amphiphilic polymeric particle that is composed of poly(*N*-isopropylacrylamide)/polyethyleneimine (PNIPAm/PEI) with a core-shell nanostructure, was used as the nanoreactor which is capable of self-reducing metal salt to generate metal nanoparticle without the aid of additional reducing agent. It also serves as the template which can control the growth of metal nanoparticle, as well as encapsulate and stabilize the resulting metal nanoparticle. Since the PNIPAm/PEI microgel is sensitive to both temperature and solution pH, and can be stably dispersed in water, the accessibility of the encapsulated metal nanoparticles can be controlled through turning solution pH and temperature. Thus this type of metal/polymer composite particles are promising smart catalyst for aqueous-based organic synthesis.

The thesis begins with the introduction of metal/polymer composite particles. It reviews current approaches in synthesizing this type of composite materials such as chemical methods, biological synthesis and polymer template mediated synthesis. Drawbacks of these methods on the synthesis of composite particles are also pointed out in details. To address these problems, a novel type of polymer material, namely amphiphilic core-shell particles, is proposed as a green nanoreactor to generate composite particles without the need to use conventional reducing agent. The

background of the amphiphilic core-shell particles including their synthesis, unique features and potential applications are subsequently discussed.

Chapter two discusses the rationale of using amphiphilic core-shell particles and the challenges for their usage. Specific objectives of the research are then described.

Chapter three provides detailed research methodologies implemented in this work including materials used, synthetic methods, measurements and characterization with various analytical tools such as particle size and surface charge measurements; FTIR; NMR; UV-Vis spectroscopy; field emission scanning electron microscopy (FESEM); transmission electron microscopy (TEM); X-ray diffraction spectroscopy (XRD); X-ray photoelectron spectroscopy (XPS); and atomic force microscopy (AFM).

Chapter four describes gold nanoparticle formation using a PNIPAm/PEI core-shell microgel to generate smart metal/polymer composite particles. The microgel template acts not only as the nanoreactor for gold salt reduction, but also as the stabilizer and immobilizer for the encapsulation of resultant gold nanoparticles. The kinetics of gold salt reduction and gold nanoparticle formation were carefully investigated. Results indicated that the reduction rate of PEI/PNIPAm microgels is 625 times faster than the native PEI. Factors affecting the formation of Au/PNIPAm/PEI composite particles such as solution pH, temperature, amino to gold salt ratio and temperature of the composite particles have been systematically investigated. Physical properties of the resulting composite particles such as particle size, surface charge, colloidal stability, morphology, nanostructure and gold nanoparticle property were

carefully examined. The mechanism of gold nanoparticle formation on the PEI shell was also proposed.

Chapter five extends the established system from gold nanoparticles to bimetallic nanoparticles (i.e. Au@Ag) using a successive reduction method through utilizing the pre-synthesized gold nanoparticles in microgel template as seeds for the silver nanoparticles to grow and develop. The favorable formation of the second metal nanoparticles was attributed to the under-potential difference between gold and silver ions.

Chapter six demonstrates the catalytic activities of both the gold (Au) and gold with silver (Au@Ag) in microgel template through the reduction of *p*-nitrophenol to *p*-aminophenol as a catalytic model. Results from this study showed that the use of gold nanoparticles increased the reduction rate by ten folds. Furthermore, when bimetallic nanoparticles (Au@Ag) were used, the reduction rate further increased by a factor of ten. Investigation of the effects of pH and temperature on the catalytic activity of the gold nanoparticles in microgel template was also systematically carried out. Results showed that in a pH range of 3 – 11, their corresponding catalytic activities decreased as pH increased. At pH 3, catalytic activity was calculated at $7.50 \times 10^{-3} \text{ s}^{-1}$. But increasing solution pH to 7 resulted in ten times slower in reduction rate ($7.4 \times 10^{-4} \text{ s}^{-1}$), and it eventually ceased at pH 11. When temperature increased, catalytic activity decreased. At 25°C, the catalytic activity was at peak of $7.4 \times 10^{-4} \text{ s}^{-1}$. But when temperature was increased to 29°C, catalytic activity decreased to $3.16 \times 10^{-4} \text{ s}^{-1}$, and further down to

1.33×10^{-4} when temperature reached 33°C . This behavior demonstrates that tuning the solution pH and temperature enable us to control the catalytic activity.

Chapter seven sums up the overall conclusions on the syntheses of the composite particles and the effect studies to be conducted in the future. It further discusses the significance and implications made in the work, and provide recommendations for future studies.

Publications

1. Noel Peter Bengzon Tan, Cheng Hao Lee, Lianghai Chen, Kin Man Ho, Yan Lu, Pei Li* “Green Synthesis of Gold/Polymer Nanocomposites Using Polymeric Amine-Based Particles As Nanoreactors and Templates” Submitted to *Small*.
2. Noel Peter Bengzon Tan, Cheng Hao Lee, Pei Li* “Facile Green Synthesis of Smart Metal/Polymer Composite Particles and Their Turntable Catalytic Activities” (In preparation).

Conferences and Symposia

1. Noel Peter Bengzon Tan. “Gold nanoparticles in different core-shell type templates”, *Oral Presenter*, Graduate Research Seminar, International Polymer Colloid Group (IPCG) Conference 2013, Shanghai, China, June 23-28, 2013.
2. Lianghai Chen, Noel Peter Bengzon Tan, Pei Li. “Green synthesis of smart gold nanoparticle/polymer composite particles”, *Abstract of Papers*, International Polymer Colloid Group (IPCG) Research Conference, Shanghai, China, June 23-28, 2013.
3. Noel Peter Bengzon Tan, Cheng Hao Lee, Pei Li. “PEI-based smart template for generation of Au@Ag composite particles with high and tunable catalytic activity”, *Abstract of Papers*”, International Polymer Colloid Group (IPCG) Research Conference, Shanghai, China, June 23-28, 2013. (**Best Poster Award**)
4. Noel Peter Bengzon Tan, Cheng Hao Lee, Pei Li. “High Catalytic Activity of Au@Ag Nanoparticles Supported on PEI-based Core-Shell Particles”, *Abstract of Papers*, The 20th Symposium on Chemistry Postgraduate Research in Hong Kong, P.R. China, April 27, 2013.
5. Lianghai Chen, Noel Peter Bengzon Tan, Pei Li. “ Kinetic study of green synthesis of gold nanoparticles in smart core-shell microgel template”, *Abstract of Papers*, The 20th Symposium on Chemistry Postgraduate Research in Hong Kong, P.R. China, April 27, 2013.

6. Noel Peter Bengzon Tan, Pei Li. “One-pot synthesis of pH- and Temperature-Responsive Core-shell Microgels Containing Gold Nanoparticles”, *Abstract of Papers*, 19th Ostwald-Kolloquium “Dynamics on the Mesoscopic Scale – Structuring under Non-equilibrium Conditions”, Berlin, Germany, September 20-21, 2012.
7. Noel Peter Bengzon Tan, Cheng Hao Lee, Pei Li. “Smart Core-Shell Microgel as Template for Gold Nanoparticle Synthesis”, *Abstract of Papers*, The 19th Symposium on Chemistry Postgraduate Research in Hong Kong, P.R. China, April 14, 2012. (**Best Oral Presenter Award**)
8. Noel Peter Tan, Cheng Hao Lee, Kin Man Ho, Pei Li. “Green synthesis of Au Nanoparticles in Smart Core-Shell Microgels”, *Abstract of Papers*, The 4th Asian Symposium on Emulsion Polymerization and Functional Polymeric Microspheres, Hong Kong, P.R. China, December 11-14, 2011.
9. Tan Noel Peter Bengzon, Kin Man Ho, Pei Li. “Thermoresponsive Core-Shell Microgels@Au Nanocomposite Particles As an Efficient Nanocatalysts in *p*-Nitrophenol Reduction”, *Abstract of Papers*, The 18th Symposium on Chemistry Postgraduate Research on Hong Kong, City University of Hong Kong, Hong Kong, P.R. China, April 30, 2011.

ACKNOWLEDGEMENTS

Life is an interminable lore. We never stop learning as long as we live. This PhD journey has been one of my most challenging achievements in the academic field. I always thought it is an independent work. However, in the course of this endeavor, I've realized that we need other people to help us understand, to learn, to share our best and worst moments and be an inspiration. Thus, I am truly grateful to the people behind my success.

I give my foremost gratitude to my PhD advisor, Prof. Pei Li, who has guided me throughout my PhD studies and thesis preparation. She has led me into a fascinating scientific world of nanotechnology and gave me a space to explore my passion for scientific research. Her valuable trainings in Polymer Chemistry and presentation skills have greatly improved my skills as an effective researcher. With her continuous support and encouragement, I am able to convince myself that there are many things to improve and thus to become a better scientist in the future. Truly she has influenced me in many ways.

I am thankful to the examination committee for providing me valuable comments and suggestions to improve the quality of my dissertation, Prof. Wai-kin Chan and Dr. To Ngai.

My many thanks to my group colleagues who were there to make my postgraduate life more colorful: Dr. Edmond Ho, Mr. Max Wong, Mr. Chun Ho Yam,

Miss Sandra Siu, Miss Suqing Tan and Miss Joyce Lou. I especially thank Dr. Samuel Lee who has shared a significant contribution to the completion of my thesis.

In this journey, I've realized that it is impossible to just live within the four corners of my laboratory and office. It was during this time that I also explored different places and met different faces. Somehow we need some space and meet new friends to fill us up for a good rest and enjoy the things we should not miss in life. My heartfelt gratitude goes to the many international postgraduate students whom I have shared my experiences, who have empathized me in this journey. I am also thankful to other people outside school who gave me an inspiration to enjoy and live life: Chris, Louis, David, Adam, Antonio, Jacky and most especially JD.

I gratefully acknowledge the financial support of the Hong Kong Polytechnic University in granting me scholarships and support for my studies and international conferences.

Finally, I am thankful to my parents who have a big influence in pursuing my dream of becoming a famous scientist and to my brother and sisters for their encouragement.

I could not come this far without support from these people and institution. My success is not fully mine but I am just an instrument to bring out a significant contribution to science. I will never stop dreaming, imagining and being hungry for knowledge and discovering things for the preservation of human life.

TABLE OF CONTENTS

CERTIFICATE OF ORIGINALITY	i
ABSTRACT.....	ii
PUBLICATIONS, CONFERENCES, SYMPOSIA	vi
ACKNOWLEDGEMENTS.....	viii
TABLE OF CONTENTS.....	x
LIST OF FIGURES.....	xvii
LIST OF TABLES.....	xxxvi
LIST OF SCHEMES.....	xxxvii
LIST OF ABBREVIATIONS.....	xxxviii
LIST OF SYMBOLS NOMENCLATURE.....	xl

Chapter 1 Introduction to metal/polymeric composite particles 1

1.1 Definition and synthesis of metal/polymeric composite particles

1.2 Synthesis of gold nanoparticles

1.2.1 Chemical Methods

1.2.2 Non-chemical methods

1.2.2.1 Electrochemical method

1.2.2.2 Thermal decomposition

1.2.2.3 Photochemical method

1.2.2.4 Sonochemical method

1.2.2.5 Laser ablation method

1.2.2.6 Microwave assisted method

1.2.3 Biological Synthesis

1.2.4 Polymer mediated synthesis

1.3 Polymer-based template and nanoreactors for the formation of metal/polymer composite particles

1.3.1 Homopolymers

1.3.2 Block copolymers

1.3.3 Dendrimers

1.3.4 Polymer particles

1.3.4.1 Microgel particles

1.3.4.2 Core-shell particles with polyelectrolyte brushes

1.4 Applications of metal/polymeric composite particles

1.5 Drawbacks of current methods on the synthesis of metal/polymeric composite particles

1.6 Introduction to amphiphilic core-shell particles

- 1.6.1 Particle synthesis and polymerization mechanism
- 1.6.2 Unique features of core-shell particles
- 1.6.3 Potential applications of core-shell particles
- 1.6.4 Smart core-shell particles
 - 1.6.4.1 Temperature sensitivity
 - 1.6.4.2 pH sensitivity

Chapter 2 Objectives92

- 2.1 Rationale of using water-dispersible core-shell particle as a template and a nanoreactor
 - 2.1.1 The core component
 - 2.1.2 The shell component
- 2.2 Challenges
- 2.3 Specific Objectives

Chapter 3 Experimental Section.....99

- 3.1 Materials
- 3.2 Synthetic Methods
 - 3.2.1 Synthesis of core-shell particles
 - 3.2.2 Synthesis of Au/core-shell composite particles
 - 3.2.3 Synthesis of Au@Ag/core-shell microgel composite particles
- 3.3 Measurements and Characterization
 - 3.3.1 Particle size and *Zeta*-potential Measurements
 - 3.3.2 Fourier Transform Infrared (FT-IR) Spectroscopy

- 3.3.3 Nuclear Magnetic Resonance (NMR) Spectroscopy
- 3.3.4 Ultraviolet Visible (UV-vis) Spectroscopy
- 3.3.5 Field Emission Scanning Electron Microscopy (FESEM)
- 3.3.6 Transmission Electron Microscopy (TEM)
- 3.3.7 Atomic force microscopy (AFM)
- 3.3.8 X-ray Diffraction Spectroscopy (XRD)
- 3.3.9 X-ray photoelectron Spectroscopy (XPS)

**Chapter 4. PNIPAm/PEI Core-Shell Microgels as Dual Nanoreactors
and Templates for Synthesis of Smart Gold/Polymer
Composite Particles. 123**

- 4.1 PNIPAm/PEI as a multifunctional template for the synthesis of gold nanoparticles and composite particles
 - 4.1.1 Microgel as a nanoreactor for gold ion reduction
 - 4.1.1.1 Kinetics of Au salt reduction and formation of gold nanoparticles
 - 4.1.1.2 Proposed mechanism of gold salt reduction using amino group in the PEI shell of the core-shell template
 - 4.1.2 Microgel as a stabilizer of gold nanoparticles
 - 4.1.3 Microgel as an immobilizer of gold nanoparticles
 - 4.1.4 Microgel as a smart regulator of gold nanoparticle accessibility

4.2 Measurement and Characterization of gold/microgel (Au/PNIPAm/PEI) composite particles

4.2.1 Particle size and size distribution

4.2.2 Colloidal stability

4.2.3 SEM and TEM images

4.2.4 UV-vis spectroscopy

4.2.5 FTIR and NMP Spectroscopy

4.2.6 HRTEM and Crystallinity of Au nanoparticles (XRD)

4.2.7 Surface composition of composite particles (XPS)

4.3 Factors affecting the formation of Au/PNIPAm/PEI composite particles

4.3.1 Effect of pH

4.3.1.1 Characterization of Au/PNIPAm/PEI composite particles in electron microscopies

4.3.1.2 pH- Dependent formation of composite particles

4.3.1.3 Comparison of kinetics of gold nanoparticle formation in microgel under different pH conditions

4.3.2 Effect of solution temperature

4.3.2.1 Characterization using electron microscopies

4.3.2.2 Temperature dependent formation of composite particles

4.3.2.3 Comparison of kinetics of gold nanoparticle formation with microgels in different temperature

4.3.3 Effect of amino to gold salt ratio (N/Au)

- 4.3.3.1 Characterization of particle morphology using electron microscopies
- 4.3.3.2 N/Au dependent formation of composite particles
- 4.3.3.3 Size and surface charge of composite particles
- 4.3.4 Effect of heating on Au/PNIPAm/PEI composite particles
 - 4.3.4.1 Characterization of thermally treated gold composite particles using electron microscopies
 - 4.3.4.2 Particle size and colloidal stability
- 4.4 Conclusions

Chapter 5 Synthesis of Bimetallic of Au@Ag Using PNIPAm/PEI Core-Shell Microgel Templates.....209

- 5.1 Synthesis of Au@Ag bimetallic nanoparticles using core-shell microgel template
- 5.2 Characterization of original template and composite particles
 - 5.2.1 Particle size and colloidal stability
 - 5.2.2 Morphologies of composite particles
 - 5.2.3 UV-vis spectroscopy
 - 5.2.4 HRTEM and Crystallinity of Au@Ag nanoparticles
 - 5.2.5 X-ray photoelectron spectroscopy (XPS)
- 6.3 Conclusion

Chapter 6	Catalytic activities of Au/PNIPAm/PEI and Au@Ag/PNIPAm/PEI.....	230
6.1	Catalytic activity of Au/PNIPAm/PEI composite particles	
6.1.1	Influence of pH and temperature sensitivity of microgel template on the catalytic activity	
6.2	Catalytic activity of Au@Ag/PNIPAm/PEI composite particles	
6.3	Comparison of the catalytic activities between Au and Au@Ag in PNIPAm/PEI template	
6.4	Conclusion	
Chapter 7	Concluding Remarks and Future Study.....	248
7.1	Summary of the Major Findings	
7.2	Significance and Implications of this Study	
7.3	Recommendation for Future Work	
Chapter 8	References.....	256

LIST OF FIGURES

Chapter 1

- Figure 1.1** TEM images of metal/polymer composite particles showing different ways to encapsulate the metal nanoparticles (dark dots): (a) PNIPAM-*b*-PMOEGMA/gold nanocomposite^[1], (b) PS-*co*-PGA/ gold nanoparticles^[2], (c) PS/poly(aminoethylmethacrylate hydrochloride)/gold particles PNIPAM-*co*-GMA/gold nanoparticles^[3], (d) PNIPAM-*b*-PMOEGMA/ gold nanostructures with immobilized silver nanoparticles^[4] 3
- Figure 1.2** a) TEM image of the Turkevich method gold sol reduction with sodium citrate solution, magnification x50,000, a mean diameter of 20.0 ± 1.5 ^[6], b) TEM image of the Brust-Schiffrin thiol-derivatized gold nanoparticles with a diameter range of 1-3 nm.^[7] 5
- Figure 1.3** Preparation of anionic mercapto ligand-stabilized gold nanoparticles in water.^[9] 6
- Figure 1.4** General scheme for place –exchange reactions between alkanethiol-AuNPs and various types of functionalized thiols.^[10] 7
- Figure 1.5** a) Electrochemical formation of Pd metal nanoparticles stabilized by tetraoctylammonium bromide. b,c,d) TEM images of Pd metal nanoparticles formed at different current densities of 5.0, 0.8, 0.1 mA/cm² respectively.^[22] 9

Figure 1.6 Schematic diagram for thermal decomposition of gold acetate powder producing gold nanoparticles. ^[23]	11
Figure 1.7 TEM images of gold nanoparticles produced from photochemical synthesis in different sizes and shapes in different concentration of reducing agent (sodium oxalate, 0.1M): a) 68µL with more spherical gold nanoparticles, b) 65 µL with increased hexagonal and truncated triangular gold nanoparticles, c) 62µL with decreased gold spherical nanoparticles. ^[24]	12
Figure 1.8 TEM image of gold nanoparticles deposited on chitosan. ^[25]	14
Figure 1.9 Sonochemically synthesized gold nanoparticles in different organic solvents. a) Dimethyl sulfoxide (DMSO), b) Tetrahydrofuran, c) Acetonitrile. ^[26]	15
Figure 1.10 Schematic illustration of the microwave assisted synthesis of gold nanoparticles. ^[27]	16
Figure 1.11 Schematic diagram on the reduction of metal ions to nanoparticles in microorganisms both intra- and extra-cellular precipitation. ^[28]	17
Figure 1.12 TEM images of gold nanoparticles growing in the inner and outer layer of the <i>Acidithiobacillus thiooxidans</i> spp. Bacteria. ^[29]	18
Figure 1.13 TEM images of composite particles of gold metal nanoparticles with, a) <i>P.jadini</i> (yeast) and b) <i>V.luteoalbum</i> (fungal cultures). ^[30]	20
Figure 1.14 TEM images of gold nanoparticle formation in cystolic fungus extract (<i>C.albicans</i>) in different concentration and incubation time. a) and	21

b) with 1 mL extract in 12 hours and 24 hours of incubation, respectively.
c) and d) with 5 mL of extract in 12 hours and 24 hours incubation,
respectively. ^[31]

Figure 1.15 Synthesis of gold nanoparticles from soybeans. ^[32]	22
Figure 1.16 TEM images of gold nanoparticles produced from leaf extracts of <i>Magnoliakobus</i> and <i>Diopyros kaki</i> in different concentrations (v/v) of the extract, a) 10%, b) 20%, c) 50% at 60°C for 30 minutes and d) Effect of leaf extract concentration on the gold nanoparticle average size. ^[33]	23
Figure 1.17 Important mechanisms of heavy metal tolerance in plants. ^[34]	24
Figure 1.18 Adsorption and cobridging of (a) PVP molecules in (b) a surface layer via Au-atoms on a gold particle. ^[40]	27
Figure 1.19 PAAm-induced synthesis and stabilization of gold nanoparticles in water. ^[41]	28
Figure 1.20 a) Synthetic route of the PoPD-gold nanoparticles, b) FESEM images of PoPDsubmicrospheres, c) FESEM images of PoPDsubmicrospheres decorated with gold nanoparticles. ^[42]	29
Figure 1.21 Aggregates generated by PEI, PEI-1R, PEI-2R. ^[43]	30
Figure 1.22 Schematic illustration of the formation of PSSMA-coated metal nanoparticles. ^[44]	31
Figure 1.23 Classification overview of hybrid colloids made from organic/inorganic materials. ^[51]	33

Figure 1.24 Polymer-mediated assembly approaches to fabrication of ordered nanocomposites and their possible utilization. ^[52]	34
Figure 1.25 Schematic fabrication of Au@PVP nanoparticles by SI-ATRP. ^[53]	36
Figure 1.26 Preparation of gold nanoparticles within PNIPAM hydrogel. SEM/TEM images of a) before and b) after formation of gold nanoparticles. ^[54]	37
Figure 1.27 a) Schematic diagram on the formation of the hybrid compound micelles (loaded with Au nanoparticles in its core), b) TEM image of the Au/polymeric nanocomposite. ^[55]	39
Figure 1.28 Proposed mechanism of AuCl ₄ ⁻ reduction and particle formation using PEO-PPO-PEO block copolymer. ^[56]	40
Figure 1.29 Preparation of hybrid polymeric micelles (HPMs) and the reversion of the core-shell template releasing gold nanoparticles from its core to the shell region. ^[57]	42
Figure 1.30 a) Schematic preparation of gold nanoparticle / diblock copolymer (poly(<i>tert</i> -butylstyrene) -b-poly(sodium sulfamate/carboxylate-isoprene)) (BS-SCI) hybrid assemblies, b) TEM image of the BS-SCI hybrid particles (inset is an HRTEM). ^[58]	43
Figure 1.31 a) Schematic illustration of two types of hybrid micelles incorporated with Au nanoparticles, b) HRTEM images of the hybrid giant micelles using CCL and c) SCL as templates. ^[61]	45

Figure 1.32 a) Schematic diagram on the synthesis of corona filled block copolymer (PS- <i>b</i> -PAA), b and c are TEM images of Ag/PS- <i>b</i> -PAA in different silver nitrate concentration. ^[62]	46
Figure 1.33 Schematic illustration of preparation of composite nanoparticles. ^[63]	47
Figure 1.34 Schematic illustration and TEM images of gold/polymeric composite particles of PIB/AuNP@PI- <i>b</i> -P2VP (a,d,g), PI/PS/AuNNP@PS- <i>b</i> -P2VP-1 (b,e,h,) and PMMA/AuNP@PS- <i>b</i> -P2VP-2 (c,f,i). ^[63]	49
Figure 1.35 Chemical structure of polyamidoamine (PAMAM) dendrimer ^[64] .	50
Figure 1.36 Formation of Au nanoparticles in PEG-attached PAMAM dendrimers ^[65]	51
Figure 1.37 Chemical structure of hydroxyl-terminated poly(amido amine) (PAMAM) (G4-OH). ^[66]	52
Figure 1.38 Dendrimer encapsulated nanoparticle scheme ^[67] .	52
Figure 1.39 Effective process showing semiconductor, metal and magnetic nanoparticles formation in gel networks. ^[76]	55
Figure 1.40 Chemical structures and reaction for the synthesis of poly(glycidyl methacrylate-co- <i>N</i> -isopropylacrylamide)[(poly(GMA-co-NIPAM))] template .	56
Figure 1.41 Synthesis of thermosensitive hybrid metal-core-shell particles with gold nanoshells. ^[77]	57

- Figure 1.42** Schematic illustration of the synthesis of core-shell Au-polyaniline nanoparticles. TEM images of a) Au nanoparticles incorporated into the microgel templates. b) Au coated with polyaniline incorporated within the microgel templates. ^[79] 59
- Figure 1.43** a) Schematic diagram on the synthesis of gold and gold/silver nanoparticles using a microgel template. b) TEM image of gold nanoparticles grown on the microgel, c) seeded growth gold nanoparticles. ^[80] 61
- Figure 1.44** TEM images of gold nanoparticle loaded in a) room temperature and b) at 50°C. ^[81] 62
- Figure 1.45** A) TEM image of Au/PS/PANI composite particles, B) SEM image of the Au/PS/PANI composite particles. ^[82] 63
- Figure 1.46** a) Low and b) high resolution TEM images of PNIPAM-AA microgels loaded with gold nanorods. Scale bars are 1 μm and 100 nm, respectively. ^[83] 64
- Figure 1.47** a) Sketch of collapsed PNIPAM microgel with polyelectrolyte-coated Au nanorod, b) TEM image of PNIPAM microgel with Au nanorods. ^[84] 65
- Figure 1.48** Scheme for the formation of gold nanoparticles using a spherical polymeric polyelectrolyte. ^[85] 66
- Figure 1.49** a) Formation and immobilization of gold nanoparticles in PS-PIL template. b and c) TEM images of gold nanoparticles on the surface of the template. ^[85] 67

Figure 1.50 a) Schematic diagram of the silver nanoparticles trapped inside the nano-type PS-PEGMA template. b) and c) Cryo-TEM Images of the Au in PS-PEGMA nanocomposite. ^[86]	69
Figure 1.51 Schematic diagram for the synthesis of PS-PIL template for metal nanoparticle formation and immobilization. ^[87]	70
Figure 1.52 Generalized scheme for the biomedical application of gold nanoparticles. ^[88] .	72
Figure 1.53 Schematic representation of drug delivery from temperature-sensitive hydrogel. ^[90]	73
Figure 1.54 Reduction of <i>p</i> -nitrophenol to <i>p</i> -aminophenol monitored by UV-Visible spectroscopy. ^[92]	74
Figure 1.55 Schematic representation of catalytic oxidation of benzyl alcohol in the presence of gold nanoparticles immobilized in thermosensitive microgels ^[92] .	74
Figure 1.56 UV-Vis spectra of gold nanoparticles in polymeric composite particles, showing different colors at 25°C (blackline) and 40°C (in gray line). (a) Au nanoparticles in GMA- <i>co</i> -PNIPAm, (b) AuAg in GMA- <i>co</i> -PNIPAm. ^[93]	75
Figure 1.57 Examples of core-shell particles produced using our synthetic route. ^[104]	79

Figure 1.58 Formation mechanism of amphiphilic core-shell particles via graft polymerization of vinyl monomer from a water soluble polymer containing amine group in aqueous media. ^[104]	81
Figure 1.59 a) TEM image of poly(<i>n</i> -butyl acrylate) /chitosan core-shell particles, b) Antibacterial activity in different laundering cycles. ^[80]	84
Figure 1.60 Schematic illustration for preparation of fluorescent polymeric core-shell particle for cupric ion detection. ^[110]	85
Figure 1.61 Futuristic image of an intelligent multifunctional particles. ^[115]	87
Figure 1.62 Chemical structure of PNIPAm and water molecules (O) below the LCST ^[116]	88
Figure 1.63 Structure of branched PEI in solution. ^[117]	89
 Chapter 2	
Figure 2.1 Chemical structure of poly(<i>N</i> -isopropylacrylamide) and <i>N,N'</i> -methylene-bis-acrylamide.	93
 Chapter 3	
Figure 3.1 Formation of core-shell microgel (PNIPAm/PEI) via graft copolymerization of NIPAM from b-PEI using TBHP as initiator.	101
Figure 3.2 Schematic diagram on the synthesis of gold nanoparticles using PNIPAm/PEI as template.	103
Figure 3.3 Illustration of Au@Ag synthesis using the microgel template.	105

Figure 3.4 Schematic diagram of a particle with double layer.	107
Figure 3.5 Schematic diagram of an SEM set-up. ^[133]	112
Figure 3.6 Schematic diagram of a TEM set-up. ^[134]	114
Figure 3.7 Schematic diagram of AFM set-up.	117
Figure 3.8 Bragg's Law reflection representation. ^[136]	119
Figure 3.9 XPS working principle based on photoelectric effect.	121

Chapter 4

Figure 4.1 TEM images of the a) PEI-based microgel template, b) Au/(PNIPAm/PEI) composite particles synthesized at 25 ⁰ C and pH 7.30. c) Heated Au/PNIPAM/PEI composite particles at 60 ⁰ C.	127
Figure 4.2 1)TEM images of Au/(PNIPAm/PEI) composite particles generated at 60 ⁰ C. 2) TEM measurement of particle size and distribution.	127
Figure 4.3 Time courses of the absorbance monitored at 525 nm during the formation of gold nanoparticles using PNIPAm/PEI (25 ⁰ C, pH 5.6).	129
Figure 4.4 Comparison of Au salt reduction in different templates. Solid circles represent data using PNIPAm/PEI core-shell particles as a template. Hollow circles represent data using branched PEI in solution as template. Conditions for both synthesis: 25 ⁰ C, pH 5.6, 200 rpm, N/Au = 28.5. The overall rate constant of reaction is based on the change of absorbance per time ($\Delta A/t$), which is proportional	131

to the reduction of gold ions to gold nanoparticles.

- Figure 4.5** Proposed mechanism in the oxidation of the amine group to imine. 133
- Figure 4.6** Conformational changes of microgel template from stimuli response to solution pH and temperature. 138
- Figure 4.7** AFM micrographs of PNIPAM/PEI microgel particles treated (a) at 29°C; (b) at 45°C and (c) from 45°C and cooled to 29°C. Scale bar: 200 nm. 139
- Figure 4.8** Particle size and size distribution of pure microgel template and Au/(PNIPAm/PEI) composite particles synthesized at optimum conditions of 25°C and pH 7.30. 141
- Figure 4.9** Surface charge profile of Au composite particles in different solution pH. 142
- Figure 4.10** Surface charge profile of Au composite particles in different temperature. 144
- Figure 4.11** a) SEM image of Au/(PNIPAm/PEI) composite particles, b) TEM image of Au/(PNIPAm/PEI) composite particles. These particles were synthesized at 25°C and at pH 7.30. 146
- Figure 4.12** TEM micrograph of single PNIPAm/PEI microgel surrounded with Au NPs and size distribution histograms of AuNPs. 147
- Figure 4.13** UV-vis spectra showing the reduction of gold nanoparticles in PNIPAm/PEI microgel with increasing time (min). Absorption peak is at 525 nm. Conditions of the synthesis: 25°C, pH 5.6, 200 rpm, N/Au = 28.5. 148
- Figure 4.14** FTIR analysis of pure (black ink) and Au loaded (red ink) microgel. 150

Figure 4.15	NMR spectra of pure microgel (upper) and Au loaded microgel (lower).	151
Figure 4.16	HRTEM image of Au nanoparticle embedded within a microgel template.	153
Figure 4.17	XRD spectra of Au/(PNIPmM/PEI) composite particles.	153
Figure 4.18	XPS survey scans of PNIPAm-PEI microgel with immobilized Au nanoparticles. Inset is the Au 4f core-level spectra obtained from PNIPAm-PEI microgelwith immobilized Au nanoparticles.	156
Figure 4.19	XPS survey scans of elements of convolute C 1s, N1s and O1s.	156
Figure 4.20	XPS survey scan of Au in PNIPAm/PEI microgel.	157
Figure 4.21	TEM images of Au nanoparticles in PNIPAm/PEI microgels synthesized at pH 3, 25°C, 250 rpm, 2 hrs. reaction with N/Au mole ratio = 28.5.	159
Figure 4.22	Single composite particle containing AuNPs inPNIPAm/PEI template synthesized at 25°C, pH 3, 250 rpm, 2 hrs. reaction with N/Au mole ratio = 28.5.	160
Figure 4.23	TEM images of Au nanoparticles in PNIPAm/PEI template synthesized at pH 5, 25°C,250 rpm, 2 hrs. reaction with N/Au mole ratio = 28.5.	161
Figure 4.24	Single composite particle containing AuNPs inPNIPAm/PEI template synthesized at 25°C, pH 5, 250 rpm, 2 hrs. reaction with N/Au mole ratio = 28.5.	162
Figure 4.25	TEM images of Au nanoparticles in PNIPAm/PEI microgels	163

synthesized at pH 7, 25°C, 250 rpm, 2 hrs. reaction with
N/Au mole ratio = 28.5.

Figure 4.26 Single composite particle containing AuNPs in PNIPAm/PEI template 164

synthesized at 25°C, pH 7, 250 rpm, 2 hrs. reaction with
N/Au mole ratio = 28.5.

Figure 4.27 TEM images of Au nanoparticles in PNIPAm/PEI microgels 165

synthesized at pH 9, 25°C, 250 rpm, 2 hrs. reaction with
N/Au mole ratio = 28.5.

Figure 4.28 Single composite particle containing AuNPs in PNIPAm/PEI 166

template synthesized at 25°C, pH 9, 250 rpm, 2 hrs. reaction
with N/Au mole ratio = 28.5.

Figure 4.29 TEM images of Au nanoparticles in PNIPAm/PEI microgels 167

synthesized at pH 12, 25°C, 250 rpm, 2 hrs. reaction with
N/Au mole ratio = 28.5.

Figure 4.30. Single composite particle containing AuNPs in PNIPAm/PEI 168

template synthesized at 25°C, pH 12, 250 rpm, 2 hrs. reaction
with N/Au mole ratio = 28.5

Figure 4.31 Representative TEM images of composite particle containing AuNPs in 169

PNIPAm/PEI templates synthesized in different pH conditions: a) 3, b) 5,
c) 7, d) 9, d) 12 (reaction conditions: at 25°C, 250 rpm, 2 hours reaction
with N/Au mole ratio = 28.5)

- Figure 4.32** Degree of protonated amines versus solution pH. Insert is the structure
conformation of the PEI during protonation and deprotonation. 170
- Figure 4.33** Kinetic comparison of gold nanoparticle formation in different pH
conditions of microgel template. (Conditions: [microgel] = 400 ppm;
molar ratio of N/Au³⁺ = 28.5; 200 rpm at 20 °C) 172
- Figure 4.34** TEM images of Au nanoparticles in PNIPAm/PEI microgels
synthesized at 5°C, pH 7.0, 250 rpm, 2 hrs. reaction with
N/Au mole ratio = 28.5. 174
- Figure 4.35** Single composite particle containing AuNPs inPNIPAm/PEI template
synthesized at 5°C,pH 7.0, 250 rpm, 2 hrs. reaction with N/Au mole ratio
= 28.5. 175
- Figure 4.36** TEM images of Au nanoparticles in PNIPAm/PEI microgels
synthesized at 15°C,pH 7.0, 250 rpm, 2 hrs. reaction with
N/Au mole ratio = 28.5. 177
- Figure 4.37** Au nanoparticle using PNIPAm/PEI. The reaction took placed
at 15°C,pH 7.0, 250 rpm, for 2 hours. N/Au mole ratio = 28.5. 178
- Figure 4.38** TEM images of Au nanoparticles in PNIPAm/PEI microgels
synthesized at 25°C,pH 7.0, 250 rpm for 2 hours.
N/Au mole ratio = 28.5. 179

Figure 4.39	Single composite particle containing AuNPs inPNIPAm/PEI template synthesized at 25°C,pH 7.0, 250 rpm for 2 hours. N/Au mole ratio = 28.5.	180
Figure 4.40	TEM images of Au nanoparticles in PNIPAm/PEI microgels synthesized at 30°C,pH 7.0, 250 rpm for 2 hours. N/Au mole ratio = 28.5.	181
Figure 4.41	Single composite particle containing AuNPs inPNIPAm/PEI template synthesized at 30°C,pH 7.0, 250 rpm for 2 hours. N/Au mole ratio = 28.5.	182
Figure 4.42	TEM images of Au nanoparticles in PNIPAm/PEI microgels synthesized at 35°C,pH 7.0, 250 rpm for 2 hours. N/Au mole ratio = 28.5.	183
Figure 4.43	Particle size distribution of AuNPs inPNIPAm/PEI template synthesized at 35°C,pH 7.0, 250 rpm for 2 hours. N/Au mole ratio = 28.5.	184
Figure 4.44	TEM images of Au nanoparticles in PNIPAm/PEI microgels synthesized at 45°C,pH 7.0, 250 rpm for 2 hours. N/Au mole ratio = 28.5.	185
Figure 4.45	Particle size distribution of AuNPs inPNIPAm/PEI template Synthesized at 45°C,pH 7.0, 250 rpm for 2 hours. N/Au mole ratio = 28.5.	185
Figure 4.46	TEM Images ofAu@PNIPAm/PEI in different synthesistemperature a) 5°C ,b) 15°C, c) 25°C, d) 30°C, e) 35°C, f) 45°Cconducted in	188

pH 7.0, 250 rpm, 2 hrs. reaction with N/Au mole ratio = 28.5.

- Figure 4.47** Kinetic comparison of gold nanoparticle formation in different temperature conditions of microgel template. Inset is the Arrhenius plot of the kinetic rate constants at different temperatures. (Conditions: [microgel] = 400 ppm; molar ratio of N/Au³⁺ = 28.5; 200 rpm at pH 9.16, stirring rate of 200 rpm). 189
- Figure 5.48** Single composite particle synthesized at 25°C, pH 5.6, 200 rpm for 24 hours. The N/Au mole ratio = 28.5. 192
- Figure 4.49** Composite particle synthesized at 25°C, pH 5.6, 200 rpm for 24 hours reaction. N/Au mole ratio = 14.30. 193
- Figure 4.50** Single composite particle synthesized at 25°C, pH 5.6, 200 rpm for 24 hours reaction with N/Au mole ratio = 14.30. 194
- Figure 4.51** Morphology of gold nanoparticles synthesized with N/Au mole ratio=9.50 (conditions: 25°C, pH 5.6, stirring at 200 rpm for 24 hours). 195
- Figure 4.52** Composite particles and different shapes of Au nanoparticles synthesized with N/Au mole ratio = 9.50. Spherical Au nanoparticles has an average size of 30.50 nm (conditions: 25°C, pH 5.60, 200 rpm 24 hours). 196
- Figure 4.53** Comparison of Au/PNIPAm/PEI composite particles in different 197

amino to gold mole ratios (N/Au). All samples were synthesized at room temperature, pH 5.6, 200 rpm, for 24 hours.

- Figure 4.54** UV- vis spectra of different N/Au mole ratios, black curve represents the 28.5 mole ratio, red curve represents 14.30 and blue represents the 9.50. All other synthetic conditions of the three mole ratios were the same. 198
- Figure 4.55** Size distribution of Au clusters synthesized by PNIPAm/PEI microgels with N/Au mole ratio of 28.5 (conditions: 25°C, pH 5.6, stirring at 200 rpm for 24 hours) 202
- Figure 4.56** Post-treatment of Au/PNIPAm/PEI composite microgels at 60 °C for 20 min. (N/Au mole ratio of 28.5). 203
- Figure 4.57** Post-treatment of Au/PNIPAm/PEI composite microgels at 92 °C for 20 min. (N/Au mole ratio of 28.5). 204
- Figure 4.58** Post-treatment of Au/PNIPAm/PEI composite microgels at 92 °C for 1 hour (N/Au mole ratio of 28.5). 205
- Figure 4.59** Particle size and *zeta*-potential profile at different stages. 206

Chapter 5

- Figure 5.1** a) Au@Ag synthesized on the aminopropyl functionalized magnetic microspheres^[177], b) TEM image of Au@Ag synthesized in polyelectrolyte-multilayers using poly(styrene sulfonate).^[167] 210
- Figure 5.2** TEM images of a) PNIPAm/PEI template (Hydrodynamic ave. size: 380±5.0 nm) , b) Au/PNIPAm/PEI seeds (Hydrodynamic ave. size: 284 ± 2.1 nm), c-f) Au@Ag/PNIPAm/PEI (Au/Ag = 0.50, Hydrodynamic ave. size: 270.6 ± 4.1 nm). 217
- Figure 5.3** Au@Ag bimetallic nanoparticles found within the PNIPAm/PEI template. Particle size distribution on the right side. 217
- Figure 5.4** a) Single PNIPAm/PEI particle template with Au@Ag bimetallic nanoparticles, b) Localized Au@Ag bimetallic nanoparticles within the PNIPAM/PEI core-shell interface. 218
- Figure 5.5** UV-vis spectra of Au/(PNIPAm/PEI), Au/(PNIPAm/PEI), Au@Ag/(PNIPAm/PEI) using the same metal ion concentration (N/Au = N/Ag = N/AuAg = 14.09 mole ratio). All composites were synthesized at room temperature, pH 5.50, stirring at 200 rpm for 30 minutes absorption, followed by 30 minutes heating at 60°C. 219
- Figure 5.6** UV-vis spectra of nanoparticles in PNIPAm/PEI template in different Ag to Au mole fractions. Pure silver (0.0); 10% Au (0.1); 30% Au (0.3); 50% Au (0.5); 70% Au (0.7); 90% Au (0.9); Pure Au (1.0). 220

Figure 5.7 (a) HRTEM images of a single Au@Ag nanocrystal with corresponding lattice parameters of Au and Ag, (b) SAED of bimetallic (Au@Ag) in PNIPAm/PEI template.	222
Figure 5.8 Survey scan of Au-Ag bimetallic nanoparticles @PNIPAm-PEI microgel film (Au/Ag of 50/50 mol. ratio)..	224
Figure 5.9 Survey scan of Au-Ag bimetallic nanoparticles@PNIPAm-PEI microgel film (Au/Ag of 50/50 mol. ratio).	225
Figure 5.10 Survey scan of Au-Ag bimetallic nanoparticles@PNIPAm-PEI microgel film.(Au/Ag of 90/10 mol. ratio).	226
Figure 5.11 XPS spectrum of (a) C 1s ; (b) N 1s and (c) O 1s of Au-Ag@PNIPAM-PEI microgel sample with Au/Ag of 90/10 mol. ratio).	226
Figure 5.12 XPS spectrum of deconvoluted (a) Au4f and (b) Ag3d of Au-Ag@PNIPAm-PEI microgel sample with Au/Ag of 90/10 mole ratio).	227
 Chapter 6	
Figure 6.1 Different types of polymers hybrids with catalytic applications. ^[180]	231
Figure 6.2 Catalytic reduction reaction of <i>p</i> -nitrophenol to <i>p</i> -aminophenol using Au/PNIPAm/PEI composite particles.	233
Figure 6.3 a) UV-vis spectra of the sodium borohydride reduction of <i>p</i> -nitrophenol to <i>p</i> -aminophenol without the use of a catalyst, b) Plot of $\ln(C_t/C_0)$ as a function of time of control experiment for the reduction of <i>p</i> -nitrophenol	234

to *p*-aminophenol.

- Figure 6.4** UV-vis spectroscopy profile for the reduction of *p*-nitrophenol to *p*-aminophenol using Au/ (PNIPAm/PEI) composite particle as catalyst. 235
- Figure 6.5** Plot of $\ln(C_t/C_0)$ as a function of time for the reaction catalyzed by Au/PNIPAm/PEI (N/Au=28.20 mole ratio). 236
- Figure 6.6** Effect of temperature on the catalytic activity of Au/ (PNIPAm/PEI) composite particle used as catalyst for reduction of *p*-nitrophenol to *p*-aminophenol at pH=5.6. 239
- Figure 6.7** Effect of pH on the catalytic activity of Au/ (PNIPAm/PEI) composite particle used as catalyst for reduction of *p*-nitrophenol to *p*-aminophenol at room temperature. 241
- Figure 6.8** UV-vis spectroscopy profile for the reduction of *p*-nitrophenol to *p*-aminophenol using Au@Ag/ (PNIPAm/PEI) composite particle as catalyst. 244
- Figure 6.9** Plot of $\ln(C_t/C_0)$ as a function of time for the reaction catalyzed by Au/ PNIPAm/PEI in different N/Au mole ratios and Au@Ag bimetallic nanoparticles in PNIPAm/PEI. 246

LIST OF TABLES

Table 3.1 Conductivity of particle dispersion in each repeated centrifugation/redispersion cycles of PNIPAm/PEI microgels.	102
Table 4.1 Synthesis temperature and its corresponding average gold nanoparticle size.	186
Table 4.2 Particle size and <i>zeta</i> -potential profile of Au composite particles in different N/Au mole ratios with original template.	200
Table 5.1 Particle size and <i>zeta</i> -potential profile of the original template (PNIPAm/PEI), Au/PNIPAm/PEI and Au @Ag composite particles.	215
Table 5.2 XPS Analysis results of Au and Ag peak positions (spin-orbit doublet) with two different Au/Ag mole ratios after reduction treatment	228
Table 5.3 XPS Analysis results of Au/Ag surface atomic ratio with two different Au/Ag mole ratios after reduction treatment.	228
Table 6.1 Linearity of the reaction rate constant at different temperatures.	237

LIST OF SCHEMES

Chapter 4

Scheme 4.1 Schematic diagram on the formation of gold nanoparticles in microgel template. 126

Scheme 4.2 Schematic procedure for the heating process of gold/polymer complex precursor to form fully grown gold composite particles. 201

Chapter 5

Scheme 5.1 a) Formation of bimetallic nanoparticles using gold/PNIPAm/PEI composite particles, b) Formation of Au@Ag nanoparticles using Au nanoparticle as seed. 213

LIST OF ABBREVIATIONS

PEI	polyethyleneimine
PMMA	poly(methyl methacrylate)
PNIPAm	poly(<i>N</i> -isopropylarylamide)
PMMA/PEI	poly(methyl methacrylate)/polyethyleneimine
PNIPAm/PEI	poly(<i>N</i> -isopropylarylamide)/polyethyleneimine
TBHP / <i>t</i> -BOOH	<i>tert</i> -butyl hydroperoxide
MBA	<i>N,N'</i> -methylenebisacrylamide
Au/AuNP	gold/ gold nanoparticles
Ag/AgNP	silver/ silver nanoparticles
Au@Ag	gold with silver bimetallic nanoparticles
Au/PNIPAm/PEI	gold nanoparticles within PNIPAm/PEI template
Au@Ag/PNIPAm/PEI	gold with silver bimetallic nanoparticles within PNIPAm/PEI template
VPTT	volume phase transition temperature
LCST	lower critical solution temperature
PDI	polydispersity index
SPB	spherical polymeric brush
HPM	hybrid polymeric micelle
PEMs	polyelectrolyte multilayers
FTIR	Fourier transform Infrared
¹ H-NMR	proton nuclear magnetic resonance
SEM	scanning electron microscope

TEM	transmission electron microscope
AFM	atomic force microscope
XPS	x-ray photoelectron spectroscopy
XRD	x-ray diffraction spectroscopy
UV-vis	ultraviolet – visible spectroscopy

LIST OF SYMBOLS AND NOMENCLATURE

D_h	hydrodynamic size
k	Boltzman constant
D	diffusion coefficient
η	dispersant viscosity
ζ	<i>zeta</i> -potential
λ	electron wavelength
E_k	kinetic energy
E_b	binding energy
h	Planck's constant
$\Delta A/t$	change of UV-vis absorbance per time
r	rate of disappearance of reactant A
$\frac{d[A]}{dt}$	differential form of the rate of disappearance of reactant A
$k[A]$	product of constant k and the concentration of reactant A
$A_{400,t}$	absorbance of <i>p</i> -nitrophenol at 400 nm at elapsed time <i>t</i> ,
$A_{400,t=0}$	initial absorbance at 400 nm prior to addition of the catalyst
C_t	concentration of <i>p</i> -nitrophenol at time <i>t</i>
C_0	concentration of <i>p</i> -nitrophenol at initial state
k	rate constant of activity

Chapter 1

Introduction to Metal/Polymeric Composite Particles

In this chapter, a comprehensive literature review of metal/polymeric composite particles is examined. Figures are provided to fully illustrate the author's ideas. All figures captioned with references are adopted from its original source. Later, current problems of existing technologies are discussed. Further, amphiphilic core-shell particles of Prof. Pei Li's group is introduced and its potential as a nanoreactor and template for synthesis of metal nanoparticles and composite particles.

1.1 Definition and Synthesis of Metal/Polymeric Composite Particles

There is no strict definition of metal/polymeric composite particles to date. They come in different terms and play of words such as polymer-embedded nanocomposite, hybrid nanoparticle, nanoparticle-filled polymers, and nanostructured polymeric reactor for metal nanoparticle formation or simply just polymer colloids with metal nanoparticles. One logical way to describe this type of composite material is the incorporation of metal nanoparticles into a polymeric system. Metal nanoparticles that can be incorporated in polymeric systems come in different kinds, such as magnetic, semiconductor and noble metals. Polymeric systems are the carrier of these metal nanoparticles. They are mostly referred to as polymer templates. These templates can either be soluble (colloidally soluble) or insoluble (solid or heterogeneous) polymers.

Embedding metal nanoparticles into polymers is the easiest and convenient way for metal nanoparticles' stability, handling and its use for applications. Metal /polymeric composite materials in a colloidal system are mainly composed of two distinct materials; the polymer (e.g. homopolymers, copolymer, multi-component polymer, etc.) and the metal nanoparticles (e.g. Au, Ag, Pt, Pd, etc). The composite particles are stably suspended in a dispersing medium such as water or organic solvent. These materials are synthesized to optimize the use of metal nanoparticles that gives a synergistic property with its polymer support. Figure 1 shows the possible ways to encapsulate the metal nanoparticles within the polymeric particles. The metal nanoparticles can be used as a core of the composite (Figure 1.1a and b ^[1-2]). They can also form and be immobilized on the particle shell (Figure 1c ^[3]). In Figure 1d ^[4], metal nanoparticles are seen in both the core and the shell.

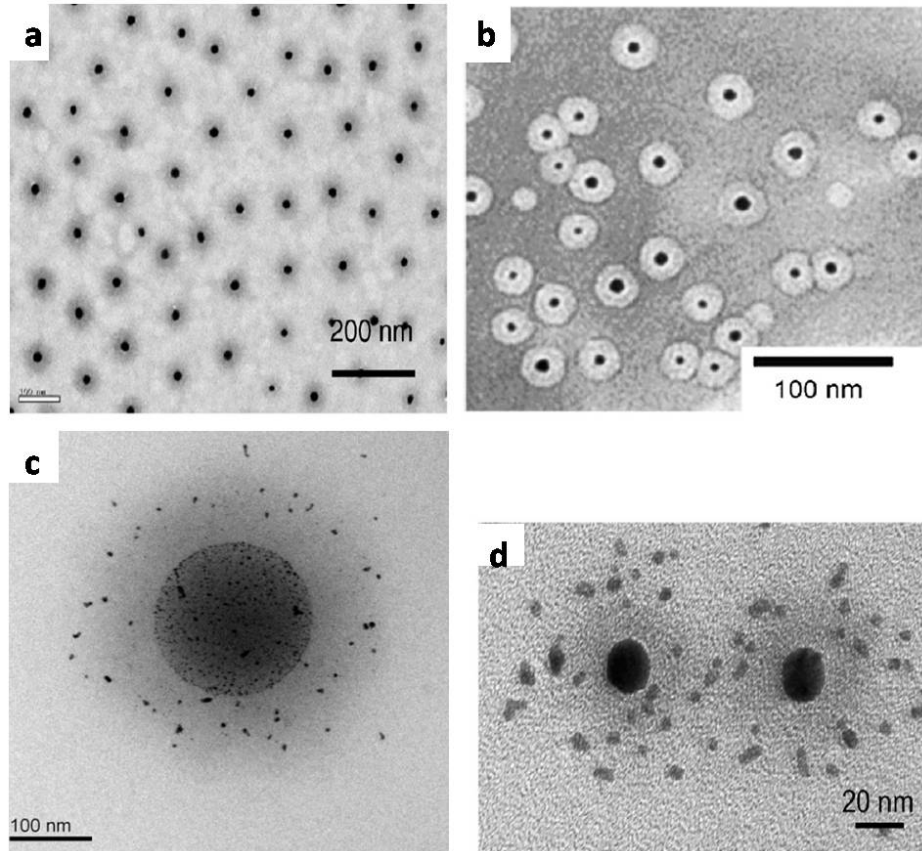


Figure 1.1 TEM images of metal/polymer composite particles showing different ways to encapsulate the metal nanoparticles (dark dots): (a) PNIPAm-*b*-PMOEGMA/gold nanocomposite,^[1] (b) PS-*co*-PGA/ gold nanoparticles,^[2] (c) PS/poly(aminoethylmethacrylate hydrochloride)/gold particles PNIPAm-*co*-GMA/gold nanoparticles,^[3] (d) PNIPAm-*b*-PMOEGMA/ gold nanostructures with immobilized silver nanoparticles^[4].

1.2 Synthesis of Gold Nanoparticles

There are two general approaches in synthesizing metal nanoparticles; top-down and bottom-up. Top-down methods are known to follow physical methods such as lithography and etching methods of bulk metals to nanoscopic scale. Bottom-up

approaches are more common these days since they follow more conventional wet chemical methods of synthesis. The bottom-up approach has also an advantage of generating uniform nanoparticles with controlled size and shape.

1.2.1. Wet Chemical Methods

Wet chemical methods which belong to bottom-up approaches were first reported by Michael Faraday more than 150 years ago.^[5] In general, this approach uses metal salt solution which is directly mixed with reducing agents (e.g. hydrogen, alcohol, hydrazine or borohydride) in the presence of stabilizing agents (e.g. ligands, polymers or surfactants). The most common and cited synthesis of gold nanoparticles are in the works of Turkevich *et al.*^[6] and Brust-Schiffrin *et al.*^[7] A standard gold colloid solution based on Turkevich's route involves the reaction of chloroauric acid with sodium citrate in solution under boiling condition ($\text{HAuCl}_4 + \text{Na}_3\text{C}_6\text{H}_5\text{O}_7 \longrightarrow \text{Au}^0$). The mixture is stirred until color changed from very grayish pink to deep wine red. The highly reproducible procedure gives spherical gold particles with a mean diameter of 20.0 ± 1.5 nm as seen in Figure 1.2a. Later on Frens^[8] was able to control the size formation of gold nanoparticles by varying the reducing agent to gold salt ratio during reduction process. However, a practical modification of this method was further investigated by Kunitake *et al.*^[9] by using sodium 3-mercaptopropionate to the pre-stabilized citrate gold nanoparticles, Figure 1.3.

Another pioneering synthetic route of gold nanoparticles is the Brust-Schiffrin method. The Brust-Schiffrin's method involves the reduction of gold salt solution using a thiol-based organic solvent in a two-phase system ($\text{HAuCl}_4 + \text{NaBH}_4 +$

$\text{CH}_3(\text{CH}_2)_{10}\text{CH}_2\text{SH} \longrightarrow \text{CH}_3(\text{CH}_2)_{10}\text{CH}_2\text{SHAu}$). Here, hydrogen tetrachloroaurate is mixed with tetraoctylammonium bromide in toluene creating a two-phase system. Vigorously mixing this system efficiently can transfer all the tetrachloroaurate into the organic layer, in which dodecanethiol is further added. While being stirred, sodium borohydride solution is mixed as well. The organic layer is then separated, evaporated and mixed with ethanol to get rid of excess thiol. The mixture is further kept for 4 hours at -18°C , giving a dark precipitate. The crude product is further dissolved in toluene and precipitated in ethanol. TEM image of the gold nanoparticles synthesized in this method is seen in Figure 1.2b with a diameter range of 1-3 nm. Further examination of these particles revealed a cuboctahedral and icosahedral structures.

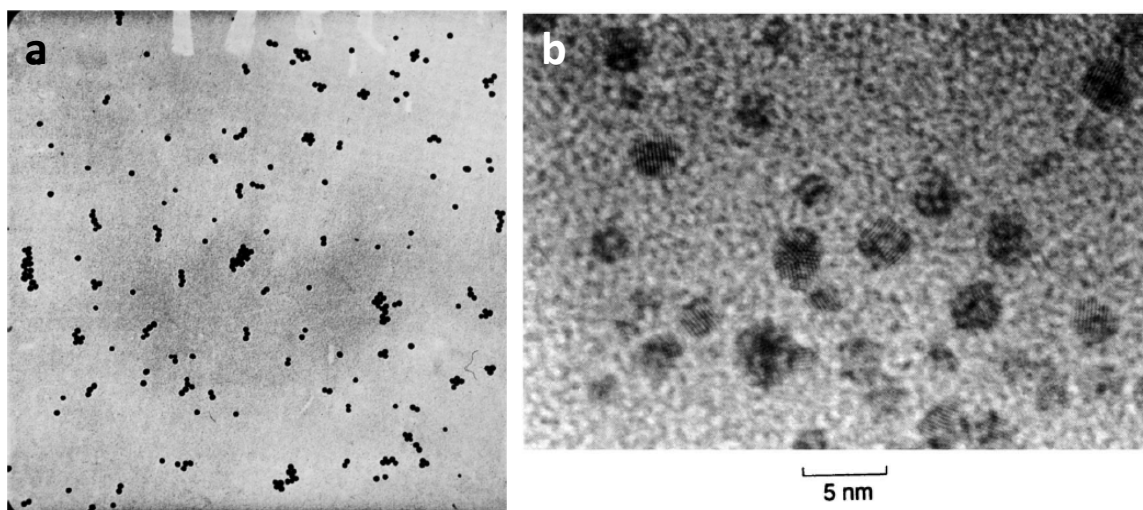


Figure 1.2 a) TEM image of the Turkevich method gold sol reduction with sodium citrate solution, magnification $\times 50,000$, a mean diameter of 20.0 ± 1.5 ^[6], b) TEM image of the Brust-Schiffrin thiol derivatized gold nanoparticles with a diameter range of 1-3 nm. ^[7]

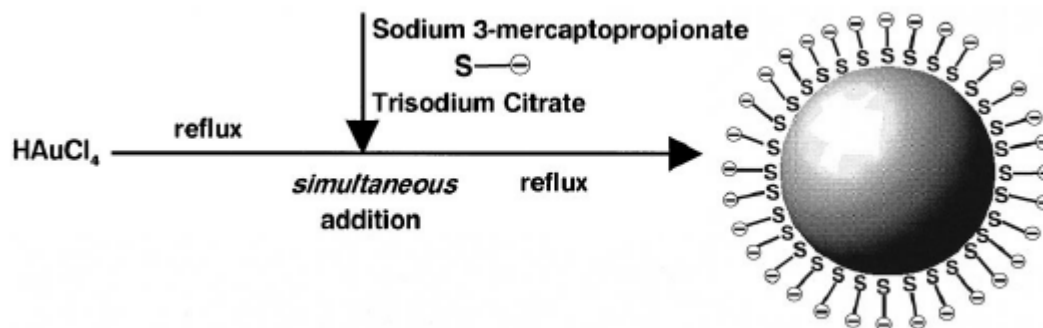


Figure 1.3 Preparation of anionic mercapto ligand-stabilized gold nanoparticles in water. ^[9]

A modified Brust-Schiffrin process was carried out by Murray *et al.* ^[10] using different functional thiols. This method was named as “place exchange” process wherein various functionalities such as bromine, cyanide, ferrocenyl, alcohol, formaldehyde and anthraquinone were used in replacement of a simple alkane group, Figure 1.4. These types of place exchangers are classified as ligands in general, wherein they attach themselves into gold nanoparticles to protect and stabilize.

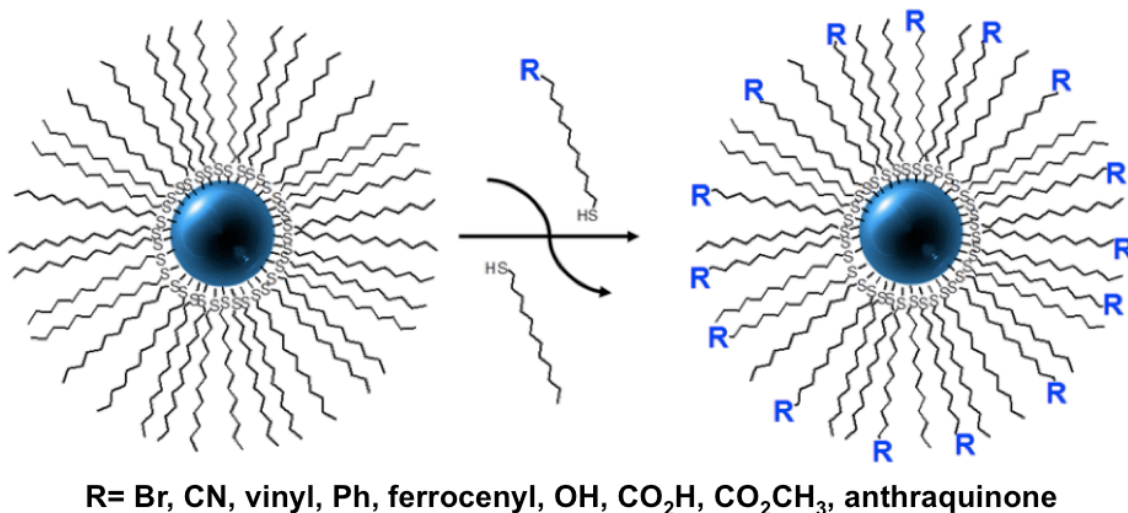


Figure 1.4 General scheme for place-exchange reactions between alkanethiol-AuNPs and various types of functionalized thiols. ^[10]

Sulfur Ligands are another class of ligands such as xanthates, ^[11] disulfides, ^[12] di and trithiols, ^[13-14] and resorcinarene tetrathiols ^[15] have also been used to stabilize gold nanoparticles. One big disadvantage in these types of ligands is that they are not good stabilizing agents like the thiols. They do not bind strongly to gold nanoparticles. Other ligands explored using a modified Brust biphasic method include phosphine, ^[16] amine, ^[17] carboxylate, ^[18] and isocyanide ^[19]. Gold nanoparticles were also obtained by replacing citrate functionalized gold with acetone, ^[20] and iodine, ^[21] modifying the original Turkevitch method.

In addition to conventional wet chemical synthesis, other approaches to prepare gold nanoparticles have been widely developed which can be classified into three approaches: 1) Non-chemical methods that use external energies such as in electrochemical and thermal decomposition of metal salt solution, photochemical,

sonochemical and laser ablation synthesis; 2) Biological sources such as the use of plant extracts and microorganism-assisted formation of metal nanoparticles; 3) Polymer mediated synthesis, which makes use of polymer as template for the generation of metal nanoparticles. This is an emerging type of template system to overcome the common problem of metal nanoparticle aggregation. These templates come in different forms and synthetic routes that have its advantages and disadvantages. To further elaborate this part, the following sub-sections will give us a clear picture of the different methods that are currently used.

1.2.2 Non-chemical Methods

Although chemical reduction methods of synthesizing gold nanoparticles are simple and convenient, contamination of the final products with the presence of excess reducing agents, surfactants and other chemicals may hinder applications of the gold nanoparticle. Thus, alternative routes of synthesis of metal nanoparticles that do not require the use of chemical reductants are discussed here.

1.2.2.1 Electrochemical Method

The electrochemical synthesis of palladium metal nanoparticles was first demonstrated in the work of Reetz and Helbig ^[22] using a two-electrode set-up consisting of two bulk metal sheets (i.e. Pd as anode and Pt as cathode). In this system the supporting electrolyte is made of tetraalkylammonium salt which serves as stabilizers of metal clusters formed. Figure 1.5a demonstrates the formation of Pd nanoparticles through the electrochemical synthetic process. This process starts from the dissolution of the bulk metal in anode creating Pd metal ions. The Pd ions migrate to the

cathode through electrostatic interaction. At the cathode vicinity, Pd cations are reduced to zero-valent metal atoms through electron transfer from the anode to the Pd cations. At this stage, nucleation and growth of the Pd metal nanoparticle take place. The tetraalkylammonium ions arrest the further growth of the Pd metal nanoparticles by serving as a protective agent around the metal clusters formed. In the end, a black precipitate is formed in the bottom. The dried precipitate can be fully dispersible in tetrahydrofuran solution. The mean Pd particle size is inversely proportional to the current density applied. The mean Pd diameters of 1.4, 3.1, and 4.8 nm can be obtained when current density is 5.0, 3.1 and 4.8 mA/cm² respectively (Figure 1.5 b,c,d).

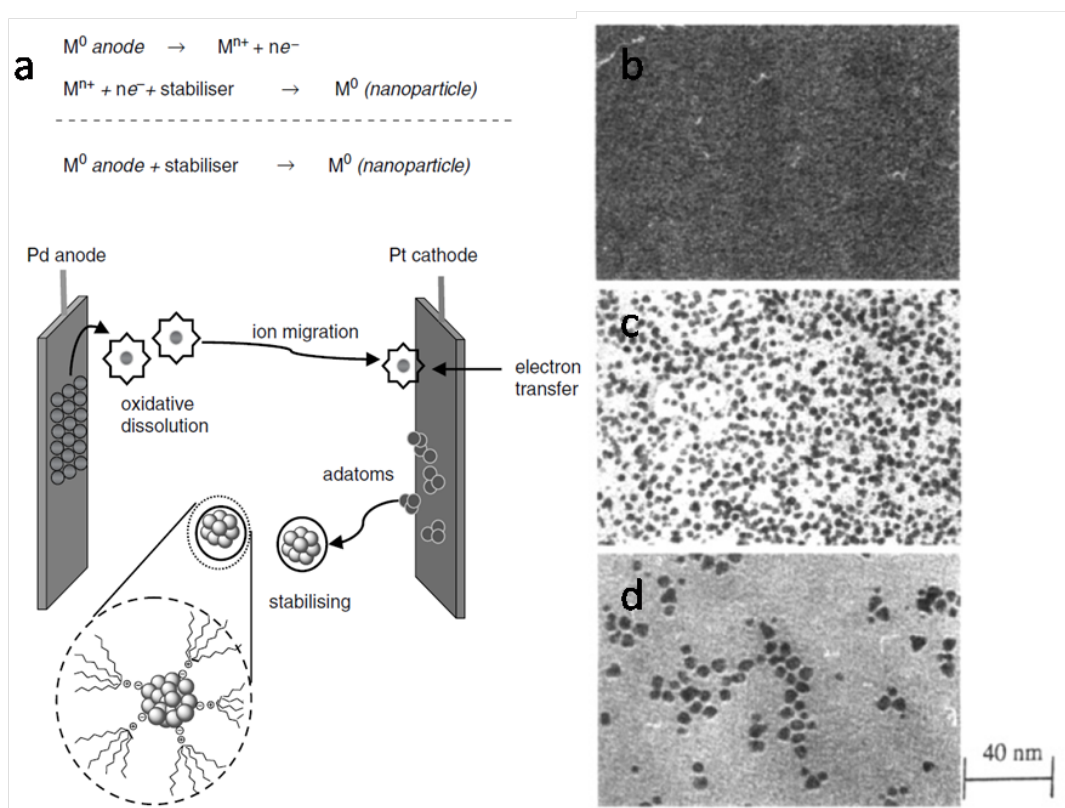


Figure 1.5 a) Electrochemical formation of Pd metal nanoparticles stabilized by tetraoctylammonium bromide. b,c,d) TEM images of Pd metal nanoparticles formed at different current densities of 5.0, 0.8, 0.1 mA/cm² respectively.^[22]

1.2.2.2 Thermal Decomposition

Thermal decomposition process to obtain gold nanoparticles is demonstrated in the work of Bakrania,^[23] wherein gold (III) acetate ($\text{Au}(\text{C}_2\text{H}_3\text{O}_2)_3$) powder is heated in a hot plate at a rate of 25 °C per minute in air. A high speed video camera was used for imaging the gold acetate decomposition and formation of gold nanoparticles. Gold acetate powder has sizes ranging from 0.5–1.0 mm. A schematic gold acetate decomposition and gold particle formation mechanism is presented below (Figure 1.6) to clearly illustrate the process. In this figure, gold acetate crystallite grains are direct precursors to the initial gold particles formed. The crystallite grain dimensions therefore dictate the minimum dimension of the gold nanoparticles. Here, the heating causes the slow decomposition of the gold acetate as observed through the discoloration of the powder and a rapid fragmentation of the particles is carried out. This process is exothermic where fragments carry a higher temperature than the decomposition temperature around 100°C. Formation of gold vapor cloud and nucleation of gold nanoparticles eventually follow the thermal decomposition stage. Differences in the size of the clouds and the number density of gold affect the number of initial nucleation sites present within the cloud. Highly-dense fragment of clouds results to more gold nanoparticles and consequently larger gold nanoparticles in size. Hence in this case the

average crystallite size of 160 nm would yield spherical gold nanoparticles with an average diameter of 63 nm.

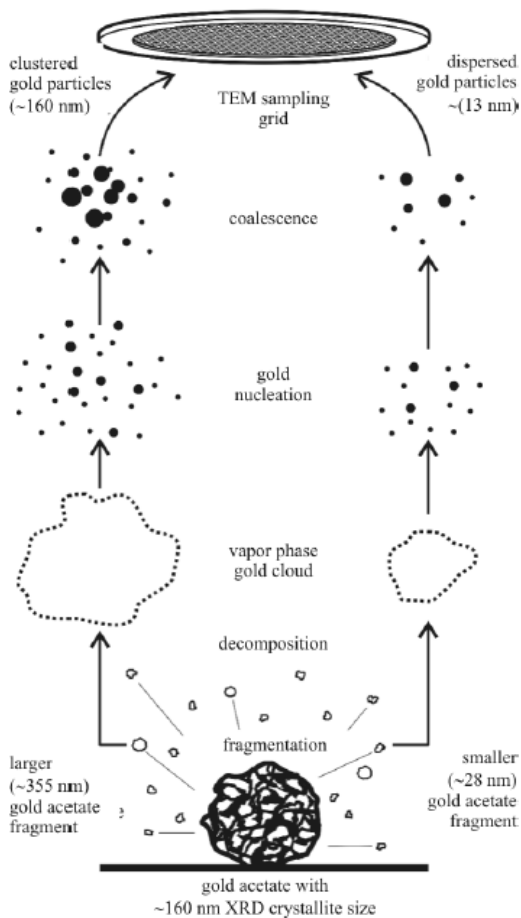


Figure 1.6 Schematic diagram for thermal decomposition of gold acetate powder producing gold nanoparticles. [23]

1.2.2.3 Photochemical Method

Photochemical synthesis was made possible in the study of Huang's team. [24] Irradiating UV light was used as a source of energy to generate gold nanoparticles in

different shapes. Herein, they used sodium oxalate as a reducing agent and tetrachloroaurate as the source of metal ions. The synthesis was carried out at room temperature using a low-pressure mercury lamp (8 W, $\lambda = 306 \text{ nm}$) for 10-20 minutes. Different shapes of gold nanoparticles could be synthesized with this method. Based on the absorption band of UV-Vis spectroscopy and TEM images, particle size of 522 nm indicates spherical gold, while diameters greater than 700 nm indicate the presence of other than spherical gold nanoparticles. . Non-spherical particles consist of hexagonal and truncated triangular morphologies (Figure 1.7). In this experiment, the generation of gold nanoparticles results to polygonal morphologies as the exposure to UV light increases.

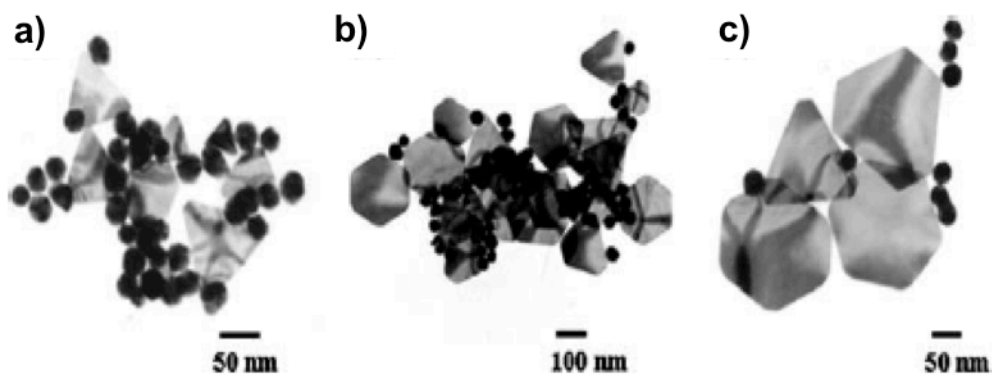


Figure 1.7 TEM images of gold nanoparticles produced from photochemical synthesis in different sizes and shapes in different concentration of reducing agent (sodium oxalate, 0.1M): a) 68 μL with more spherical gold nanoparticles, b) 65 μL with increased hexagonal and truncated triangular gold nanoparticles, c) 62 μL with decreased gold spherical nanoparticles. ^[24]

1.2.2.4 Sonochemical Method

A sonochemical route of gold nanoparticle generation was carried out by Okitsu *et al.* [25] using chitosan and aqueous gold salt solution (NaAuCl_4). This method involves the use of extremely high temperatures and pressure generated in the cavitation bubbles that result to radical and thermal reactions. A cylindrical glass vessel was used as a reactor mixed with the saturated solution of NaAuCl_4 , propanol and chitosan powder. Ultrasonication was carried out from a 200 kHz, 200 W Kaijo 4021 for ten minutes, giving a violet powder. The gold nanoparticles produced in this process were deposited on chitosan matrix. The UV-Vis absorption was observed at 580 nm, which was quite high compared to the most often observed absorbance at ca. 520 nm. The large peak shift was due to the formation of gold nanoparticle clustering as observed in the TEM image (Figure 1.8). Ultrasonication converts propanol to reducing species by creating acetone ketyl radicals. This was created by both thermal reaction of propanol in the cavitation bubbles or at the interfacial regions of the bubbles. The reducing species then gives off electron to gold(III) ions forming into gold nanoparticles. The gold nanoparticles are then adsorbed on the chitosan surface, which acts as a binder and stabilizer preventing further aggregation and growth. The resulting product is a composite Au/chitosan material.

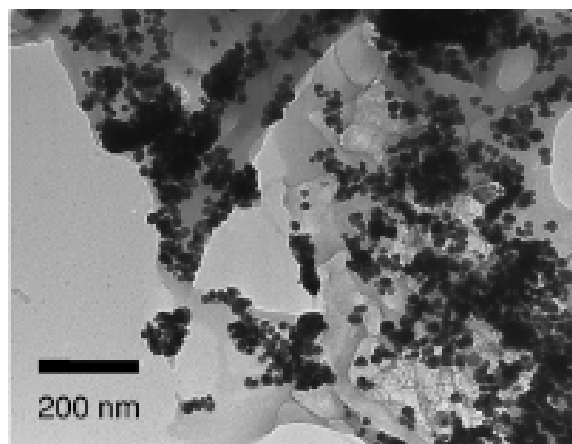


Figure 1.8 TEM image of gold nanoparticles deposited on chitosan. ^[25]

1.2.2.5 Laser Ablation Synthesis

The laser ablation technique for obtaining gold nanoparticles was demonstrated by Amendola ^[26], where a laser from Nd: YAG (laser pulses at 1064 nm) was used in a gold plate solution containing organic solvents such as dimethyl sulfoxide (DMSO), tetrahydrofuran (THF) and acetonitrile (CH₃CN). The pulse used was of about 10 J/cm at a 10 Hz repetition rate for 10 minutes. Aside from obtaining the gold nanoparticles, laser was also used for reshaping and reducing gold nanoparticle size. Gold nanoparticles produced were at average sizes of 2.4, 4.1 and 1.8 using solvents DMSO, THF and CH₃CN respectively (Figure 1.9). Prolong exposure to laser causes reshaping and reduction of gold nanoparticle size. This was due to the photo-thermal effect wherein the increased temperature allows the formation of a layer of vapor on the surface of the nanoparticles.

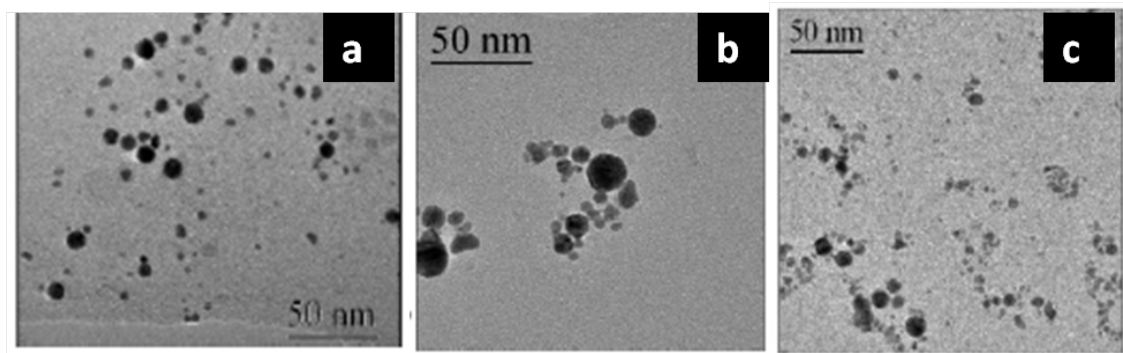


Figure 1.9 Sonochemically synthesized gold nanoparticles in different organic solvents.

a) Dimethyl sulfoxide (DMSO), b) Tetrahydrofuran, c) Acetonitrile. ^[26]

1.2.2.6 Microwave Assisted Method

Microwave assisted method of generating gold nanoparticles has also been used to speed up reaction rate for mass production capability. A one-step synthesis of polyethylene glycol (PEG)-coated gold nanoparticles by rapid microwave heating was studied by Seol et al. ^[27] In this study, a microwave heating system (2.45 GHz, 1600W) was used for the synthesis of PEG-coated gold nanoparticles. As seen in Figure 1.10, a glass bottle which contains the gold salt solution (0.88 mM HAuCl₄), the reducing agent (5.0 mM Trisodium citrate (Na₃Ct)) and the coating material (0.1 mM PEG) was mixed with a magnetic stirrer and undergone microwave heating in a microwave cavity. In this synthesis, the solution temperature was raised to 90 °C when the microwave was set at 10W and sustained for five minutes. At a ramping rate of 124.2 °C/ min, uniform and stable gold nanoparticles were produced at 14.3±2.5 nm. The effect of microwave radiation as a heating source drives the chemical reaction rapidly through the uniform

energy transfer into the solution. The microwave radiation increases probability of collision between molecules, and decreases in the activation energy. These factors improved the reaction rates, yields and uniformity of gold nanoparticles.

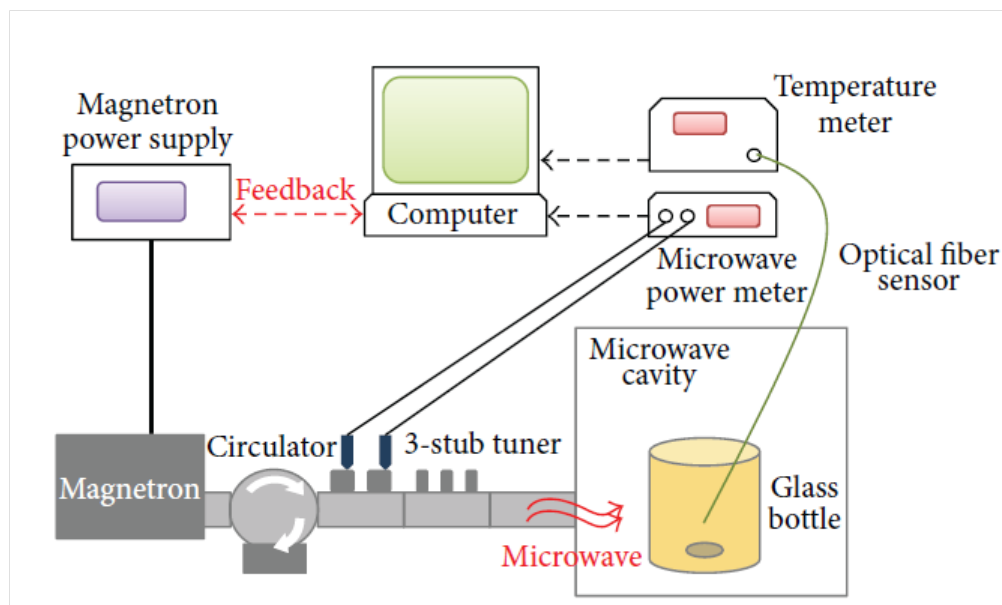


Figure 1.10 Schematic illustration of the microwave assisted synthesis of gold nanoparticles.^[27]

1.2.3 Biological Synthesis

The main driver for the biological synthetic route for metal nanoparticles was for the creation of an environmentally friendly synthetic platform. This encompasses the use of inexpensive reagents and less hazardous chemicals. This process can be carried out in circumneutral pH and mild temperature. The biological pathways for metal nanoparticles synthesis use microorganism (e.g. bacteria, cyanobacteria and algae),

plants and plant extracts. The mechanism in the bio-reduction of metal ions involves both intracellular and extracellular precipitation of metal nanoparticles within the microorganism (Figure 1.11).^[28] Biomolecules such as proteins are mainly responsible for the synthesis of gold nanoparticles while enzymes produced in the outer layer membrane of the microorganism are responsible for reduction of gold ions.

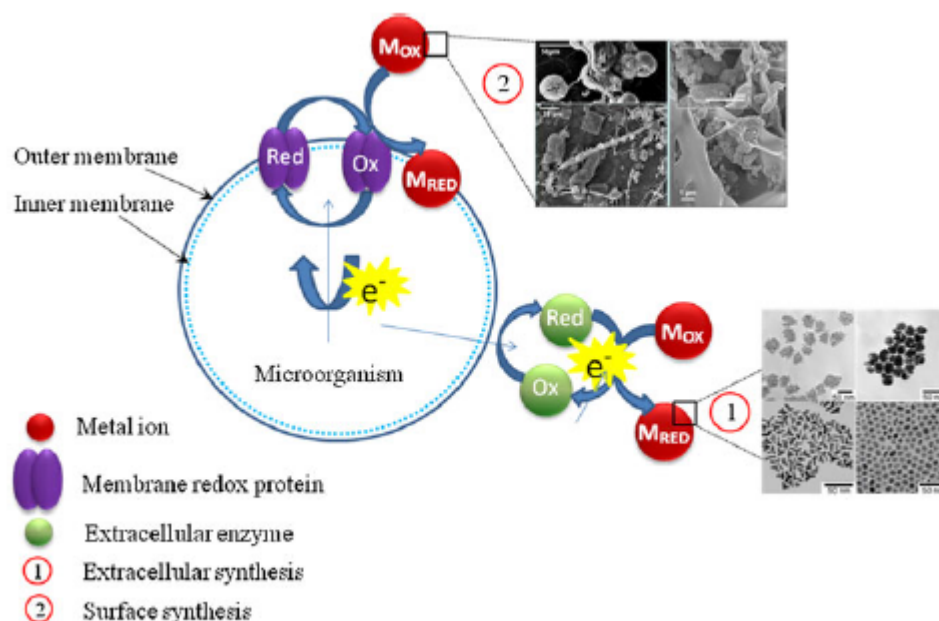


Figure 1.11 Schematic diagram on the reduction of metal ions to nanoparticles in microorganisms both intra- and extra-cellular precipitation.^[28]

A bacterial species, *Acidithiobacilluethiooxidans* spp. was also used to generate gold nanoparticles using gold sulfate complex, $[\text{Au}(\text{S}_2\text{O}_3)_2]^{3-}$.^[29] The bacteria were initially cultured at room temperature in thiosulfate media. Cultures were then incubated for 4 weeks, transferred and grown at room temperature with shaking (200 rpm) to obtain active bacteria. In a successful experiment, gold at 0.24mM solution was added

to the growth medium (100 mL). The cultures were then inoculated 1% (v/v) of inoculums from the concentration of 10^8 bacteria cells/mL to the flasks and incubated at room temperature with shaking for 75 days. A TEM image in Figure 1.12 shows gold particles deposited along the outer wall layer, periplasm, and cytoplasmic membrane of the bacteria cell.

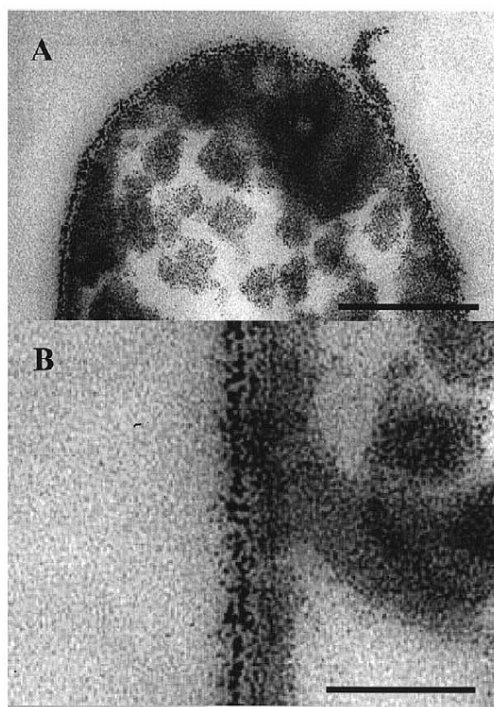


Figure 1.12 TEM images of gold nanoparticles growing in the inner and outer layer of the *Acidithiobacillus thiooxidans* spp. Bacteria. ^[29]

The possible mechanism of the generation of gold nanoparticles using this type of bacteria was speculated to be caused by the degradation of the gold salt complex ($\text{Au}(\text{S}_2\text{O}_3)_2^{3-}$) by the *A.thiooxidans* bacteria. As a result, elemental gold precipitated as fine-grained colloids inside the cells and on the surface of the bacterial cell. When

($\text{Au}(\text{S}_2\text{O}_3)_2^{3-}$) was decomplexed, it produced Au^+ and $\text{S}_2\text{O}_3^{-2}$. Au^+ was then reduced to Au^0 .

Yeast (*P. jadinii*) and fungal (*V. luteoalbum*) cultures ^[30] were also used as medium for gold nanoparticle formation. Cultures were cultivated in test tubes with nutrient medium and incubated with shaking at 28 °C for 24-48 hours. Figure 1.13 shows the composite particles of yeast and fungal cultures with gold metal nanoparticles. The images confirmed the formation of gold metal nanoparticles inside the cells of the yeast and fungus, particularly in the cytoplasm. Various morphologies were formed such as spherical, triangular, hexagonal and other irregular shapes. Gold metal nanoparticles varied in sizes with an average approximate size of 100 nm. Spherical particles were the majority among the morphologies present. It has been suggested in this study that the cellular mechanism of gold nanoparticle formation was due to the presence of proteins and enzymes. To achieve better control on particle sizes and shapes, the effect of different process parameters such as pH, temperature, growth stage of the cells and time exposure of gold ions have been investigated.

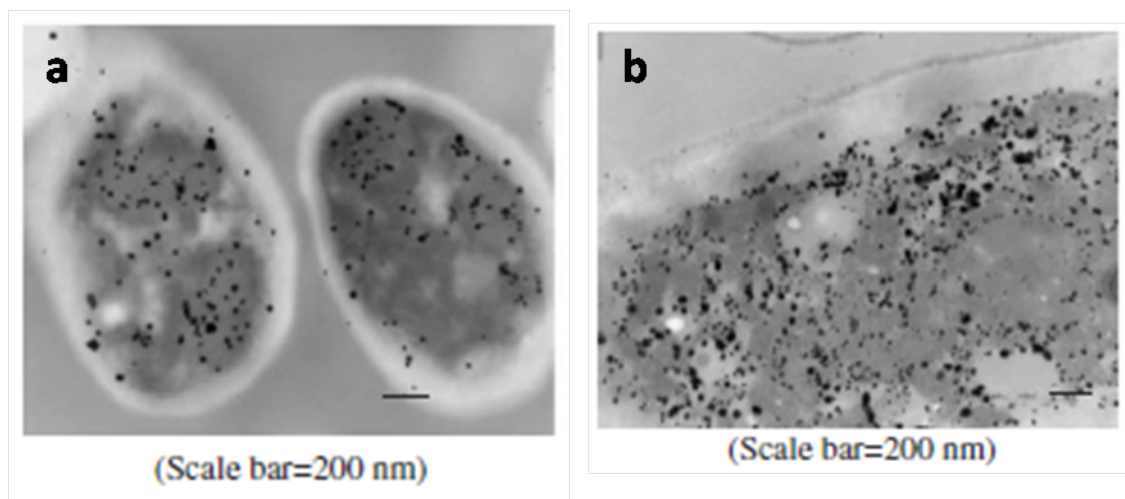


Figure 1.13 TEM images of composite particles of gold metal nanoparticles with, a) *P.jadini*(yeast) and b) *V.luteoalbum*(fungal cultures).^[30]

Another biologically mediated synthesis of gold nanoparticles was demonstrated by Chauhan *et al.*^[31] In this study, *C. albicans* was cultured on YEDP agar plates and cells were harvested after 24 hours. Certain amounts of the fungal extract were added to HAuCl₄ solution in aqueous medium. The mixture was incubated for 24 hours. Figure 1.14 shows the TEM images of different composite particles of gold nanoparticles within the fungus extract (*C. albicans*). These composite materials were synthesized in different concentrations of the extract (1 ml and 5 mL) and the time of incubation (12 hours and 24 hours). Figures 1.14a and b were synthesized with a lower concentration of the extract in 12 and 24 hours of incubation, respectively. At lower concentration of the extract, the size and number of non-spherical gold particles was clearly observed. The sizes ranged from 60-80 nm. However, at higher concentration of the extract (Figure 1.14c and d), more identical gold nanoparticle spheres were observed with sizes from 20-40 nm. The edge length of the gold particles decreased with the increase of the

amount of extract. The presence of NADH- dependent reductase or nitrate-dependent reductase present in the extract caused the rapid reduction of gold ions into nanoparticles. It is also speculated in this study that glutathione and glutathione-like compound, phytochelatin mainly caused the formation of gold nanoparticles.

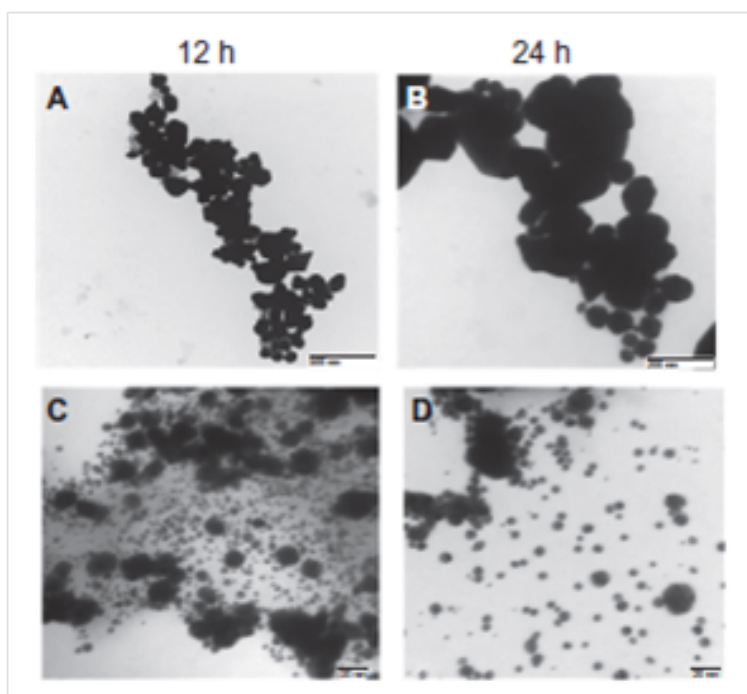


Figure 1.14 TEM images of gold nanoparticle formation in cystolic fungus extract (*C.albicans*) in different concentration and incubation time. a) and b) with 1 mL extract in 12 hours and 24 hours of incubation, respectively. c) and d) with 5 mL of extract in 12 hours and 24 hours incubation, respectively. ^[31]

Plants and leaf extracts have also been proven to be alternative sources of biocompatible reducing agents of gold nanoparticles. Soybeans, in particular, are a big source of phytochemicals that contain functional groups such as carboxy, amino, thio

and hydroxyl units responsible in the synergistic chemical reduction of gold salts to metal nanoparticles. Shukla *et al.* [32] used soybeans in the generation and stabilization of gold nanoparticles. Mixing the aqueous sodium tetrachloroaurate with soybean extract at 25 °C produced a purple color within 2-6 hours and completed reaction within 24 hours (Figure 1.15). In this method, spherical gold nanoparticles produced have an average size of 15 ± 4 nm. The phytochemicals present in the soybeans composed of proteins (glycin, β -conglycinin, trypsin), isoflavones and amino acids (L- tryptophan, L-tyrosine, L-arginine, L-aspartic acid) that played a major role in the overall reduction of gold salts to its corresponding nanoparticles. Aside from reducing the gold ions to nanoparticles, proteins also provide coating on the gold nanoparticles giving stability in solution.

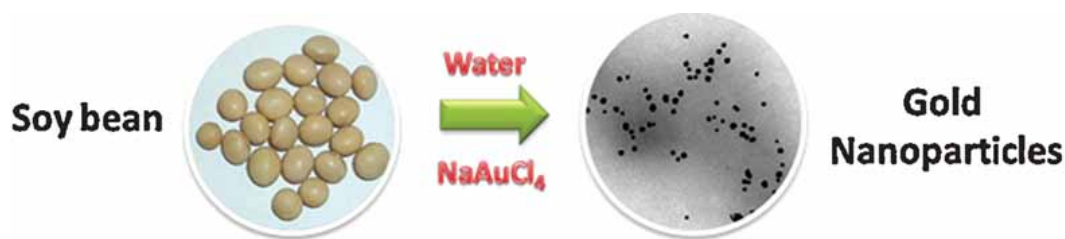


Figure 1.15 Synthesis of gold nanoparticles from soybeans. [32]

Leaf extracts of *Magnolia kobus* and *Diopyros kaki* [33] were used as reducing agents in the generation of gold nanoparticles. This process carried out at 95°C, had more than 90% conversion of gold ions to metal nanoparticles.. Figure 1.16 shows the TEM images and the leaf extract concentration effect on the size of the gold nanoparticles. The increase in concentration of leaf extract resulted in the decrease of the average particle size from 28, 25 and 10 nm using 10%, 20% and 50% leaf extract.

At a low concentration of leaf extract, the gold nanoparticles produced were mostly hexagonal or triangular particles. Increasing the leaf extract concentration produces other morphologies of spherical gold nanoparticles.

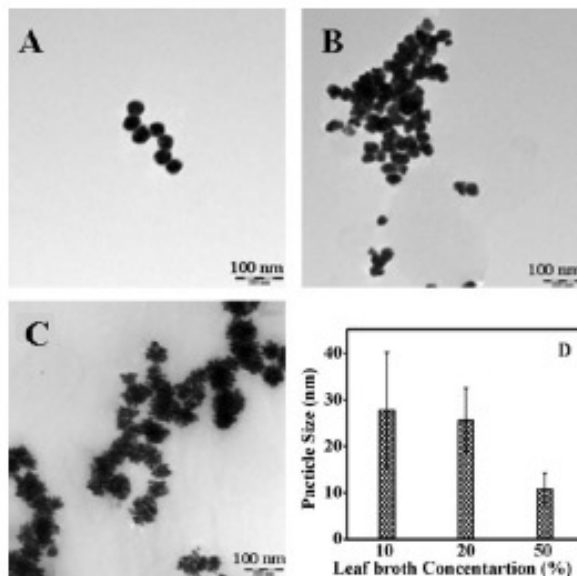


Figure 1.16 TEM images of gold nanoparticles produced from leaf extracts of *Magnoliakobus* and *Diopyros kaki* in different concentrations (v/v) of the extract, a) 10%, b) 20%, c) 50% at 60°C for 30 minutes and d) Effect of leaf extract concentration on the gold nanoparticle average size. ^[33]

In recent years, development of plant extract - based synthesis of metal nanoparticles has been investigated. Plants seem to be the best candidate suitable for large scale biosynthesis of metal nanoparticles. Using plant-based synthesis results into

more stable and faster rate of synthesis compared in the case of microorganism. ^[34] This also eliminates the elaborate process of maintaining cell cultures for microorganism.

The ability of obtaining metal nanoparticles in plants sprung after when plant biomolecules were employed for the remediation of metal-contaminated water or detoxification ability ^[35]. The natural phenomenon of heavy metal tolerance of plants has interested researchers to investigate the related biological mechanisms in photosynthesizing metal nanoparticles (Figure 1.17). It has been shown that many plants can actively uptake and bioreduce metal ions from soils and solutions during the detoxification process, thereby forming insoluble complexes with the metal ion forming nanoparticles.

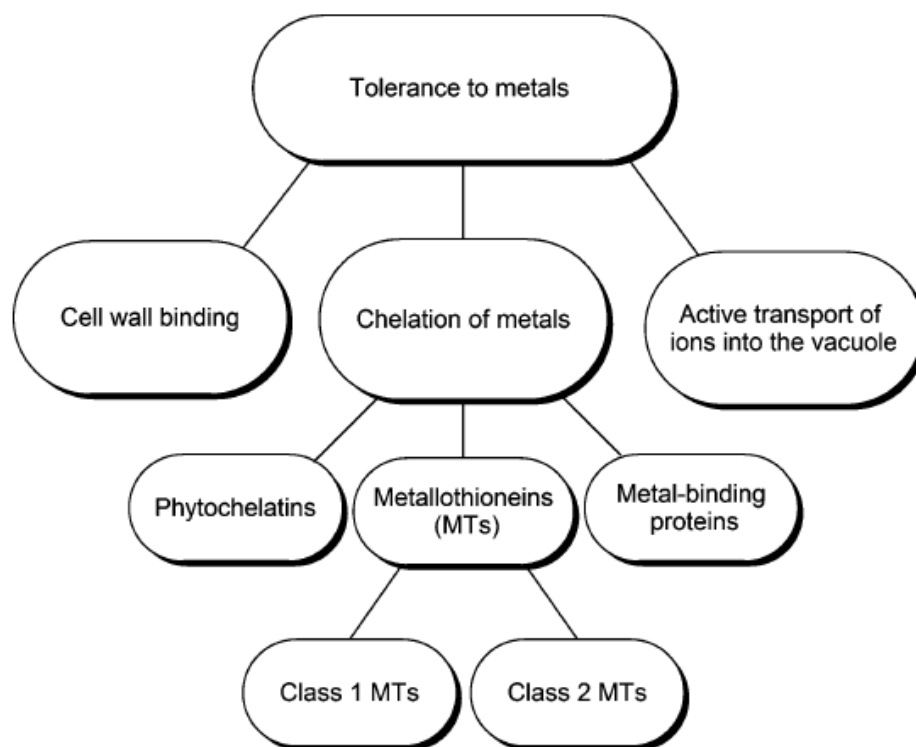


Figure 1.17 Important mechanisms of heavy metal tolerance in plants. ^[34]

It was not until Gardea-Tooresdey *et al.* [36] who have used plant to synthesize gold and silver nanoparticles using *Medicas sativa* (alfalfa). The alfalfa plants were grown in AuCl_4^- ions rich environment. They were able to produce crystalline state gold nanoparticles with icosahedral (4 nm) and face centered cubic (fcc) twinned particles (6-10 nm). The study suggested that the carboxyl or other oxygen containing ligands on the biomass are the functional groups responsible for the binding and the reduction for gold in the biomass. Another study on the mechanism of gold nanoparticle formation in *Cinnamonum camphora* leaf was investigated by Huang *et al.* [37] Their study suggested that the polyol components and the water-soluble heterocyclic components were mainly responsible for the reduction of chloroaurate ions and the stabilization of the nanoparticles, respectively. Another study also synthesized rod -shaped gold nanoparticles using *Avena sativa* (oats). [38] It was concluded that the biomass carrying more positive functional groups (e.g. amino groups, sulfhydryl groups and carboxylic groups) allowed the Au (III) ions to get more closure to binding sites and approved the reduction of Au(III) to Au(0). Plant extracts that contain organic acids, peptides, proteins and amino and saccharides have proven to have synergistic reduction power for the bioreduction of chloroaurate ions into gold nanoparticles. [39]

1.2.4 Polymer Mediated Synthesis

Polymers that have both reducing and stabilizing properties have been developed in many research studies concerning the synthesis of metal nanoparticles. These types of polymers are considered to perform a one-step polymer- mediated synthesis. Having

both abilities to reduce and stabilize metal nanoparticles results to higher purity and homogeneity of products. This one-step process is attributed for its low cost and relatively high efficiency and environment-friendly approach. The commonly used polymers containing dual components of reducing and stabilizing metal nanoparticle synthesis are poly(N-vinyl-2-pyrrolidone)(PVP),^[40] poly(allylamine)(PAAm),^[41] poly(*o*-phenylenediamine) (PoPD),^[42] poly(ethyleneimine)(PEI)^[43] and poly(4-styrenesulfonic acid-*co*-maleic acid) (PSSMA).^[44] This section will discuss how these polymers can perform both reducing and stabilizing properties of metal nanoparticle synthesis.

Poly(N-vinyl-2-pyrrolidone) (PVP) is a homopolymer with polyvinyl backbone, terminal hydroxyl groups and a large amount of C=O double bond. The O atoms of PVP have a strong adhesive force to metal nanoparticles that can easily attach to the metal surface. At first, PVP was used as a stabilizer to protect metal nanoparticles from agglomeration^[45]. However, PVP can interfere in the reducing reaction of metal ions.^[46] Possible mechanisms have been studied in the reducing capacity of the PVP. These include free radical mechanism, oxidation of the hydroxyl end groups^[47] and the C=O double bond.^[48] Figure 1.18 shows PVP molecules disperse in a solution and cobridge a surface layer onto Au clusters during particle growth.

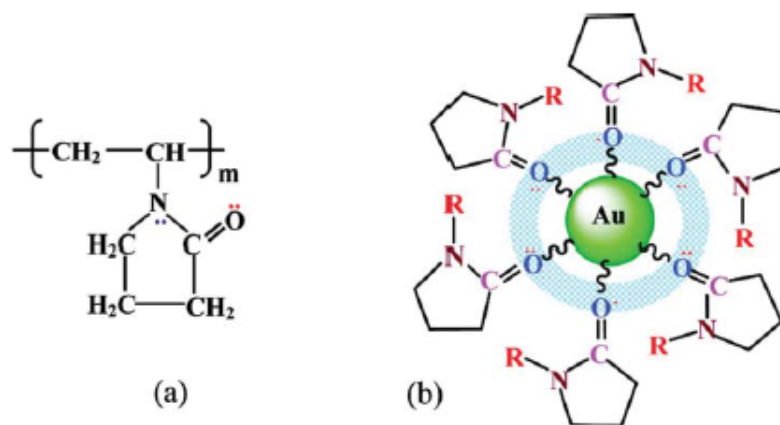


Figure 1.18 Adsorption and cobridging of (a) PVP molecules in (b) a surface layer via Au-atoms on a gold particle. ^[40]

Another type of a dual component polymer is poly(allylamine) (PAAm). PAAm is a water-soluble polymer that can trap nanoparticles. It has been used for reducing and stabilizing gold and silver nanoparticles at room temperature. ^[48] The abundance of amino groups in the PAAm molecules drives the reduction of gold ions into metal nanoparticles. Figure 1.19 illustrates the process of PAAm-induced synthesis of gold nanoparticles in aqueous solution.

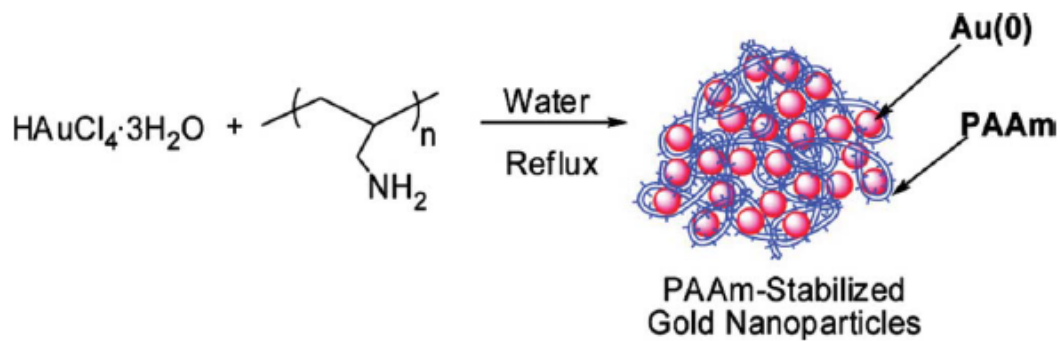


Figure 1.19 PAAm-induced synthesis and stabilization of gold nanoparticles in water.

[41]

Another redox-active conducting polymer, PoPD, a derivative of polyanilines, has been investigated to reduce and stabilize gold nanoparticles of different morphologies. ^[49] Figure 1.20 illustrates the formation of the gold nanoparticles using this type of polymer. First, gold salt precursor was added into the PoPD hollow microspheres. PoPD contain reducing groups on its inner and outer surface, which gradually reduce the gold metal ions to metal nanoparticles. It was suggested in this study that the strong bonding between the π electrons and amine groups of PoPD and the gold nanoclusters provided an efficient stabilizing effect.

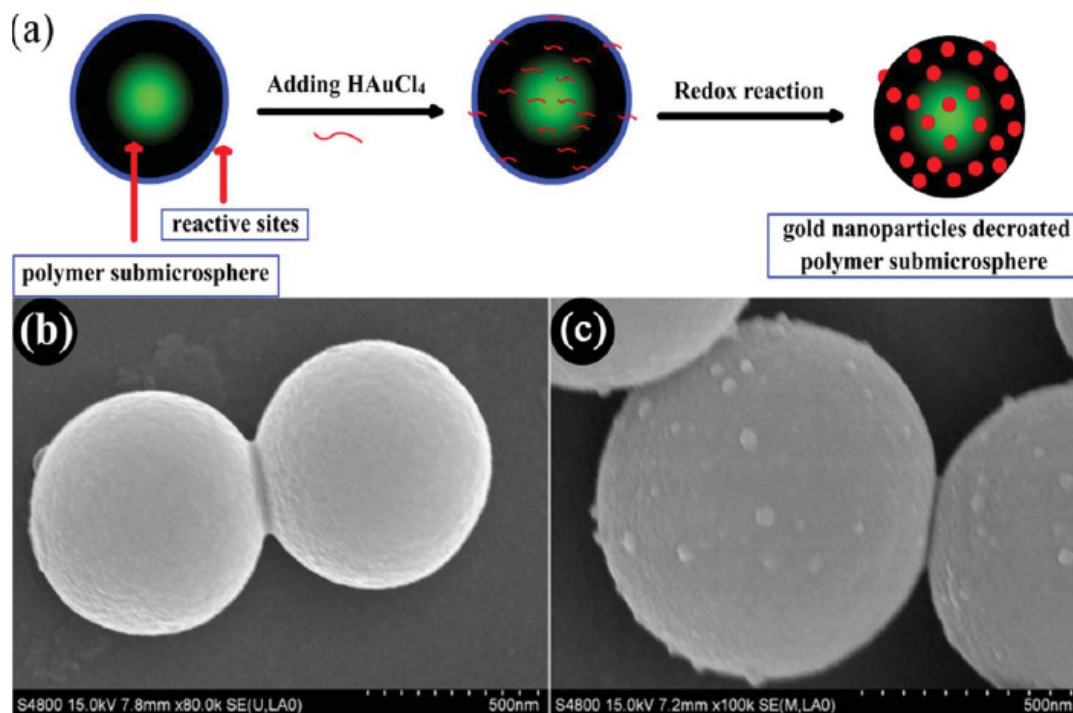


Figure 1.20 a) Synthetic route of the PoPD-gold nanoparticles, b) FESEM images of PoPD submicrospheres, c) FESEM images of PoPD submicrospheres decorated with gold nanoparticles. ^[42]

Linear PEI is a pale yellow transparent liquid soluble in aqueous solution. Commercial PEI is a hyperbranched polymer containing primary, secondary, and tertiary amino groups. This type of polymer has not only been investigated for its ability to protect gold nanoparticles from agglomeration but also reducing power, which is attributed to the presence of the amino groups. ^[50] Kuo *et al.* ^[43] investigated the reducing effect of PEI's amino groups (e.g. mono, and di-alkylated (PEI-1R, PEI-2R)), Figure 1.21. Both mono and di-alkylated PEI were added into the same amount of Au solutions. It was found out that the three types of polymers (i.e. PEI, PEI-1R, PEI-2R) have similar structures and properties. However, the aggregates of PEI-1R and PEI-2R

chains tend to be better-structured that mimics a micellular structure and even a well-rounded shape. Consistently, the nanoparticles generated by the PEI are less compact, while the PEI-1R and PEI-2R contribute to well- structured nanostructures. The authors attributed this phenomenon to the fact that non-alkylated PEI cannot provide protection to the gold nanoparticles as alkylated ones. Alkylated PEIs also tend to produce smaller structures than the non-alkylated PEIs.

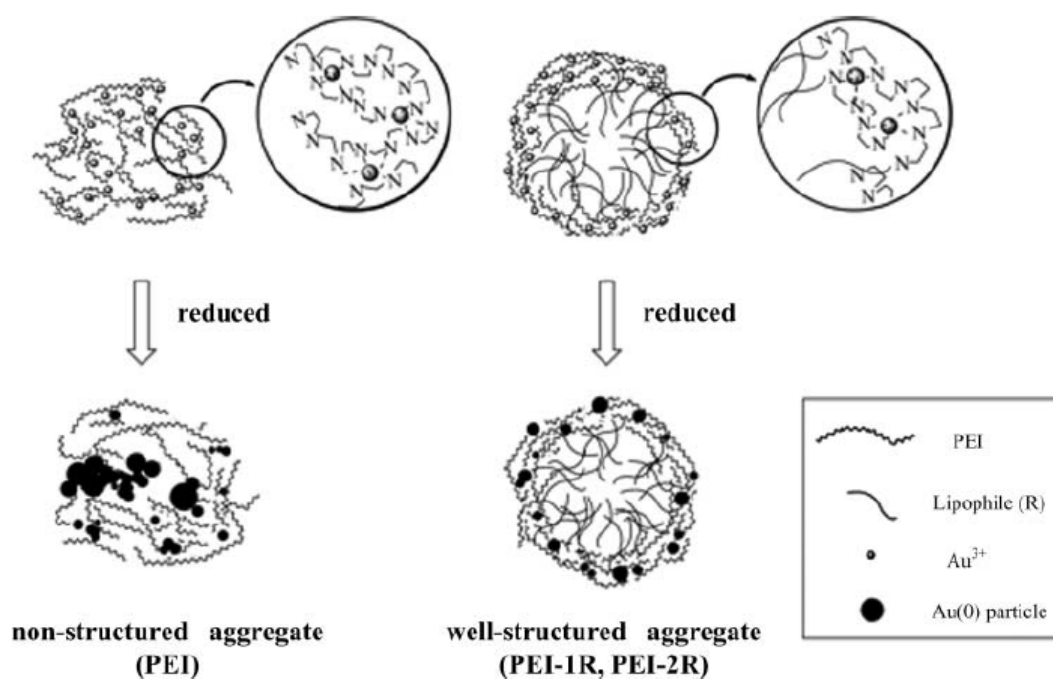


Figure 1.21 Aggregates generated by PEI, PEI-1R, PEI-2R .^[43]

Recently, Cai *et al.*^[44] have reported the use of PSSMA, an anionic polymer, its use to synthesize different metal nanoparticles without the use of any reducing agents.

Different metal precursors were added into the aqueous solution of PSSMA and the reduction was initiated by mild thermal treatment, Figure 1.22.

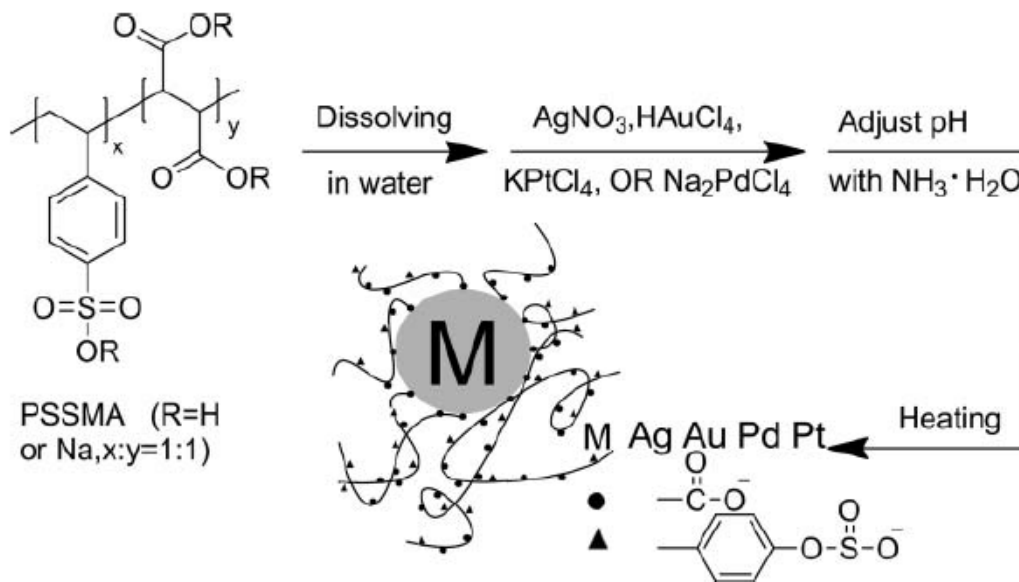


Figure 1.22 Schematic illustration of the formation of PSSMA-coated metal nanoparticles. ^[44]

1.3 Polymer-Based Templates and Nanoreactors for the Formation of Metal/Polymer Composite Particles

In the recent review of Karg, ^[51] he has classified the inorganic/organic colloids based on eight factors as illustrated in Figure 1.23, namely polymerization techniques, organic materials used, inorganic materials used, structure, complexity, hierarchy, property and application/use. Polymerization technique in incorporating metal or metal oxides in polymers may vary from emulsion or precipitation polymerization where

covalent binding between the nanoparticle surface and the polymer backbone is required. Different inorganic materials can be incorporated into the colloidal polymer. This ranges from noble (e.g Au, Ag, Pt, Pd), metal oxides and semiconductors (e.g. ZnO, Fe₂O₃, CdSe, CdTe). The structures of the resulting inorganic/organic composite particles vary in three different forms. Core-shell structures with inorganic cores and organic shells are the most common form. Some have the organic layer filled with the inorganic nanoparticles. And the emerging ones are organic templates with adsorbed inorganic nanoparticles on its exterior core or surface. The hierarchy is based on whether the organic layers are grown on the inorganic nanoparticles or nanoparticles grown on the organic layers. Its complexity is based on the components of the organic components used (e.g. homopolymer, copolymers). The properties of these hybrid colloids can range from plasmonic, magnetic, photoluminescence and catalytic. Some hybrid colloids can have two properties in one. Applications are based on their properties whether it can be used in catalysis, photonics, sensing, actuator and drug delivery.

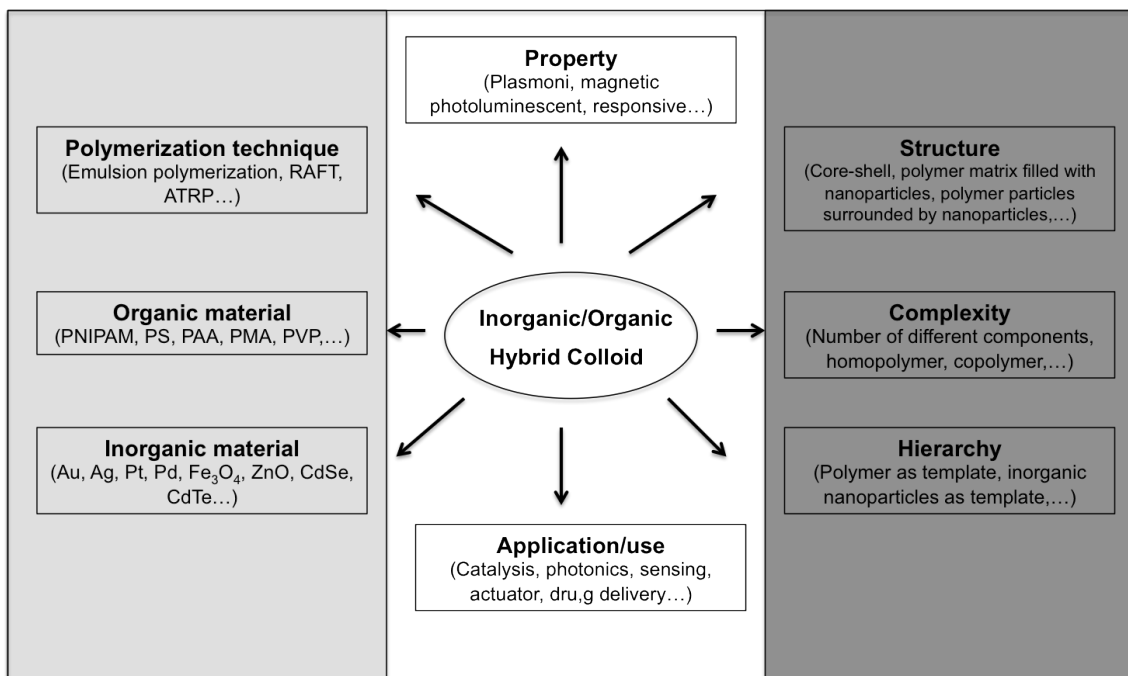


Figure 1.23 Classification overview of hybrid colloids made from organic/inorganic materials. ^[51]

Polymer assisted process or polymer template synthesis of metal nanoparticles have received significant attention due to several reasons: 1) Low concentration of polymer is needed to sterically stabilize metal nanoparticles; 2) Presence of functional groups in the polymer serves as both reducing and stabilizing agent. 3) The presence of polymer is capable of controlling the size and morphology of the metal nanoparticles produced. Various metal nanoparticles have been incorporated into different types of polymers through mixing polymeric materials with inorganic particles. A synergistic effect of metal nanoparticle and polymer results in the significant interest for the synthesis of hybrid particles. Figure 1.24 shows different types of polymer mediated assembly approaches, ^[52] and how each type of polymer influences the composite design

in terms of the polymers' ability that can control the metal nanoparticle properties and inter-particle distance. In this platform, composite particles are synthesized in a two-step process. First, metal nanoparticles are pre-formed through classical method such Turkevich and Brust-Schiffin methods. This is then followed by partial or complete exchange of the metal nanoparticle monolayer with functionalized ligands. Homopolymers can be used to form porous aggregates with metal nanoparticles that can be used as catalyst. Dendrimers on the other hand can be used to control interparticle-distance between metal nanoparticles. This type of composite particle can be utilized in the sensing devices. Copolymers that can shape and control metal nanoparticles can be further be used for the formation of complex 3D structures and selective patterning of metal nanoparticles which can be useful in the nanoelectronic devices.

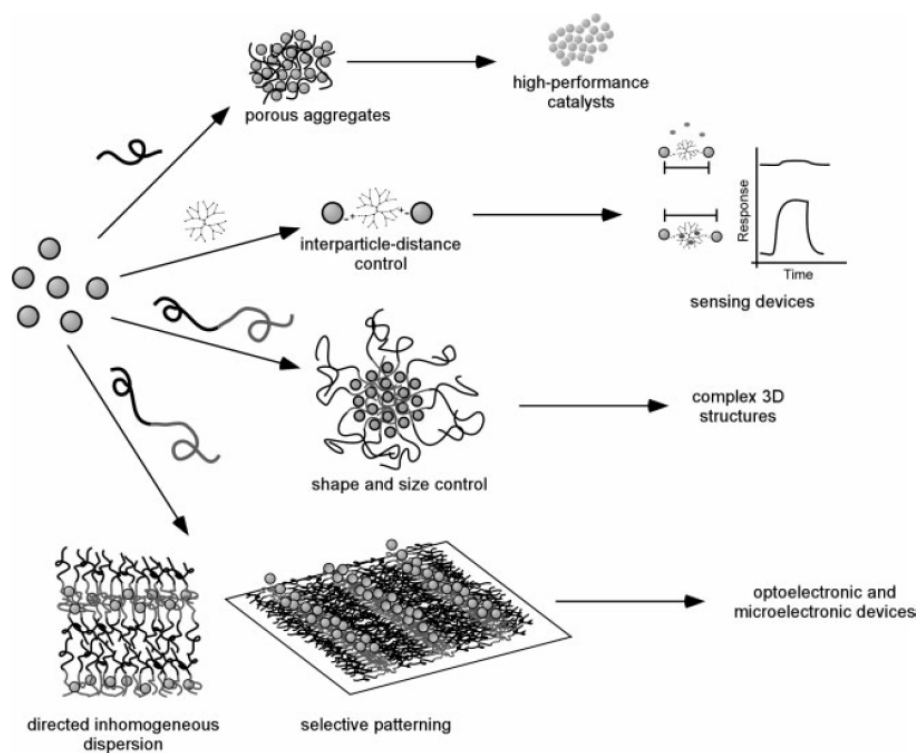


Figure 1.24 Polymer-mediated assembly approaches to fabrication of ordered nanocomposites and their possible utilization. ^[52]

Another emerging type of polymer mediated synthesis of metal nanoparticles is the use of colloidal polymers as template. This type of template is in a form of core-shell structure. This template can be made from different types of polymers and polymerization techniques. Specific examples of metal/polymer composite materials using different types of polymers are illustrated below.

1.3.1. Homopolymers

A typical example of a homopolymer with metal nanoparticle is the gold nanoparticle/poly(4-vinylpyridine) (Au@PVP) composite particles. ^[53] Au@PVP was synthesized by using a citrate-stabilized gold nanoparticles modified by a disulfide initiator for surface-initiated atom-transfer radical polymerization (SI-ATRP). Polymerization of vinylpyridine then occurred in the surface of the gold nanoparticles at ambient conditions (Figure 1.25).

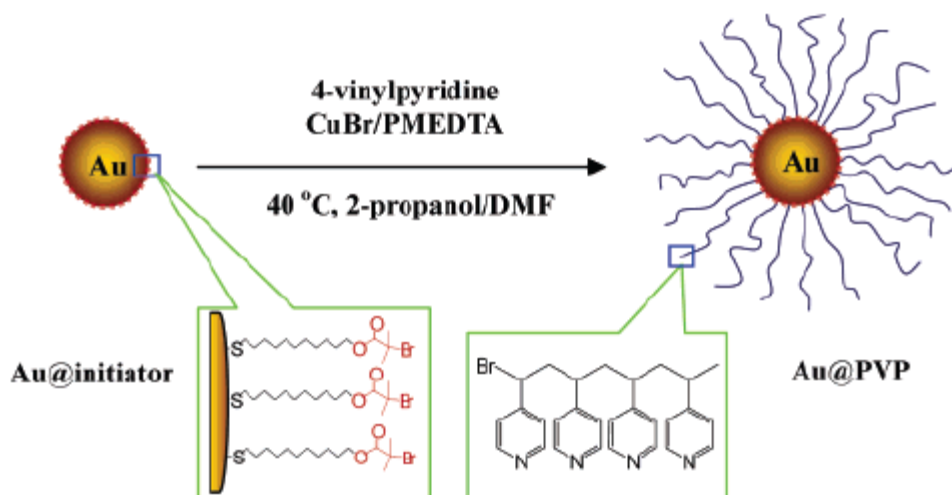


Figure 1.25 Schematic fabrication of Au@PVP nanoparticles by SI-ATRP. ^[53]

Hydrogel such as poly(*N*-isopropylacrylamide) (PNIPAM) was also used in the synthesis of gold nanoparticles ^[54] as shown in Figure 1.26. In this synthesis, cross-linked PNIPAM hydrogel was pre-formed using a conventional radical polymerization at 70 °C using *N,N'*-methylenebisacrylamide as crosslinker and ammonium persulfate as initiator. The hydrogel polymer matrix serves as a protective template to fully encapsulate gold nanoparticles without aggregation. A reducing agent was used in the reduction of gold ions. Light irradiation was essential in the efficient encapsulation of the gold nanoparticles within the hydrogel polymer because it raises temperature of the reaction and causes the shrinking of the polymer matrix and the consequently trapping of the gold nanoparticles.

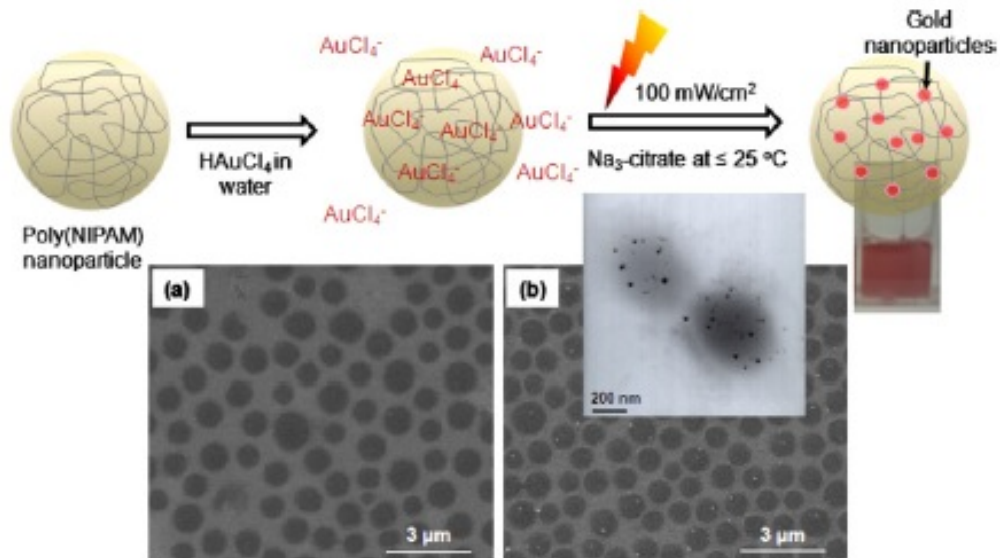


Figure 1.26 Preparation of gold nanoparticles within PNIPAM hydrogel. SEM/TEM images of a) before and b) after formation gold nanoparticles. ^[54]

1.3.2 Block Copolymers

Mantzaridis and Pispas ^[55] were able to encapsulate Au nanoparticles into the core with a functional group of polyvinylpyridines (P2VP) as core and polystyrene (PS) as corona. This amphiphilic block copolymer (PS-*b*-P2VP) serves as a nanoreactor for Au formation. Later on, they have created a bigger hybrid block copolymer using the original Au-loaded nanoparticles. This was carried out by successive utilization of different solvent, evaporation, dissolution and another block copolymer, polyisoprene-*b*-polystyrene (PI-*b*-PS). Figure 1.27a shows the schematic diagram in the formation of Au nanoparticles into the core of a giant block copolymer. Such hybrid starts from the formation of a smaller block copolymer (PS-*b*-P2VP). Immersed in a toluene solvent,

the block copolymer has rearranged itself to a core and corona structure. HAuCl_4 in ethanol was used as salt precursor which dissociates into gold ions and complex with the pyridine group of the P2VP blocks. Later on, hydrazine was added to reduce the gold ions into metallic gold. The Au loaded PS-*b*-P2VP nanocomposite was further added to another block copolymer, PI-*b*-PS dissolved also in toluene. Toluene evaporation took place and formed into thin film. N-heptane solution was used for selective dissolution of the PI block alone. The resulting composite had a PI corona and a Au loaded block copolymer core. Figure 1.27b shows a TEM image of the hybrid compound micelle. The darker shade of the composite material exhibits the core where the Au nanoparticles reside while less dark area around the core is the corona.

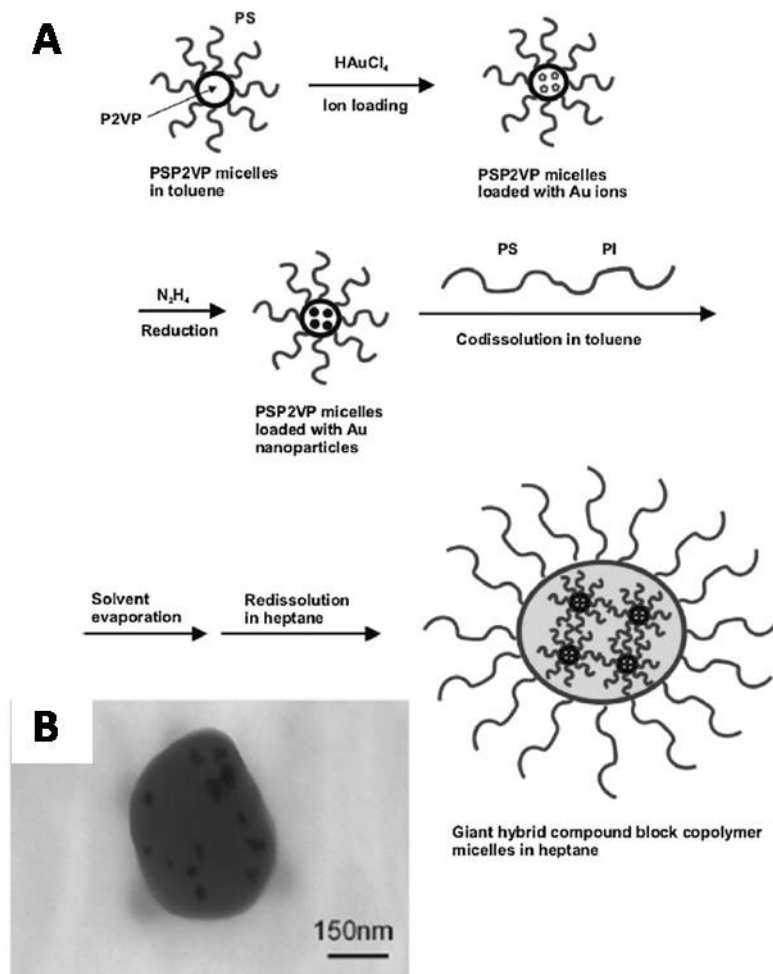


Figure 1.27 a) Schematic diagram on the formation of the hybrid compound micelles (loaded with Au nanoparticles in its core), b) TEM image of the Au/polymeric nanocomposite. ^[55]

Block copolymers such as poly(ethylene oxide)-poly(propylene oxide)-poly(ethylene oxide) (PEO-PPO-PEO) can also be used in the stabilization of gold nanoparticles in the absence of a reducing agent. ^[56] In this synthesis, a three step mechanism was proposed as illustrated in Figure 1.28. First is the cluster formation of gold nanoparticle by complexation of gold ions with the copolymer. The copolymers

form pseudo-crown ether structures with AuCl_4^- ions. Reduction of AuCl_4^- ions was via oxidation of the polymer by the metal center. The second step involves the adsorption of the copolymers into the surface of gold nanoparticle cluster and further complexation of gold ions. The adsorption of copolymers into the gold surface was due to the amphiphilic character of the PEO-PPO-PEO block copolymer. The addition of gold ion complexation into the cluster forms a particle bigger than the original size. The last step is the growth of the metal particle and the colloidal stabilization by the copolymer. The repeated reduction of AuCl_4^- ions into the cluster forms bigger and bigger metal particle, thus the growth of particle occurs.

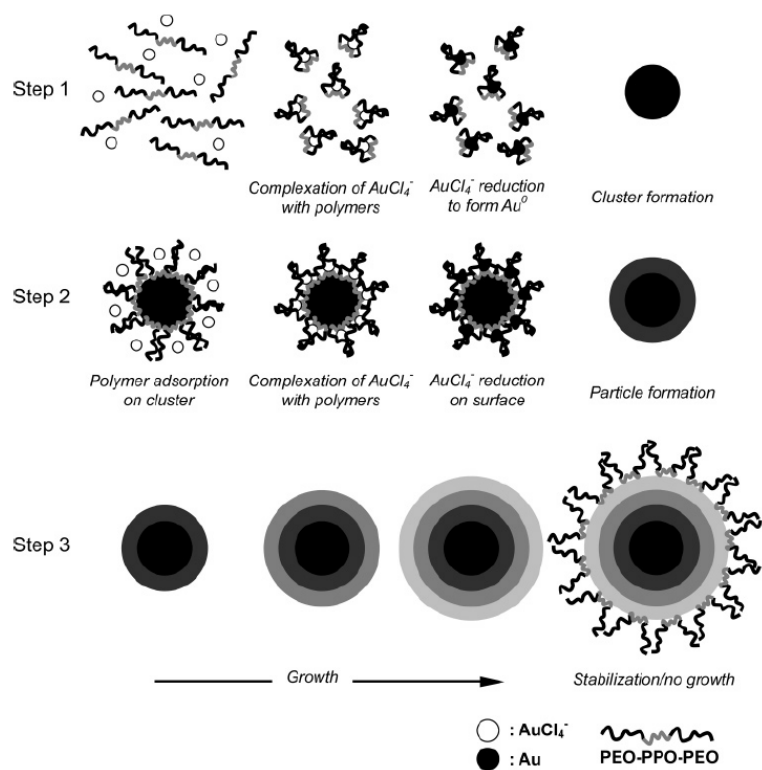
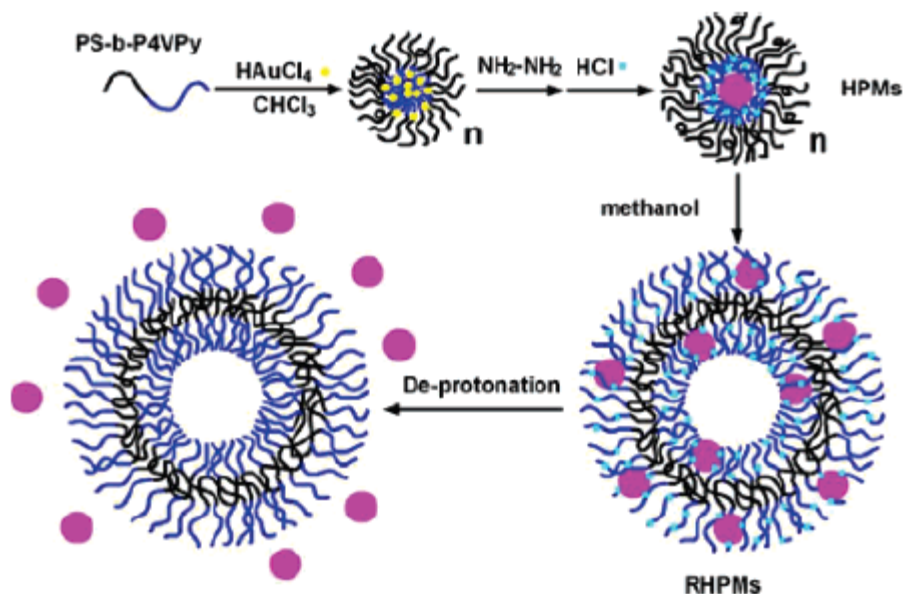


Figure 1.28 Proposed mechanism of AuCl_4^- reduction and particle formation using PEO-PPO-PEO block copolymer. ^[56]

Hou *et al.* created an hybrid polymeric micelles containing gold nanoparticles. ^[57]

Figure 1.29 demonstrates the preparation of hybrid polymeric micelles (HPMs), its gold nanoparticle formation and the reversion of the template. The synthesis of the hybrid particle starts from the micellization of the copolymer poly(styrene)-b-poly(4-vinylpyridine) (PS-b-P4VP) carrying gold nanoparticles. This was carried out by mixing the block copolymer with the gold salt solution in chloroform solvent under sonication. A 10 fold concentration of hydrazine hydrate and hydrochloric acid was added to the mixture to reduce gold salt to nanoparticle. The resulting HPM was structured with P4VP/AuNP as the core and PS the shell. This hybrid was stabilized by the protonated core-forming P4VP block chains. Protonated P4VP was insoluble in chloroform and binds sufficiently to gold nanoparticles. The reversion of the core-shell template was carried out by a controlled addition methanol solvent, leading to the formation of the vesicle-like reversed hybrid polymeric particles. In this case, the gold nanoparticles are now located in the shell with the protonated P4VP shell. Once deprotonated, the gold nanoparticles in the shell region could be released.



^a Black solid lines represent PS chains, and blue solid lines represent P4VP chains.

Figure 1.29 Preparation of hybrid polymeric micelles (HPMs) and the reversion of the core-shell template releasing gold nanoparticles from its core to the shell region. ^[57]

Meristoudi *et al* reported another type of amphiphilic micelles which were used to generate gold nanoparticles embedded on its corona. ^[58] The template that was composed of a hydrophobic core poly(*tert*-butylstyrene) and a hydrophilic corona of poly(sodium sulfamate/carboxylate-isoprene) (BS-SCI). The block copolymer was synthesized through anionic polymerization technique. The core-shell structured templates were generated through self-assembly of the block copolymer in water. The preparation of the hybrid particle is demonstrated in Figure 1.30. Adding gold salt solution to the micellar solution resulted in the coordination of the gold ions into the

BS-SCI micelle template. Gold nanoparticles were formed after 18 hours through mixing the metal salt solution as indicated by its color change from colorless to dark red solution. The gold nanoparticles preferentially coordinated at the corona or shell component of the micelle, where the amine group resides. The amine group in the corona block of the template serves as both a reducing agent and stabilizer. It is well-known that the reduction of HAuCl_4 to Au^0 occurred due to the electron transferred from the amine to the metal ion. [59,60]

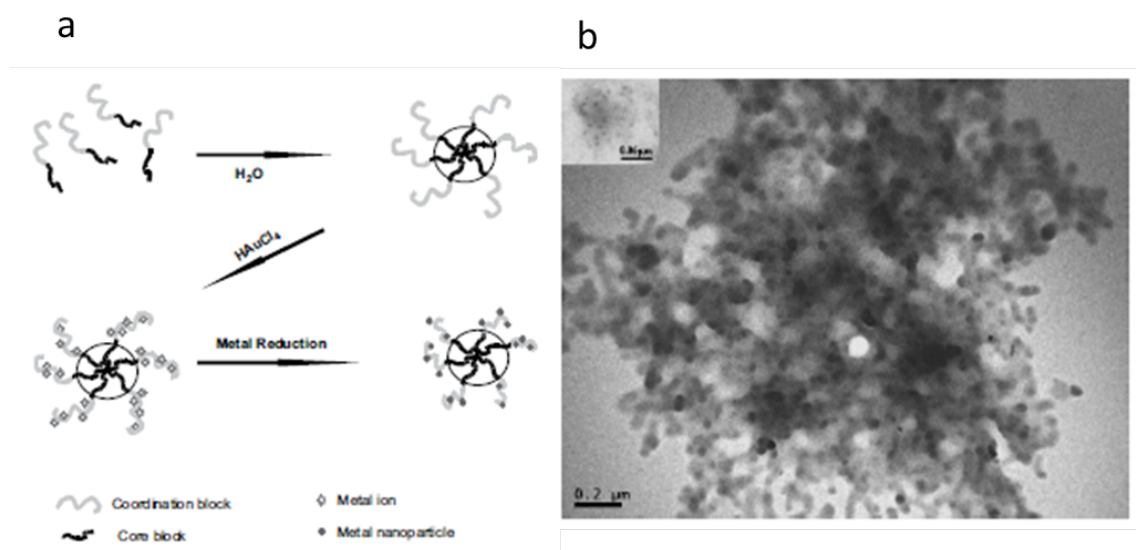


Figure 1.30 a) Schematic preparation of gold nanoparticle / diblock copolymer (poly(*tert*-butylstyrene) -*b*-poly(sodium sulfamate/carboxylate-isoprene)) (BS-SCI) hybrid assemblies, b) TEM image of the BS-SCI hybrid particles (inset is an HRTEM). [58]

Zhou *et al* reported the use of a diblock copolymer, poly(1-3'-aminopropyl)-4-acrylamido-1,2,3-triazole hydrochloride)-*b*- poly(*N*-isopropylacrylamide) (PAPAT-*b*-

PNIPAM) dissolved in dioxane/water mixture as for Au nanoparticle formation through an *in situ* reduction of gold ions using sodium borohydrate as a reducing agent in an aqueous media and at room temperature.^[61] The presence of the primary amine moieties in the PAPAT block is responsible for the metal complexation. Two approaches were carried out in this study in incorporating the Au nanoparticles inside the temperature sensitive block copolymer. At room temperature, Au nanoparticles were attached to the core (PAPAT) part of the block copolymer which was cross-linked with the glutaricdialdehyde at the same time. In this route, the PAPAT block contains highly reactive primary amine moieties, naming it as core cross-linked micelles (CCL). When temperature was raised at 50°C, the PNIPAM component shrunk while the crosslinked PAPAT polymer became the corona component and eventually encapsulated the Au nanoparticles. This type of micelle was called shell cross-linked (SCL) micelle. A closer examination of the TEM images of Au loaded templates of CCL (Figure 1.31b) and SCL (Figure1.31c) reveals the presence of Au nanoparticles and their location.

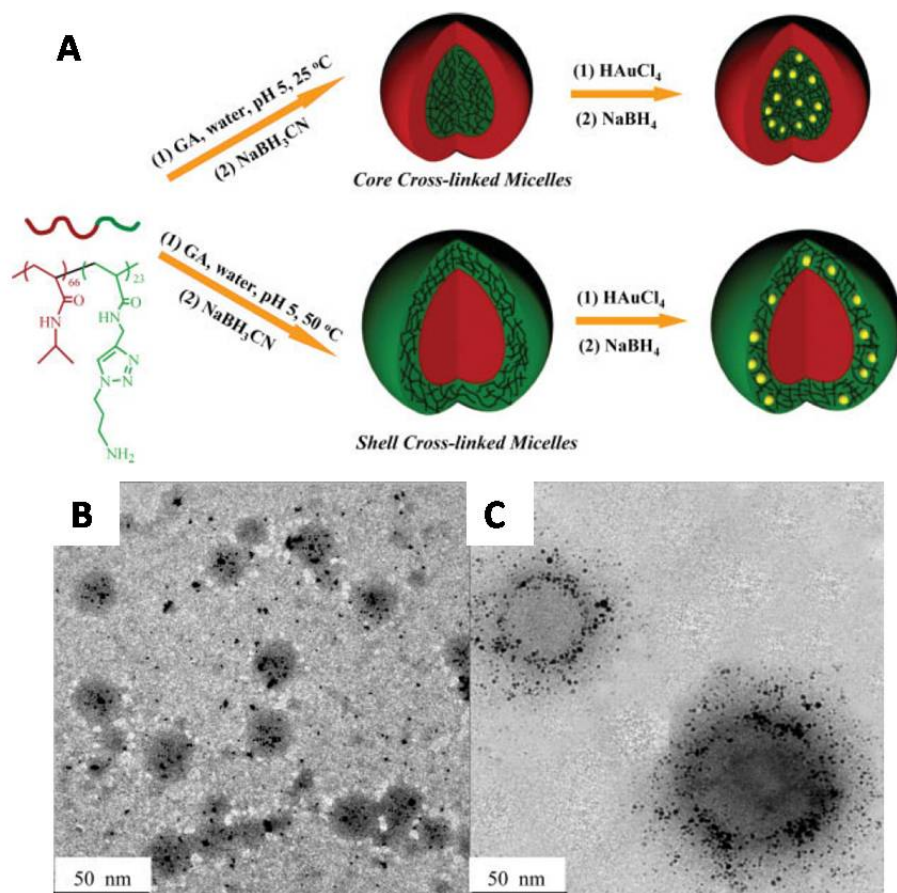


Figure 1.31 a) Schematic illustration of two types of hybrid micelles incorporated with Au nanoparticles, b) HRTEM images of the hybrid giant micelles using CCL and c) SCL as templates. ^[61]

Lei *et al* have demonstrated the formation of silver nanoparticles on the corona component of the polystyrene-*b*-polyacrylic acid (PS-*b*-PAA) dissolved in tetrahydrofuran (THF) with the help of poly(ethyleneimine) (PEI) solution as the reducing agent. ^[62] Figure 1.32a represents the preparation of the Ag/ PS-*b*-PAA composite. Prior to the use of the block copolymer, silver ions were first complexed

with the PEI solution. The PEI-Ag⁺ complex aqueous solution was added to the block copolymer mixture producing the self-assembly of the PEI-Ag⁺ / PS-*b*-PAA. Ag⁺ ion finally reduced and formed within the PAA corona component of the block copolymer. The reaction took place in ambient temperature with further purification through centrifugation and washing. TEM images show two different types of silver nitrate loading. Figure 1.32c shows thicker Ag nanoparticle compared to the Figure 1.32b.

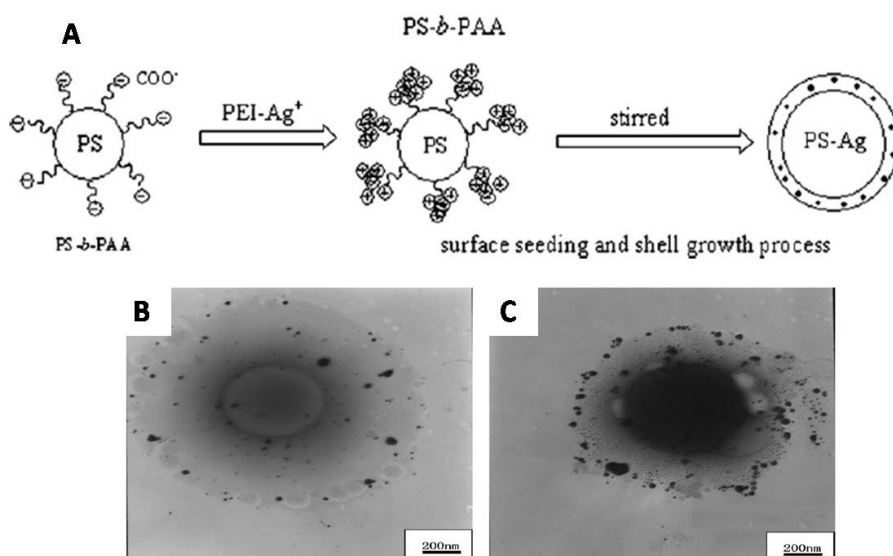


Figure 1.32 a) Schematic diagram on the synthesis of corona filled block copolymer (PS-*b*-PAA), b and c are TEM images of Ag/PS-*b*-PAA in different silver nitrate concentration. [62]

Another novel route of fabricating metal-polymeric composite particles is by amphiphilic block copolymer micelles as template. This type of synthesis uses solvent evaporation technique to promote phase-separated structures of the composite particles (e.g. Janus and core-shell structures). [63] Such process is called the self-organized precipitation method (SORP). Phase-separated structured particles containing gold

nanoparticles were synthesized by combining polymers of different hydrophobic-hydrophilic properties with pre-formed gold nanoparticle (Figure 1.33). The pre-formed nanoparticles were stabilized through a block copolymer poly(styrene-block-2-vinylpyridine) dissolved in toluene. Hydrazine was used as a reducing agent for the formation of gold nanoparticles. Gold nanoparticles were stabilized through the pyridine moieties of the block copolymer. Different polymers were then added to the gold / block copolymer composite particles dissolved in tetrahydrofuran (THF) solvent. Evaporation of the THF solvent was carried out at room temperature for two days. After evaporation, an opaque dispersion was obtained.

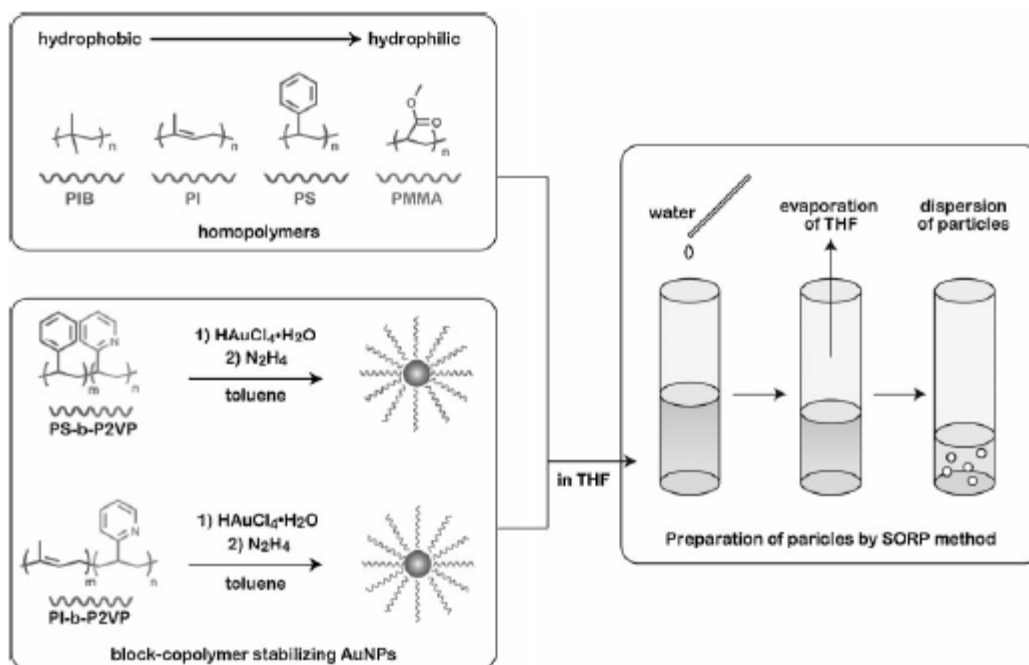


Figure 1.33 Schematic illustration of preparation of composite nanoparticles. ^[63]

Schematic illustration and TEM images of the gold/polymeric composite particles are shown in Figure 1.29. Three different kinds of structures of gold/polymeric

composite particles emerge in this synthetic route. The first type is a core-shell type of template where gold nanoparticles are located around the shell component. This can be observed in Figure 1.34a, d, g. The homopolymer poly(isobutylene) (PIB) was mixed with the AuNP@PI-b-P2VP. Here the shell is composed of the PI block of the copolymer since it is more hydrophilic than PIB. Thus, PIB is contained in the core. The second type (Figure 1.34b, e, h) is a janus particle wherein the homopolymer, poly(1,4-isoprene) (PI) has almost the same hydrophilicity with the poly(styrene) in the block copolymer. Gold nanoparticles are also attached in the block copolymer as well. Thus, the resulting image of the composite particles shows half of the particle filled with gold nanoparticles. The third type (Figure 1.34c, f, i) is another core-shell type of template. However, the gold nanoparticles are attached in the core, wherein the block-copolymer is attached. The mixture is composed of poly(methylmethacrylate) and the AuNP@PS-b-P2VP. Since PMMA is more hydrophilic than the AuNP@PS-b-P2VP, PMMA becomes the shell while the gold /copolymer component becomes the core.

The structural differences were strongly dependent on the hydrophilic-hydrophilic interaction of the polymer to the solvent. Chi (δ) value is one of the parameters to evaluate the hydrophilicity of the polymers. A higher δ value means high hydrophilicity. The δ values of PIB, PI, PS and PMMA are 15.5, 16.5, 18.6, 19.3 MPa^{1/2} respectively. Thus, in the case of PIB with Au@PI-b-P2VP, PI is more hydrophilic than PIB. This results in the formation of the PI moiety in the shell while the PIB as the core.

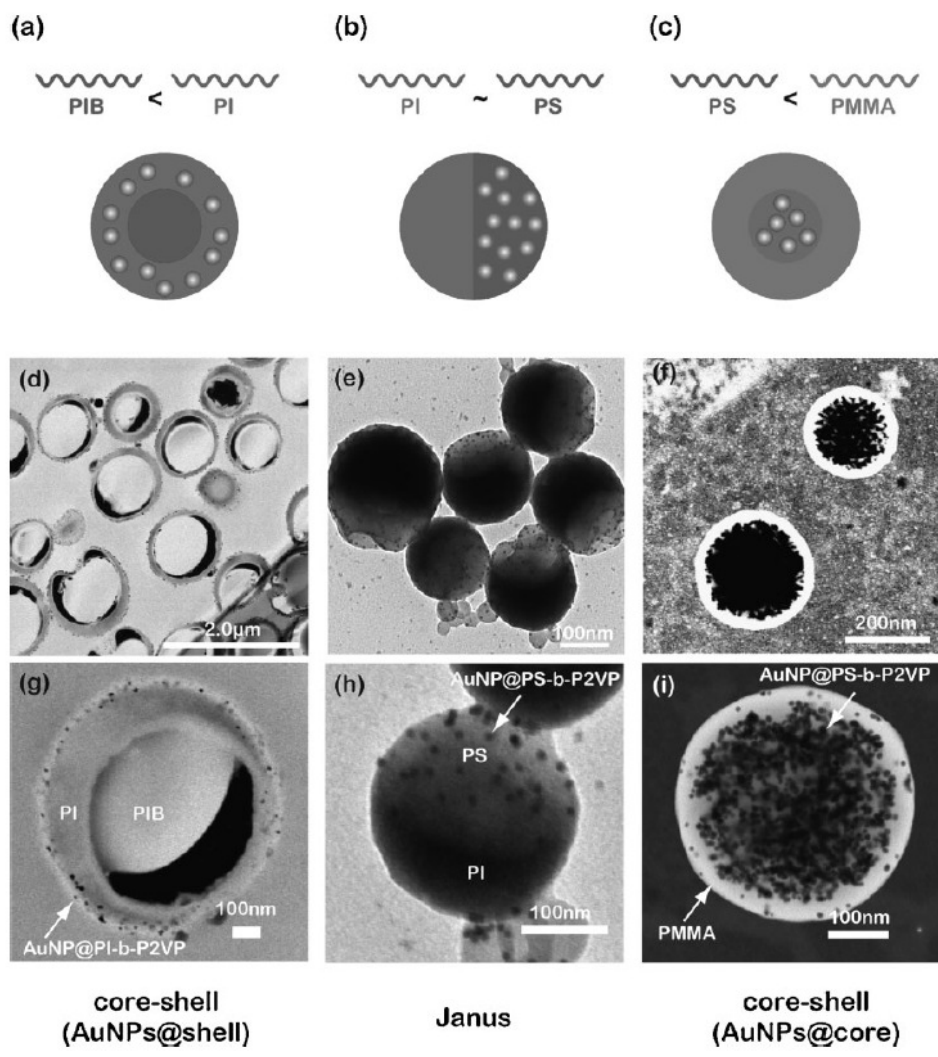


Figure 1.34 Schematic illustration and TEM images of gold/polymeric composite particles of PIB/AuNP@PI-b-P2VP (a,d,g), PI/PS/AuNNP@PS-b-P2VP-1 (b,e,h,) and PMMA/AuNP@PS-b-P2VP-2 (c,f,i).^[63]

1. 3.3 Dendrimers

Aside from using block copolymers, dendrimers have also been used to form and stabilize metal nanoparticles. Dendrimers are highly branched molecules that come in different generations. A commonly used one is the poly(amidoamine) (PAMAM), Figure 1.35.

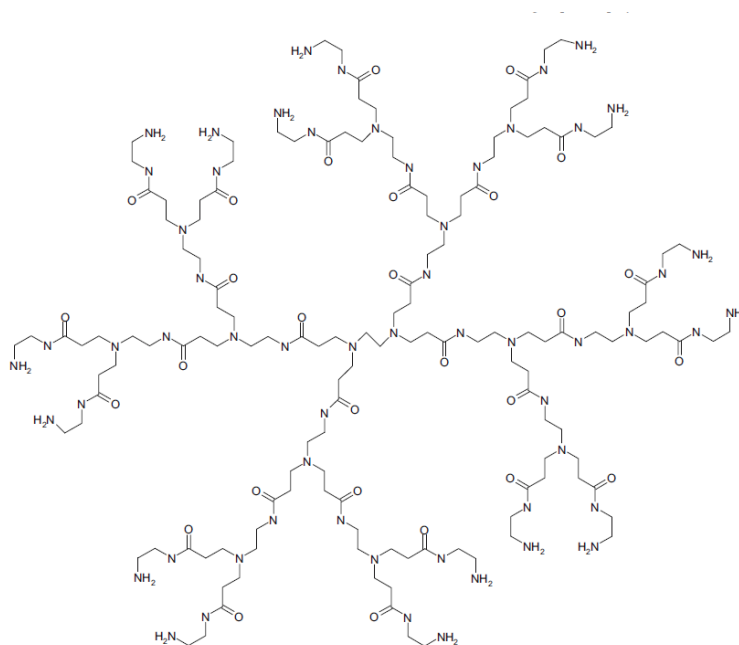


Figure 1.35 Chemical structure of polyamidoamine (PAMAM) dendrimer. ^[64]

For example, Umeda *et al.* have synthesized a fourth generation PAMAM with poly(ethylene glycol) (PEG) attached to it. ^[65] From this template, they were able to form Au nanoparticles through the binding of the gold ions to its tertiary amine group in the PAMAM core. Further reduction was carried out with the use of sodium borohydride solution. The PEG attached to it was used to make the system biocompatible. In the end, the PEG-attached dendrimers with Au nanoparticles

exhibited a strong photo-induced heat generating properties. Figure 1.36 illustrates the formation of Au nanoparticles into the core part of the dendrimer. At first, gold ions were attracted to the center part of the PAMAM core where the amine functional group resides. Later on, reduction was responsible for the formation of metallic gold.

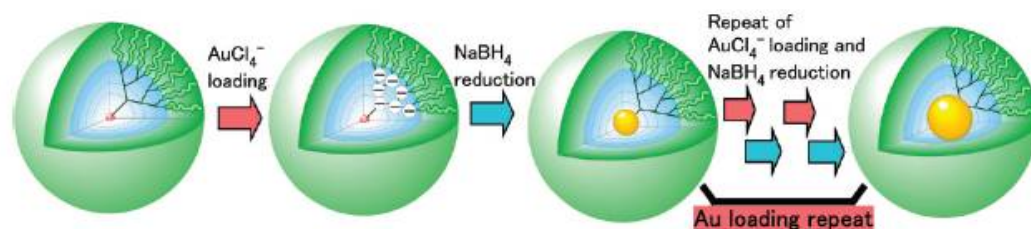


Figure 1.36 Formation of Au nanoparticles in PEG-attached PAMAM dendrimers.^[65]

A commonly used dendrimer is the hydroxyl-terminated poly(amido amine) (PAMAM) (G4-OH),^[66] Figure 1.37, which was able to encapsulate Pt and Pd metal nanoparticles as well.^[67] In this synthesis, appropriate metal ions are first mixed with the dendrimer solution forming complex with interior of the dendrimer. A chemical reducing agent was then added to reduce the metal ions to its corresponding metal nanoparticles (Figure 1.21). In this case, the dendrimer is used as a template and a stabilizer as well.

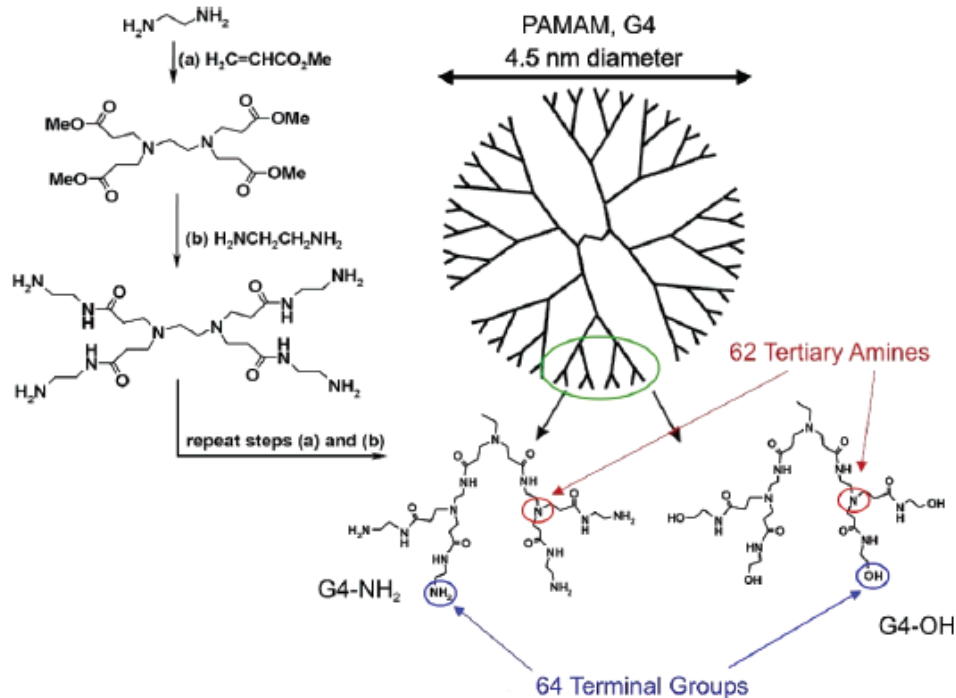


Figure 1.37 Chemical structure of hydroxyl-terminated poly(amido amine) (PAMAM) (G4-OH).^[66]

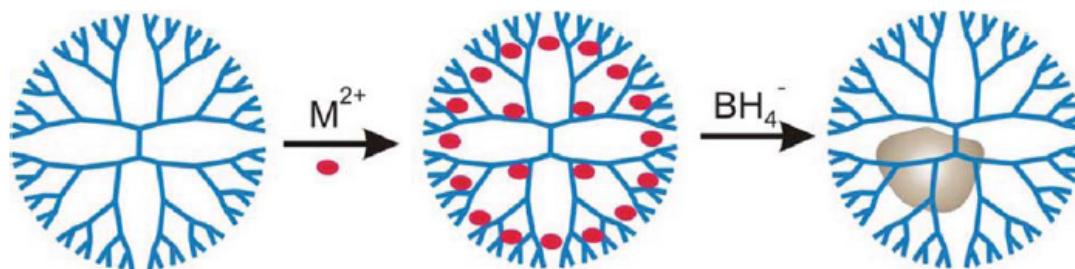


Figure 1.38 Dendrimer encapsulated nanoparticle scheme.^[67]

1.3.4 Polymer Particles

An emerging technique in generating metal nanoparticles and metal-polymeric composite particles is the use of a polymer template that possesses a core/shell or

core/corona structure. Here, a pre-formed polymeric template is used either as a platform for metal nanoparticle formation, or a stabilizer of metal nanoparticles. Different types of polymers have been used as templates and nanoreactors for metal nanoparticle formation. Selected examples of polymer particles for the fabrication of gold nanoparticles and its composite particles are discussed below.

1.3.4.1. Microgel Particles

Polymer microgels are colloidal particles having a crosslinked network that swells in a suitable solvent. When dissolved in water they are called hydrogels. Microgels can either be physically or chemically crosslinked. This type of colloidal particles are known for its stimuli-responsive ability to undergo reversible volume phase transition when subjected to change in temperature, ^[68] pH, ^[69] ionic strength, ^[70] solvent ^[71] and the action of electromagnetic fields. ^[72] The swelling and/or deswelling action of the microgel is caused by the imbalance of the repulsive and attractive forces within the particles. Inter-particle ionic repulsion constitutes the repulsive forces within the particle while hydrogen bonding and Van der Waals interactions cause attractive forces. Due to its stimuli-responsive ability, they are common called as smart materials. Some microgels are not only responsive to a single parameter but could be multiple as well.

This type of polymeric particle has been used in many synthetic routes for metal nanoparticles. Due to its stimuli-responsiveness, the transition from hydrophilic to hydrophobic state of the polymer layer allows an “expire” and “inspire” water behavior,

allowing the polymer to breathe and entrap small nanoparticles into the polymer network. ^[73] They are classified as soft template that creates soft-based composed particles. ^[74] Applications of these metal/polymeric composite particles or hybrid materials are especially useful in the emerging mesotechnology. ^[75] This term refers to the interface between macroscopic and nanoscopic scale devices which holds a promising potential in the future. The combination of both metal nanoparticles and microgels gives conception to the preparation of hybrid particles with multifunctional properties with synergistic effects of the metal nanoparticles and the stimuli-responsive nature of the polymer. The synthesis, characterization and applications of microgel stabilized metal nanoparticles have attracted enormous interest in the past decade. Zhang *et al.* ^[76] gave a review on the use of microgel metal nanoparticles as a facile nanotechnological approach. In Figure 1.39, gel networks give efficient capacity to load or embed metal nanoparticles and /or metal oxides that not only provide stabilization but also prevent further oxidation.

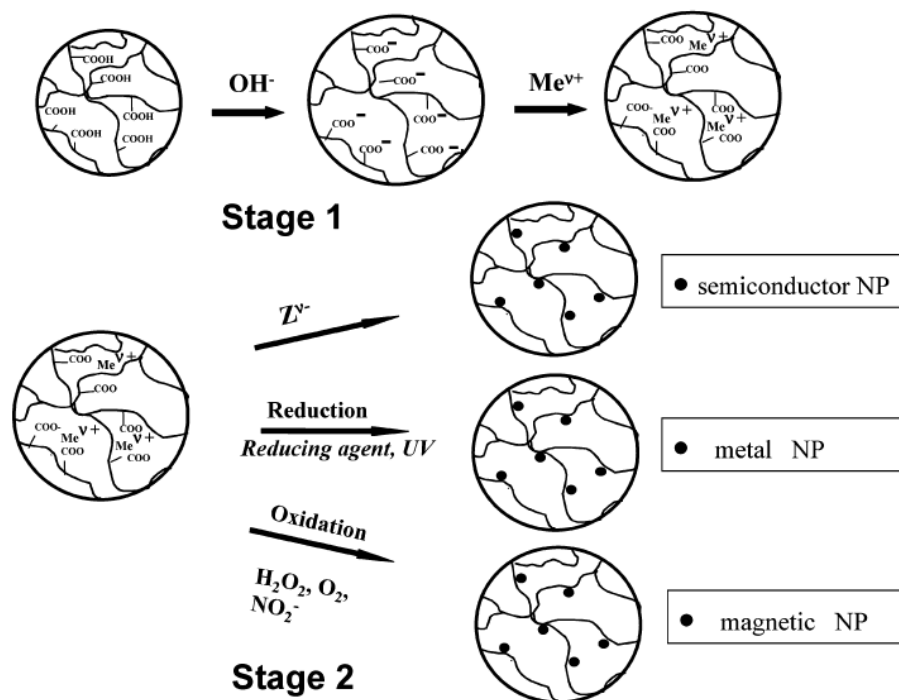


Figure 1.39 Effective process showing semiconductor, metal and magnetic nanoparticles formation in gel networks. ^[76]

Thermo-sensitive core-shell particles dispersible in water have been used to generate gold nanoparticles and its composite particles. ^[77] The core is composed of poly(glycidyl methacrylate-co-*N*-isopropylacrylamide) [(poly(GMA-co-NIPAM))] and the shell with pure PNIPAM. Synthesis of the hybrid particle is shown in Figure 1.41. The synthesis of the hybrid particle starts from the preparation of the template itself. The template was synthesized through soap free copolymerization of GMA and NIPAM using a crosslinker, *N, N'* – methylenebisacrylamide (MBAAm) and V-50 as initiator (Figure 1.40). ^[78]

growth. The thickened gold nanoparticles within the template were kept stable within the critical thickness of the gold nanoshells produced.

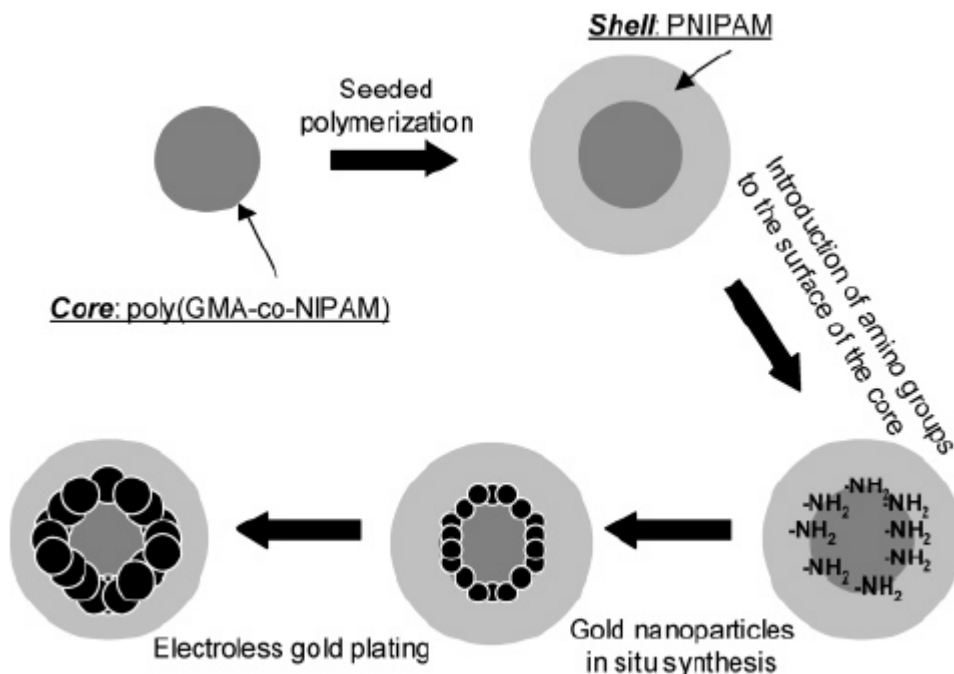


Figure 1.41 Synthesis of thermosensitive hybrid metal-core-shell particles with gold nanoshells. ^[77]

A soft copolymer particle, poly(*N*-isopropylacrylamide)-co-poly(acrylic acid) (PNIPAM-co-PAA) template was also used in the construction of core-shell gold-polyaniline (Au-PANI) nanoparticles (Figure 1.42). ^[79] In this study, the microgel template and the gold nanoparticles were independently synthesized before they were mixed together. The copolymer microgel was synthesized by a surfactant-free emulsion polymerization method using *N*-isopropyl acrylamide, and acrylic acid with the use of a crosslinker *N,N'*-methylenebisacrylamide initiated with ammonium persulfate

$[(\text{NH}_4)_2\text{S}_2\text{O}_8]$ under nitrogen at 70 °C for 4 hours. Purification of the microgel was carried out through series of centrifugation, filtration, and dialysis. Gold nanoparticles were separately synthesized using gold salt solution (HAuCl_4) in the presence of trisodium citrate. The average size was at 18 nm. The incorporation of these AuNPs was carried out by mixing it with the prepared microgel template particles at pH 7 and room temperature. The possible mechanism of the incorporation of gold nanoparticles into the microgel template was through the exchange with water molecules within the template. This process is entropic driven thus very spontaneous. The gold nanoparticles are then trapped within the template due to the physical entanglement of the microgel particle network and/or Van der waals interactions. Carboxylic acids and amides present in the microgel further give affinity to the gold nanoparticles immobilization within the template. To prepare the gold-PANI core-shell nanoparticles, aniline and ammonium peroxydisulfate (APS) was mixed for aniline polymerization (Figure 1.42b). The resulting dispersion was further centrifuged and washed thoroughly with water, ethanol to remove the microgel template and impurities leaving only the gold-coated with polyaniline nanoparticles.

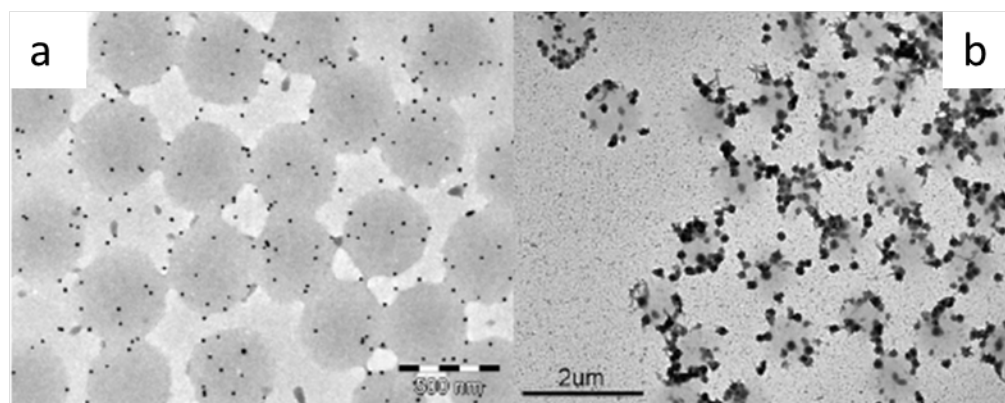
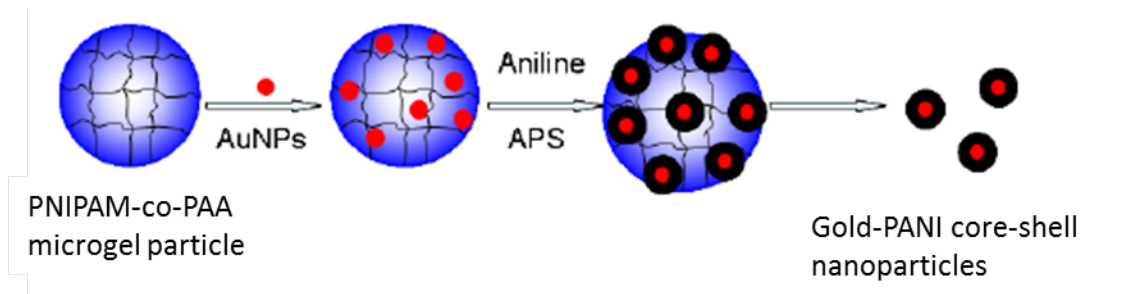


Figure 1.42 Schematic illustration of the synthesis of core-shell Au-polyaniline nanoparticles. TEM images of a) Au nanoparticles incorporated into the microgel templates. b) Au coated with polyaniline incorporated within the microgel templates. ^[79]

Suzuki *et al.* ^[80] reported copolymerization of glycidyl methacrylate (GMA) and *N*-isopropylacrylamide (NIPAM) by a soap-free emulsion polymerization with the use of methylenebisacrylamide (MBAAm) as crosslinker. Figure 1.43a shows the schematic representation of the formation of silver and gold-silver metal nanoparticles in the microgel network. The successful immobilization of metal nanoparticles into the microgel was made possible by first functionalizing the PNIPAM shell with amino group using 2-aminoethanethiol. Inclusion of the amino group in the microgel showed

an increase in microgel's size due to osmotic pressure. Gold salt precursor was then added and further reduced with sodium borohydride. Successive reduction of gold ions was carried out by taking the original gold-polymeric composite as seed. Metal nanoparticles became larger as further reduction was carried out. The group was able to demonstrate the color change of the gold nanocomposite by manipulating the temperature of the system. Also shown in Figure 1.43a is its ability to respond to temperature. At 25 °C, the microgel swells, making the gold nanoparticles in far distance from each other. However, when it reaches 40°C, it shrinks and eventually making the gold nanoparticles to be closer. Moreover, when the gold nanoparticles are closer to each other, it resembles as a bigger particle and thus gives a higher UV absorbance compared to its original size. Again, this change of UV absorbance was triggered by the interparticle interaction of gold nanoparticles. TEM image (Figure 1.43b) shows that the gold nanoparticles were located inside the microgel network rather than escaping from its surface. This was due to the strong interaction between the amino group and the gold nanoparticles. Successive reduction of gold ions through seeded growth process resulted to a larger gold nanoparticles as depicted on the TEM image, Figure 1.43c).

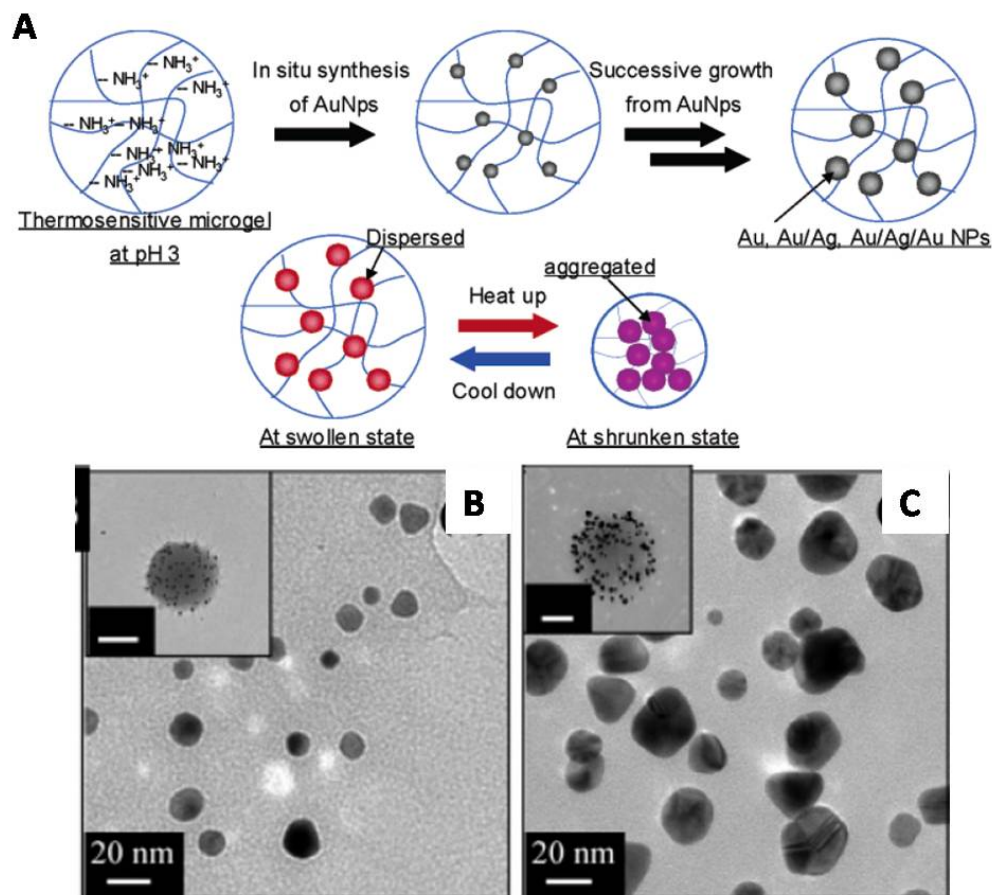


Figure1. 43 a) Schematic diagram on the synthesis of gold and gold/silver nanoparticles using a microgel template. b) TEM image of gold nanoparticles grown on the microgel, c) seeded growth gold nanoparticles. ^[80]

Suzuki *et al.* also reported the use of a core-shell template that was composed of poly(glycidyl methacrylate) (GMA) rich core and a poly(*N*-isopropylacrylamide) rich shell in aqueous medium. ^[51] Further modification was carried out in this template by incorporating thiol functional groups. The modified microgel was used in the synthesis of

gold nanoparticles by mixing with gold salt precursor and subsequent reduction with sodium borohydride. Figure 1.44 shows gold nanoparticle-loaded microgels at different temperature conditions. Due to its temperature responsive ability, a reversible color change was observed when temperature was change from 25°C to 40°C. This indicates the temperature dependence of the surface plasmon resonance of the gold nanoparticles present inside the microgel.

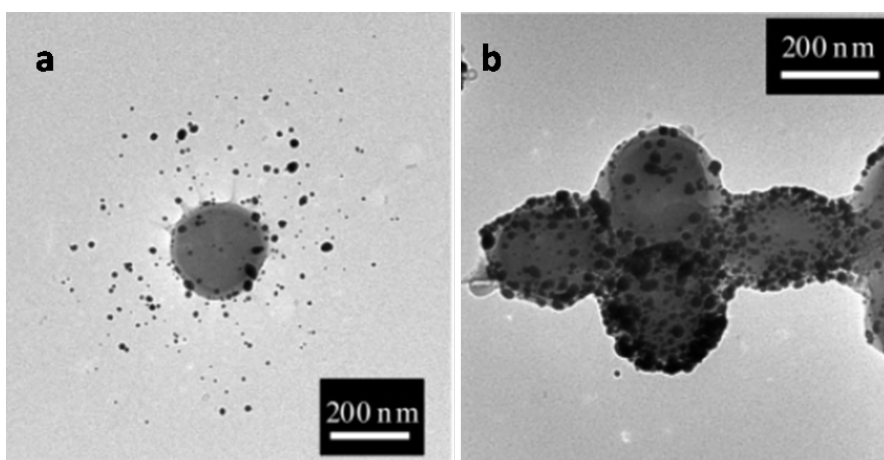


Figure 1.44 TEM images of gold nanoparticle loaded in a) room temperature and b) at 50°C. ^[81]

Polymeric template that is composed of polystyrene (PS) core and a polyaniline (PANI) shell has also been reported for the fabrication of gold polymer composite particles. ^[82] The synthesis of the template was carried out by polymerization of aniline on the pretreated polystyrene beads using ammonium persulfate as initiator.. Gold nanoparticles were independently synthesized with trisodium citrate prior to its incorporation into the template. The synthesized gold nanoparticles (ca. 20 nm) are then mixed with the core-shell structured template, PS/PANI. Figure 1.45 shows both the

TEM and SEM images of the composite particles. It was found that the pre-synthesized gold nanoparticles easily adsorbed on the surface of PS/PANI template. The adsorption of the gold nanoparticles was caused by the electrostatic effect between the electronegative citrate-stabilized gold nanoparticles and the cationic PS/PANI surface.

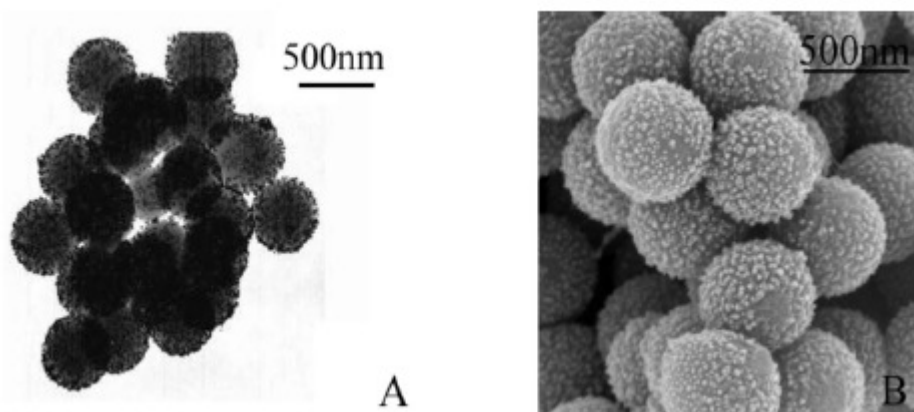


Figure 1.45 A) TEM image of Au/PS/PANI composite particles, B) SEM image of the Au/PS/PANI composite particles. ^[82]

Gorelikov *et al.* ^[83] used a negatively charged copolymerized microgel (poly(*N*-isopropylacrylamide-acrylic acid) P(NIPAM-AA) through surfactant free polymerization as template for gold nanorods. The gold nanorods were synthesized independently through stabilization with cetyltrimethylammonium bromide (CTAB), making it positively charged. Embedding the pre-synthesized gold nanorods into the microgel was possible through electrostatic interaction. The gold nanorods in this hybrid colloid absorb near-infrared light that can be used for drug delivery. A low and high resolution TEM is shown in Figure 1.46. Gold nanorods were evenly distributed

throughout the microgel template. A similar method of synthesizing gold nanorods into a microgel template was further developed by Karg *et al.* [84] when they used poly(*N*-isopropylacrylamide) with high surface charge to attract pre-formed positively charged gold nanoparticles. The gold nanoparticles were further modified to enhance its negative charge by wrapping them with two polyelectrolytes, poly(styrene sulfonate) and poly(allylamine hydrochloride) (PAH) (Figure 1.47).

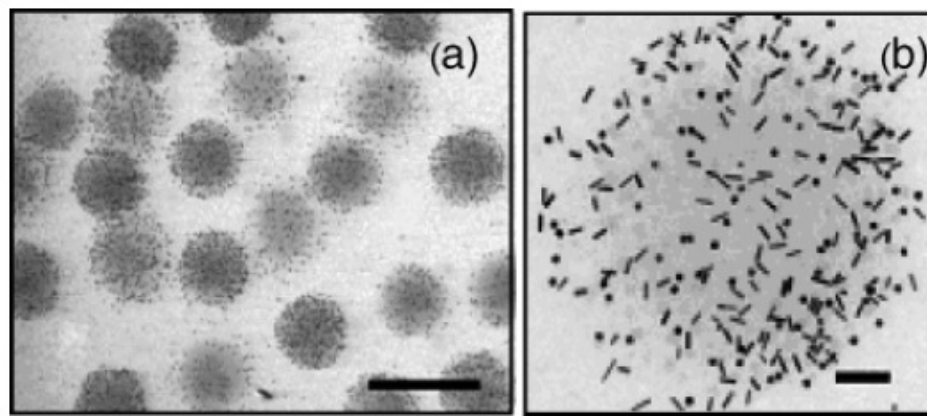


Figure 1.46 a) Low and b) high resolution TEM images of PNIPAM-AA microgels loaded with gold nanorods. Scale bars are 1 μm and 100 nm, respectively.

[83]

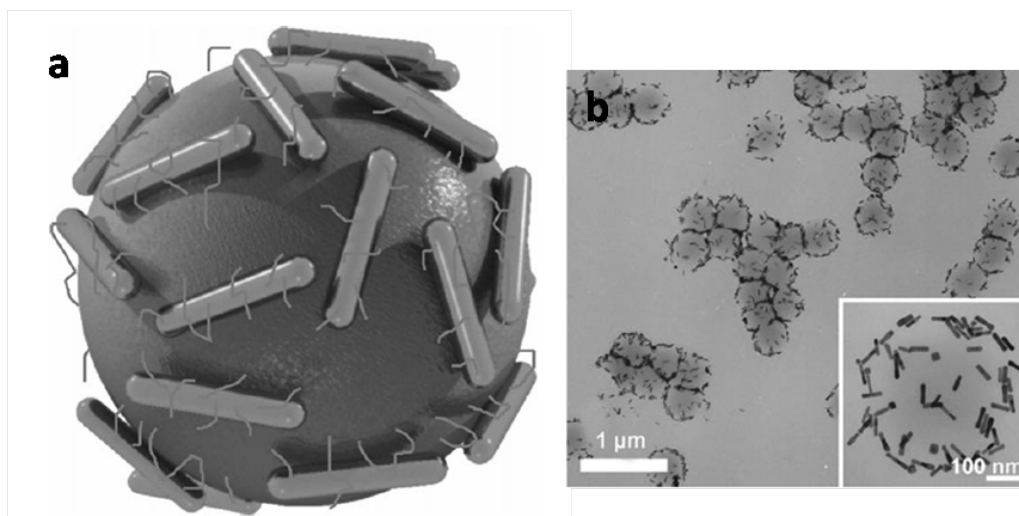


Figure 1.47 a) Sketch of collapsed PNIPAM microgel with polyelectrolyte-coated Au nanorod, b) TEM image of PNIPAM microgel with Au nanorods. ^[84]

1.3.4.2 Core-shell Particles with Polyelectrolyte Brushes

Spherical polyelectrolyte brushes (SPBs), composing of a solid polystyrene core grafted with long cationic polyelectrolyte chains of poly (2-aminoethyl methacrylate hydrochloride) (PAEMH) were used as a nanoreactors for gold nanoparticle formation. ^[85] The incorporation of gold nanoparticles into the SPB is demonstrated in Figure 1.48. When SPBs are immersed in water, its polyelectrolyte brushes swell that form a dense layer of chains from the surface of its core. The counterions responsible for metal ion exchange reside within the brush layer of the SPB template. When AuCl_4^- ions are added into the system, they expel Cl^- ions from the brush layer. The AuCl_4^- ions are then confined within the brushes and immobilized within. Addition of a reducing agent

such as sodium borohydride, reduces gold salts to gold nanoparticles which are formed and confined within the template's brush layer. The confinement of the gold nanoparticles are evident during the shrinking of the composite particles, giving a densely crosslinked mesh. Gold nanoparticles can be expelled from the SPB template upon addition of NaCN solution in the presence of O₂. Upon this reaction, the brush chains of the SPB stretch again and assumed their previous conformation.

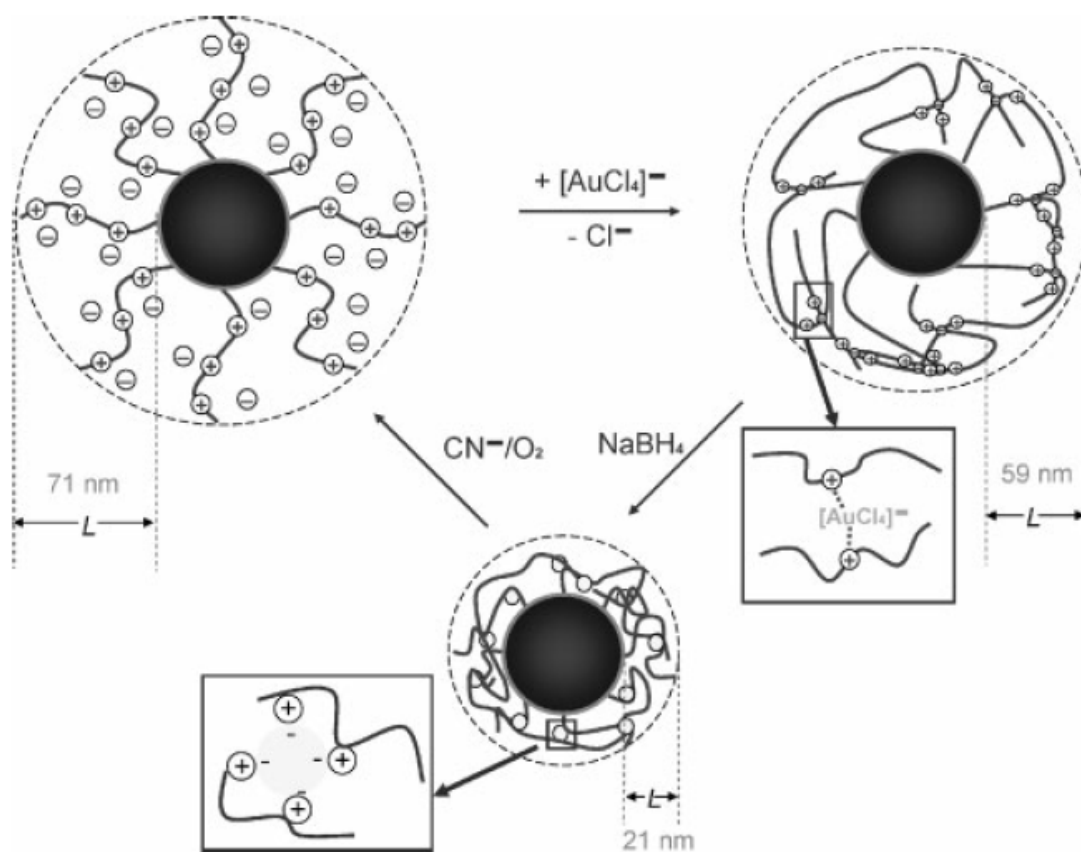


Figure 1.48 Scheme for the formation of gold nanoparticles using a spherical polymeric polyelectrolyte. ^[85]

Later on the formation and immobilization of gold nanoparticles was carried with the use of a gold salt precursor and a reducing agent. Figure 1.49a illustrates the mechanism of the Au nanocomposite. The metal ions (AuCl_4^-) are first introduced into the brush layer of the template by the counterion exchange mechanism. Shrinking of the whole system was evident due to the partial cross linking of the gold ions and its surrounding polyelectrolyte brush. Upon the action of the reducing agent, the gold ions are converted into metal nanoparticles. These metal nanoparticles are located on the particle surface, as seen in Figure 1.49b and c. The difference of this type of template is that it ensures that metal nanoparticles are strongly attached on the surface rather than being penetrated through its brush.

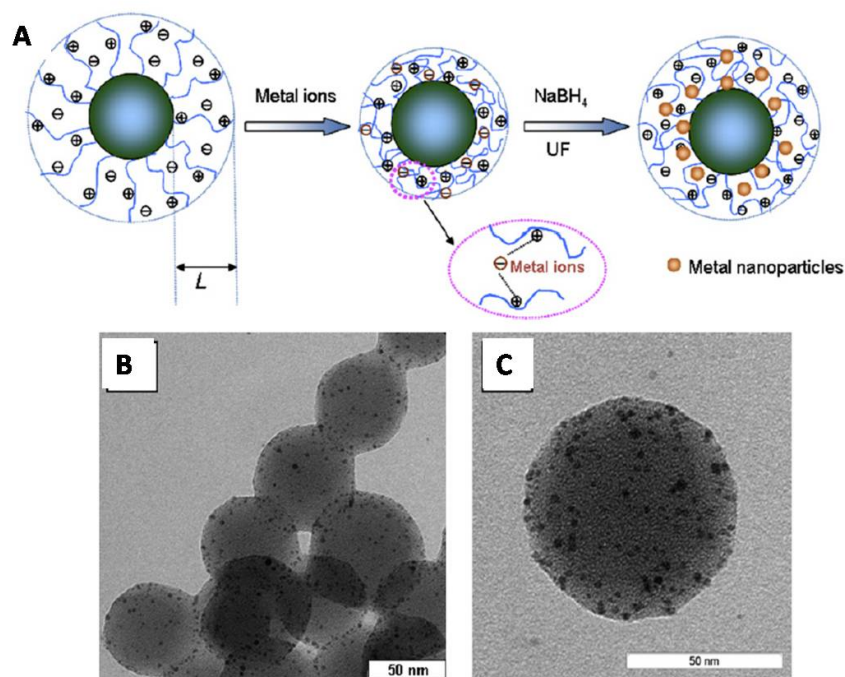


Figure 1.49 a) Formation and immobilization of gold nanoparticles in PS-PIL template.

b and c) TEM images of gold nanoparticles on the surface of the template.

[85]

Ballauff *et al.* have developed a template called a nano-tree as novel template for the synthesis of composite particles. ^[86] Basically the shell part of the system is composed of branches like trees. This type of colloidal system was synthesized by first producing the core, polystyrene (PS) through a conventional emulsion polymerization. Second is the attaching of the photo initiator on the surface of the core. The photo-initiator used was 2[*p*-(2-Hydroxy-2-methylpropiophenone)]-ethyleneglycol (HMEM) that resulted into radicals on the surface of the core. The water-soluble macromonomer, poly(ethylene glycol) methacrylate (PEGMA) was then polymerized from the the surface of the core forming tree like structures. Figure 1.50a illustrates the use of this PS-PEGMA template to produce silver nanoparticles with a reducing agent. In this case, PEGMA has high affinity to metal nanoparticles due to its hydroxyl groups located on the tip of the brush. And due to its highly branched structure shell, silver nanoparticles formed are not easily detached from the nano-tree network due to its steric hindrance. Thus immobilization of silver nanoparticles and its stability are very much enhanced in this type of template. Figure 1.50b and c displays the Cryo-TEM images of these nano-type template with immobilized silver nanoparticles. It is observed that the silver nanoparticles are attached inside the highly branched nano-tree shell.

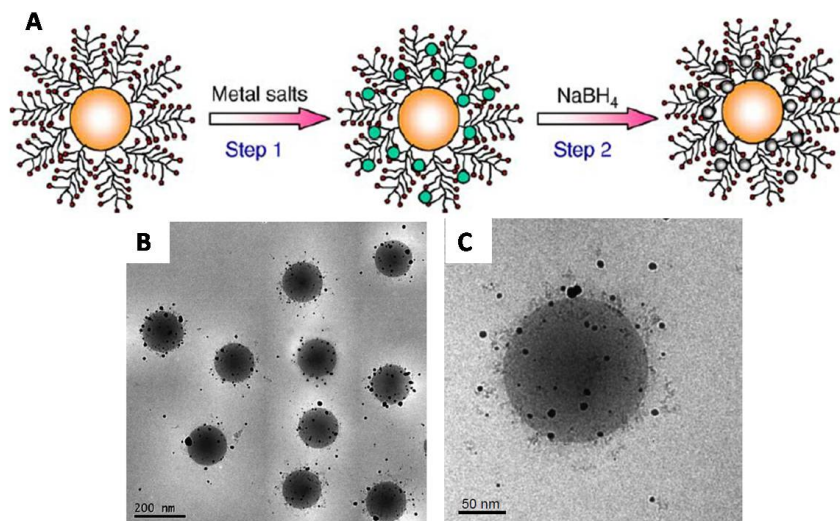


Figure 1.50 a) Schematic diagram of the silver nanoparticles trapped inside the nano-type PS-PEGMA template. b) and c) Cryo-TEM Images of the Au in PS-PEGMA nanocomposite. ^[86]

Lu *et al.* have used a poly(ionic liquid) (PLI) chains to attach metal nanoparticles on the surface of the polymeric template. ^[87] The polymeric template used in this study has a polystyrene (PS) core and covered with chains of vinylimidazolium type of PLI grafted densely on PS core. These templates are brush-like particles that exhibit an overall cationic charge. Polymeric template, such as polystyrene-poly(ionic liquid) (PS-PIL) was first synthesized by photo-emulsion polymerization of styrene A photo initiator, 2[*p*-(2-hydroxy-2-methylpropiophenone)]-ethyleneglycol (HMEM) was used to create radical on the surface of the PS core. Radical polymerization followed with the use of the PIL. The PIL becomes the shell layer or the brush component of the template. A schematic diagram is shown in Figure 1.51.

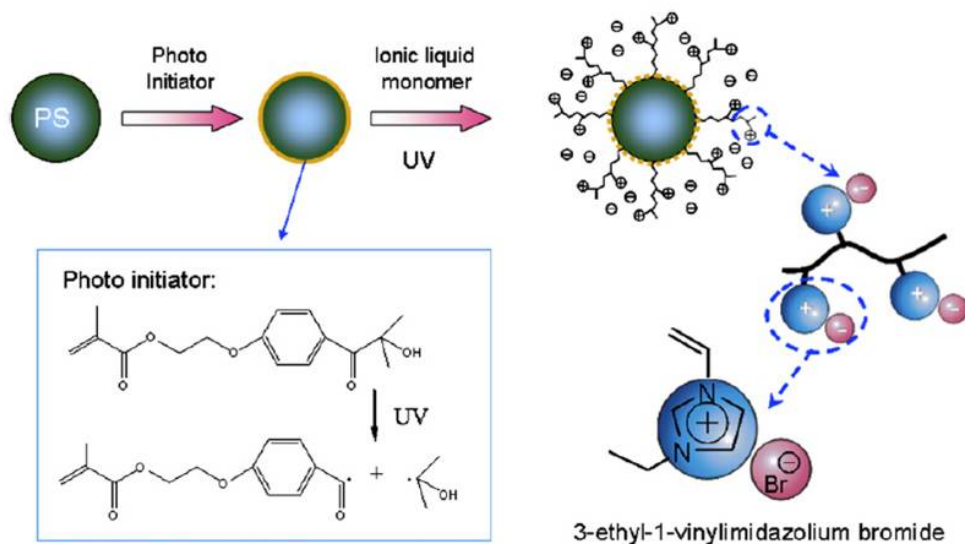


Figure 1.51 Schematic diagram for the synthesis of PS-PIL template for metal nanoparticle formation and immobilization. ^[87]

1.4 Applications of Metal/Polymeric Composite Particles

The increasing interest of using gold nanoparticles stabilized in microgels have had a significant attention in the past decade. These composite particles combine the properties of the gold nanoparticle and the microgel's smart responsiveness. These properties include high surface area to volume ratio, quantum size and electrodynamic interactions. On the other hand, the microgel polymeric templates possess stimuli responsive ability to manipulate its structure and morphology. The synergistic combination of the properties of gold nanoparticles and its microgel template results to a unique hybrid particle, which opens up its applications in biomedicine, catalysis, sensing and nanoelectronics.

Biomedicine is one of the most exploited fields of applications of gold nanoparticles. Below is the generalized scheme (Figure 1.52) that gold nanoparticles are used in the biomedical field. This range of applications is due to optical properties of the gold nanoparticles which are attributed to their plasmon resonance associated with the collective excitation of conduction electrons in a wide region (from visible to infrared).^[88] The biomedical application of gold nanoparticles ranges from diagnostics, therapy and immunology. Most of these stabilized gold nanoparticles were generated through the classical wet chemical methods by the use of reducing agents and stabilizers. Comparing to other polymeric systems, stimuli-responsive polymeric system with gold nanoparticles has not yet been fully utilized in the biomedical applications. Metal nanoparticles immobilized with thermally responsive polymer have the ability to convert external stimuli to heat to the polymer displaying a sharp property changes in response to temperature changes.^[89] This allows external control over polymer properties. With this platform, few studies have carried out to investigate its application in drug delivery and cancer therapy.

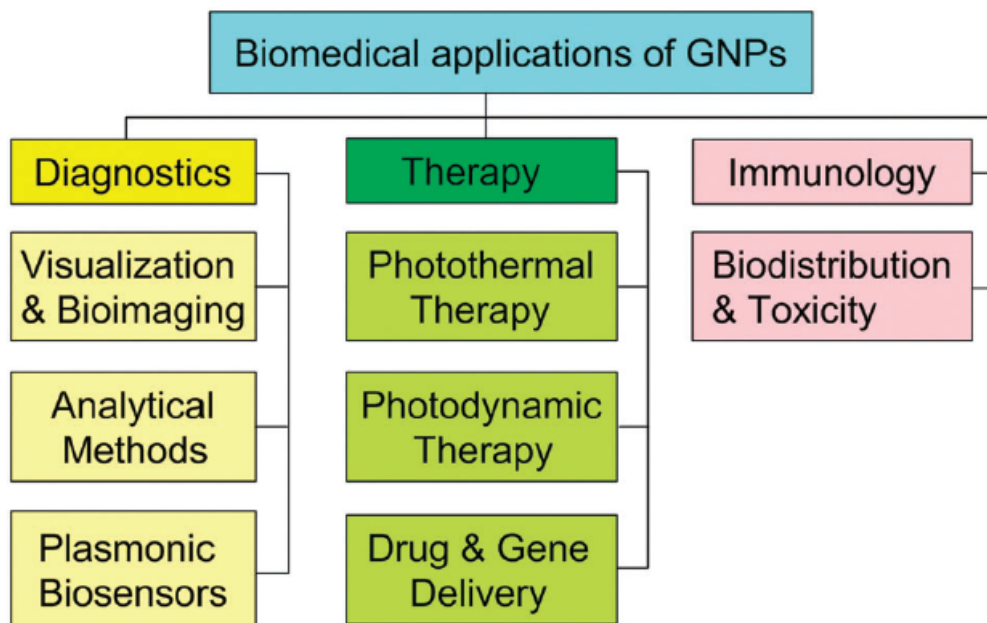


Figure 1.52 Generalized scheme for the biomedical application of gold nanoparticles. ^[88]

In the study of Sersehn *et al.* ^[90], photothermally modulated drug was demonstrated using a composite of Poly(*N*-isopropylacrylamide-co-acrylamide) Poly(NIPAAM-co-AAm) and gold-gold sulfide nanoparticles. Upon irradiation with near infrared (NIR) light, the hydrogel shrinks as it exceeds the LCST, causing a burst release of soluble molecules within the matrix (Figure 1.53). Molecules such as ovalbumin and bovine serum albumin and methylene blue were carried out in this investigation. A similar study was also carried out in the photothermal delivery of insulin ^[91].

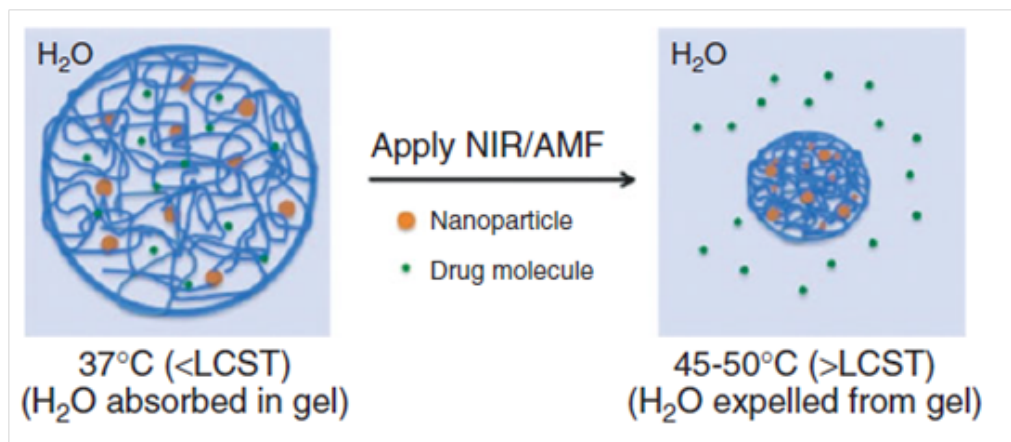


Figure 1.53 Schematic representation of drug delivery from temperature-sensitive hydrogel. ^[90]

One of the most studied metal/polymeric systems is its catalytic activity. Enhanced and modulated catalytic activity of gold nanoparticles embedded on temperature sensitive core-shell particles was demonstrated by Ballauff's group. The composite Au/poly(styrene)/PNIPAM was used as nanoreactors for catalytic oxidation of alcohol. Catalytic property of these composite materials on the reduction of *p*-nitrophenol to *p*-aminophenol was investigated through monitoring the product formation by UV-Vis spectroscopy (Figure 1.54). Temperature sensitivity of the core-shell microgel modulated the accessibility of the gold nanoparticles embedded within the system (Figure 1.55).

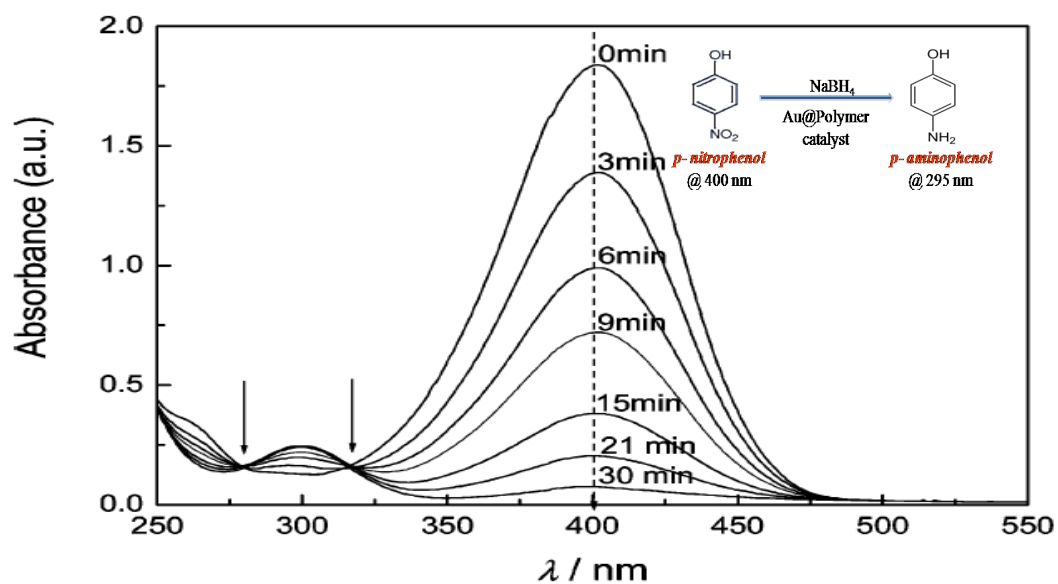


Figure 1.54 Reduction of *p*-nitrophenol to *p*-aminophenol monitored by UV-Visible spectroscopy.^[92]

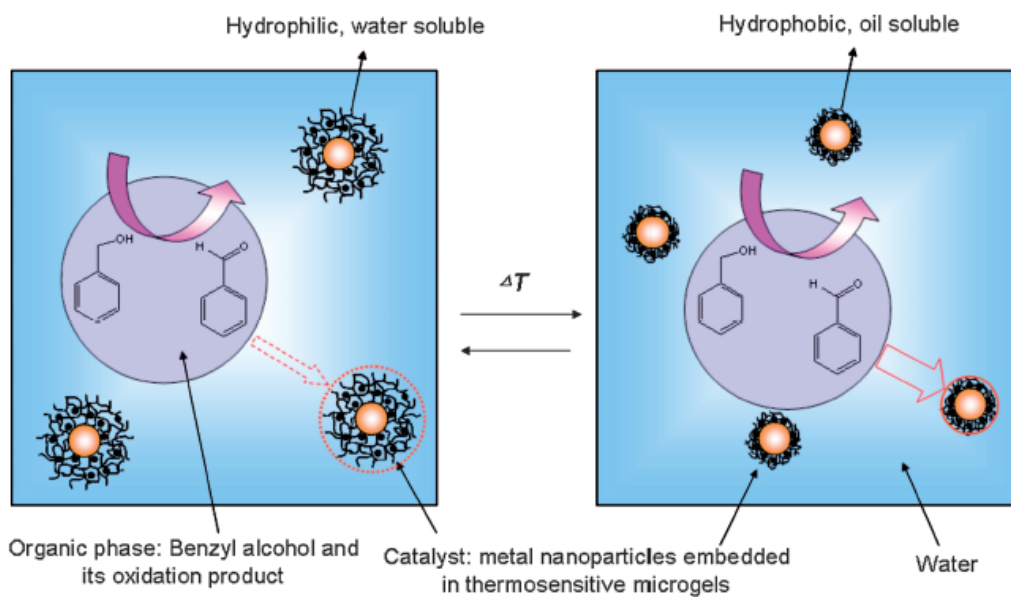


Figure 1.55 Schematic representation of catalytic oxidation of benzyl alcohol in the presence of gold nanoparticles immobilized in thermosensitive microgels.

[92]

Color tunability of the metal/polymer composite was demonstrated by Kawaguchi's group through incorporating gold nanoparticles in NIPAM and glycidyl methacrylate (GMA) copolymerized microgels. ^[93] The color tunable hybrid microgel was possible due to the inter-particle interactions of the surface plasmon resonance as shown in Figure 1.56. This type of optical property can further be applied in sensing. Similar result was demonstrated by Weiping *et al.* ^[94] In their study, they used a smart composite particle of poly(*N*-isopropylacrylamide) (PNIPAM)-grafted dextran (DexPNI) as template and sodium borohydride as the reducing agent.

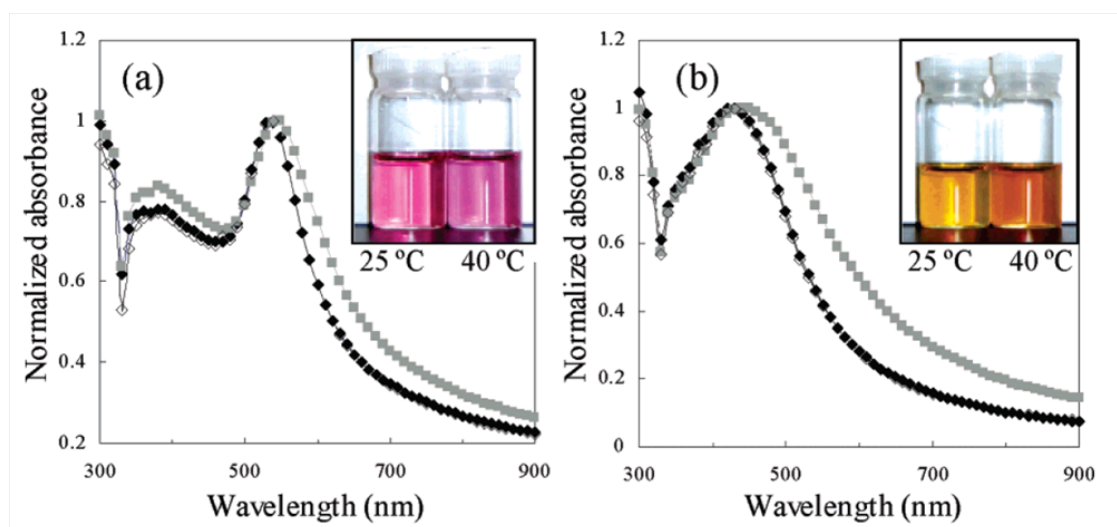


Figure 1.56 UV-Vis spectra of gold nanoparticles in polymeric composite particles, showing different colors at 25 °C (black line) and 40 °C (in gray line). (a) Au nanoparticles in GMA-co-PNIPAM, (b) AuAg in GMA-co-PNIPAM. ^[93]

1.5 Drawbacks of current methods on the synthesis of metal/polymeric composite particles

Current methods of synthesizing metal nanoparticles are obviously in a myriad of different routes of chemical reduction of metal salt precursors. Although the current methods have shown reliability of their synthesis and producing quite uniform size distribution of metal nanoparticles, environmental issues are basically set aside or worst not met. As previously discussed in the earlier section, the electrochemical and thermal decomposition methods are far way exploited the use of energy (e.g. photoirradiation, ultrasound irradiation and high temperature boiling process)^[95]. Furthermore, long and tedious synthetic procedures are generally required, giving low yields^[96] and highly polydispersed metal nanoparticles. This can be observed in a microemulsion reverse micelle metal nanocomposite.^[97] For metal nanoparticles bound ligands, the consequence of the difficulty in dispersing in water hinders the surface modification and functionalization for further applications,^[98] which may eventually alter the nanoparticle properties.^[99]

In the case of the direct reduction of metal salt precursor, reducing agents such as sodium borohydride and hydrazine are considered to be toxic chemicals.^[100] Most of these synthetic routes utilizing these strong reducing agents come in excess which may create undesirable products.^[101] Furthermore, impurities are left behind that may affect the functionality of the composite material and its potential applications. Thus, a long and tedious purification process is generally required which consumes more materials that utilizes huge amount of solvent and other reagents. Furthermore, the current

technology is far way scalable due to its low throughput and complicated route. Thus, further development of cost-effective and reliable production methods are highly desirable.

The development of hybrid colloidal particles that can be useful for future applications in catalysis and health care faces the issue of leaching.^[102] Leaching refers to the movement of metal nanoparticles from its polymeric template which can be detrimental to its environment. Further applications of these hybrid colloids require non-toxic and non-cancerogenous materials. Some structures of metal/polymeric composite particles are not efficient enough to carry out its application. This refers to structures wherein the metal nanoparticles are embedded within the core of the template. In this way, when used as catalyst, the surface area of the metal nanoparticles is not easily accessed by the reactants, thus resulting in inefficient catalytic performance.^[103]

The future challenges in creating unique metal/composite systems to address the current synthetic and application limitations are listed below:

- 1) To create a unique template that is an all-in-one platform. It can reduce metal ions to nanoparticles, immobilize the resultant nanoparticles, and stabilize the composite particle.
- 2) Smart templates that can regulate the accessibility of the metal nanoparticles through controlling external stimulus such as pH, temperature and electrolyte.
- 3) The template is also capable of immobilizing other organic and biological molecules for protection and deliveries.

- 4) The composite particles can be easily purified and recovered without the need to undergo a long and tedious purification step.
- 5) The synthesis should be scalable for commercialization.

1.6 Introduction to amphiphilic core-shell particles

Prof. Li's group has developed a simple yet versatile synthesis of a variety of amphiphilic core-shell particles.^[104] The novel synthetic approach developed enables us to synthesize a wide variety of core-shell particles with different chemical structure, composition, size, and functionality. The amphiphilic particles produced have a well-defined core-shell structure with sizes ranging from 60-500 nm in diameter and a narrow particle size distribution. The core diameter, shell thickness and surface functionality can be easily altered through the control of reaction conditions. The core property can be varied from hard, soft and temperature-sensitive to hollow particles. The shell component can use a wide range of commercially available and inexpensive amine containing water-soluble polymers, from natural to synthetic polymers. The process uses aqueous-based Chemistry, which is environmentally benign and the particles are easy to synthesize in high solids content (up to 30%) in the absence of surfactant. Figure 1.57 shows morphologies of different particles containing either biopolymer or synthetic polymer shells and different polymer cores.

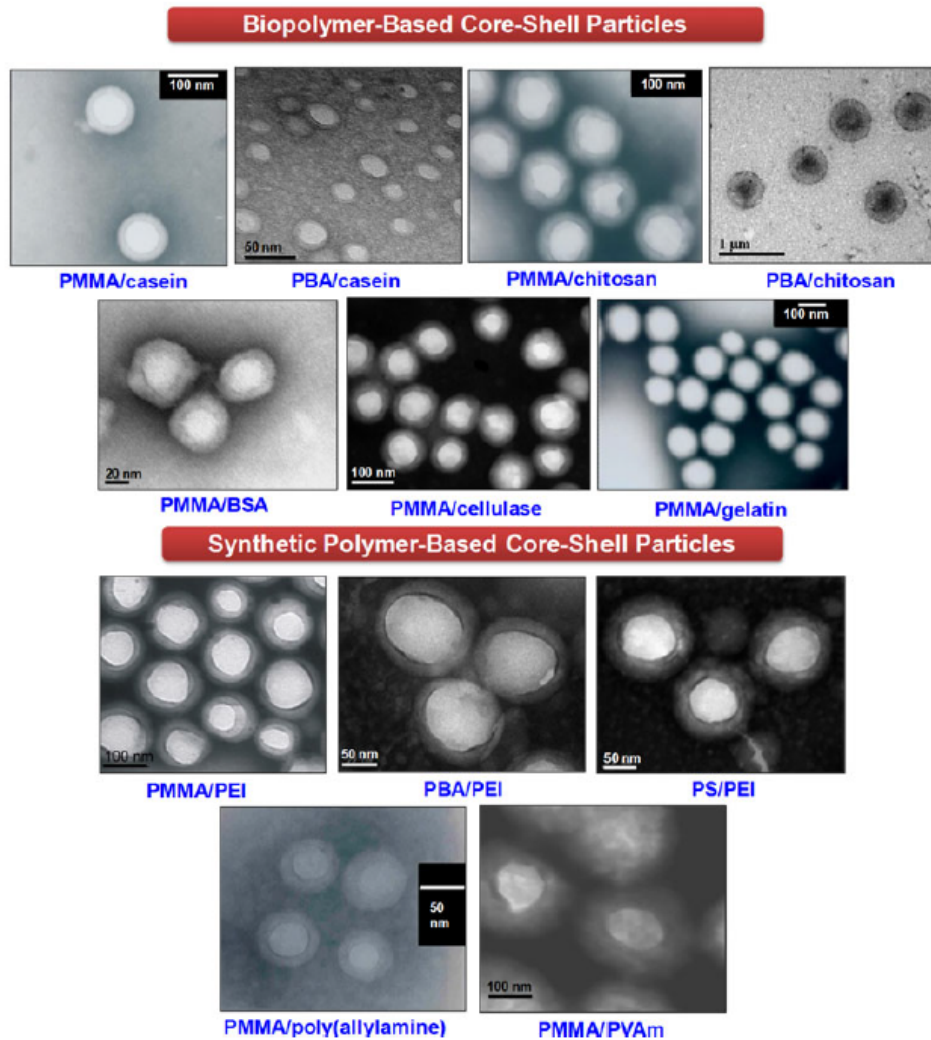


Figure 1.57 Examples of core-shell particles produced using our synthetic route. ^[104]

1.6.1 Particle synthesis and polymerization mechanism

Figure 1.58 illustrates the mechanism of particle formation through the graft copolymerization of vinyl monomer from a water-soluble polymer containing amino group. Alkyl hydroperoxide (ROOH) such as *tert*-butyl hydroperoxide (*t*-BuOOH)

primarily interacts with the amino group of the polymer backbone (i.e. PEI is mostly used), forming a redox pair. Subsequent electron transfer and loss of proton result in the formation of amino radical and alkoxy radical (RO \cdot). The amino radical is capable of initiating graft polymerization of the vinyl monomer in water. The resulting amphiphilic macro-radicals can undergo self-assembly to form polymeric micelle-like microdomains, where become loci for the subsequent polymerization of the monomer. The later stage of polymerization is similar to emulsion polymerization. At the same time, the generated RO \cdot radical can either initiate homopolymerization of the vinyl monomer inside the micelle or abstract a hydrogen atom from the polymer backbone to create a backbone radical that also can initiate graft polymerization of the vinyl monomer. As a result, core-shell particles with hydrophobic polymer cores and water-soluble polymer shells can be produced with narrow particle size distribution and well-defined core-shell nanostructure.

Novel feature of this synthetic approach is that it combines graft copolymerization, *in situ* self-assembly of the resulting amphiphilic graft copolymers and emulsion polymerization in a one-step synthesis. This versatile methodology allows us to design and tailor-made particles for specific applications through selection of appropriate water-soluble polymers and hydrophobic monomers.

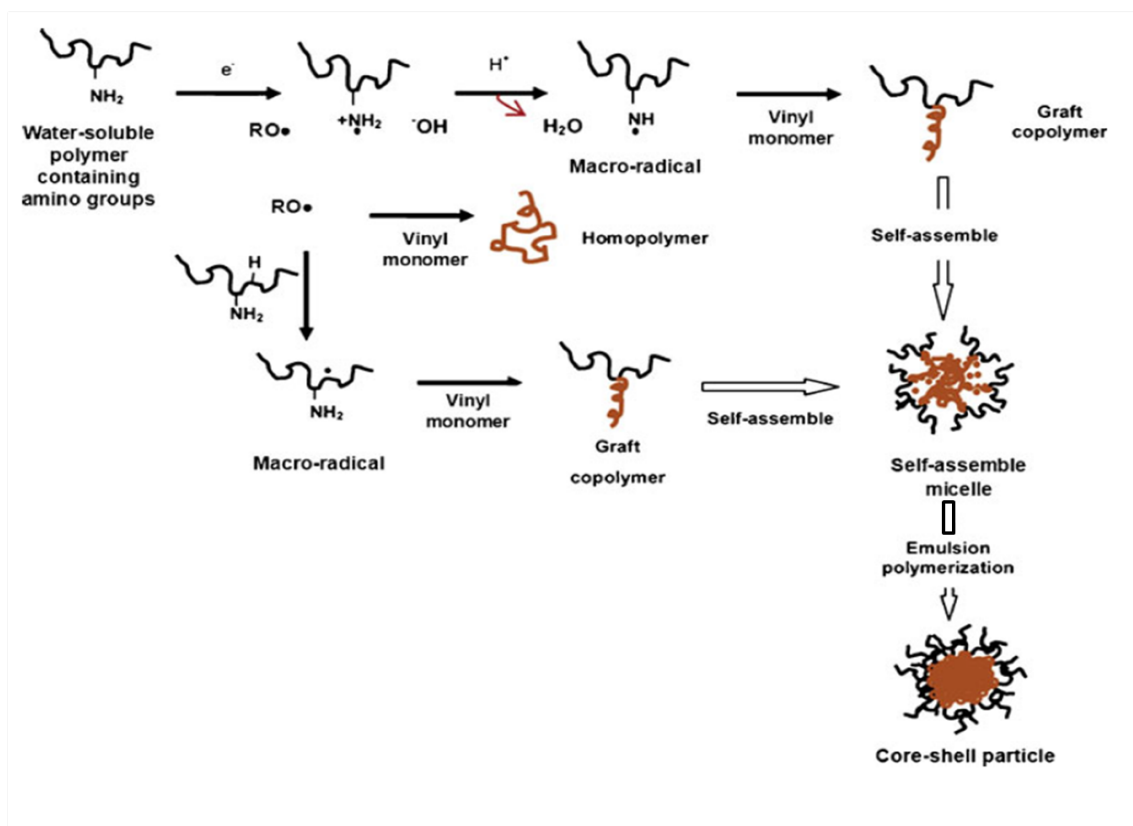


Figure 1.58 Formation mechanism of amphiphilic core-shell particles via graft polymerization of vinyl monomer from a water-soluble polymer containing amine group in aqueous media. ^[104]

1.6.2 Unique features of core-shell particles

The unique features of these core-shell particles come from its very nature of versatility through manipulating or engineering the shell and / or core components. The different hydrophilic shells (e.g. synthetic and natural) provide different surface functional groups. It allows further chemical modifications and bio-conjugation. It is capable of encapsulating and packing active molecules such as therapeutic and imaging

agents. It is the same component that provides colloidal stability. Lately, the synthetic shells have shown chemical activity to reduce metal salt. It can complex with metal nanoparticles, making them more stable and immobilized. The hydrophobic cores provide different structures and mechanical properties (e.g. hard, soft, temperature sensitive and hollow). It can also encapsulate metal or molecules, thus protecting their sensitivity.

1.6.3 Potential applications of core-shell particles

A diverse field of application is expected to spring from this type of polymeric core-shell particles due to the amphiphilic core-shell particle properties such as high surface area-to-volume ratio, well-defined nanostructure with tunable composition, surface functionality and good water dispersibility. Application in gene deliveries, enzyme immobilization, catalysis, chemical sensing, smart coating and imaging have been explored and some are on the process of investigation.

Dr. Li's group has used a well-defined core-shell particle, namely poly(methyl methacrylate)/polyethyleneimine (PMMA/PEI) synthesized through above mentioned graft polymerization technique, as nanocarriers for gene delivery. ^[105,106,107] The core-shell particles carry highly positive charges ($>+40\text{mV}$) which can attract plasmid DNA molecules (*pDNA*), which carry negatively charged functional group, into the PEI shells of the particles. The thickness and the molecular weight of the PEI shell influence the complexing ability of the nanoparticles. The condensed *pDNA* in the core-shell particle

can be protected from enzymatic degradation. Cytotoxicity studies showed that the PMMA/PEI core-shell particles are at least three times less toxic than the branched PEI polymer (25 kDA).

The group has also attempted to immobilize cellulose onto various types of core-shell particles such as PMMA/PEI, PMMA/chitosan, PMMA/casein particles. ^[108] A more recent study was demonstrated using the cationic polyelectrolyte shells showing a high loading capacity from 250 to 530 mg/g and highly retained activities from 70% to 90%. Another successful immobilization of cellulase was carried out into the PMMA nanoparticle using a one-pot direct synthetic method. ^[109] The nanoparticle produced a well-defined PMMA core and a thick and evenly distributed cellulase shell. Improved properties can be further achieved such as broader working pH and better thermal stability.

The group has also applied a core-shell particle that consisting of a poly(*n*-butyl acrylate) core and chitosan shell (PBA/Chitosan) as an antibacterial coating for cotton fabrics. ^[110] The core-shell particles have a highly positive surface charge that is able to coat on a cotton fabric through a conventional pad-cure-dry process. The cotton was successfully coated with this particle without the use of chemical binders. Antibacterial activity revealed a 99% bacterial reduction when the fabric was coated with the particle. After 50 laundering, bacterial reduction was maintained at 90%. The fabric treated with the core-shell particle had a better air permeability while surface morphology was not affected. It gave a better fabric hand feel than the chitosan coated only fabric (Figure 1.59).

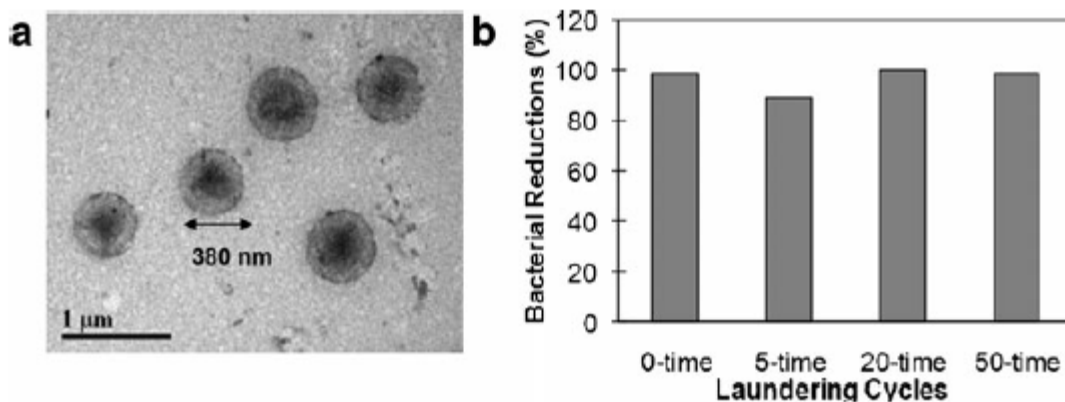


Figure 1.59 a) TEM image of poly(*n*-butyl acrylate) /chitosan core-shell particles, b) Antibacterial activity in different laundering cycles. ^[80]

Chemical Sensing is one of the potential applications of amphiphilic core-shell particles based on fluorescence technique. Recent studies by other group demonstrated that an amphiphilic core-shell particle is able to load dye on its hydrophobic core component at the same time can attach ligands for selective binding of an analyte such as Cupric ions (Cu(II)) ^[111] In this study, Nile red dyes were incorporated into the hydrophobic poly(methyl methacrylate) (PMMA) core using a soaking method while Cu(II) ions were complexed into the hydrophilic poly(ethyleneimine) shell. Thus the PEI/Cu(II) shell complex serves as an acceptor while the dye-loaded PMMA core acts as the donor. From this platform, quenching of fluorescence intensity via energy transfer process is possible (Figure 1.60). The advantage of using an amphiphilic core-shell particle is that they provide a large surface-area-to-volume ratio and functional groups for binding different types of fluorescent probes for multiple analyte detections.

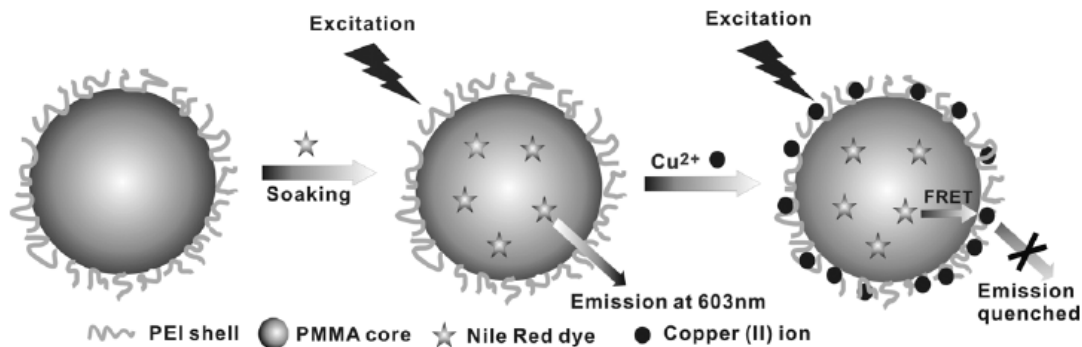


Figure 1.60 Schematic illustration for preparation of fluorescent polymeric core-shell particle for cupric ion detection. ^[110]

Immobilization of metal nanoparticles such as gold, silver, platinum and palladium have been explored in many studies in order to improve catalytic activities. However, one of the common problems in synthesizing metal nanoparticles is its aggregation due to strong Van der Waals attractive forces between nanoparticles. Thus, a suitable support is highly ideal. The criteria for creating a platform should have the following requirements: 1) an inert carrier system; 2) metal nanoparticles should not be blocked by any components of the support; 3) the carrier has the ability to recover the metal nanoparticle catalyst; 4) the carrier should allow the growth of the nanoparticles. ^[112] One of the most successful incorporation of metal nanoparticles in microgel systems which have been demonstrated by the group of Ballauff *et al.* Ag nanoparticles immobilized in poly(styrene)/poly(*N*-isopropylacrylamide) (PS/PNIPAm) core-shell system was possible by 1) immobilization of Ag ions onto the particle shell; 2) reduction of the immobilized Ag ions using sodium borohydride, generating Ag nanoparticles. ^[113] A similar approach was carried out in the same core-shell particle in

embedding metal nanoparticles and used as a smart nanoreactor for the catalytic oxidation of benzyl alcohol.^[114] Due to the temperature responsiveness of the PNIPAm microgel network located on the shell, metal nanoparticles embedded on them are fully accessible by reactants when below the volume phase transition temperature (VPTT) of the PNIPAm. The smart nanoreactor is demonstrated in Figure 1.55 wherein when it is above the VPTT, PNIPAm shell shrinks, exposing the metal nanoparticles and becomes more accessible to the reactant molecules. However, when it is below the VPTT of PNIPAm, the shell swells, covering the metal nanoparticles embedded within. Thus, diffusion of the reactant molecules to the surface of the metal nanoparticles is hindered and the catalytic reaction becomes slow.

1.6.4 Smart core-shell particles

Smart particles are nanoscale to few micrometers in size that possess stimuli responsive properties (e.g. changes in pH, temperature, ions, light or other external energies). These external stimuli can cause changes in the particles properties, dimension, structure and interactions within the particles. When a particle is exposed to these stimuli or any stimulus, conformational rearrangement or changes in their aggregation state occur. These types of materials can be used in both technical and biomedical applications.

Figure 1.61 illustrates a futuristic depiction of a smart particle which is described as an intelligent particle, resembling as an artificial cell.^[115] This complex image of a particle displays many compartments that interact, exchange chemicals, receive energy,

perform mechanical work, alter the chemical and physical properties. With its many jobs in one system, this image further depicts the multifunctionality of the particles. This image was created based on the analysis of the current state of research in the field of stimuli responsive particles. ^[115]

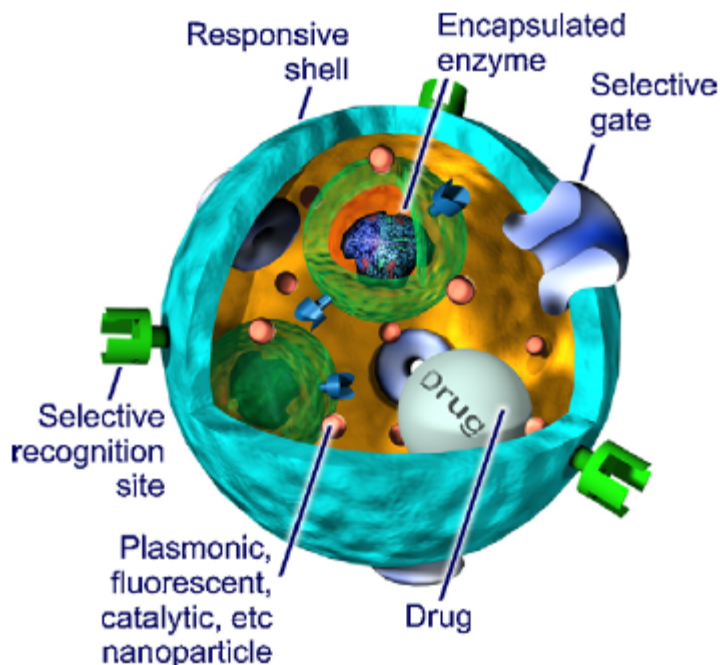


Figure 1.61 Futuristic image of an intelligent multifunctional particles. ^[115].

1.6.4.1 Temperature sensitivity

PNIPAm is a typically famous temperature-sensitive polymer and mostly studied in many systems because its solution behavior to water varies with temperature. At lower temperature (lower than its LCST of 32 °C), PNIPAm is highly solvated due to hydrogen bonding between the amide group of PNIPAm and the water molecules. At

this temperature, the polymer-solvent interaction is stronger than the intra polymer-polymer interaction. There is also a cage-like structure formation of water molecules around the isopropyl group of PNIPAm. ^[116] Thus, two sites are responsible for the hydrophilicity of PNIPAm molecules as illustrated in Figure 1.62. However, at elevated temperature, the hydrogen bonding between the water molecules and amide groups of NIPAm is weakened. This change in molecular interaction results in the increase of hydrophobic effect of the microgel. The breaking of the hydrogen bonds between the polymer and the solvent is entropically driven, creating a weaker polymer-solvent interaction compared to its polymer-polymer interaction. Consequently this results in a phase separation transforming from a coil to globular structure of PNIPAm at the phase transition temperature.

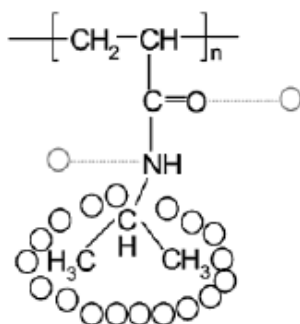


Figure 1.62 Chemical structure of PNIPAm and water molecules (O) below the LCST. ^[116]

- 2) It is also through the high local concentration of amino groups that gives PEI a high capacity for metal uptake.
- 3) It is of the same principle that PEI is able to complex with metal ions (chelating properties). Furthermore, it has the ability to reversibly complex labile metal ions.
- 4) With the highly branching of PEI comes its flexibility towards molecular conformation. This enables the PEI to achieve an optimum configuration for complex formation.
- 5) Due to its highly cationic branches, it can also complex and condense negatively charged DNA and RNA combined with its inherent proton sponge behavior that accounts for excellent efficiency in gene delivery. ^[121]

The unique properties of PEI has been used in many fields of applications such as in organic wastewater treatment, ^[122] heavy metal ion uptakes, ^[123] carbon dioxide removal in space shuttle applications, ^[124] and most recently it has been investigated as alternative carrier to viral vectors. ^[125]

Branched PEI is one of the earliest known cationic flocculants and often employed in treating industrial effluents. ^[126] Small flocs formed by coagulation are transformed into larger agglomerates through adsorption into the PEI. The process involves PEI bridging in which the cationic nature of PEI bound to a floc particle has looped and dangling chains which can attach to nearby particles.

Metal chelating properties of PEI was used in the heavy metal sorption (e.g. Pb(II), Zn(II), Ni(II)) in a modified PEI sorbents. ^[123] The modified PEI was found out

to be of higher recovery and needs only weak acid washing compared to other organic resins. It also gave high mechanical resistance.

The ability of amino functional groups of PEI to remove carbon dioxide was studied Satyapal *et al.* ^[124] to create an easily regenerated sorbent system in space. The invented sorbent was capable of removing low concentrations of carbon dioxide and was therefore less cost intensive than the usual membrane separation systems. This has led space crafts to reduce launch weight and storage volume.

PEI is considered as one of the most potent nonviral polymeric gene vectors. This is attributed to its pH buffering capacity. PEI's unique property helps the gene carriers to escape the endosomal barrier avoiding lysosomal degradation which is an essential step to achieve gene transfection. ^[127] However, it has a limitation on its degradability and toxicity for therapeutic applications. This has led many researchers to explore in designing degradable PEI's by cross-linking them with various degradable cross-linkers.

Chapter 2 Objectives

2.1 Rationale of using water-dispersible core-shell polymer particles as a template and a nanoreactor

The development of metal/polymeric composite particles in this study is based on the idea of embarking the potential applications of the core-shell particles developed by the group of Prof. Pei Li. In this particular study, we focused on the use of Poly(*N*-isopropylacrylamide)/polyethyleneimine (PNIPAm/PEI) core-shell microgel that is composed of a temperature-sensitive poly(*N*-isopropylacrylamide) core with a pH-sensitive polyethyleneimine shell as a polymeric template for reducing, immobilizing and stabilizing gold nanoparticles. These core-shell polymeric particles, specifically PEI based, can support and encapsulate metal nanoparticles and form stable composites in aqueous media. Here, the core and the shell components of the microgel template were carefully examined to understand its mechanisms that would further prove the advantages of using PEI-based core-shell particles to generate and encapsulate metal nanoparticles. Some other types of amphiphilic templates were also tested, but only for comparison purposes and no comprehensive studies were conducted.

2.1.1 The core component

The core component of microgel template used in this study comprises the temperature-sensitive region of the whole structure. This polymer is the poly(*N*-isopropylacrylamide) (PNIPAm) which has been previously described in section 1.6.4.1.

Chemical structure of this polymer is shown in Figure 2.1. This section discusses the roles of this component in relation to the generation of the gold nanoparticles using the copolymer template. Three points are discussed here. First is the contribution in the copolymer template, and second is the role of the core during the generation of the gold nanoparticles, and lastly its effect to its subsequent application.

First, as part of the copolymer template, the PNIPAm forms the core of the template and conserves its form as a core. The core is formed based on the mechanism as described in section 1.6.1. During synthesis, PNIPAm undergoes phase transition from a swollen hydrated state to a shrunken dehydrated state because the reaction temperature of 80 °C, is above its reversible lower critical solution temperature (LCST) of 32 °C. Thus the polymer behaves like hydrophobic molecule, resembling the core component of the template. The PNIPAm was also crosslinked by the use of *N,N'*-methylene-bis-acrylamide (MBA) (Figure 2.1) . The crosslinking of the PNIPAm helps the structure of the core to be intact and in a well-defined morphology.

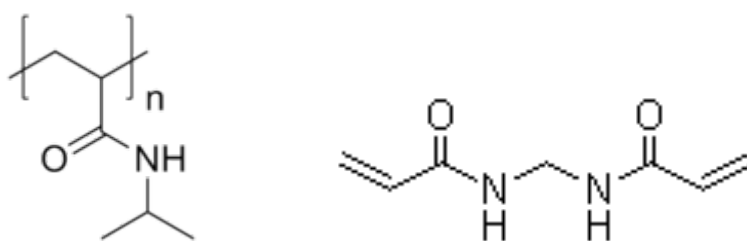


Figure 2.1 Chemical structure of poly(*N*-isopropylacrylamide) and *N,N'*-methylene-bis-acrylamide

Second, due to the temperature sensitivity of the PNIPAm, the generation of gold nanoparticles is affected by its coil or globule structure below or above its LCST. [128] The conformational changes of the PNIPAm through shrinking and swelling influence the whole structure of the microgel template in general. The shrinking and swelling phenomena of the microgel template will then affect the availability of the amino groups which are responsible for the attraction and reduction of gold ions to nanoparticles.

Moreover, gold nanoparticles' accessibility can also be manipulated through the template's conformational changes in response to temperature. In the same platform, the optical property of the gold nanoparticles embedded within the microgel template can also be controlled following the swelling and shrinking of the polymer template. When temperature goes below its LCST, the PNIPAm core becomes more hydrophilic that it is swollen into a hydrated state. Thus, gold nanoparticles are pushed further from each other. This results to the increase of interparticle distance between gold nanoparticles. However, when the solution temperature goes beyond the LCST, the PNIPAm core becomes hydrophobic and tends to considerably shrink its full volume. This drags in the whole composite particles as well as the gold nanoparticles embedded within. The interparticle distance between gold nanoparticles become less and less as it is dragged by the PNIPAm core.

The recovery of the gold nanoparticles together with its template can be carried out mostly by centrifugation or ultrafiltration. Thus, the composite particles can be easily recovered and subsequently reused. When the composite particles are exposed to

a temperature higher than its volume phase transition temperature (VPTT), it becomes turbid after a short time. When prolonged, the composite particles float and precipitate. Thus it can be separated by simple decantation or filtration.

2.1.2 The shell component

The main component of the shell is polyethyleneimine. The property of which has been discussed in Section 1.6.4.2. The PEI contains amino groups that are capable of reducing metal salts ions to form metal nanoparticles in the absence of reducing agents. This provides a greener synthetic system towards the development of a cleaner and safer synthetic strategy to produce gold nanoparticles and its composite materials.

The gold nanoparticles generated are anchored on the hydrophilic PEI shell which gives easy access to the nanoparticle's surfaces, thus leading to a better interaction with the reactants in the solution during a catalytic reaction. Thus, encapsulation of gold nanoparticles on the outer shell of the particle will allow targeted molecules to easily interact with the gold nanoparticles.

Aside from its self-reducing ability to reduce metal ions to nanoparticles, polyethyleneimine is also pH-sensitive. When exposed to a low pH, the shell component is protonated, resulting in swelling the whole structure of the template. However, at a high pH, the shell is deprotonated, making the shell and the template to shrink. Just like the core component, the shell also affects the whole structure of the microgel template,

and thus the generation of the gold nanoparticles and its application as a composite particle.

The swelling and the shrinking phenomenon can also affect the inter-particle distance between the gold nanoparticles anchored on the PEI shell. As the particles swells, the gold nanoparticles are separated from each other, while it comes closer when it shrinks. The effect of the gold nanoparticles' inter-particle distance to catalysis is critical in this sense. The closer are the gold nanoparticles from each other, the more hindrance there will be during catalytic reactions. However, when the gold nanoparticles are away from each other, its particle surface is maximized for catalytic reactions. The subsequent effects on the its particle size upon changes in the inter-particle distance between nanoparticles is also evident on the optical properties. Different sizes of gold nanoparticles emit different visible color upon absorption of UV-vis light.

2.2 Challenges

The synthetic route for this study offers the advantage of ambient conditions, faster kinetics, minimal reactants used, and economical and producing ready-to-use nanocomposite particles. However, there are questions that remain to be challenging.

Few studies on water-soluble PEI macromolecule on reducing metal ions to nanoparticles with low efficiency have been reported. ^[129] To the best of our knowledge, there is no comprehensive study on how a nanostructured PEI such as in a core-shell template reduces metal ions to nanoparticles. Thus this study will attempt to elucidate

the mechanism of the amino reducing ability of the nanostructured PEI in forming gold nanoparticles and its reduction capability with respect to the branched PEI structures and nanostructured PEI.

The second challenge in this study is how to efficiently encapsulate the gold nanoparticles generated in the PEI shell of the template. Since the gold nanoparticles are generated within the PEI shell through its amino groups, it is not yet known how to make them stick on its shell without leaking from the template. This will give an impact on how it can be an effective nanoparticle container aside from being a nanoreactor.

Lastly, the stability of resulting composite particles is of high interest here. Stability here means how the template can prevent the gold nanoparticles to aggregate from each other and how can it also prevent the composite particles from attracting each other, thus preventing them from precipitation. This actually means both the stability of the gold nanoparticles within the template and the stability of the composite particles in aqueous system.

2.3 Specific objectives

The long term objective of this study is to develop an easy and green synthetic method to prepare metal/polymeric composite particles in water. Specifically, a smart microgel, (PNIPAm/PEI) is used as a template for the reduction, immobilization and stabilization of gold metal nanoparticles. The PNIPAm/PEI also functions as a smart core-shell template which has the ability to react to certain stimulus such as pH and

temperature. In this way, manipulation of these two parameters will be demonstrated in the synthesis of the composite particles and its applications. At this stage of the study, a basic understanding of the physical and chemical phenomenon is important to build a strong foundation on the knowledge, structure and interaction of these composite particles. This study aims to give a basic knowledge on the morphological phenomenon involved in the synthesis and its smart responsiveness to its environmental stimulus. Specific objectives include:

1. Selection of the most appropriate PEI-based core-shell particle as a multi-functional template (nanoreactor, stabilizer and immobilizer) for the formation of gold/polymer composite particles.
2. Formation of gold nanoparticle using a PNIPAm/PEI core-shell microgel as a multi-functional template to generate smart metal/polymer composite particle. The following effect studies were carried out to investigate its relation to the synthesis of gold nanoparticles: 1) Effect of solution pH; 2) Effect of reaction temperature; 3) Effect of molar ratio of amine to gold salt; 4) Effect of heating of the gold/polymer composite particles.
- 3) Formation of bimetallic nanoparticles (i.e. Au@Ag) using a successive reduction method through utilizing the pre-synthesized gold nanoparticles in the microgel template as seeds for the silver nanoparticles to grow and develop.
- 4) Study of catalytic activities of both the gold (Au) and gold with silver (Au@Ag) in microgel templates through the reduction of *p*-nitrophenol to *p*-aminophenol as a catalytic model.

Chapter 3 Experimental Section

This chapter focuses on the detailed synthesis and characterization of the microgel template, the gold/polymeric composite particles and the bimetallic (Au@Ag) composite particles. The microgel template was obtained in a single step reaction with TBHP-induced graft copolymerization of NIPAm from polyethyleneimine. The gold/microgel composite particles were synthesized using the pre-synthesized microgel template by in-situ reduction of gold salt solution into the colloidal microgel system. Bimetallic nanoparticles were synthesized using Au/PNIPAm/PEI composites as seed particles. Molecular and morphological characterization techniques are also discussed in this chapter.

3.1 Materials

Spindle-crystals of *N*-isopropylacrylamide (NIPAm, Aldrich) were obtained by a repeated recrystallization of NIPAm. Recrystallization was carried out in a toluene and *n*-hexane (1:5 v/v) mixture enriched poly(ethyleneimine) (PEI, 750K) in a 50% wt solution in water, *N,N'*-methylenebisacrylamide (MBA), *tert*-butyl hydroperoxide (*t*-BuOOH or TBHP, 70% solution in water), deuterium oxide (99.9 atom % D), hydrochloric acid (HCl, 2M) were all used without further purification sourced from Aldrich Chemical Co.. Hydrogen tetrachloroaurate (III) trihydrate (HAuCl₄·3H₂O) and silver nitrate solution (AgNO₃) were obtained from Sigma Aldrich. Deionized water or Milli-Q water was used for dilution purposes and dispersion medium.

3.2 Synthetic Methods

3.2.1 Synthesis of core-shell particles

Figure 3.1 exhibits the formation of core-shell microgel template via the graft copolymerization of NIPAm from b-PEI using t-butyl hydroperoxide (TBHP) as an initiator. The polymerization mechanism has been previously discussed in Chapter 1. In a typical batch weight of 107 g, the PEI (1.27 g) was first mixed in 50 mL water, followed by adjusting its pH to 7 with 2 M HCl solution (3.0 mL). Purified NIPAm monomer (2.31 g) and MBA (0.23 g) were mixed in 50 mL water and charged to the prepared PEI solution in a three-necked water-jacketed flask equipped with a condenser, a magnetic stirrer, and inlet pipes, followed by purging nitrogen for 30 minutes. Dilute TBHP solution (2.14 mL, 100 mM) was added to the mixture, and stirred (800 – 900 rpm) at 80°C for 2 hours. An opalescent mixture appeared after a few minutes of the reaction and a white latex dispersion was obtained. The particles were purified by repeated centrifugation at 18000 rpm at 10 °C for 2 hours in each cycle until conductivity was close to that of water used.

In this recipe, PEI to (NIPAm+MBA) was 1:4 weight ratio. The crosslinking degree was set at 10% (MBA : NIPAm = 1 :9 w/w). The total solids content (PEI + NIPAM + MBA) was 3 w%. . The concentration of TBHP in the reaction mixture was 2 mM.

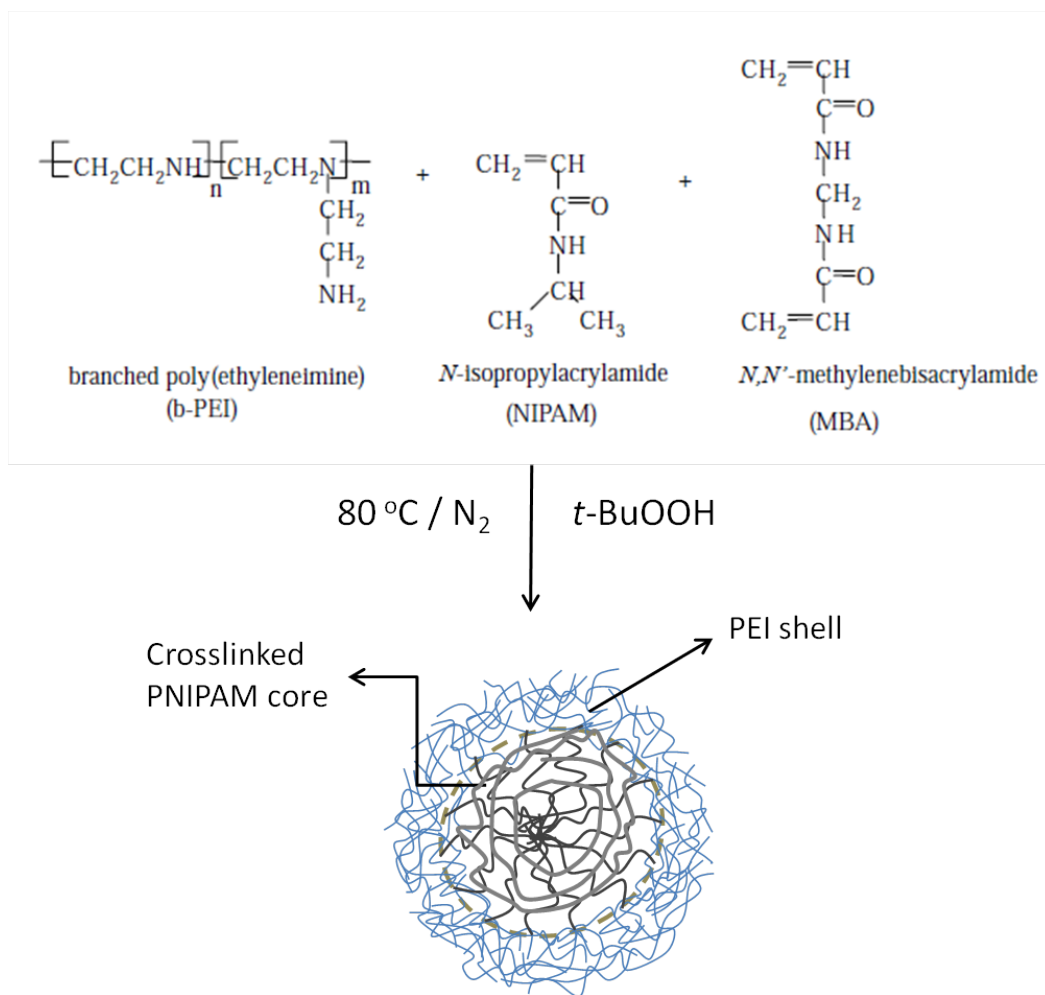


Figure 3.1 Formation of core-shell microgel (PNIPAm/PEI) via a graft copolymerization of NIPAm from b-PEI using TBHP as initiator.

Purification of PNIPAm/PEI microgel particles

It is very important that the microgel dispersion is pure and with a minimum amount of free PEI as possible. The presence of the free PEI in the colloidal template will affect the reduction of metal ions to nanoparticles and the location of the metal nanoparticles as well. The PNIPAm/PEI microgel particles were purified through

a repeated centrifugation and redispersion cycle with deionized water. Results in Table 3.1 shows that after 9 cycles, solution conductivities of two samples were similar to conductivity value of the deionized water of less than 10 $\mu\text{S}/\text{cm}$. Results also indicated that solution conductivities of the first four cycles decreased considerably from 333 and 315 to 18 and 17.3 ($\mu\text{S}/\text{cm}$) of the two samples, respectively. But there was only a small reduction in their 4th to 9th cycles.

Table 3.1 Conductivity of particle dispersion in each repeated centrifugation/redispersion cycle of the PNIPAm/PEI microgels

Cycles	Sample's Conductivity ($\mu\text{S}/\text{cm}$)	
	Sample 1	Sample 2
1	333.0	315.0
2	65.5	25.5
3	23.2	19.5
4	18.0	17.3
5	15.4	14.8
6	12.7	13.0
7	9.9	11.5
8	8.4	10.8
9	7.9	10.4

3.2.2 Synthesis of Au/core-shell composite particles

The preparation of the Au nanocomposite (Au/(PNIPAm/PEI)) particles was carried out via the addition of hydrogen tetrachloroaurate(III) trihydrate ($\text{HAuCl}_4 \cdot 3\text{H}_2\text{O}$) solution into the as-prepared PNIPAm/PEI: A Au salt stock solution ($\text{HAuCl}_4 \cdot 3\text{H}_2\text{O}$, $1.317 \times 10^{-3} \text{ M}$) was purged under N_2 for 30 minutes and stored in a refrigerator for subsequent usage. A volume ratio of 20:1 of the PNIPAm/PEI microgel dispersion (400 ppm) and hydrogen tetrachloroaurate(III) trihydrate ($\text{HAuCl}_4 \cdot 3\text{H}_2\text{O}$, $1.317 \times 10^{-3} \text{ M}$) solution was mixed with continuous stirring at 250 rpm. The reaction was carried out at various temperatures and pHs for 2 hours. Further heating of the composite particles was carried out at 60°C and 92°C for an hour. The resulting gold loaded microgels were purified by centrifugation at 12000 rpm for 1 hour at 10°C . Figure 3.2 illustrates the schematic diagram of this synthesis.

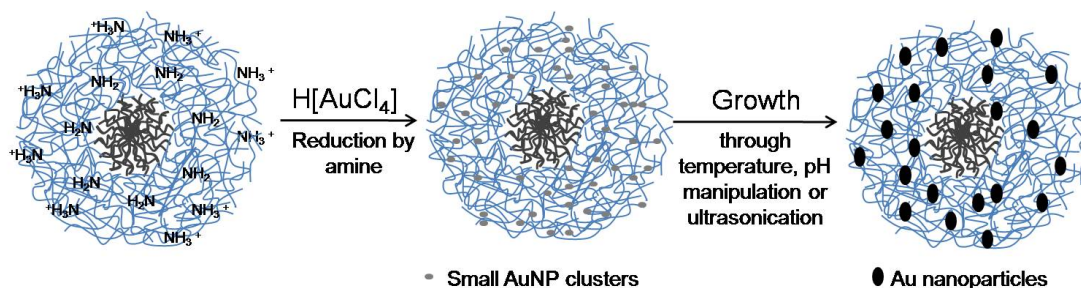


Figure 3.2 Schematic diagram on the synthesis of gold nanoparticles (AuNPs) using PNIPAm/PEI as template.

3.2.3 Synthesis of Au@Ag/core-shell microgel composite particles

Au@Ag bimetallic nanoparticle synthesis was carried out through a successive reduction of Au and Ag metal ions. Gold metal ions were first reduced into the shell compartment of the microgel as described in 3.2.2. These gold metal nanoparticles were then used as a seed for the successive reduction of the silver ions to silver nanoparticles. Figure 3.3 illustrates the synthesis of these bimetallic nanoparticles using the gold composite as seed particles. A 1:1 and 1:9 molar ratios of Au:Ag were used in this study. For example, in 1:1 ratio, Au salt stock solution ($\text{HAuCl}_4 \cdot 3\text{H}_2\text{O}$, 1 mL, $1.317 \times 10^{-3} \text{ M}$) and the Ag salt solution (AgNO_3 , 1 mL, $1.317 \times 10^{-3} \text{ M}$) combination was used. While for 1:9 ratio, Au salt stock solution ($\text{HAuCl}_4 \cdot 3\text{H}_2\text{O}$, 1 mL, $1.317 \times 10^{-3} \text{ M}$) and the Ag salt solution (AgNO_3 , 9 mL, $1.317 \times 10^{-3} \text{ M}$) combination was used. A 30-minute mixing of the composite particles was carried out to further reduce the silver ions to metal nanoparticles. This was followed by heating at 60°C for 30 minutes.

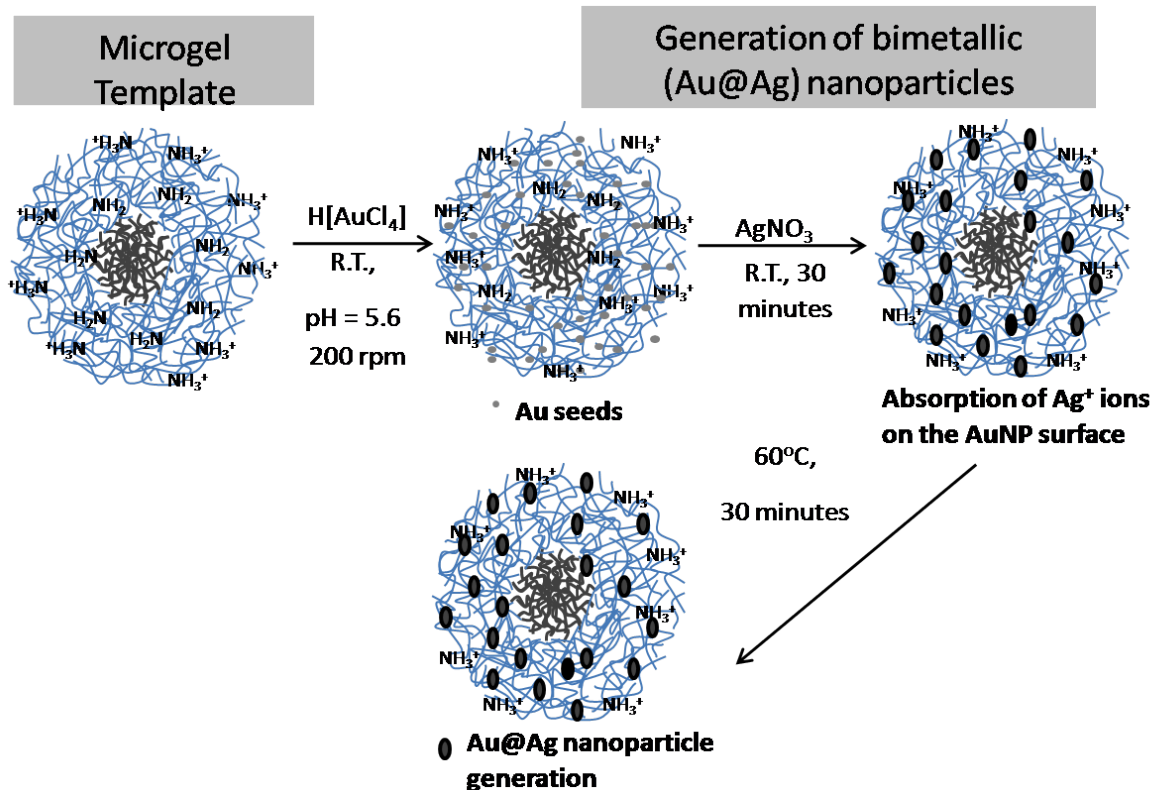


Figure 3.3 Illustration of Au@Ag synthesis using the microgel template.

3.3 Measurements and Characterization

3.3.1 Particle size and *zeta*-potential measurements

Particle size measurement gives the hydrodynamic diameter of the particles in a colloidal system, while the *zeta*-potential gives the electrical potential of the particles. The particle size is measured through a dynamic light scattering technique. When light hits a small particle, the light scatters in all direction (Rayleigh scattering). This only happens when the particle is smaller compared to the wavelength of the light source. In a monochromatic and coherent light source, dynamic light scattering measures a time-dependent fluctuation in the scattering intensity. Fluctuation was caused by

Brownian motion of small molecules, causing the change of distance between scatter points with time. The scattered light then undergoes a constructive or destructive interference by the surrounding particles and fluctuation of scattered light. The time-dependent fluctuation is transformed into an autocorrelation function [i.e. $G(\tau) = \int I(t)I(t+\tau) dt$]. Smaller particles give faster decay rate while large particles give lower rate. From the autocorrelation function, the exponential decay gives a diffusion coefficient, D . Hydrodynamic size, D_h is calculated from the Einstein-Stokes equation [130] using the diffusion coefficient (Eq 3.1):

$$\langle D_h \rangle = \frac{kT}{3\pi\eta D} \dots\dots\dots 3.1$$

where k is the Boltzman constant, η is the dispersant viscosity, T is the temperature (K), and D is the diffusion coefficient.

In this study, samples were performed in a Beckman Coulter Delsa Nano particle analyzer using He-Ne laser irradiation as a light source with wavelength of 632.8 nm and 30 mW. The measurements were carried out at 25 °C with sample concentration ranging from 200 to 400 ppm.

Zeta-potential measures the charge that exists around a particle measured in milliVolts (mV). This also dictates its stability in a colloidal system. This potential of a particle can be based on an electrical double layer model (Figure 3.4). The colloidal particle is surrounded by two layers; stern and diffuse layers. The inner layer is called the stern layer wherein oppositely charged ions strongly attract to the particle, while the outer layer is composed of different ionic charges that are less firmly associated. Within

the diffuse layer, there is an imaginary boundary in which the ions and particles form a stable entity. This means that ions within this boundary are carried out during the movement of the particle. However, ions outside this boundary do not travel with the particle. This imaginary boundary is called the slipping plane or the shear plane, where potential exist and known as *zeta*-potential. The magnitude of the *zeta*-potential indicates the stability of the colloidal system. For solid particles dispersed in a liquid, if all the particles in suspension have a large negative or positive (± 30 mV) *zeta*-potential, they will repel each other and prevents flocculation of the particles. It should be noted that pH affects the *zeta*-potential. Small changes in the pH or ionic strength of the medium affect its *zeta*-potential. Thus, a *zeta*-potential quoted without pH is a meaningless number.

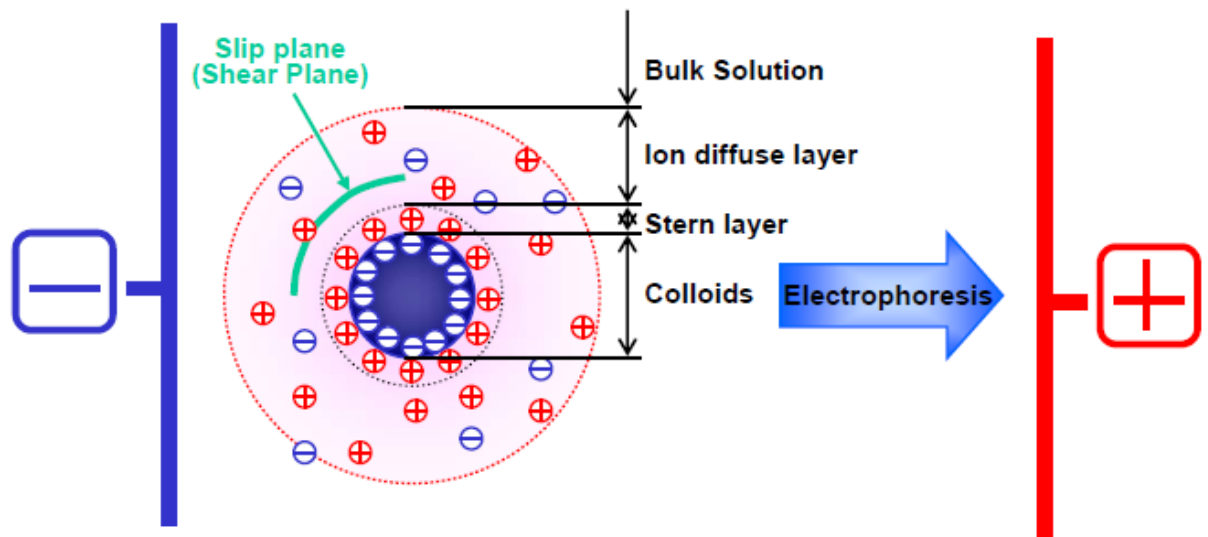


Figure 3.4 Schematic diagram of a particle with double layer.

In this study, electrophoretic light scattering measurements for *zeta*-potential was performed in the same machine for particle size determination (Beckman Coulter Delsa Nano). When a voltage is applied to the system of interest, particles are attracted to the electrode of the opposite polarity. This process is called electrophoresis. This is a non-invasive and quick mean to measure the particle Doppler shift from scattered light. This also gives an unequivocal measure of the sign of the *zeta*-potential. The velocity of the particles measured under unit electric field is referred to as electrophoretic mobility. From this mobility, *zeta* -potential, ζ can be measured using the Henry equation (Eq 3.2):

$$\zeta (mV) = \frac{U\eta_0}{\epsilon_0 D} f \quad \dots\dots\dots 3.2$$

where U is the electrophoretic mobility, ζ is the *zeta*-potential, ϵ_0 is the permittivity of vacuum, f is the Henry's function and η_0 is the viscosity and D is the dielectric constant. Value of the Henry's constant, f in this case, is 1.5 when using the Smoluchowski equation. Samples for *zeta*-potential measurements were diluted to 100 – 200 ppm with 1mM NaCl and performed at 25 °C with pH ranging from 5.5 – 6.0.

3.3.2 Fourier Transform Infrared (FT-IR) Spectroscopy

Fourier Transform Infrared spectroscopy identifies organic and inorganic species based on its absorbance of infrared light wavelength intensity and characteristics.

Specific band wavenumber position and its characteristics identify a specific chemical structure and functional groups present in the sample. Upon infrared irradiation on the sample, chemical bonds interact with light by stretching, contracting and bending. Specific chemical bonds absorb infrared radiations in a range of wavenumber that identifies its functional groups. Example of this is the C=O (carbonyl group) that appears to have a stretched infrared absorbance around 1700 cm^{-1} . In this study, FTIR measurements were performed in a Fourier Infrared Spectroscopy (FTIR) spectrophotometer (Thermo Scientific Nicolet 380). Sample was prepared by freeze drying a 1 mL of the sample solution. The dried sample was mixed with KBr salt (1:3 sample :KBr salt) and pressed into disk. It was then measured with a spectral range of $400 - 4000\text{ cm}^{-1}$.

3.3.3 Nuclear Magnetic Resonance (NMR) Spectroscopy

Nuclear magnetic resonance spectroscopy (NMR) detects quantum-mechanical transitions induced by electromagnetic radiation in a system of discrete levels of electron or nuclei placed in a static magnetic field.^[131] As a result, it gives the chemical environment of the sample through its atomic nuclei response to magnetic field. Subatomic particles such as electrons, protons and neutrons spin on their axes. In many atoms, these spins are paired against each other such that the nuclei of the atoms have no overall spin. However, in some atoms such as ^1H and ^{13}C , their nuclei possess an overall spin. A nucleus in a magnetic field gets excited by rotating on its axis. Application of

electromagnetic field excites transitions between energy levels. Resonance conditions occur when the frequency of the magnetic field is equal to the Larmor frequency of the observed nucleus. Nuclei with multiple Larmor frequencies are inherent in most samples. This is due to more than single magnetically equivalent functional groups such as CH, CH₂, and CH₃. This leads to frequencies or chemical shifts of several resonance.

All ¹H-NMR measurements were performed and recorded on a Bruker Avances DPX-400 FTR spectrometer. The apparatus operates in Larmor frequency of 400.13 MHz per proton. A 30° pulse of 9.5 μs and acquisition delay of 2s were used for ¹H spectral accumulation. A “π-τ-π/2 acquisition” inversion recovery sequence was used for T1 measurements and the FT data were fitted using the online Bruker Software SIMFIT. Purified and freeze dried sample was dissolved into Deuterium Oxide (D₂O) (5mg/mL) and introduced into a 5 mm diameter NMR tube.

3.3.4 Ultraviolet Visible (UV-vis) Spectroscopy

UV-Vis spectrometer obtains light absorption readings in the near UV and visible regions of the electromagnetic spectrum. A light source in the instrument is separated into its component wavelength using a prism or diffraction grating. The spectrometer scans across the UV/Vis region and plots the differences in absorption versus wavelength. Arbitrary unit of absorbance from 0-3% (y-axis) is plotted against the wavelength absorbance (x-axis). UV-Vis spectrometer is used in sample that transmits, usually liquids. Gases and solids samples are treated with monochromatic

beam that is directed through the sample. For opaque samples, reflectance mode is used instead. Metal/polymeric composite particles such as Au/polyaniline have been analyzed using the this technique to monitor the presence of gold nanoparticles and its growth within the polymeric template ^[132].

In this study, UV-Vis measurements were performed through a Varian Cary 4000 Spectrophotometer using a wavelength from 300 to 900 nm. Absorbance was set from 0 – 2.5 a.u.. Diluted sample was placed in a 5 mL cuvette for its measurement.

3.3.5 Field Emission Scanning Electron Microscopy (FESEM)

Scanning electron microscopy (SEM) is a surface imaging technique for materials at nanoscopic scale wherein a focused beam with high-energy electrons is used to generate a variety of signals at the surface of a sample. As a result of the electron-sample interaction through signals, send out information (i.e, morphology, chemical composition, orientation of material make-up and crystalline structure) of the sample. Selected area of the surface sample and a 2-dimensional image generated display spatial variations in these properties. Resolution is based on the wavelength of the electron (λ), as expressed in the Broglie equation (Eq. 3.3):

$$\lambda = \frac{h}{mv} \quad \dots\dots\dots 3.3$$

where λ is the wavelength of the electron, h is the Planck's constant, m is the electron mass, and v is the electron velocity. SEM works by imaging the emitted electron

which created from a field emission gun source. A high vacuum condition is required for the field emission gun to generate high electron density beam at a narrowest probe size. A high resolution images at low accelerating voltage (below 5 keV) is produced, resulting in no damage on the instrument and on the sample as well (e.g. polymers). The emitted electrons from the source beam are focused by condenser lenses to a very focal spot. These are then scanned across the sample surface with scanning coils (Figure 3.5). A tear shaped volume with nanometer to micron depth from the surface sample is required for a successful interaction of the electron beam source and the sample. Secondary electrons from the sample are emitted from its surface with the use of a photomultiplier device.

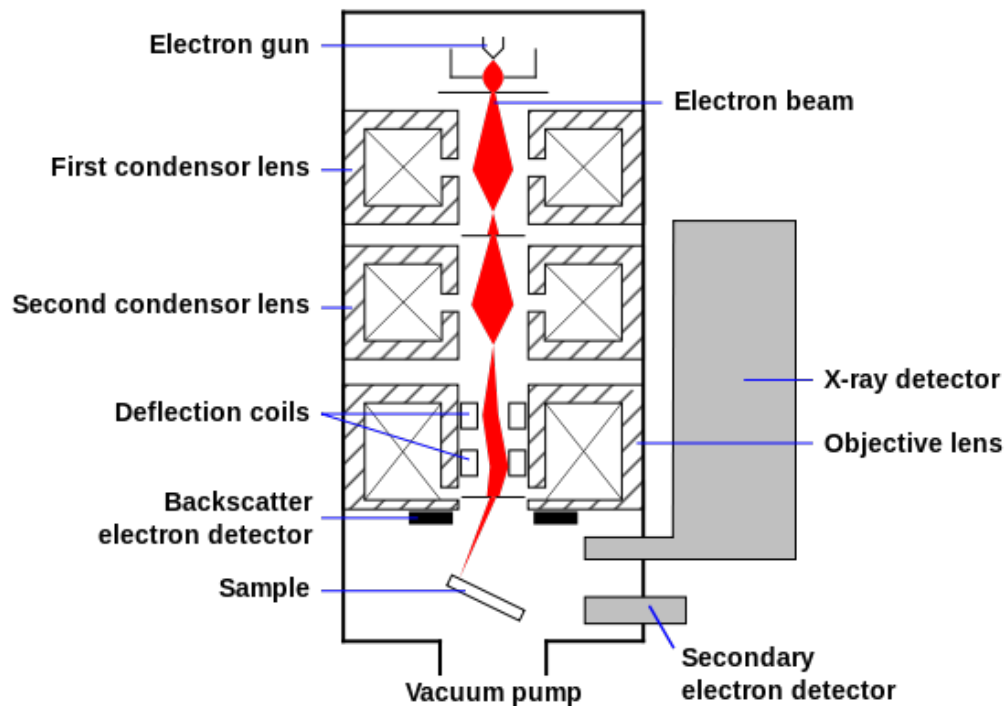


Figure 3.5 Schematic diagram of a SEM set-up^[133].

In this study, FESEM samples were examined in a JEOL-JSM 6335 Field Emission Scanning Electron microscope at an accelerating voltage of 5 kV. A few drops of diluted sample (200 ppm) solution was spread onto a glass substrate, air dried in a covered free dust environment. A thin layer of gold film was sputtered on a dried sample reaching 2-5 nm in depth in a vacuum.

3.3.6 Transmission Electron Microscopy (TEM)

Transmission electron microscopy is one of the most used instruments for surface imaging, especially for nano-scale particles (i.e. metal nanoparticles). These images were formed using transmitted electrons from the sample. It can produce magnification details up to 1,000,000 x with resolution better than 10 nm. TEM works by using a high energy electrons (up to 300 kV accelerating voltage) into a specimen. When an electron beam passes through the specimen, electrons are scattered and some are transmitted. The transmitted electron replicates the pattern of the specimen forming an enlarge image. The transmitted electron beam is highly dependent on the specimen's property (e.g. density and composition). Light and porous material will allow more electrons to pass through than in a dense material. Transmitted light is then projected into a screen for the user to see. Figure 3.6 gives a schematic diagram of the TEM set-up.

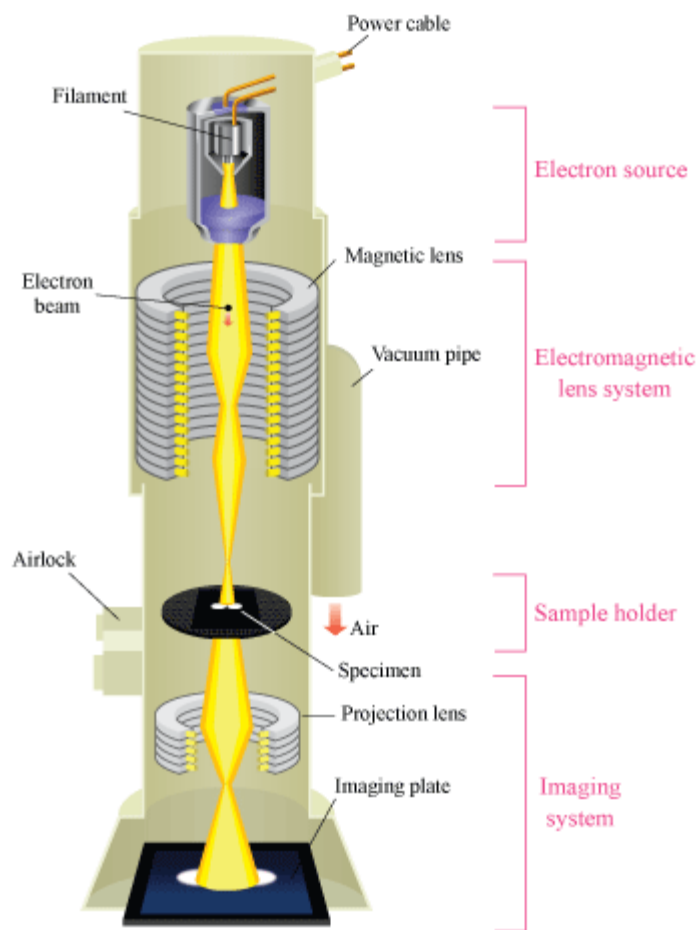


Figure 3.6 Schematic diagram of a TEM set-up^[134].

Samples were examined through the transmission electron microscope (JEOL 100CX II TEM) at an accelerating voltage of 100 kV and emission current of 50 μA equipped with a multi-scan CCD camera (1024 x 1024 pixels). Image J software was used to further extract information such as particle size, internal structure and size distributions. A high resolution TEM (JEOL, JEM-2010) was also used to observe the

metal nanoparticles formed in the microgel template using an accelerating voltage of 200 kV.

Diluted sample solution (200 ppm, 5 μ L) were dropped onto a graphite-coated copper grid (400 mesh, Electron Microscopy Science) and air-dried. No staining was employed for gold loaded microgel samples. However, for pure microgel samples, staining was carried out by dropping 2 μ L of phosphotungstic acid (PTA) (2% w/w) in deionized water for one minute. It was then air-dried at room temperature before analysis. Phosphotungstic acid ($H_3PW_{12}O_{40}$) is a heteropoly acid commonly used for imaging viruses, nerves, polysaccharides, and other biological materials using a transmission electron microscope.

3.3.7 Atomic Force Microscopy (AFM)

Atomic force microscopy (AFM) is a scanning probe microscopy (SPM) technique wherein it investigates nonconductive materials such as polymers and biological samples. This technique uses a probe apex that scans the sample surface that is most commonly used to investigate copolymer nanostructures. The resolution of the SPM is determined by the geometrical shape of the probe apex at the atomic scale achieving atomic resolution. SPM analyzes the surface structure, electronic/magnetic properties of the surface and the absorption of molecules. Aside from achieving topography of the sample, it can also manipulate single atoms and molecules on the sample surface.

In this technique, Van der Waals force between the sample and the probing tip is determined over the sample surface. The potential between two hard spheres is given by the Lennard-Jones potential equation (Eq 3.3):

$$V(r) = 4\xi \left[\left(\frac{\sigma}{r} \right)^{12} - \left(\frac{\sigma}{r} \right)^6 \right] \dots\dots\dots 3.3$$

Here, the first term of the equation 3.6, $\left(\frac{\sigma}{r} \right)^{12}$ describes repulsive force while the second term, $\left(\frac{\sigma}{r} \right)^6$ describes the attractive force. When the probing tip approaches the sample surface, it experiences attractive force, which bends the tip downward. In this specific technique, the probing technique does not touch the surface and so imaging is called non-contact or tapping mode AFM. When probing tip is bent up, repulsive force is experienced. AFM carried out in this mode is called contact mode. However, tapping mode or non-contact is mainly used in many characterizations since it allows imaging soft materials such as biomolecules and polymers.

The AFM set-up is shown in Figure 3.7. This diagram shows that the movement of the imaging tip is monitored by laser-photodiode detector. The topological profile of the sample is obtained by a computer-assisted feedback and piezo-scanner system. This allows the probing tip to move over the sample surface within a certain range of distance. In a non-contact mode, the cantilever tip is oscillated close to its resonance frequency and positioned above the surface and taps the surface for a very minute fraction of its

oscillation cycle. When the cantilever tip scans across the surface and the amplitude is kept constant, the feedback signals collected by the photodetector provides image of surface topography. ^[135] The tip-surface interaction of the oscillating cantilever gives a phase image. This phase image gives the sample properties such as softness and viscoelasticity.

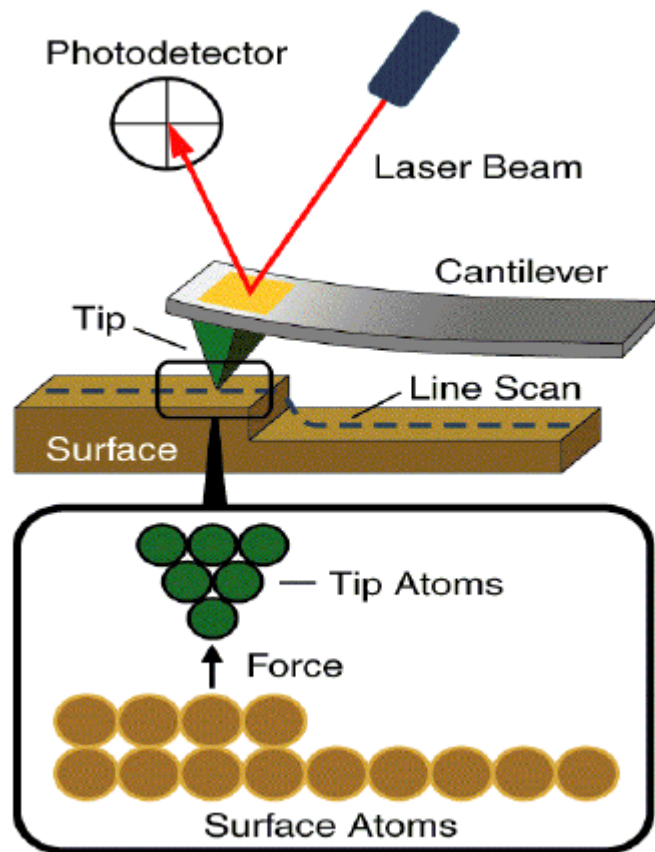


Figure 3.7 Schematic diagram of AFM set-up.

In this study, a non-contact high resonance reflex coating mode cantilever (NSC36C) was used for non-contact imaging in air. Data pixel was 512 x 512 for air

image and 256 x 256 for liquid samples. Scan rate used was 0.5Hz to 0.8Hz. Scan parameter depends on the sample conditions. For liquid sample, sample was dropped on mica substrate and dried for a day. No pretreatment was necessary. Humidity was adjusted from 40-80% by using hot water.

3.3.8 X-ray Diffraction Spectroscopy (XRD)

X-ray diffraction identifies phases of a crystalline material providing information on unit cell dimensions (crystal structures and atomic spacing) based on constructive interference of monochromatic X-rays and a crystalline sample. Constructive interference results from the interaction of the incident rays with the specimen when conditions satisfy the Bragg's Law (Eq 3.4):

$$n\lambda = 2d \sin \theta \quad \dots\dots\dots 3.4$$

where n represents the order of reflection (an integer), λ is the wavelength of the incident X-rays, d is the inter-planar spacing of the crystal and θ is the angle of incidence. Figure 3.8 illustrates the Bragg's Law principle. When X-rays of a fixed wavelength interacts with a crystal and at certain incident angles, intense reflected X-rays are produced. As a result, wavelengths of the scattered X-rays interfere constructively. Constructive interferences results in the equivalent value of the travel path and the integer multiples of the wavelength. At such phenomenon, diffracted beam of X-rays leaves the crystal at an angle equal to that of the incident beam.

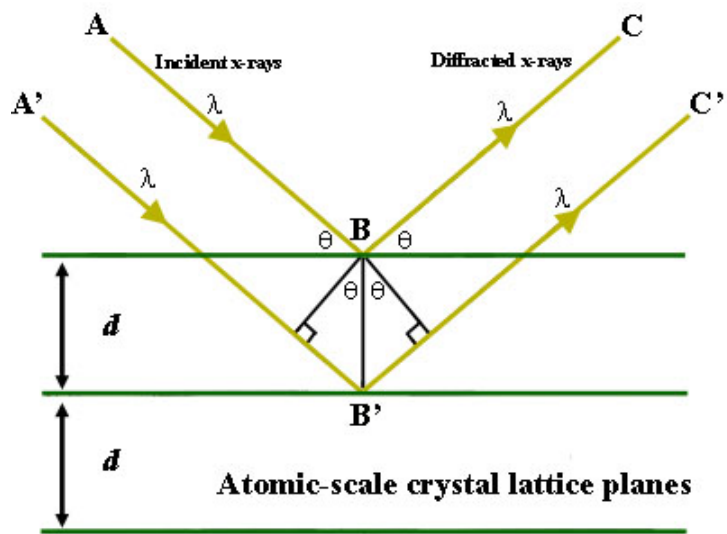


Figure 3.8 Bragg's Law reflection representation^[136].

X-ray diffraction patterns resulting from the metal nanoparticles were obtained from a high resolution RigakuSmartLab high resolution X-ray diffractometer (HRXRD). Scanning rate was 2°/min. in 2theta ranging from 10 to 80° at a high-intensity Cu K α radiation ($\lambda=1.541 \text{ \AA}$). X-ray tube generator was operated at 45 kV and 200 mA with a graphite monochromator. Sample was prepared by a repeated sputtering into a glass substrate and air dried for at least 24 hours. Thin film produced was less than 0.5 mm.

3.3.9 X-ray photoelectron Spectroscopy (XPS)

XPS is a technique based on the photoemission of electrons induced by soft X-rays. This allows the identification of multiple elements except H and He. It also provides chemical bonding and state information simultaneously with quantitative information for gold/polymer composites [137-139]. It analyzes the sample's surface from 2-10 nm depth. The working principle is presented in Figure 3.9. Soft X-rays such as Mg K α and Al K α are normally used for measurements. When soft X-ray photon of energy, $h\nu$ hits an atomic orbital electron, total energy is transferred to the electron. Since incoming photon energy is greater than the binding energy E_b of the orbital electron of the atom, electron is ejected with a kinetic energy, E_k . The kinetic energy is equal to the difference between the photon energy $h\nu$ and the sum of binding energy E_b . A work function of the analyzer is also subtracted from the photon energy. This can be expressed in the following equation (Eq 3.5):

$$E_b \cong h\nu - E_k - \phi_A \quad \dots\dots\dots 3.5$$

where h is the Planck's constant and ν is the X-ray frequency. Binding energy allows in identifying the chemical information of an atom. The binding energy is extracted from kinetic energy produced from the ejected electron. While ionization occurs, electrons that originate below the solid surface leaves the surface without energy loss, producing the peaks in the spectra.

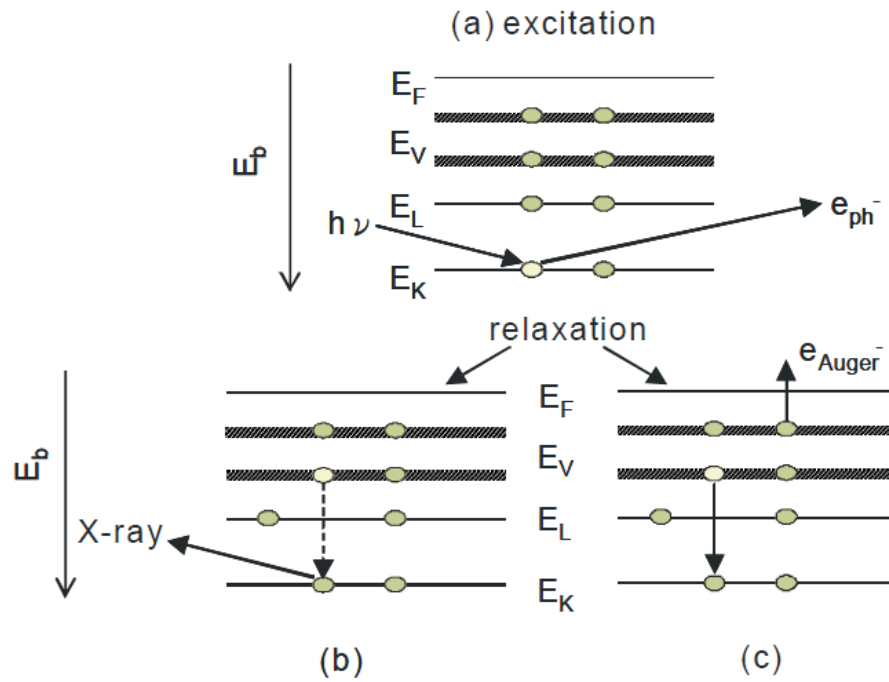


Figure 3.9 XPS working principle based on photoelectric effect.

Relative concentrations of the various constituents in the sample can be estimated based on peak area and peak height sensitivity factors. A general expression for atom fraction of any component in a sample, C_x (Eq 3.6):

$$C_x = \frac{I_x/S_x}{\sum t \frac{I_t}{S_t}} \dots\dots\dots 3.6$$

where S is the atomic sensitivity factor based on the calculated cross-section (σ) corrected for the kinetic energy dependence of the spectrometer detection efficiency and an average value for the dependence of inelastic mean free path on the kinetic energy, and I is the measured peak area.

Samples in this study were prepared by repeated sputtering of a diluted sample solution (200 ppm, 5 μ L) on a silica-based glass substrate, followed by drying. Monometallic gold/microgel sample (1mL) was sputtered on a glass substrate and dried for 24 hours in atmospheric condition. Bimetallic (Au@Ag) / microgel sample (0.5 mL) was sputtered on a glass substrate and dried at 60 °C for 15 minutes. This cycle was repeated five times. Thus, a thicker specimen was created for subsequent analysis.

Chapter 4

PNIPAm/PEI Core-Shell Microgels as Dual Nanoreactors and Templates for Synthesis of Smart Gold/Polymer Composite Particles

Three types of PEI-based core-shell particles have been examined to act as both nanoreactors and templates for the synthesis of gold/polymer composite particles. The first template studied was a hard core-shell template with PMMA as its core. The second type was core-shell microgel template with a PNIPAm as the core. The third type was the ultra-soft hollow derived from the hard particle template. The different physical properties of the core components of the template influence the template's softness and its corresponding formation and encapsulation of gold nanoparticles.

Of all the templates examined, the soft microgel template, PNIPAm/PEI microgel particles seem to be the most efficient and stable templates in the synthesis of the gold nanoparticles and its corresponding composite particles. It has the ability to carry out the reduction of gold ions to nanoparticles at the least amount of time. It produced more gold nanoparticles than the hard template, PMMA/PEI particle. Therefore, results suggested that synthesis of gold nanoparticles requires appropriate softness to control the formation of gold nanoparticles, its immobilization and stability.

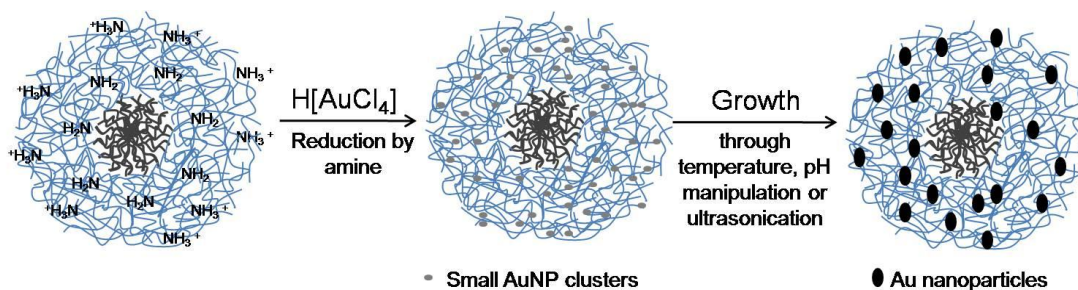
This chapter focused on the studies on the use of PNIPAm/PEI soft template in the formation of gold nanoparticles and their corresponding composite particles. In particular, this chapter will discuss on how the soft template is able to form and immobilize gold nanoparticles. It will answer questions regarding its functions in the synthesis of gold nanoparticles. Later, the measurement and characterization of the gold nanoparticle/PNIPAm/PEI composite particles (Au/PNIPAm/PEI) will be discussed. Effect studies such as pH, temperature, the amino to gold salt ratio (N/Au), and the thermal heating of the composite particles will also be investigated in detail.

4.1 PNIPAm/PEI as a multifunctional template for the synthesis of gold nanoparticles and composite particles

In this section, PNIPAm/PEI as a microgel template is discussed in terms of its multifunctional abilities in the synthesis of gold nanoparticles. These functions include as a nanoreactor, a stabilizer and immobilizer to generate gold nanoparticles. The resulting composite particles can be a smart regulator of gold nanoparticle's accessibility, which is triggered by the conformational changes of the microgel template, thus influencing the availability of the nanoparticle surface area. These conformational changes were induced by the template's stimulus response to pH and temperature of the soft template, PNIPAm/PEI. The following sections discuss in details of each function.

4.1.1 Microgel as a nanoreactor for gold ion reduction

The chemical phenomenon of gold nanoparticle formation in a microgel template can best be described in Scheme 4.1. The formation of gold nanoparticles from its ionic form is thermodynamically stable. This means that it is a fast reaction and doesn't need any activation energy to form gold nanoparticles. In fact, room temperature synthesis was carried in this study. However, two successive reactions occur simultaneously during the formation of gold nanoparticles. First is the interaction between the negatively charged gold chloride ions in solution and the cationic microgels. Microgels in solution have positive charge that can attract the negatively charged gold ions in the form of AuCl_4^- . These oppositely charged ions electrostatically attract each other. Once the gold ions are attracted into the microgel, subsequent redox reaction occurs between the gold ions and available amine groups. The gold ions are reduced while the amine groups are oxidized. The amine oxidation allows transferring electron from the amine to the gold ions, thus generating zero-state gold nanoparticles. This phenomenon has been reported by N.L. Lala *et al.* ^[140] In their work, they used an aminated poly(styrene) surface to reduce the gold ions. They have proposed that the AuCl_4^- ions could be bound electrostatically to the protonated amine functional group and then reduced intramolecularly by the amine group. Continuous growth of these small AuNPs clusters was carried out through temperature or pH manipulation, and further thermal heating.



Scheme 4.1 Schematic diagram on the formation of gold nanoparticles in microgel template.

Figure 4.1 shows TEM images of the PNIPAm/PEI template from an empty nanoreactor to a gold nanoparticle-filled composite particles. The microgel particles show core-shell structure with PNIPAm as the cores and PEI as the shells (Figure 4.1a). Figure 4.1b shows the image of gold nanoparticles formed under room temperature. They looked like clusters of small gold nanoparticles. However, these particles become clearer when heated to 60 °C for an hour as seen in Figure 4.1c. Heating the composite material facilitated the growth of the gold nanoparticles through further crystallization. The size of the gold nanoparticles was roughly estimated with an average of 17.60 ± 2.34 nm with a narrow size distribution (Figure 4.2).

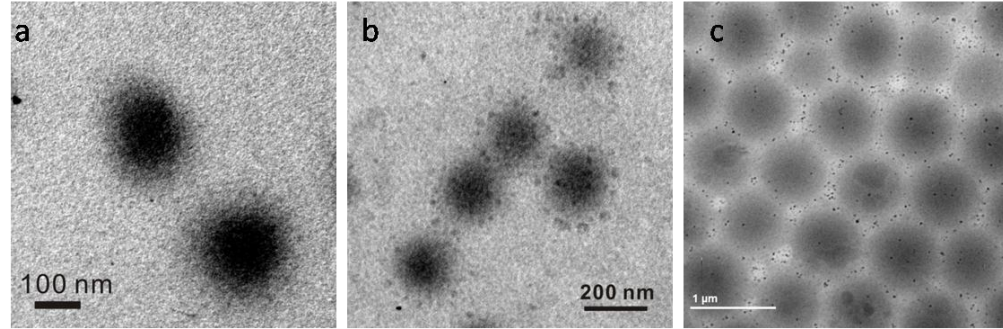


Figure 4.1 TEM images of the a) PNIPAm/PEI microgel template, b) Au/ (PNIPAm/PEI) composite particles synthesized at 25⁰C and pH 7.30. c) Heated Au/PNIPAm/PEI composite particles.

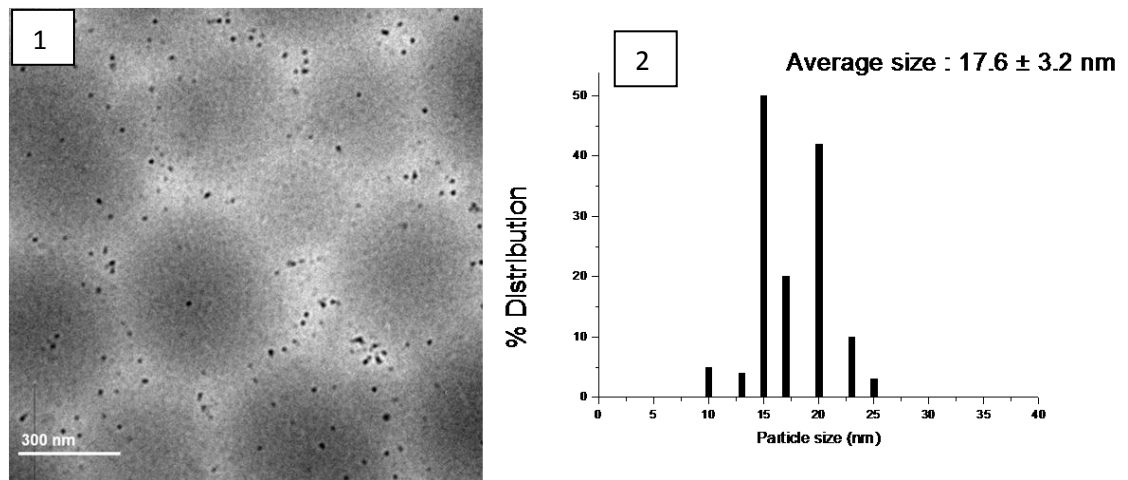


Figure 4.2 1) TEM image of Au/ (PNIPAm/PEI) composite particles generated at 60°C. 2) TEM measurement of particle size and size distribution.

4.1.1.1 Kinetics of Au salt reduction and formation of gold nanoparticles

To understand the rate of reaction in the formation of gold nanoparticles, the UV-vis absorbance at 525 nm wavelength was monitored with time. The adsorption of at 525 nm wavelength is one characteristic of gold nanoparticles. Figure 4.3 shows that the increase of the absorbance at this specific wavelength was fast in the first thirty minutes of reaction and became slower after thirty minutes until third hour of reaction. The reaction started to cease after three hours and no change of absorbance was further observed. This graph concludes that the electrostatic interaction and reduction of gold ions to nanoparticles simultaneously occurred at a fast rate during the initial stage of reaction. It is assumed that there is a fast nucleation during the initial reduction of gold ions, resulting to numerous smaller particles.

wavelength at a very short span of time, approximately in 30 minutes. The average reduction rate between 0 to 30 min is 0.35. The second part is the decrease of the reaction represented by an exponential curve behavior from 30 minutes to 3 hours. Its average reaction rate is 2.3×10^{-3} . This rate was derived from the first derivative of the exponential relationship between absorbance and time. The last part is the cease of reaction where a very slow average rate of 6.7×10^{-7} was determined.

From this data, it can be concluded that in both systems, PEI was able to reduce gold ions to nanoparticles. However, using a nanostructured PEI, such as PNIPAm/PEI core-shell particles with PEI shell, a significantly higher reaction rate occurs. In fact, the reduction rate of initial 30 minutes in the presence of PNIPAm/PEI particles is 625 times faster than the overall reaction rate of the highly branched-PEI alone. Possible reasons for this extremely fast reduction may be attributed to the following two effects:

- 1) Strong electrostatic interaction between highly positive charges of the PEI shell and negative gold ion complexes. Thus, added gold salt would immediately attract to the PEI shell layer, which is highly open.
- 2) The gold salt ions attracted into the PEI shells are surrounded by a high concentration of amino groups because the PEI molecules are confined within nanoscale range by the PNIPAm cores. Unlike free PEI molecule with extended architecture in water under acidic pH, the immobilized PEI molecules form a compact shell confined within nanoscale. Such high concentrations of amino group can effectively reduce gold salts to the nanoparticles.

3) Multivalency effect ^[141] of the PEI-based template. The multivalency effect explains that molecules carrying multivalent functional groups have the ability to reduce metal ions fast. In this case, PEI molecules attached to the microgel template carries multivalent amino groups such as primary, secondary and tertiary, responsible to the fast kinetics of gold ion reduction to nanoparticles.

The kinetic results indicates that the ability of the PEI comprising the shell region of the microgel template is able to efficiently complex the gold ions and reduce them to gold nanoparticles. Thus it is envisioned that PEI based-core-shell particle can act as both the nanoreactor and the reducing agent to generate gold nanoparticles

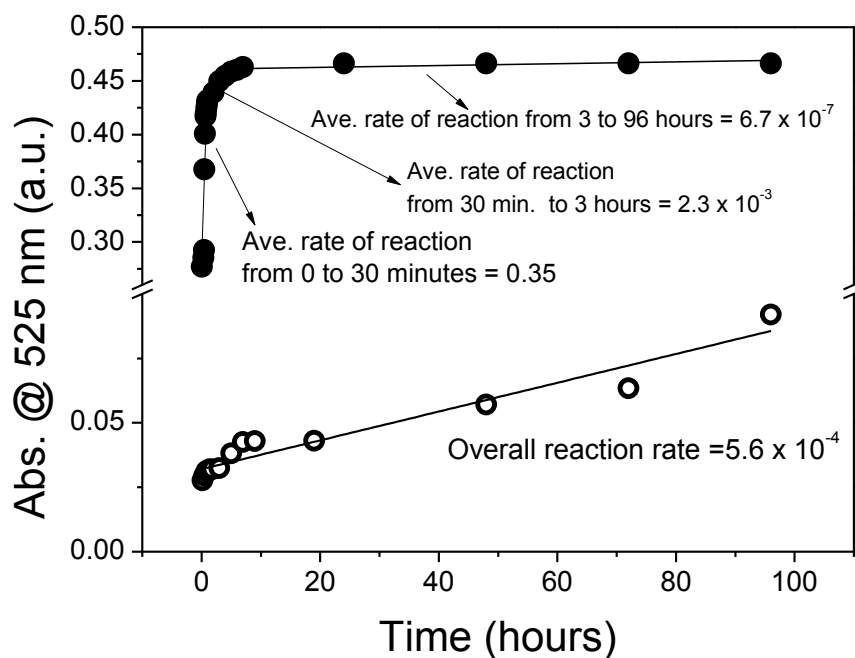


Figure 4.4 Comparison of Au salt reduction in using PNIPAM/PEI core-shell particles (Solid circles). Hollow circles represent data using only the branched PEI

in solution Conditions for both synthesis: 25 °C, pH 5.6, mixing at 200 rpm, N/Au = 28.5. The overall rate constant is based on the change of absorbance per time ($\Delta A/t$), which is proportional to the reduction of gold ions to gold nanoparticles.

4.1.1.2 Proposed mechanism of gold salt reduction using amino group in the PEI shell of the core-shell template

The above results demonstrate that amino group of the PEI molecule can act as a reducing agent to reduce gold (III) ion to gold nanoparticle. The oxidation of amine has been demonstrated in the work of Keene Richard where amine was converted to imine.^[142] Figure 4.5 is the proposed mechanism in the oxidation of the amine group to imine group. In this mechanism, the amine group is oxidized forming an imine. The first stage is the loss of an electron from the amine moiety. Such a loss results in forming unstable cationic radicals, followed by losing a proton to generate an amine radical. Further loss of an electron from amine radical forms a stable imine group forms as a final product.

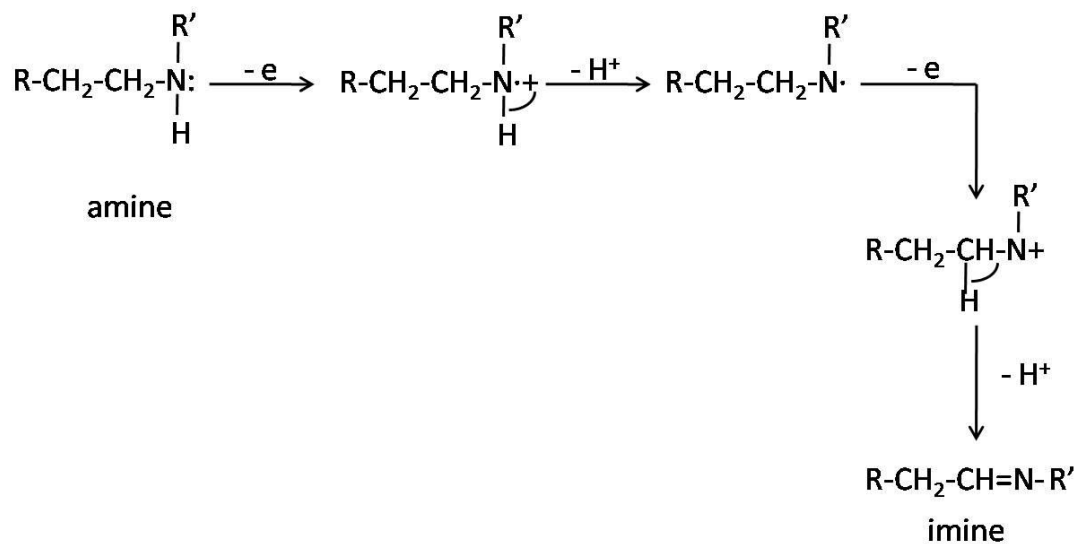


Figure 4.5 Proposed mechanism in the oxidation of the amine group to imine.

4.1.2 Microgel as a stabilizer of gold nanoparticles

The stabilization of the gold nanoparticles in the composite material is based on its ability to sustain in the colloidal system. The microgel template provides stability to composite particles through electrostatic interaction and steric effect of the PEI-shell. A combination of which is commonly termed as electrosteric interaction. The following discussions give an explanation on the contribution of both stabilizing factors.

The electrostatic interaction between the composite particles and the gold nanoparticles within composite particles themselves are the two major contributors to its stabilization. When Au nanoparticles are formed and immobilized in the particle template, the overall size of the composite particle becomes smaller than the pure

template itself (results will be shown later). This is because the formation of gold/amine complexes results in the contraction of the PEI shell. Such tightening of PEI shell after forming gold/amine complexes could reduce leaking of metal nanoparticles from its individual network-cage and form aggregates within the template. Furthermore, the repulsion between composite particles prevents them from getting attracted with each other, thus preventing them turning into bulk size and consequently form precipitates.

The steric contribution on the stabilization of the gold nanoparticles is mainly attributed to the hyperbranched structure of the PEI-shell component in the template. Amphiphilic graft copolymers are known to be the best steric stabilizers ^[143]. This accounts for the hydrophobic-hydrophilic interaction of the copolymers involved. This type of interaction is very significant on the stability of the template itself as well as the formation of the composite particles. While the PEI anchors in the gold nanoparticles, the PNIPAm core is kept together away from the shell. With this mechanism, sustaining the shape and stability of the composite particles is possible.

4.1.3 Microgel as an immobilizer of gold nanoparticles

The immobilization of the generated gold nanoparticles within the microgel template was possible through several factors rooting from the nature of the PEI-shell's property itself. First is the well-known weak bonding between the amino group and the gold nanoparticles ^[144], which results in producing discrete gold nanoparticles rather than aggregates ^[145]. Second is due to the hyperbranched characteristic of the PEI ^[146],

which envelops and shields the gold nanoparticles into its network-cage like structure. The network-cage like structure provides bulkiness that protects the gold nanoparticles and prevents them from aggregating with other neighboring nanoparticles. The PEI-shell network also has the ability to link the gold nanoparticles intact ^[147] within its boundary template. The following are four evidences to demonstrate the microgel acting as an immobilizer of gold nanoparticles:

- 1) Morphology of the gold/polymer composite particles. Figure 4.1b shows the TEM image of the generated gold nanoparticles in a core-shell microgel template. In this image, Au nanoparticles are fuzzy gray dots embedded on the microgels. They are located within the circumference of the microgel, attached on the shell region. These fuzzy gray dots are the gold nanoparticles due to the fact that it is the only main source of conductive material which transmit electron during TEM analysis. This fuzziness leads us to suspect that the gold nanoparticles are mostly attached to the surface of the PEI shells, or within the microgel structures.
- 2) Particle size of gold/polymer composite particles. The composite particles have an average hydrodynamic size of 284 ± 2.1 nm with a PDI of 0.053 which was smaller than the original average microgel size of 348 nm. The decrease in size between the pure microgel template and the gold loaded template was due to the encapsulation of the metal ions during absorption stage. As the metal ions were absorbed into the swollen shell region of the microgel, the steric effect of the PEI network could encapsulate the metal ions, resulting in shrinking of the composite material.
- 3) Colloidal stability of these composite particles was also measured and compared. It was found out that there was also a decrease in the *zeta*-potential from 30 mV to 15

mV. The decrease of the *zeta*-potential in the composite particle was due to the partial consumption of the cationic ammonium ions during the gold ion adsorption stage. However, with such decrease of the surface charge, the composite particles have sustained its stability in the colloidal system. Stability in this type of colloidal system was not only due to the electrostatic interaction, but also the steric effect of the microgel shell as discussed in the previous section.

- 4) Further proof of the encapsulated gold nanoparticles is evident in the XPS analysis as shown in Figure 5.17. The XPS analysis will be discussed in a separate section for further discussion. However, this result could not only verify the location of gold nanoparticles, but also reveals that these gold nanoparticles are found within 2 to 10 nm deep from the surface of the microgel template. Thus, immobilization occurs.

Immobilization of the gold nanoparticles can also be explained through the ligand role of the PEI shell. This ligand role leads to the complexation of the water-soluble PEI with metal ions. The complexing ability of the PEI with metal ions brings noteworthy properties^[148, 149, 150] such as metal complexes are water soluble due to the hydrophilic amine groups; high capacity for metal uptake due to the high local concentration of functional groups; easy separation of polymer complexes due to high molecular weight; high flexibility of the molecular conformation that can achieve optimum configuration, and good chemical and physical stability

4.1.4 Microgel as a smart regulator of gold nanoparticle accessibility

Another feature of PNIPAm/PEI template is its ability to regulate the accessibility of the gold nanoparticles generated within. Its ability to regulate the gold nanoparticle surface comes from the stimuli responsive nature of the PNIPAm. Particles at nanoscale to few microns that possess stimuli responsive properties are referred to as smart particles. In this case, PNIPAm/PEI is both responsive to pH and temperature. Specifically, PNIPAm is temperature sensitive while PEI is pH sensitive. The response of this soft template to temperature or pH affects its conformational arrangement. The changes on the structural arrangement of the template result in the controlled accessibility of the gold nanoparticle surface. This is further illustrated in Figure 4.6. Herein, the template with encapsulated gold nanoparticles is in different structural arrangement under different pH or temperature. At a low pH such as 3.5, the template gets protonated and swells. The swelling behavior of the template exposes the embedded gold nanoparticles within. However, when the template is in a high pH environment, where it becomes deprotonated, de-swelling of the template occurs. By this action, the gold nanoparticles embedded within are trapped in small spaces. This type of composite particle controls that degree of plasmon coupling that originates from the dipole interaction among gold nanoparticles. This process allows the control of interparticle distance between gold nanoparticles ^[151]. On the other hand, when temperature reaches beyond the LCST point of PNIPAm (i.e. 32 °C), the whole template shrinks. This causes the trapping of gold nanoparticles within the template. But when temperature is lower

than its LCST, the template is more open and becomes loose. This results to easy accessibility of the gold nanoparticles within the template.

Thus, both pH and temperature are critical to the smart responsive property of the template and to the accessibility of the gold nanoparticles.

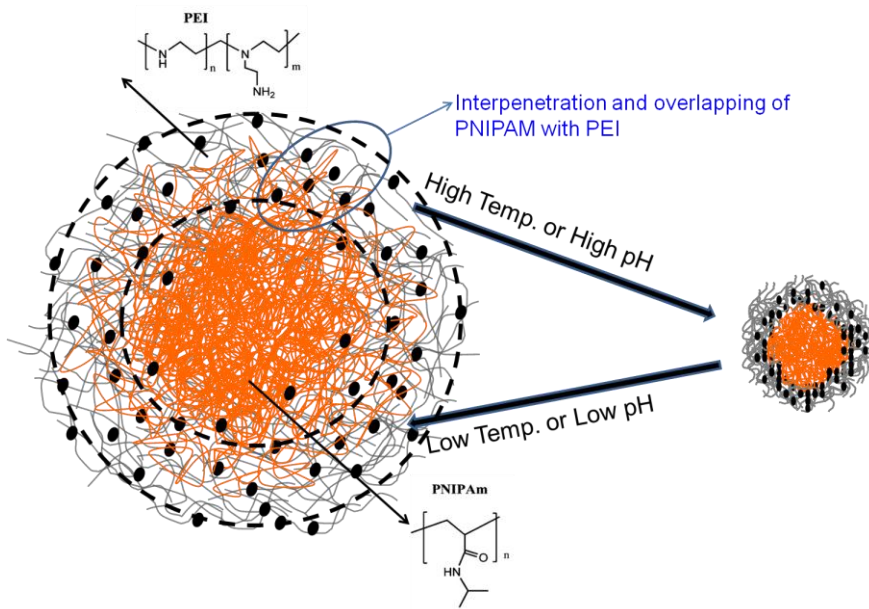


Figure 4.6 Conformational changes of microgel template from stimuli response to solution pH and temperature.

In order to have a vivid picture on the smart properties of the template by manipulating its temperature, microgel particles were subjected to different temperature conditions at 29 °C, 45 °C and back to 29 °C in solution. Morphological changes of the particles under different temperatures were captured with AFM analysis. Figure 4.7a shows an image of the template at 29 °C in a fluid mode. This image shows the microgel

templates are within the range from 100-150 nm with quasi spherical morphologies. When temperature was raised to 45 °C, the templates decrease in size and show porous surfaces. This is attributed to the shrinking of the templates as it goes beyond its VPTT. However, when the temperature was restored to 29 °C, the smooth morphology and size of the templates were restored. This demonstrates that the conformational changes of the template triggered by the response to temperature are reversible.

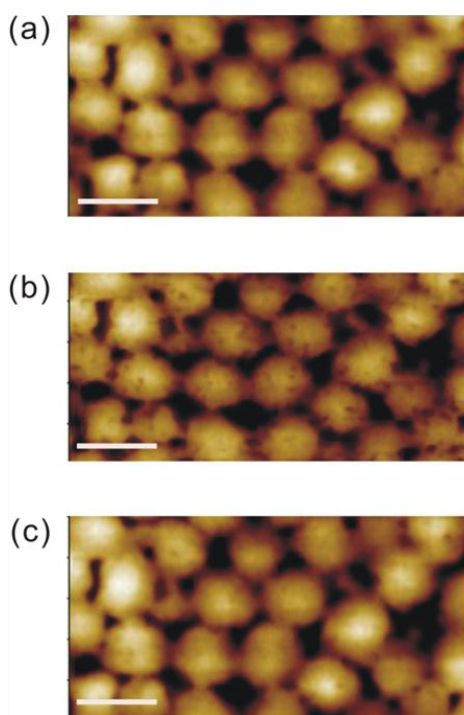


Figure 4.7 AFM micrographs of PNIPAM/PEI microgel particles measured in a fluid mode at different temperatures: (a) 29 °C; (b) 45 °C, and (c) Cooled from 45°C to 29 °C. Scale bar: 200 nm.

4.2 Measurement and Characterization of gold/microgel (Au/PNIPAm/PEI) composite particles

The measurements and characterization of PNIPAm/PEI core-shell microgels and its composite particles were performed with the following techniques based on the procedures discussed in Chapter 3.

4.2.1 Particle size and size distribution

Based on Figure 4.8, synthesized PNIPAm/PEI microgels had an average hydrodynamic diameter of 402 nm while the Au-microgel composite particles were measured at 298 nm. The polydispersity indices on both unloaded and gold loaded particles were 0.050 and 0.055 respectively. As a general observation, the particle size of the Au composite particles is smaller than the original template particle. This is due to the incorporation of the counterions into the colloidal system during the metal ion reduction stage. Furthermore, when Au nanoparticles are formed, microgel network can immobilize the in-situ generated gold nanoparticle through capturing them on its network-like structure, thus providing a steric effect on the metal nanoparticles.

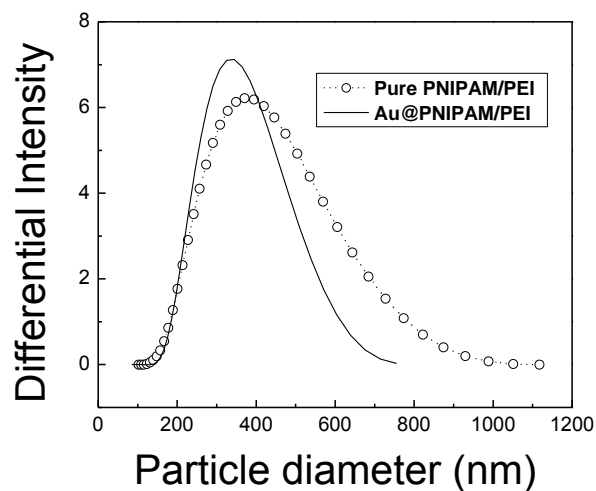


Figure 4.8 Particle size and size distribution of pure microgel template and Au/ (PNIPAm/PEI) composite particles synthesized at optimum conditions of 25°C and pH 7.30.

4.2.2 Colloidal stability

The Au composite particles were further characterized based on its surface charge that dictates its stability in solution. The surface charge is expressed in terms of *zeta*-potential of the particles. Au composite particles have an average *zeta*-potential of 15 mV at pH 7.00 in aqueous medium. The composite particles were stable enough that no aggregation or precipitation was observed after complete reduction of gold ions to nanoparticles. *Zeta*-potential, however, is affected by the solution pH in the colloidal system. Figure 4.9 demonstrates the change of the surface charge as a function of pH. In this figure, Au loaded microgels follow a three –phase behavior of *zeta*-potential in an increasing solution pH. The first phase gives an almost linear *zeta*-potential at a pH range of 2 – 6.5. The second phase is between pH 6.5 – 9.0, which gives a sharper

decrease of *zeta*-potential. The third phase is between pH 9.0 – 11.5 which gives a minimal change of *zeta*-potential values. The isoelectric point of the composite particle at pH 9.2. The uniform *zeta*-potential in the first phase is attributed to the fact that composite particles are loaded enough with Au nanoparticles that at this certain range of pH, its surface charge is not quite affected. However, increasing the pH more will affect the composite material and decreases its surface charge surpassing the isoelectric point. Further increase of pH at this stage may saturate the composite particles and then again give a very minimal or no effect on its *zeta*-potential.

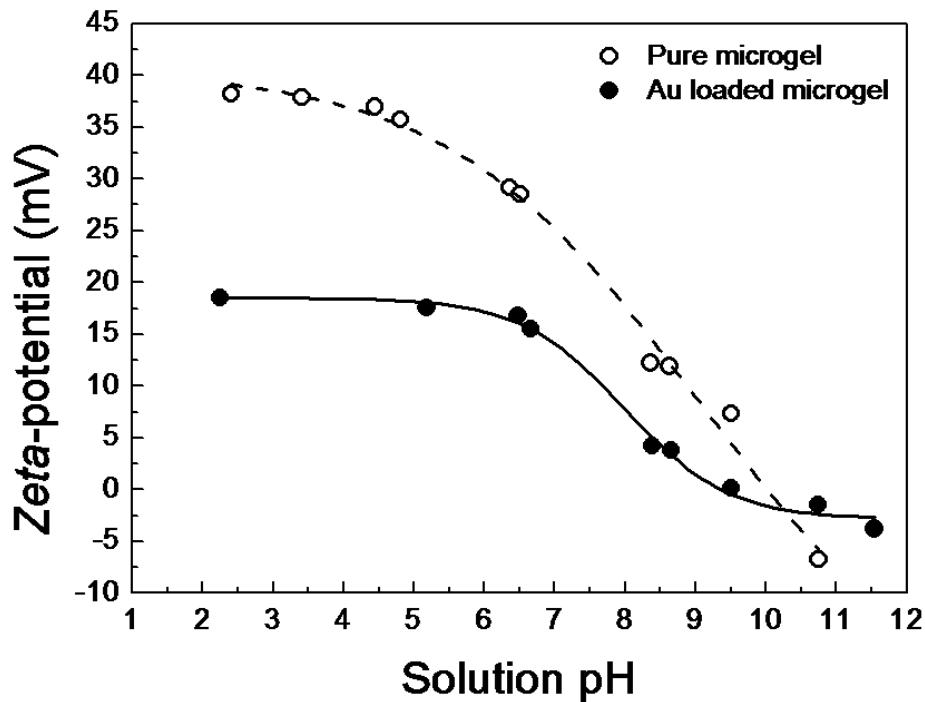


Figure 4.9 Surface-charge profile of Au composite particles (solid points) and pure PNIPAm/PEI microgel template (hollow points) in different solution pH.

Since composite particles carry a temperature-sensitive component, PNIPAm, it was appropriate to test the effect of temperature to its surface charge as well. Figure 4.10 shows that varying solution temperatures from 25 to 40 °C strongly affect the *zeta*-potential of the Au composite particles. There is an abrupt change of surface charge in the temperature range between 29 to 34°C, which crosses the VPTT of the microgels. Before and after this temperature range, the *zeta*-potential was more or less constant. The change in the surface charge is attributed to the increase of the surface charge density as the colloidal particles decrease in size. The smaller the particles, the higher are the surface charge density. Thus, the shrinking of the composite particles near its VPTT triggers the increase of the surface charge density. This phenomenon was also observed in the work of J.L. Ou *et al.*'s ^[152] group where the surface charge density was clearly shown through the *zeta*-potential to increase with decreasing particle size.

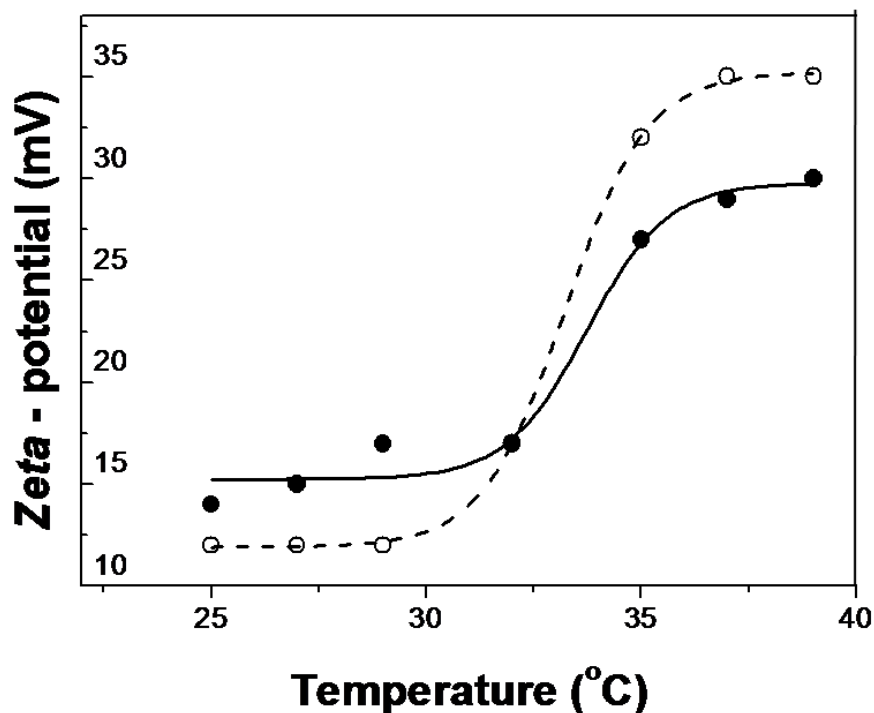


Figure 4.10 Surface charge profile of Au composite particles (solid points) and pure PNIPAm/PEI microgel template (hollow points) indifferent temperatures.

4.2.3 SEM and TEM images

Figure 4.11 shows the SEM and TEM images of the Au/(PNIPAm/PEI) composite particles. The SEM shows that these particles are in a spherical shape with narrow size distribution. The spherical shapes of these composite particles were preserved from its original microgel template (Figure 4.11a inset). However, partial agglomeration of the particles may have occurred during the drying of the SEM sample

treatment. The TEM image (Figure 4.11b) gives a clear picture of the location of the Au nanoparticles within the microgel template. In this image, Au nanoparticles are located around the circumference of the microgel attached on the shell region of the original microgel. These images show the effective immobilization of the gold nanoparticles within the microgel network. The fuzzy black dots are the gold nanoparticles due to the fact that they are the only main source of conductive material which can transmit electron during TEM analysis. This indicates that the gold nanoparticles are attached to the PEI shells of the microgel structures. The fuzzy image of the metal nanoparticles observed is a result of the microgel network bouncing back some electron beam while some passes through the embedded gold nanoparticles. Thus, the fuzzy black dot images also explain the immobilization of the gold nanoparticles within the microgel.

The hydrodynamic size of the Au composite particles was at average 284 nm with a standard deviation of 2.1 and a PDI of 0.053. This size is higher than its SEM image (ca. 230 nm) due to the swelling behavior of the microgel in water. The collapse of the PEI shell was due to the electrostatic interaction between the gold ions and the protonated amino group. The surface layer thickness decreased as the polyelectrolyte chains of the microgels interacts with the gold ions.

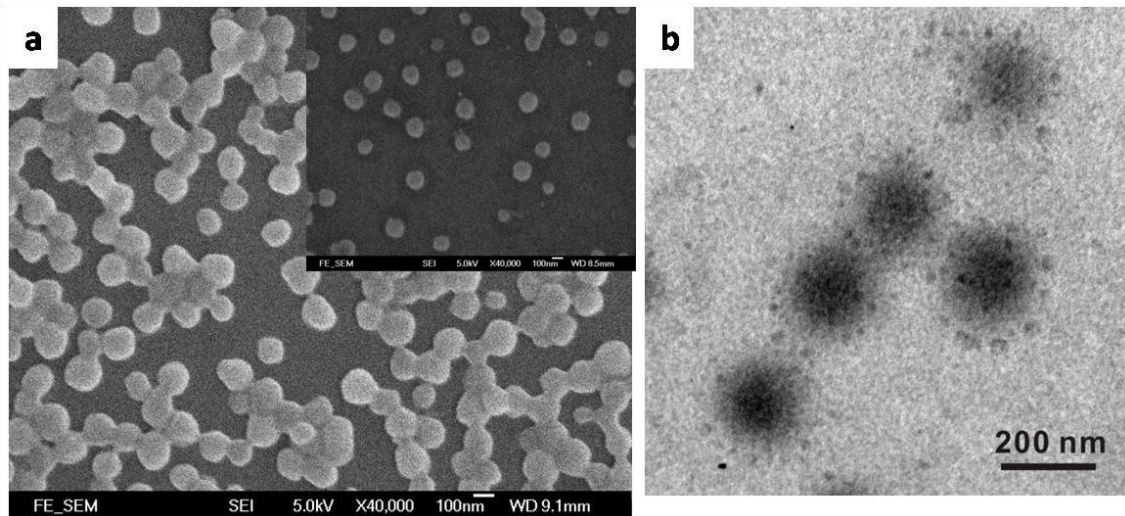


Figure 4.11a) SEM image of Au/ (PNIPAm/PEI) composite particles, inset is the original microgel template, b) TEM image of Au/ (PNIPAm/PEI) composite particles. The particles were synthesized at 25 °C and at pH 7.30.

The size of gold nanoparticles synthesized can be roughly estimated based on the TEM image in Figure 4.12. The average size is ca. 17.40 nm with a standard deviation of 2.34 nm. The measured sizes are considered to be clusters of small Au nanoparticles.

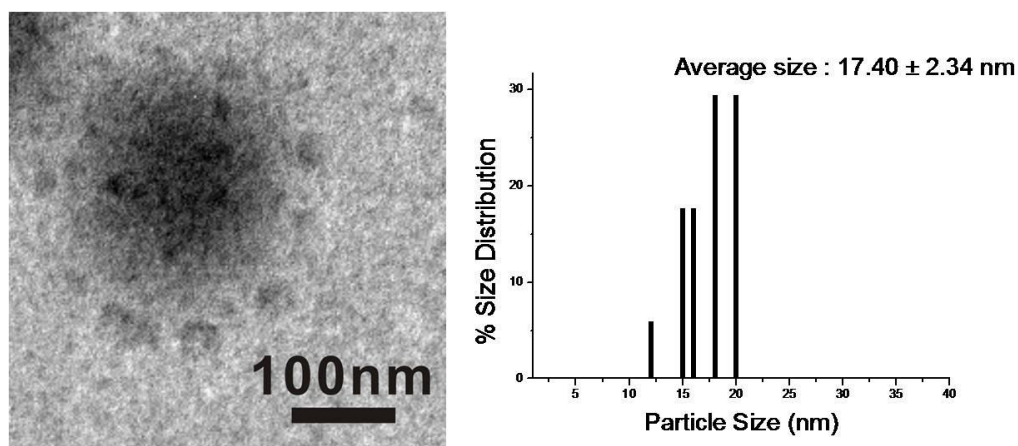


Figure 4.12 TEM micrograph of single PNIPAm/PEI microgel surrounded with Au NPs and size distribution histograms of AuNPs estimated based on TEM images (based on 25 total number of Au nanoparticles).

4.2.4 UV-vis spectroscopy

The formation of gold nanoparticles in the presence of microgel template was monitored by a UV-vis spectroscopy. Upon interaction with the electromagnetic field in the UV-vis spectrum, gold nanoparticles exhibit Surface Plasmon Resonance (SPR) at a specific wavelength. This was a result of the collective oscillation of the conduction electrons on the gold nanoparticle's surface. In this case, gold nanoparticle formation was evident at the absorbance of 525 nm wavelength (Figure 4.13). The formation of gold nanoparticles was further monitored as a function of time. Figure 4.13 demonstrates the reduction of gold ions with time. Results indicate that gold formation started after 20 minutes of reaction. This was also manifested during the reaction. The reaction mixture changed color from turbid white to light pink. Further reaction gives an

increase of absorbance of gold nanoparticles. This indicates formation of gold nanoparticles at higher concentration. However, after four hours of reaction, there were no more significant changes in the absorbance intensity. This indicates that gold nanoparticles have ceased to grow or gold ions have completely been reduced to nanoparticles. Throughout the reaction, there was no shift of the absorbance peak. This also indicates that the gold nanoparticles formed are of uniform sizes, thus controlling the nanoparticle size. Based on experimental and theoretical reports, wavelength absorbance of gold nanoparticles ranging from 520 – 525 nm are Au nanoparticles with spherical shape with sizes ranging from 15-30 nm ^[153], consistent with our results.

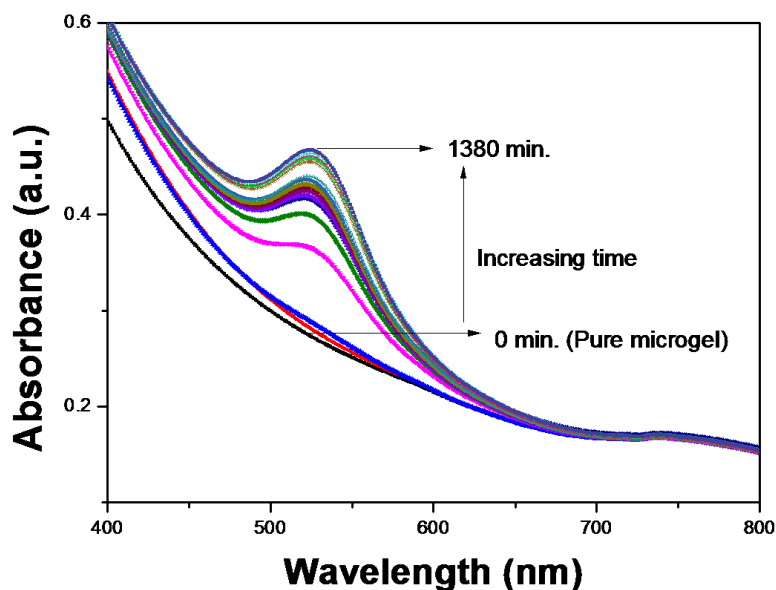


Figure 4.13 UV-vis spectra showing the reduction of gold nanoparticles ions in PNIPAm/PEI microgels as a function of time (min). Absorption peak is at 525 nm. Conditions of the synthesis: 25 °C, pH 5.6, 200 rpm, N/Au = 28.5.

4.2.5 FTIR and NMR Spectroscopy

To further prove the presence of Au nanoparticles formed within the core-shell template particles, an FTIR analysis of the microgel before and after gold loading was carried out. It is believed that the amine group of the PEI shell is responsible for the Au nanoparticles formation and immobilization. Thus it is expected that the intensity of amine groups after the formation and immobilization of gold nanoparticles will reduce or disappear.

Figure 4.14 shows the FTIR analysis of both pure and Au loaded microgels. Pure PNIPAm/PEI microgel (solid line) displays characteristics peaks at 1650–1660 cm^{-1} (C=O stretching of amide), 1535–1540 cm^{-1} , (N-H bending of amide II), 3420–3550 cm^{-1} (amine N-H stretching) and 1370–1385 cm^{-1} (C-H stretching of isopropyl), which are basically representing the PNIPAm. In addition, there are two N-H stretching peaks of the primary amine at 3300–3400 cm^{-1} and higher intensities of C-H stretching and bending at 2850–2930 cm^{-1} . When gold nanoparticles were formed and immobilized into the microgels, amine stretching at 3300–3550 cm^{-1} disappeared. In addition, the 1570 cm^{-1} representing –NH- stretching in PEI has decreased significantly. All these changes point to the same conclusion of the complexation of gold nanoparticles within the microgel template.

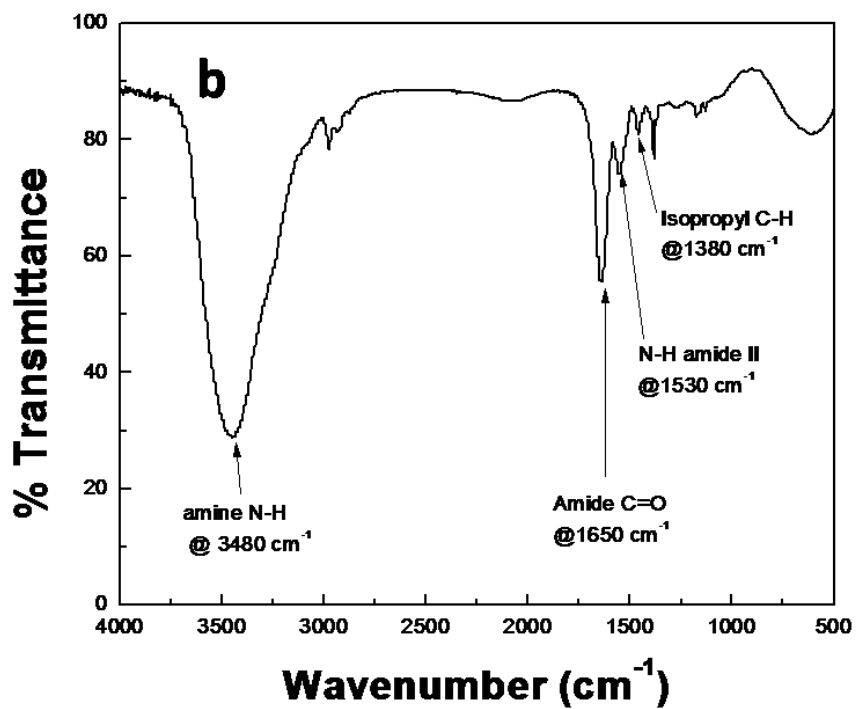
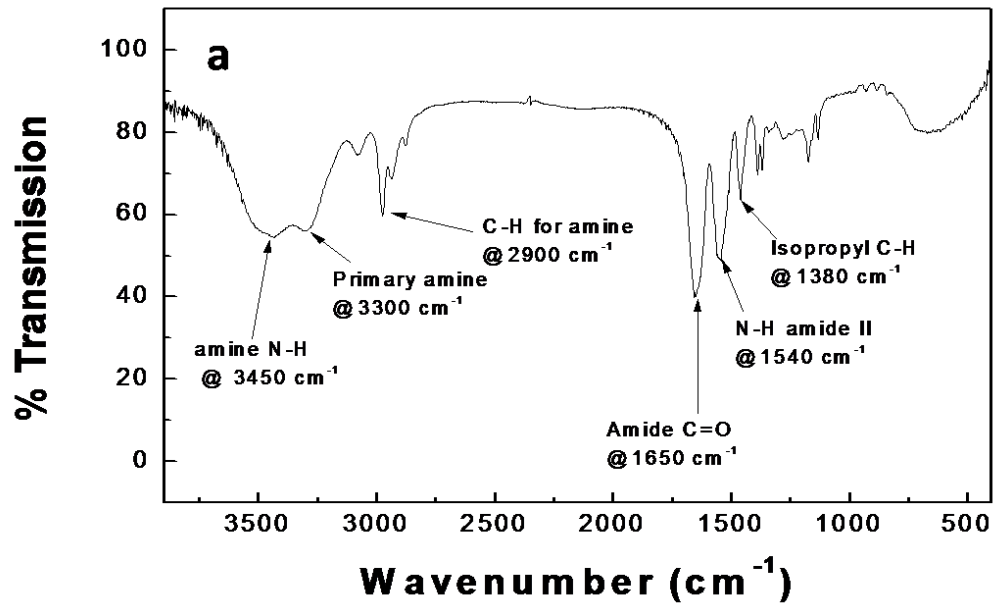


Figure 4.14 FTIR analysis of a) pure microgel template and b) Au loaded microgel.

The changes in the ^1H -NMR spectroscopic analysis between the pure and gold loaded microgel can be observed in Figure 4.15. The most obvious difference is the disappearance of the peaks between 2.6 and 3.0 ppm when gold nanoparticles were generated. These peaks represent the PEI component of the microgel. However the generation of gold nanoparticles resulted to the consumption of the amino groups in the PEI. Thus, the disappearance of these peaks is evident. The PNIPAm peaks are displayed between 1.0 and 2.0 ppm and at around 3.76 ppm. These peaks are evident in both pure and gold loaded microgels. This spectrum further proves that gold nanoparticles consume amino groups. Thus, resides in the shell component of the microgel.

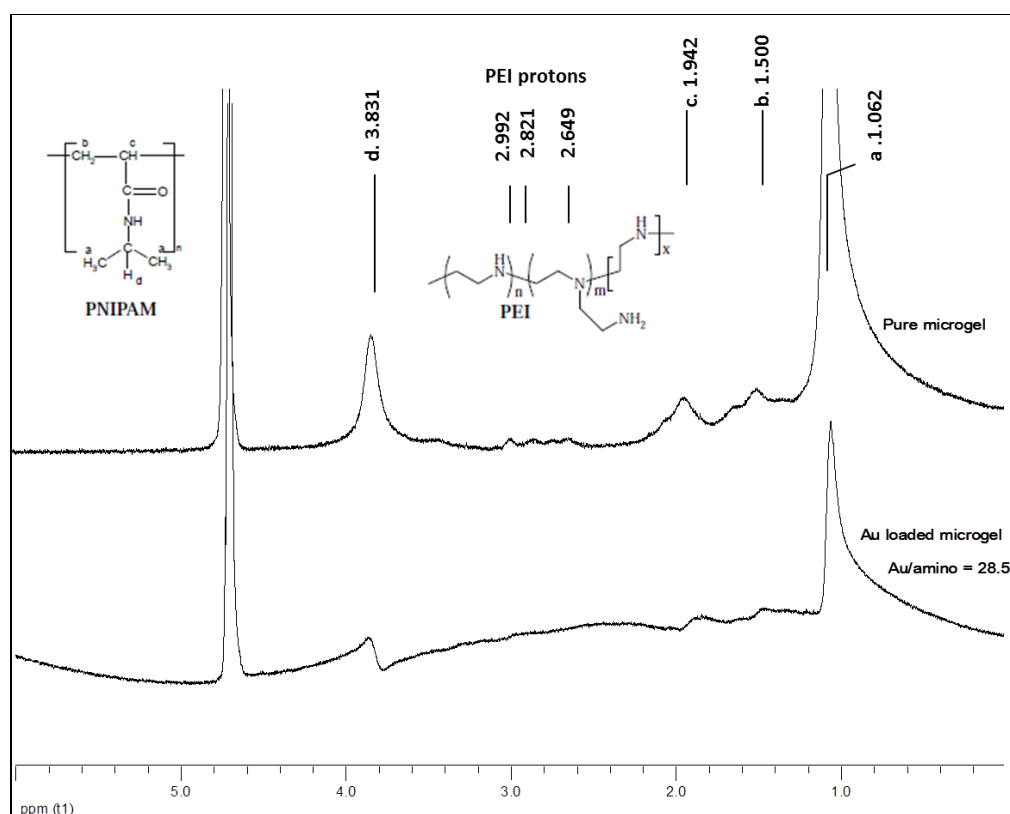


Figure 4.15 NMR spectra of pure microgels (upper) and Au loaded microgels (lower).

4.2.6 HRTEM and Crystallinity of Au nanoparticles (XRD)

A high resolution TEM (HRTEM) was performed in order to take a closer look of the image of Au nanoparticles immobilized in the shell region of the PNIPAm/PEI microgels.. Figure 4.16 shows a high resolution TEM image that reveals a five-fold twinned Au nanocrystal with a size diameter of ca. 22.5 nm. Figure 4.16 (top inset) shows the selected-area of electron diffraction (SAED) pattern over several Au nanoparticles. It reveals a ring pattern indexed as (111), (200) and (222) of a face-centered cubic (fcc) gold lattice. A 5-fold twinned boundary at the center of an Au nanocrystal can be clearly observed from various angles, suggesting the formation of a multiply twinned particle (MTP) which is close to the icosahedral gold nanostructures. The fuzzy portion of the TEM image was a result of its sensitivity to misorientation and distortion of the ideal icosahedrons^[154]. In addition to the presence of a twin boundary, the Au nanostructure is mainly composed of (111) planes with a *d*-spacing of 0.236 nm (Figure 4.16 bottom inset), and the lattice plane is separated by a twin boundary indicated as white line on the image. The fuzzy region of the Au nanocrystal was a result of the AuNPs immersed within the PEI network. Further, the crystallinity of Au nanoparticles embedded on the microgel template is analyzed through an X-ray Diffractometer as shown in Figure 4.17. It was found out that the Au nanocrystals formed a composite of structures with lattice arrangements of (111), (200) and (220) at corresponding angles of 38, 44 and 65°. This is consistent with the previous SAED analysis except for the (220) lattice. However the dominance of the (111) lattice arrangement is the same.

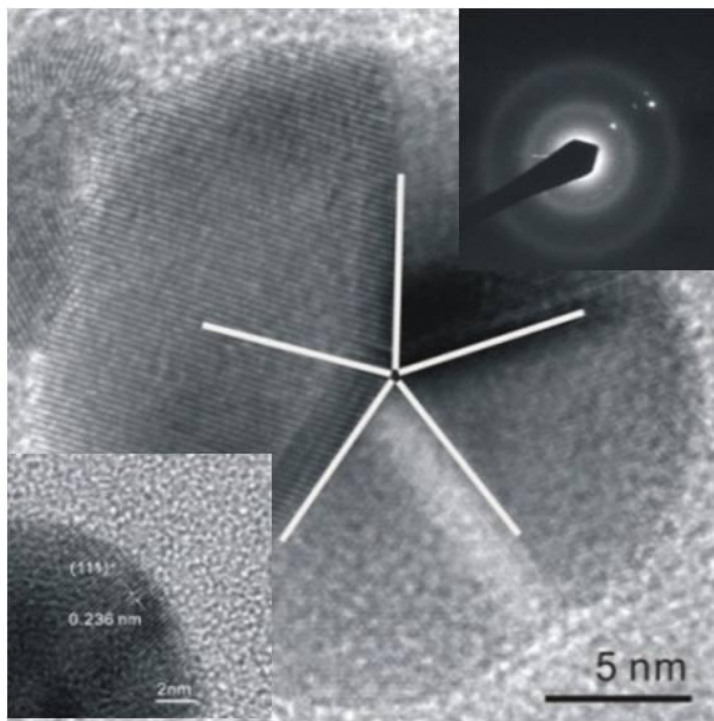


Figure 4.16 HRTEM image of Au nanoparticle embedded within a microgel template.

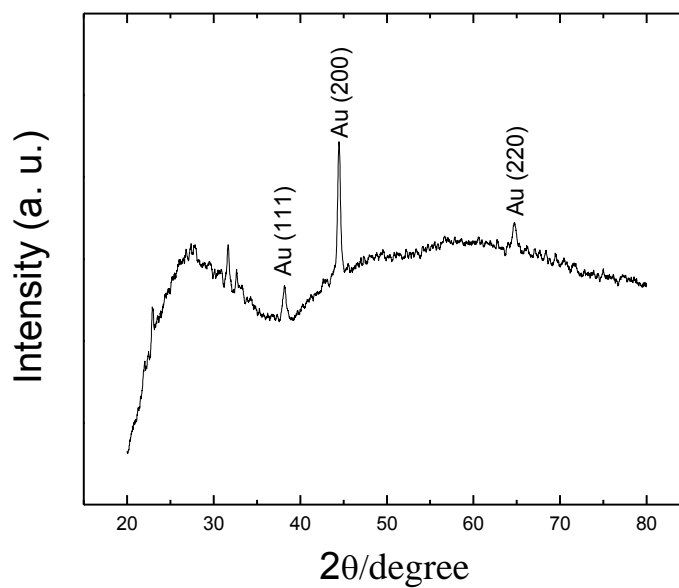


Figure 4.17 XRD spectra of Au/ (PNIPAM/PEI) composite particles.

4.2.7 Surface composition of composite particles (XPS)

In order to further verify the formation of Au nanoparticles on the the microgel, which is mainly in the shell region, an X-ray Photoelectron Spectroscopy (XPS) analysis at a depth of 10 nm was used. The XPS spectra as shown in Figure 4.18 reveals characteristic binding energies of different elements present in the Au nanocomposite systems. These elements are composed of C, O, N, Au and very minute amount of Cl. Convolutated C1s spectra were fitted with peaks at 285.0 and 287.9 eV, which were assigned to C-C/C-H and C=O bonds respectively. N1s peak fitted at 399.3 assigned to amines coordinated with AuNPs. O1s as shown in Figure 5.19 was centered at 531.2 eV corresponding to the carbonyl functional group of the microgel. Zero valence gold nanoparticles are observed from its two peak characteristics at 84.3 and 88 eV, which indicate the formation of gold nanoclusters^[155] (Figure 4.20). The gold peak positions and its peak-to-peak distance of 3.7 eV of the Au 4f doublet are the standard measure of the Au⁰ oxidation state^[156]. To further illustrate the formation of gold nanoparticles through the amine group complexation with AuNPs, a comparison of the nitrogen peak before and after gold loading was investigated. The decrease of nitrogen peaks (Figure 4.19) and its corresponding area are attributed to the attachment of AuNPs into the amine group. Once the AuNPs attached to the amine substrate, detection of N 1s through XPS analysis weakens or even disappears due to the AuNPs fully covering the amine group^[157], while a strong gold signal appears. The same nitrogen binding energy peak at 399.3 eV was observed for the amine-gold interaction in the work of Kumar *et al.*^[158] and similar to Manna *et al.*^[159]. When the AuNPs were immobilized into the PEI

shell containing amine groups, the nitrogen peak was curve fitted into two components at 399.3 and 401.2 eV which corresponds to the amine (free and coordinated to gold) and the protonated amine or ammonium. This indicates that the binding between the amine group of the PEI and the AuNP is more on metal-ligand coordination (metallic gold atom and amine) than electrostatic interaction (between ammonium and the negative charges on the surface of the particles), as the former dominates the latter. Furthermore, concentration ratio of some other elements in the XPS spectra such as C1s and O1s were also compared. It is known that the two peaks of C1s and O1s correspond to the C=O bonds binding energy, while a very minimal residual O₂ was found after gold loading. It was found out that there was no significant change of O1s to C1s ratio before (1.29) and after gold (1.20) loading. This effect may be explained by the fact that change in both the C1s and O1s will be significant enough since they both indicate the presence of the carbonyl functional group in the PNIPAm of the microgel. This proves that at a depth of at most 10 nm, PNIPAm is present within the shell region as well. The presence of such component in the shell makes the whole microgel system sensitive to temperature. The overlapping of the PNIPAm in the shell region, which is mostly PEI, is basically responsible for dragging in the whole shell network when the solution temperature goes beyond the volume phase transition temperature (VPTT).

Through the XPS analysis, this further verified our claim that the amine group residing in our PEI shell microgel is solely responsible for the formation and binding of the gold nanoparticles. Furthermore, some PNIPAm grafts are also distributed in the shell region, thus the shell would expect to be temperature-sensitive.

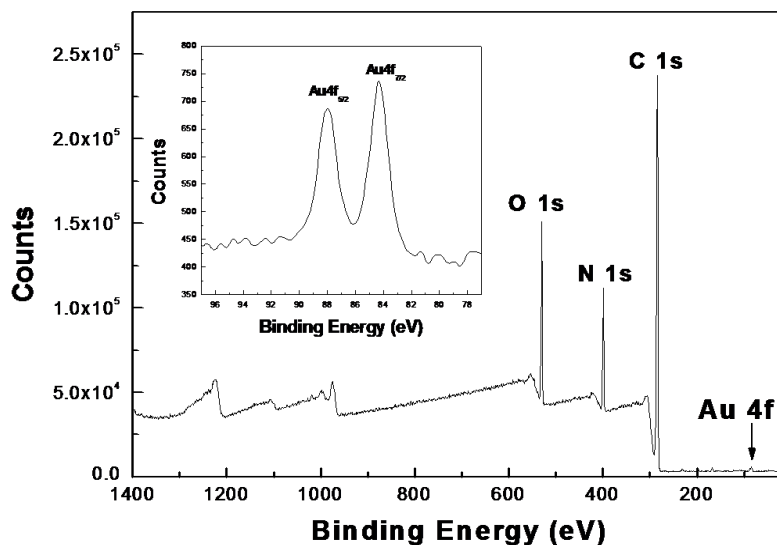


Figure 4.18 XPS survey scans of PNIPAm/PEI microgel with immobilized Au nanoparticles. Inset is the Au 4f core-level spectra obtained from PNIPAm/PEI microgel with immobilized Au nanoparticles.

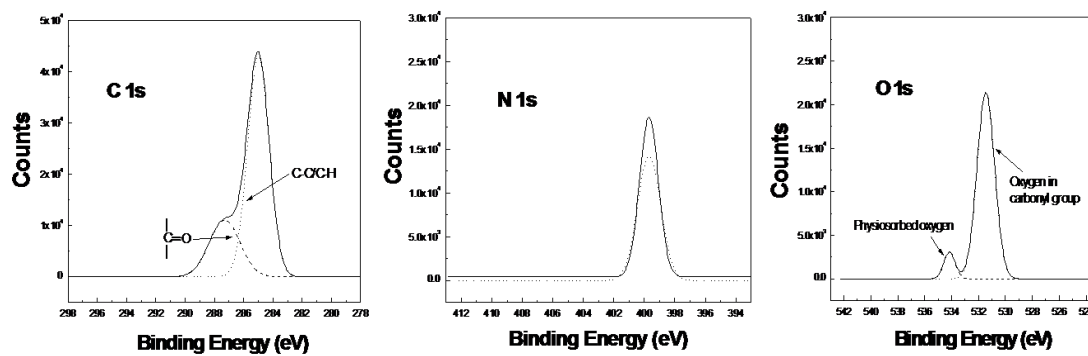


Figure 4.19 XPS survey scans of elements of convolute C 1s, N1s and O1s.

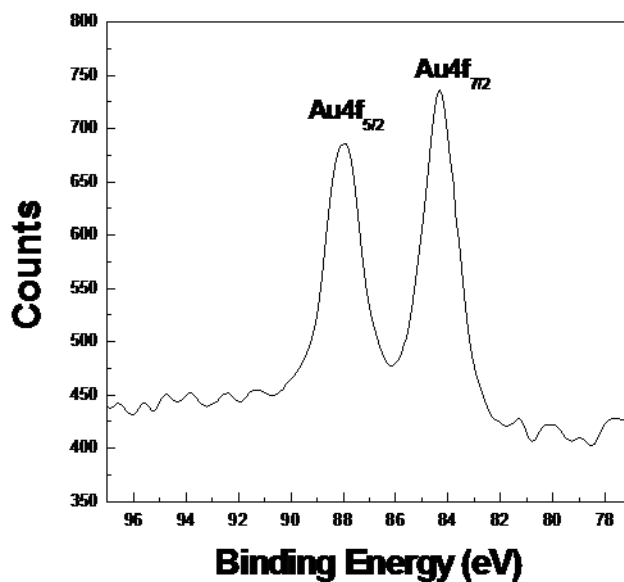


Figure 4.20 XPS survey scan of Au in PNIPAm/PEI microgel.

4.3 Factors affecting the formation of Au/PNIPAm/PEI composite particles

To deeply understand the phenomenon on the formation of gold nanoparticles using PNIPAm/PEI template, a thorough investigation was carried out in this study in terms of the effect of several factors on the synthesis of gold nanoparticles. This chapter will discuss the behavior of the template, the gold nanoparticles and the resulting composites in different conditions of its synthesis. The basic tools to understand this phenomenon are by using electron microscopy images and its kinetic behavior. Four effect studies were investigated in detailed, including pH, temperature, amino to gold salt ratio (N/Au) and the thermal treatment of the composite particles.

4.3.1 Effect of pH

Polyethyleneimine, a positively charged polymer can be protonated at lower pH and deprotonated at higher pH, resulting in the swelling and de-swelling of the whole microgel structure. Thus it was hypothesized that solution pH was critical to the formation of Au nanoparticles because it could alter the concentration of primary amine groups and compactness of the PEI. In this study, a series of pH conditions versus Au nanoparticle formation in the microgel was conducted. The effect of pH on the synthesis of Au nanoparticles in PNIPAm/PEI microgel is based on the TEM images. Experiments were conducted in pH, 3, 5, 7, 9 12. All experiments were conducted at 25°C with stirring rate of 250 rpm. The amino to gold (N/Au) mole ratio of 28.5 was the same under different solution pH.

4.3.1.1 Characterization of Au/(PNIPAm/PEI) composite particles electron microscopies

Figures 4.21 and 4.22 show the TEM images of the Au nanoparticle/(PNIPAm/PEI) composite particles obtained at pH 3. The composite particles consist of the PNIPAm/PEI microgel and the Au nanoparticles as seen in the image. The average composite particle size was 218.42 ± 24.83 nm. The Au nanoparticles are the fuzzy gray dots enclosed around the microgels. They are mainly immobilized within the PEI shell region. Few bigger Au nanoparticles formed outside the microgel template are also clearly seen in these images. They are located outside the microgels and are in darker colored dots with clearly well-defined spherical shape.

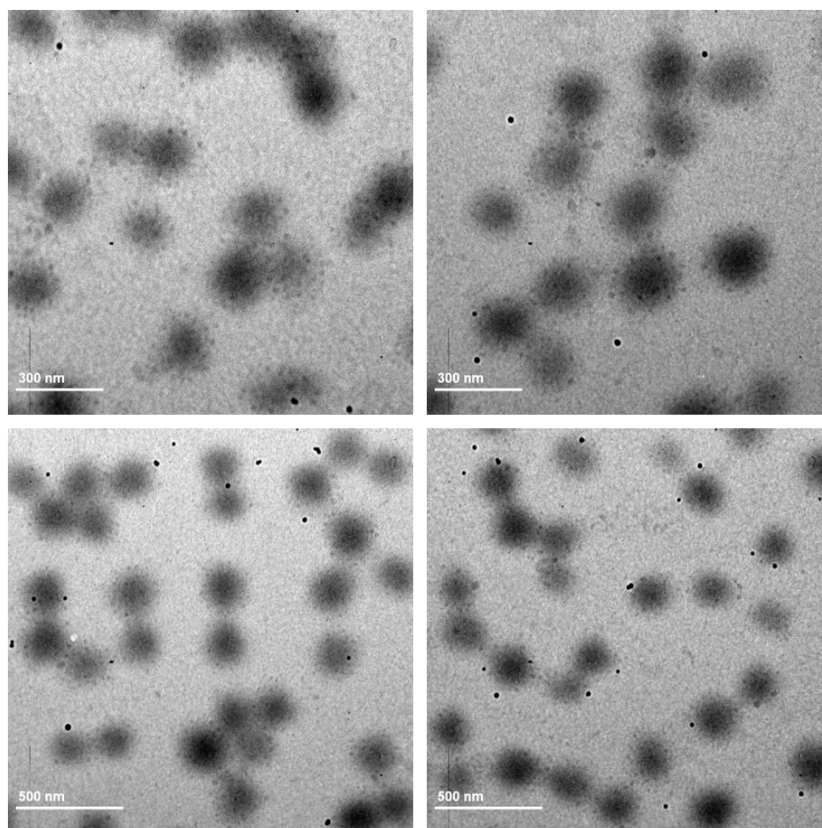


Figure 4.21 TEM images of Au nanoparticles in PNIPAm/PEI microgels synthesized at pH 3, 25°C, 250 rpm, 2 hrs. reaction with N/Au mole ratio = 28.5

A TEM image of a single composite particle synthesized at the pH 3 is shown in Figure 4.22. This composite particle is surrounded with small clusters of gold nanoparticles. The gold nanoparticles formed are on the average of 9.06 ± 2.34 nm.

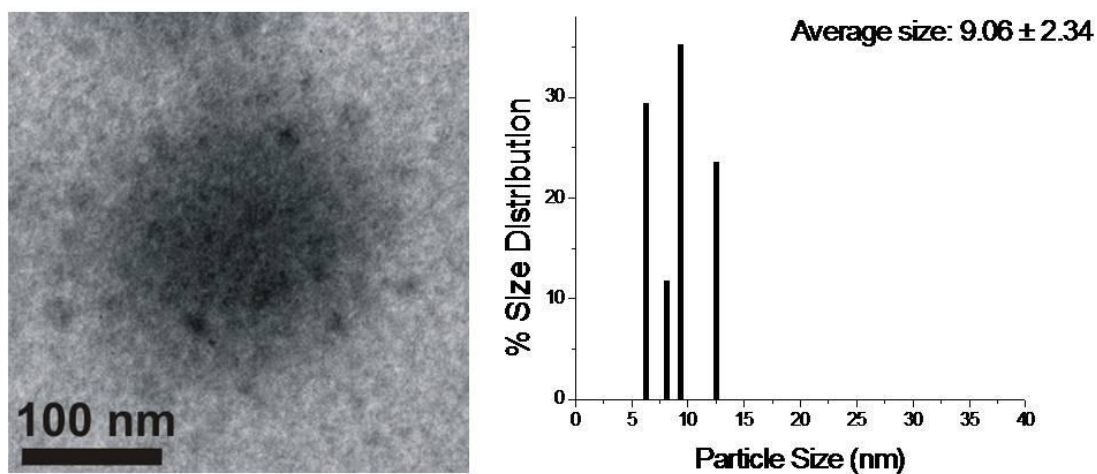


Figure 4.22 Single composite particle containing AuNPs in PNIPAm/PEI template synthesized at 25 °C, pH 3, 250 rpm, 2 hrs. reaction with N/Au mole ratio = 28.5.

Figure 4.23 shows TEM images of gold composite particles synthesized at pH 5. The average size of these particles is 224.36 ± 24.17 nm. At this condition, Au nanoparticles are more visible outside the microgel template compared to the one inside them. These gold nanoparticles have an average size of 13.10 ± 4.39 (Figure 4.24). The gold nanoparticles are bigger compared to the ones synthesized at pH 3.35.

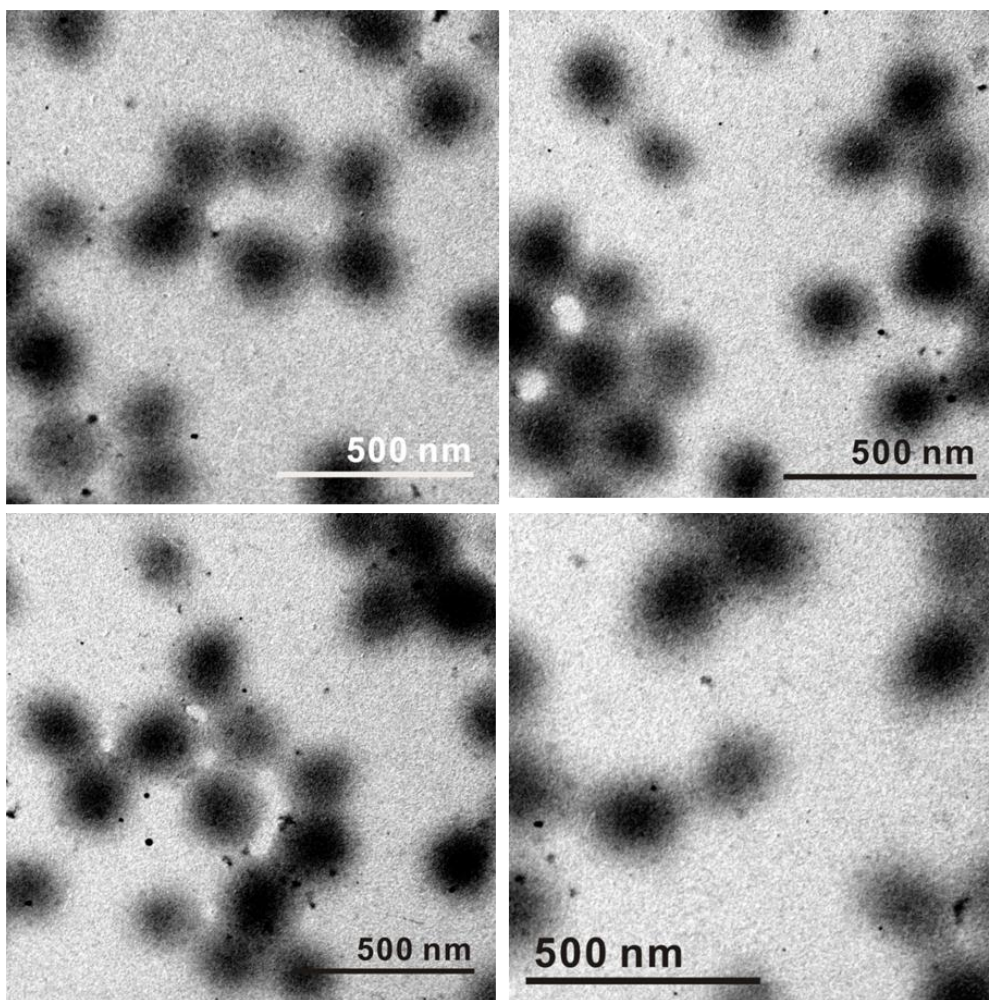


Figure 4.23 TEM images of Au nanoparticles in PNIPAm/PEI template synthesized at pH 5, 25 °C, 250 rpm, 2 hours reaction with N/Au mole ratio = 28.5.

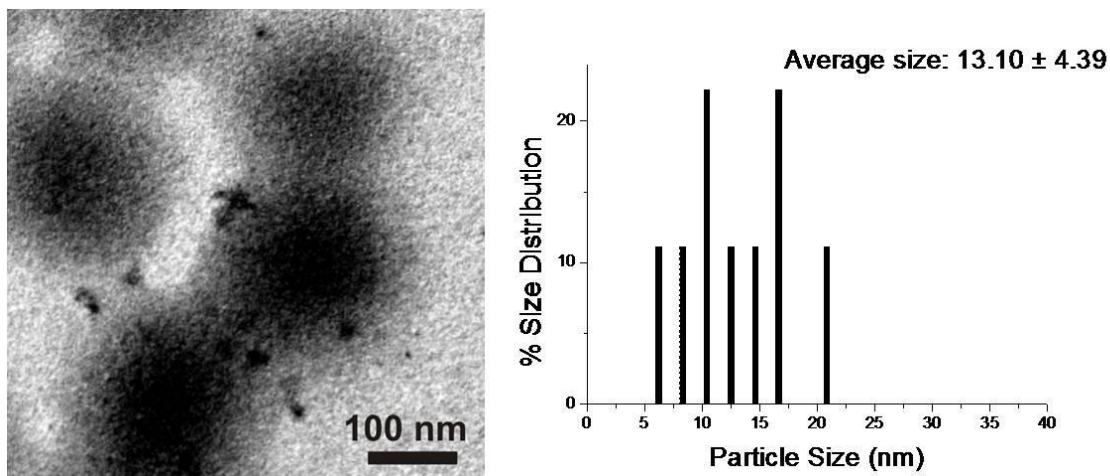


Figure 4.24 Single composite particle containing AuNPs in PNIPAm/PEI template synthesized at 25°C, pH 5, 250 rpm, 2 hrs. reaction with N/Au mole ratio = 28.5.

The synthesis of Au nanoparticles using PNIPAm/PEI microgel at pH 7 is shown in Figure 4.25. The average size of these composite particles is 226.67 ± 31.21 nm. At this condition, most if not all of the gold nanoparticles are encapsulated within the microgels or close to its surface. The gold nanoparticles forming in a single microgel were measured to have an average size of 15.78 ± 4.26 (Figure 4.26).

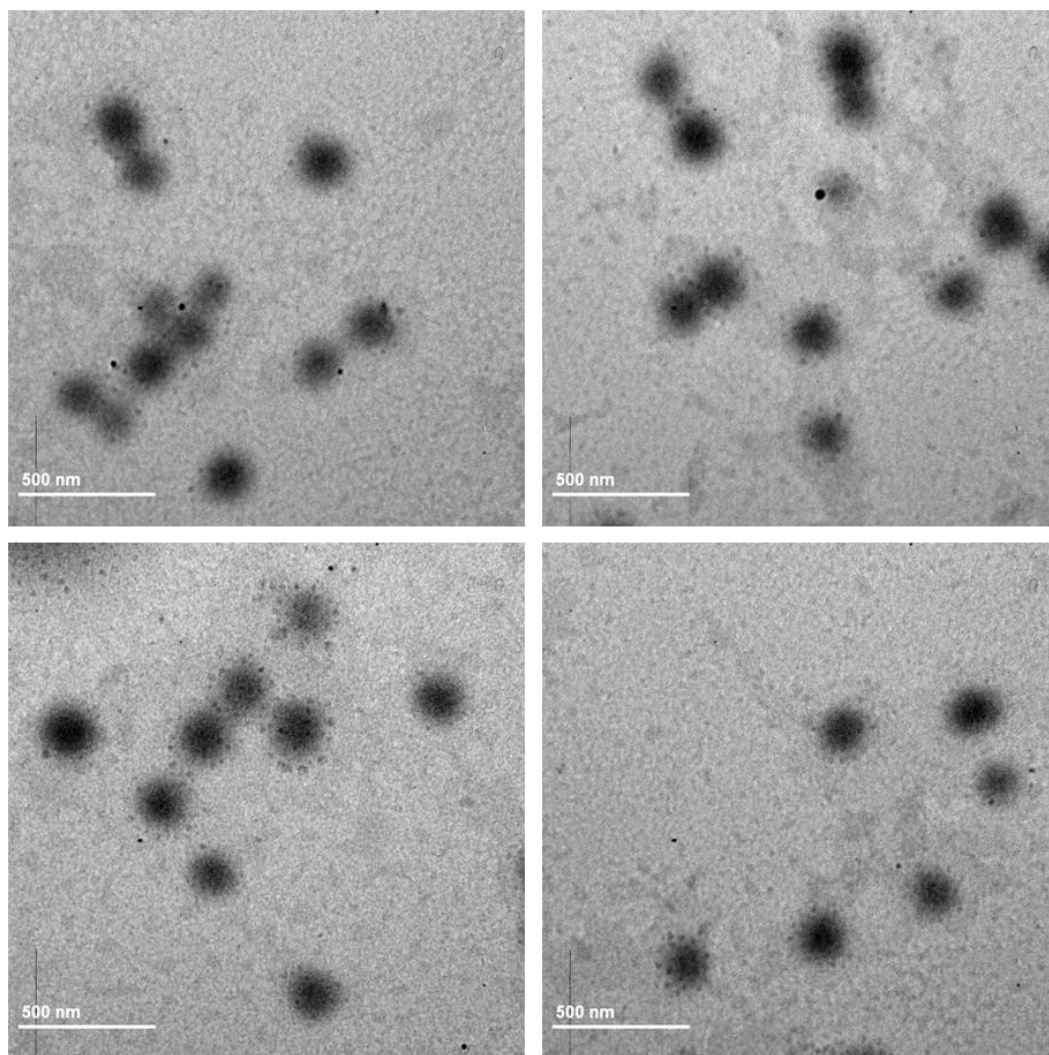


Figure 4.25 TEM images of Au nanoparticles in PNIPAm/PEI microgels synthesized at pH 7, 25 °C, 250 rpm, 2 hrs. reaction with N/Au mole ratio = 28.5.

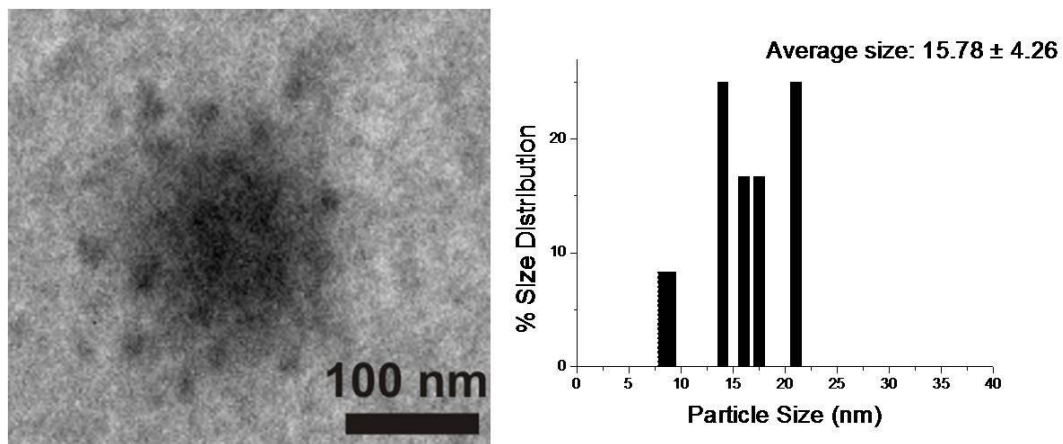


Figure 4.26 Single composite particle containing AuNPs in PNIPAm/PEI template synthesized at 25°C, pH 7.30, 250 rpm, 2 hrs. reaction with N/Au mole ratio = 28.5.

The synthesis of Au nanoparticles using PNIPAm/PEI microgel at pH 9 is seen in Figure 4.27. The average size of these composite particles is 236.76 ± 61.98 nm. At this condition, most if not all of the gold nanoparticles are encapsulated within the microgel or close to its surface. The gold nanoparticles forming in a single microgel were measured to have an average size of 15.11 ± 6.57 nm (Figure 4.28).

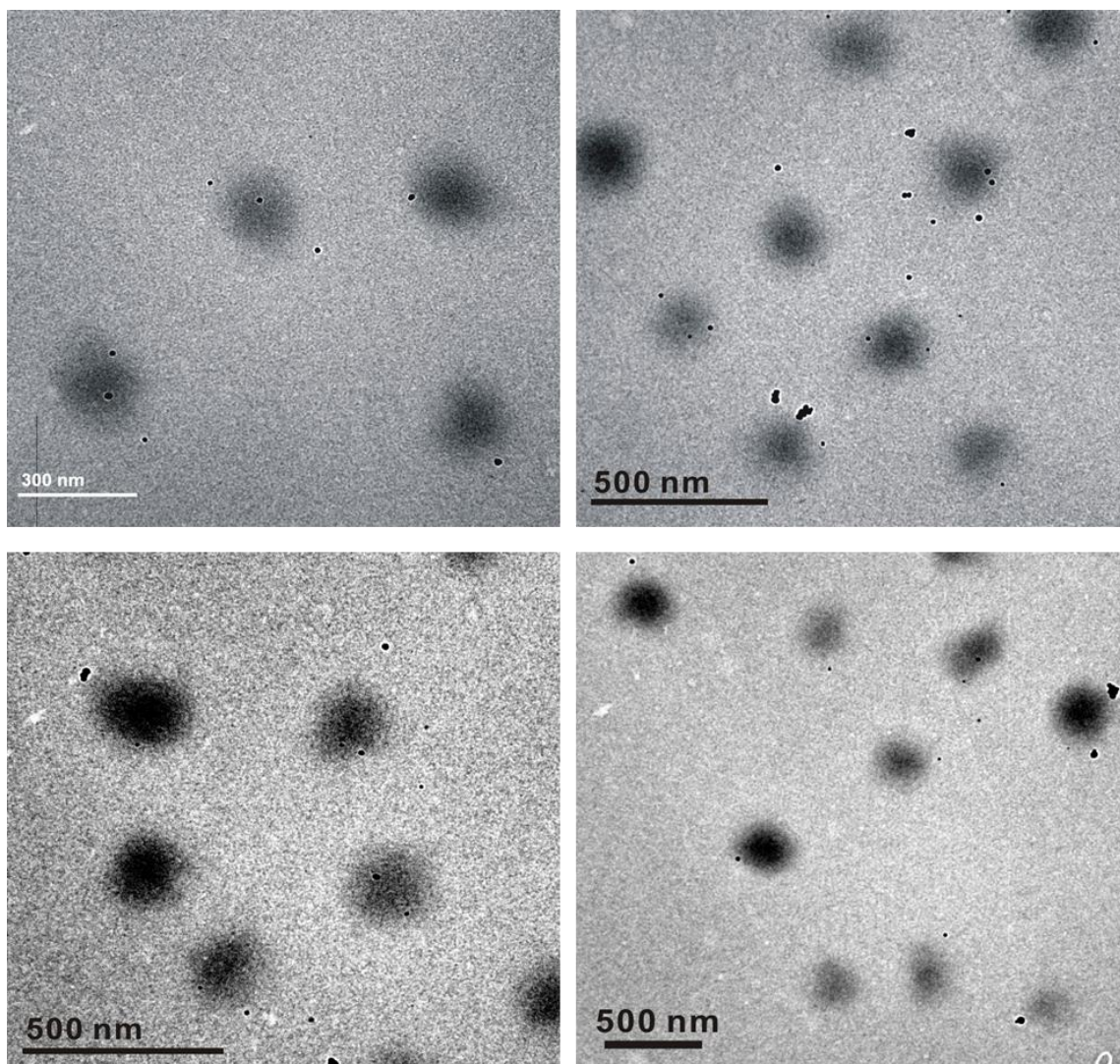


Figure 4.27 TEM images of Au nanoparticles in PNIPAm/PEI microgels synthesized at pH 9, 25°C, 250 rpm, 2 hours reaction with N/Au mole ratio = 28.5.

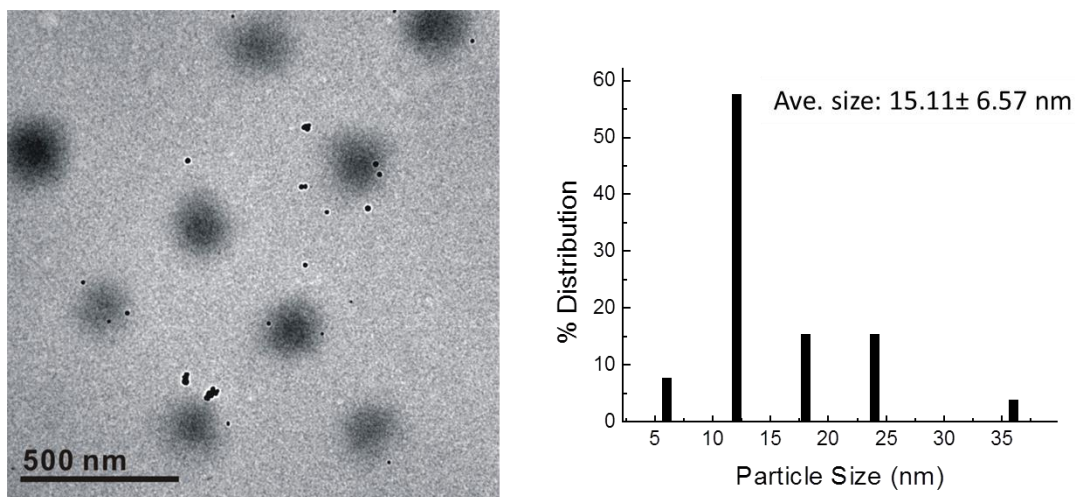


Figure 4.28 Single composite particle containing AuNPs in PNIPAm/PEI template

synthesized at 25°C, pH 9, 250 rpm, 2 hours reaction with N/Au mole ratio = 28.5.

The synthesis of Au nanoparticles using PNIPAm/PEI microgel at pH 12 is seen in Figure 4.29. The average size of these composite particles is 228.69 ± 41.66 nm. At this condition, most if not all of the gold nanoparticles are encapsulated within the microgel or close to its surface. The gold nanoparticles forming in a single microgel were measured to have an average size of 15.44 ± 2.38 nm (Figure 4.30).

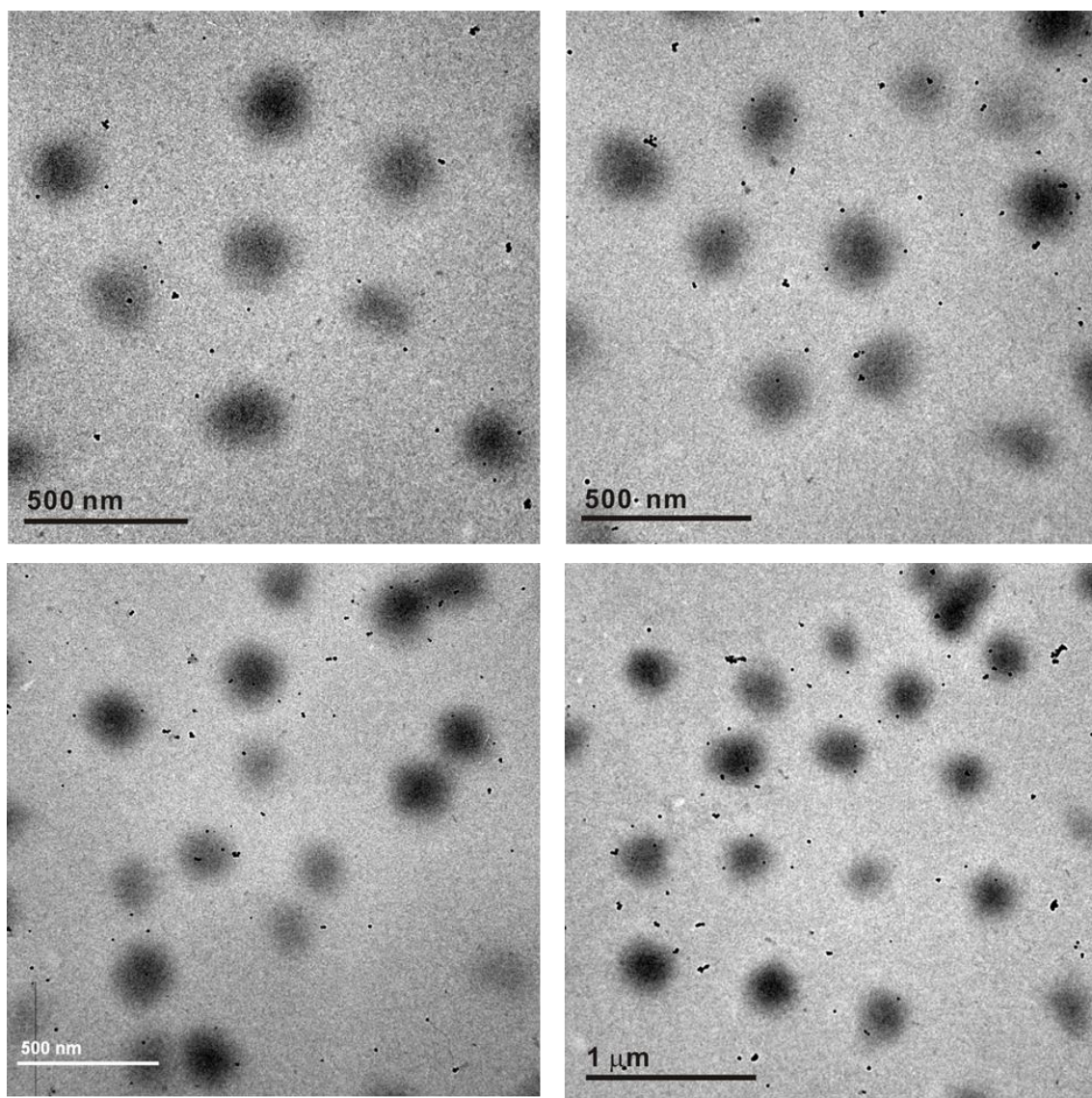


Figure 4.29 TEM images of Au nanoparticles in PNIPAm/PEI microgels synthesized at pH 12, 25°C, 250 rpm, 2 hours reaction with N/Au mole ratio = 28.5.

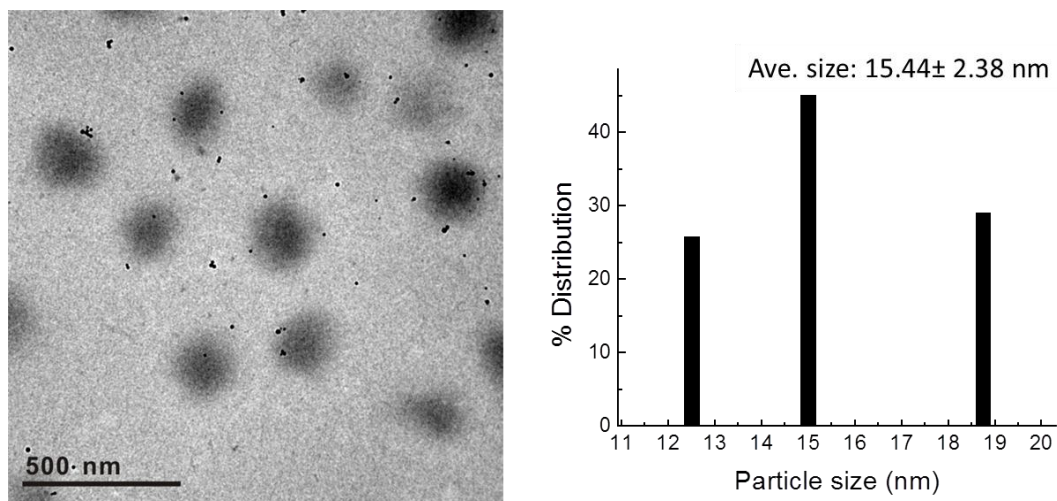


Figure 4.30. Single composite particle containing AuNPs in PNIPAm/PEI template synthesized at 25°C, pH 12, 250 rpm, 2 hours reaction with N/Au mole ratio = 28.5

The investigated pH range from 3.-12 in the synthesis of gold nanoparticles using a PNIPAm/PEI microgel template is summarized in the TEM images of Figure 4.31. These images revealed that Au nanoparticles were formed using the microgel template in all pH conditions. Gold nanoparticles are formed around the microgel shell regions. The formation of gold nanoparticles in the core-shell microgels was a result of a series of chemical reactions occurring mainly in the PEI shell region. However, judging from the five different pH synthesis conditions, it was clearly obvious that at pH 7, most if not all of the Au nanoparticles formed are encapsulated within the microgel template. Thus, pH 7 was considered to be the optimum pH condition in the synthesis of Au nanoparticle / (PNIPAm/PEI) composite particles.

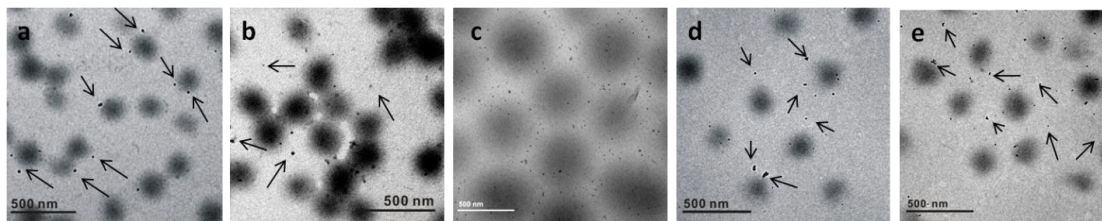


Figure 4.31 TEM images of Au/ (PNIPAM/PEI) composite particles synthesized in different solution pH a) 3, b) 5, c) 7 d) 9, e) 12. All were carried out at 25°C and 250 rpm, $N/Au^{3+} = 28.5$.

4.3.1.2 pH-Dependent formation of composite particles

The main reason for the favorable formation of gold nanoparticles at neutral pH and its immobilization is the balanced availability of the protonated amine and the amino groups in the microgel template. The protonated amino group is responsible for providing the electrostatic attraction of gold ions into the microgel. The amino group, on the other hand, is responsible for the reduction of gold ions to gold nanoparticles. The more amino group it possesses, the more is its chance to generate gold nanoparticles. As the solution pH is decreased, protonation increases and thus lowering the amino group availability. Although there is a strong interaction of gold ions and the protonated amino group, formation of gold nanoparticles is compromised. This is due to the very less availability of the reducing agent, which is the amino group. However, at higher pH such close to neutral, the microgel is less cationic and thus has a higher degree of amino groups. Higher degree of amino groups may create a more favorable formation of gold

nanoparticle, but is limited to the gold ions attracted by the protonated amine group. When pH is close to its isoelectric point, such as pH 9.5, surface charge density is near zero, thus the system become unstable due to lack of electrostatic repulsion. Figure 4.29 demonstrates the degree of protonation of the polyethyleneimine in different solution pH^[171]. This figure supports the optimum pH solution condition for the synthesis of Au nanoparticles in PNIPAm/PEI. To synthesize gold nanoparticles using the microgel template, there should be a balance between the protonated amine to attract gold ions as well as stabilize the resulting composite particles and the availability of amino groups to form gold nanoparticles. In this experiment, solution pH 7 satisfies this balanced condition and thus considered to be the optimum pH value.

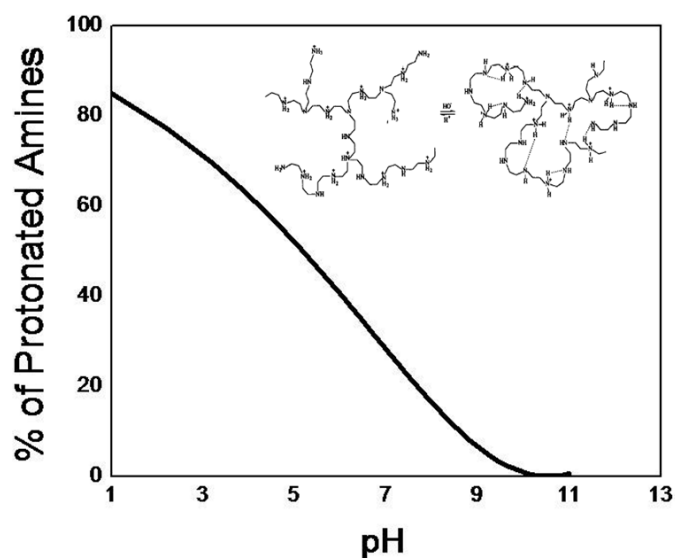


Figure 4.32 Degree of protonated amines versus solution pH. Insert is the structure conformation of the PEI during protonation and deprotonation.

4.3.1.3 Comparison of kinetics of gold nanoparticle formation in microgel under different pH conditions

The chemical reactivity of PNIPAm/PEI microgel template to form composite particles at different solution pHs was examined. Since the reduction of gold ions to zero-valent gold nanoparticles is through the free electrons transfer process from amino groups to gold ions, the degree of amine protonation would affect the concentration of amine functional group and the compactness of the shell due to the electrostatic repulsion.

Results shown in Figure 4.33 indicate that reduction rate of the gold ions to gold nanoparticles with microgel template increased with increasing solution pH. These results may be attributed to the following two main reasons:

- 1) Decreasing the solution pH increases the degree of protonation, thus reducing the number of available amine group for reduction. Therefore, the reaction rate is lowered.
- 2) A lower solution pH leads to a higher degree of amine protonation, thus enhancing charge repulsion between the PEI chains. As a result, the template size becomes larger. The expansion of the template leads to lowering the number of amine functional group in a given area, thus the reaction rate is reduced.

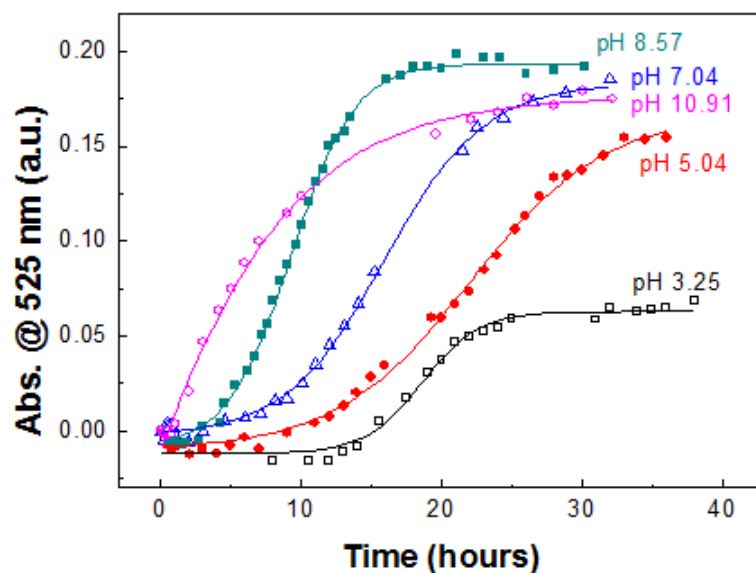


Figure 4.33 Kinetic comparison of gold nanoparticle formation in different pH

conditions of microgel template. (Conditions: [microgel] = 400 ppm; molar ratio of N/Au³⁺ = 28.5; 200 rpm at 20 °C)

Although higher pH conditions (i.e. pH 10.91 and 8.57) gave the highest kinetic rates, precipitation was evident after few days of stirring. The same phenomenon was observed at lower pH (i.e. pH 5 and 3.25) conditions. At extreme solution pHs (i.e. too low or too high pH) composite particles become very unstable where precipitation can occur. Thus, it is safe to conclude that the optimum pH condition in the formation of gold nanoparticles using PNIPAm/PEI is near neutral (i.e. pH 7.04).

4.3.2 Effect of solution temperature

Variation of solution temperature would affect the gold nanoparticle formation in the following two aspects:

- 1) Since PNIPAm/PEI microgel template is temperature-sensitive, varying solution temperature would affect the the gold nanoparticle formation and the stability of the composite particles.
- 2) The nucleation and growth of gold nanoparticles is dependent on the temperature^[160], which also dictates the size and shapes of nanoparticles formed^[161].

In this study, a systematic study of temperature effect on the synthesis of Au nanoparticles was conducted through the use of multifunctional microgel as template. Temperatures such as 5, 15, 25, 30, 35, and 45°C were investigated in the synthesis of gold nanoparticles and its composite materials.

4.3.2.1 Characterization using electron microscopies

Figure 4.34 shows the TEM images of Au nanoparticles/(PNIPAm/PEI) particles synthesized at 5 °C. In this image, both the microgel template and Au nanoparticles are seen. Au nanoparticles are those high intensity aggregated black dots formed in clusters. Microgel templates are seen in gray blurry circles in the background. The average size of the composite particles is 172 ± 41.74 nm, which is basically the size close to the original microgel template itself. The Au nanoparticles are obviously not being

encapsulated within the PNIPAm/PEI microgel template, instead they formed outside the microgels. Since naked particles are unstable in water, they tend to aggregate and form larger particles. These aggregated that Au nanoparticles were a product of individual spherically structured particles grouped together as seen in this figure.

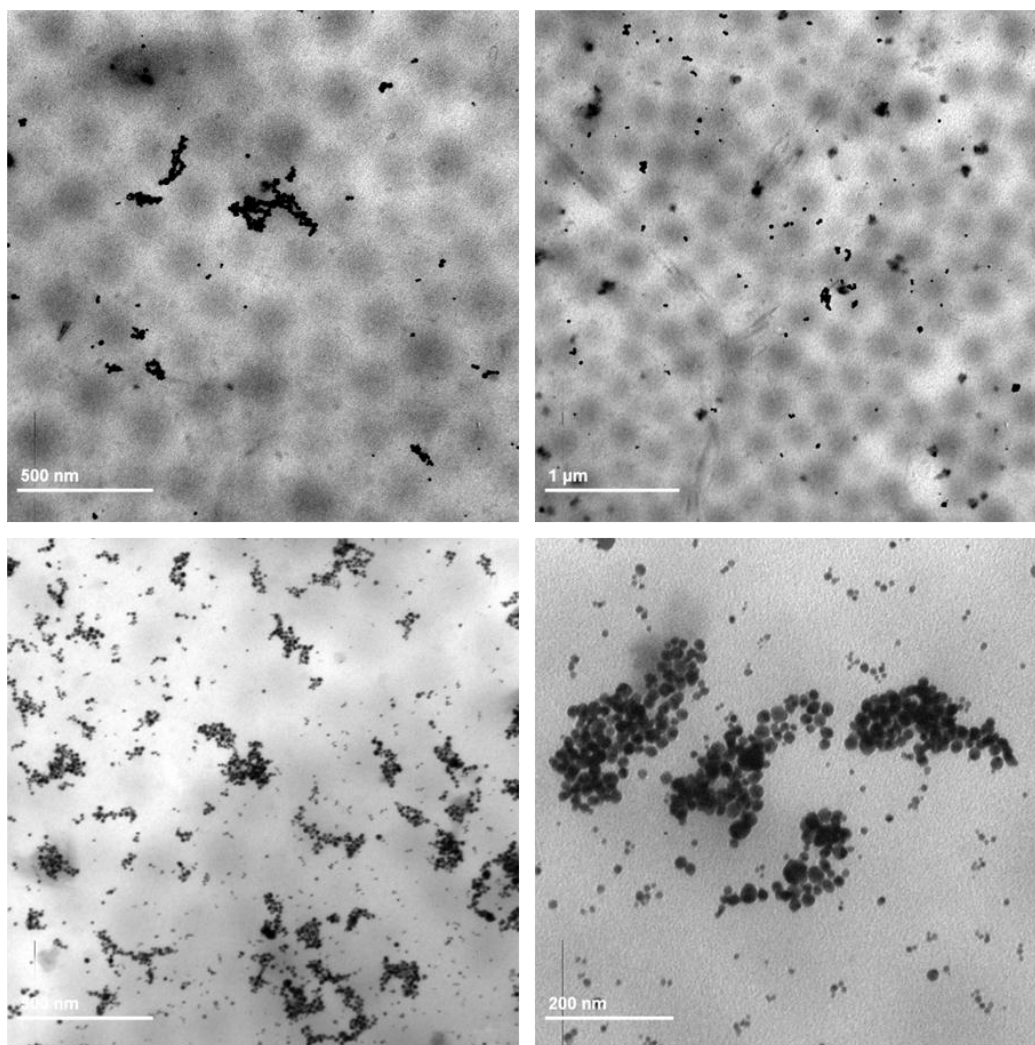


Figure 4.34 TEM images of Au nanoparticles in PNIPAm/PEI microgels synthesized at 5 °C, pH 7.0, 250 rpm, 2 hours reaction with N/Au mole ratio = 28.5.

Taking a closer look on the Au nanoparticle size distribution, a TEM image is shown in Figure 4.35. This image of a composite particle contains Au nanoparticles in a single microgel. The average size of the gold nanoparticles is 43.37 ± 18.57 nm. Although these Au nanoparticles are not seen as aggregate, they can be a product of Ostwald ripening that resulted to a bigger nanoparticle size. This phenomenon spontaneously occurs because larger particles are more energetically favored than smaller particles. This happens when free molecules in solution are supersaturated condense into larger particles. Such system was also observed in the study of Gubicza *et al.* ^[162], wherein degradation of the CTAB capped gold nanoparticles released small gold nanoparticles into solution and grows into larger particles.

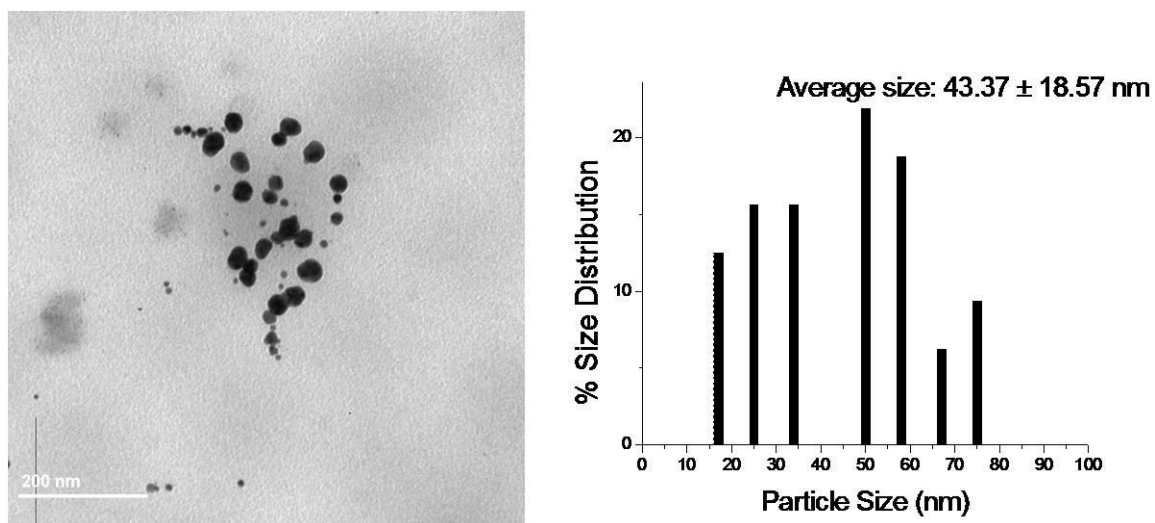


Figure 4.35 Single composite particle containing AuNPs in PNIPAm/PEI template synthesized at 5°C, pH 7.0, 250 rpm, 2 hrs. reaction with N/Au mole ratio = 28.5.

Figure 4.36 exhibits the TEM images for Au nanoparticle/(PNIPAm/PEI) composite particles synthesized at 15 °C with an average size of 285.66 ± 66.85 nm. High intensity black particles represent Au nanoparticles formed while microgels are seen in the background. Very few of the Au nanoparticles are inside the microgels, but most of them are obviously not encapsulated within the core-shell microgels. Most of the Au nanoparticles formed in small clusters or aggregates. The effect of temperature on the Au nanoparticle is more or less the same with that composite particles synthesized at 5 °C. However, there is an increase in the average size of the composite particles compared to the ones synthesized in 5 °C. Although the Au nanoparticles are still formed into clusters, they are now grouped into smaller clusters or aggregates (e.g. 2-5 Au nanoparticles) as compared to the ones synthesized at 5 °C.

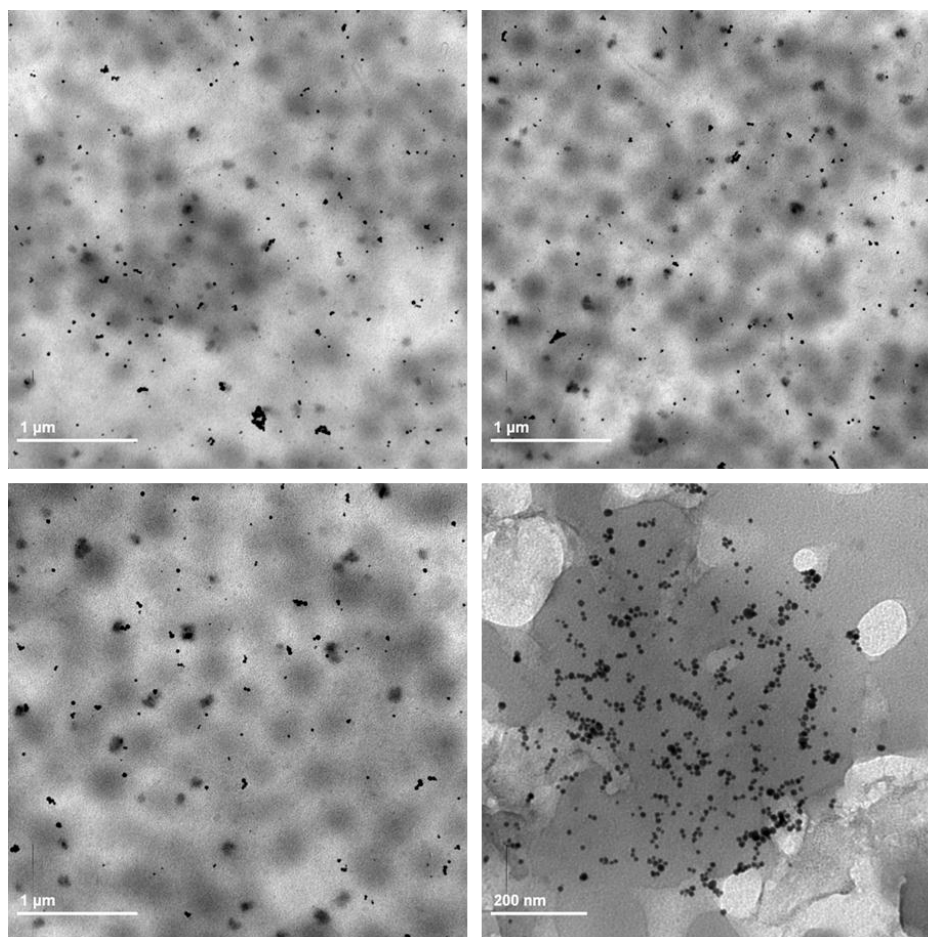


Figure 4.36 TEM images of Au nanoparticles in PNIPAm/PEI microgels synthesized at 15 °C, pH 7.0, 250 rpm, 2 hrs. reaction with N/Au mole ratio = 28.5.

Figure 4.37 gives a separate image of some microgel templates with Au nanoparticles synthesized at the same temperature of 15 °C. The Au nanoparticles are at average size of 9.21 ± 3.14 nm with spherical morphology. These Au nanoparticles are smaller than the previously formed at 5 °C.

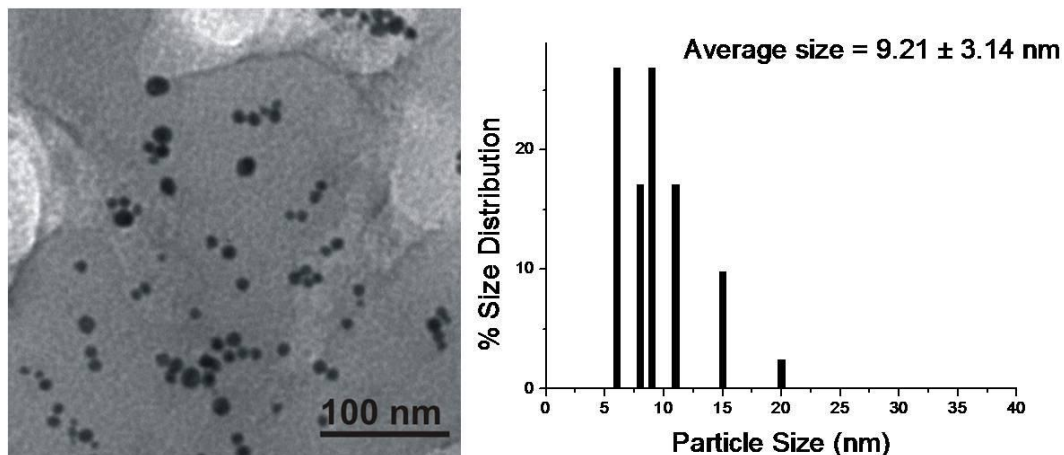


Figure 4.37 Au nanoparticle formation using PNIPAm/PEI template. The reaction took place at 15°C, pH 7.0, stirring at 250 rpm for 2 hours. N/Au mole ratio = 28.5.

Figure 4.38 shows the image of the Au nanoparticle/(PNIPAm/PEI) particle synthesized at 25 °C. The Au nanoparticles are in slightly blurry dots that are surrounding the PNIPAm/PEI microgels. These images are totally different from the previous two temperatures (5 °C and 15 °C). The Au nanoparticles are clearly encapsulated within the shell region of the microgels. Thus, they are all in blurry or fuzzy image. The average size of the composite size is 270.06 ± 90.83 nm with highly monodispersity.

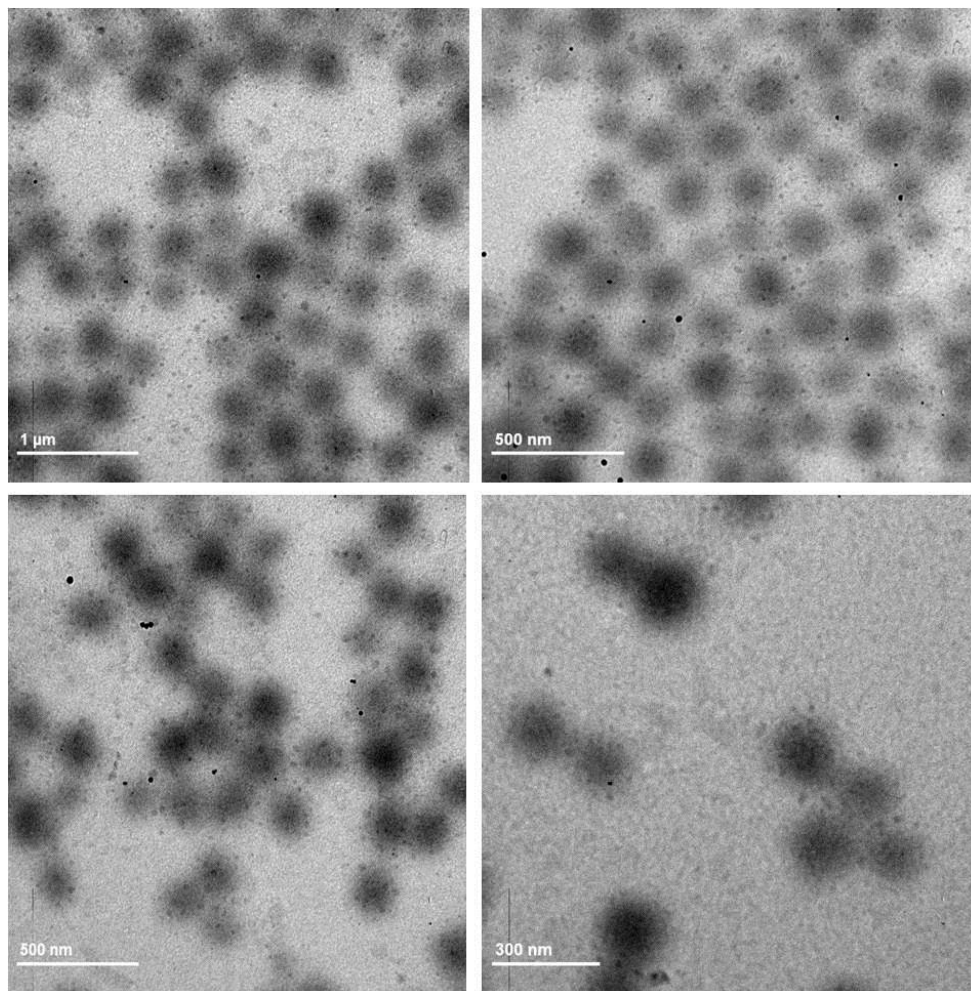


Figure 4.38 TEM images of Au nanoparticles in PNIPAm/PEI microgels synthesized at 25°C, pH 7.0, stirring at 250 rpm for 2 hours. N/Au mole ratio = 28.5.

Figure 4.39 gives an image of a single composite particle with Au nanoparticle embedded within the microgel template synthesized at 25 °C. Despite of the fuzzy image of the Au nanoparticles embedded inside the microgel, the size of the Au nanoparticles was estimated to be 16.71 ± 4.97 nm.

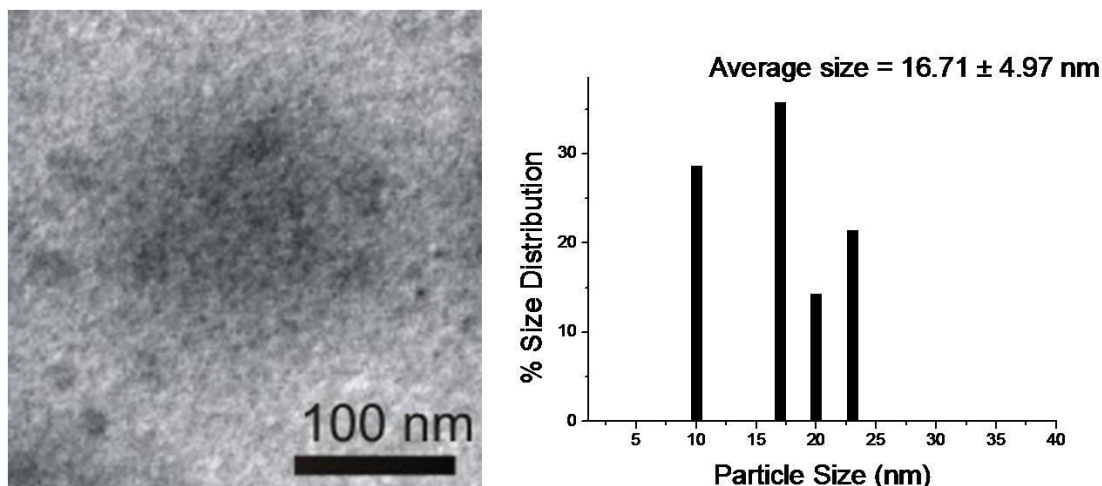


Figure 4.39 Single composite particle containing AuNPs in PNIPAm/PEI template synthesized at 25 °C, pH 7.0, stirring at 250 rpm for 2 hours. N/Au mole ratio = 28.5.

When the reaction temperature was further increased to 30 °C, the Au nanoparticle/(PNIPAm/PEI) composite particles generated at this temperature is depicted in Figure 4.40. Most of the Au nanoparticles formed are within the surrounding of the microgel's shell regions. However, the Au nanoparticles are not obviously embedded or immobilized within the shell region. Based on the color intensity of the Au nanoparticles, they are not all inside. Some have started to get out of the microgel template and some are still intact. The average size of these composite particles was estimated at 240.89 ± 48.94 nm.

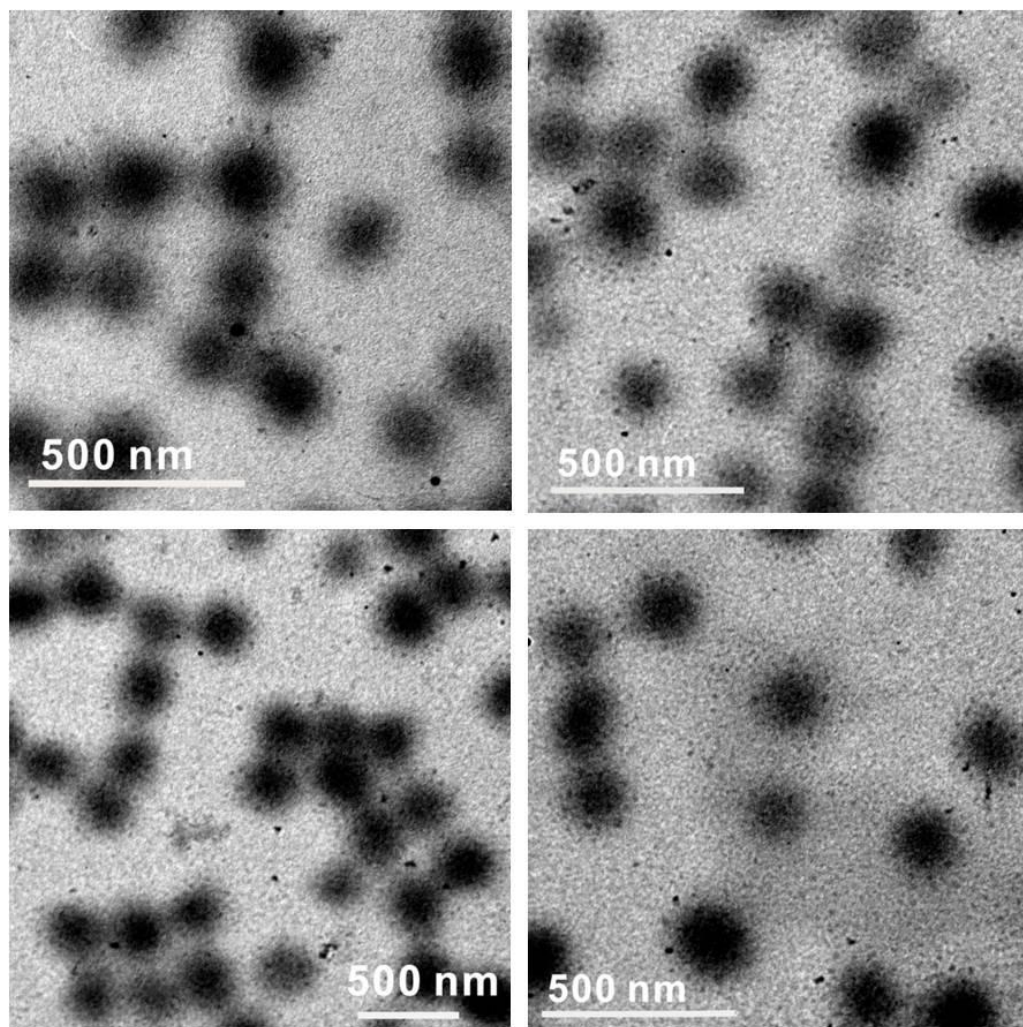


Figure 4.40 TEM images of Au nanoparticles in PNIPAm/PEI microgels synthesized at 30 °C, pH 7.0, stirring at 250 rpm for 2 hours. N/Au mole ratio = 28.5.

Figure 4.41 shows the image of a single composite particle synthesized at 30 °C. Again, this composite particle is composed of both the microgel and Au nanoparticles. The Au nanoparticles formed within the microgel are small. They are estimated at 6.80 ± 3.04 nm. These Au nanoparticles are speculated to be single particles rather than aggregates or clusters.

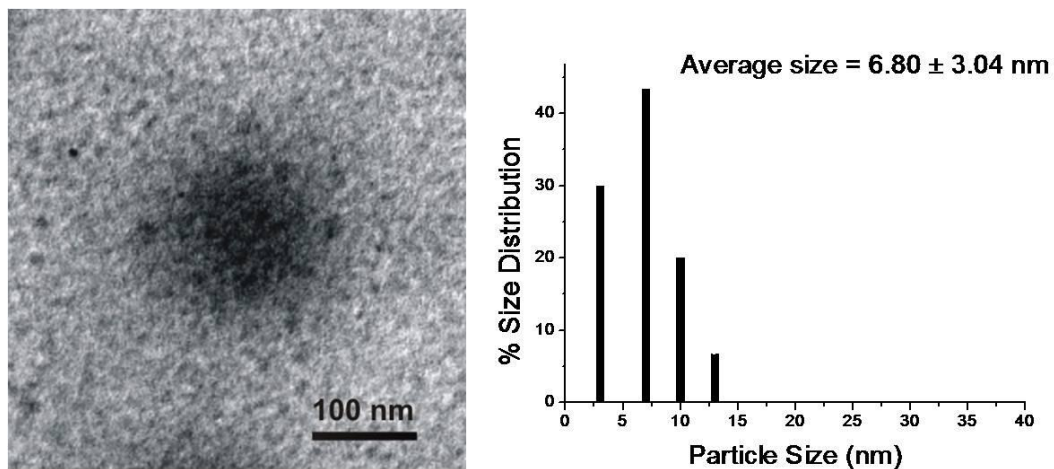


Figure 4.41 Single composite particle containing AuNPs in PNIPAm/PEI template synthesized at 30 °C, pH 7.0, stirring at 250 rpm for 2 hours. N/Au mole ratio = 28.5.

As shown in Figure 4.42, the Au nanoparticles formed during the synthesis of the composite material at 35°C have started to obviously form outside the microgel region. Although very few are still within the microgel and its surrounding, it is pretty obvious that bigger particles are starting to form outside the microgel templates. The average particle size of the composite material was estimated at 234.60 ± 24.80 nm.

Since no single microgel is seen with surrounding Au nanoparticles, Au nanoparticle size was based on those randomly located in the TEM images. The Au nanoparticle size average was estimated at 16.07 ± 9.49 nm as seen in Figure 4.43 with a wide size distribution range.

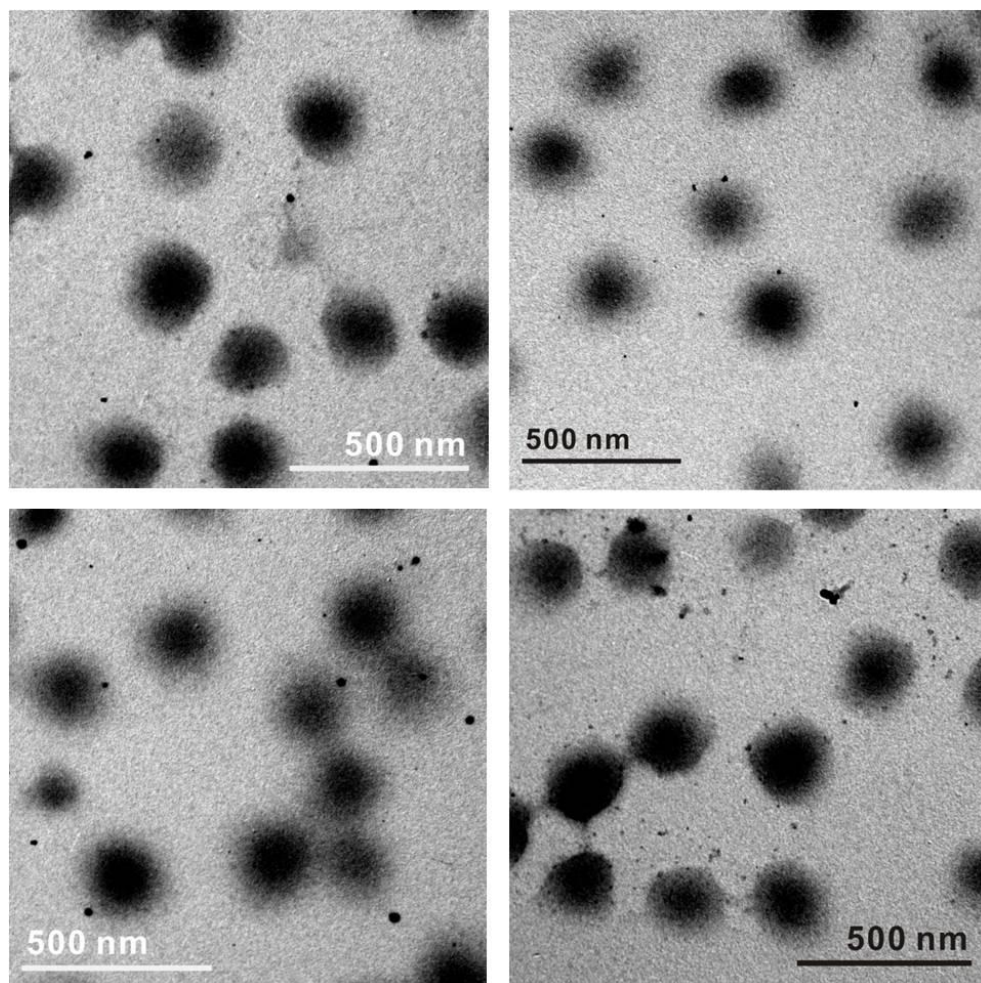


Figure 4.42 TEM images of Au nanoparticles in PNIPAm/PEI microgels synthesized at 35 °C, pH 7.0, stirring 250 rpm for 2 hours. N/Au mole ratio = 28.5.

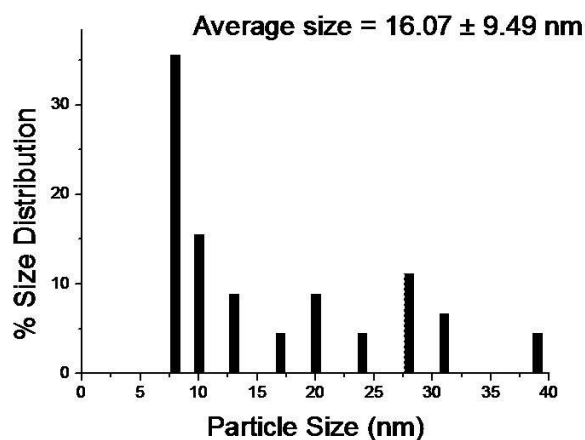


Figure 4.43 Particle size distribution of AuNPs in PNIPAm/PEI template synthesized at 35°C.

When the reaction took place at even higher temperature such as 45 °C (Figure 4.44), the formation of larger size of Au nanoparticles outside the microgels are very obvious. Few of the Au nanoparticles are anchored within the microgel template. It is pretty obvious that the ones outside the microgel template are bigger than the ones inside them. The composite particles are estimated with an average size of 231.05 ± 12.80 nm. Au nanoparticles were also measured based on the same TEM image and were plotted with size distribution (Figure 4.45). The average gold nanoparticle produced under this condition was estimated to have an average of 15.69 ± 8.50 nm in size.

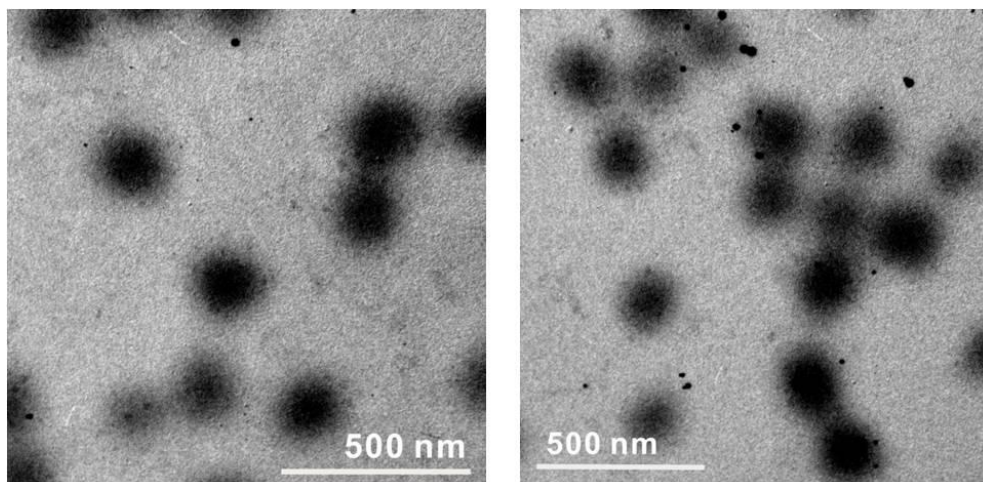


Figure 4.44 TEM images of Au nanoparticles in PNIPAm/PEI microgels synthesized at 45 °C, pH 7.0, stirring at 250 rpm for 2 hours. N/Au mole ratio = 28.5.

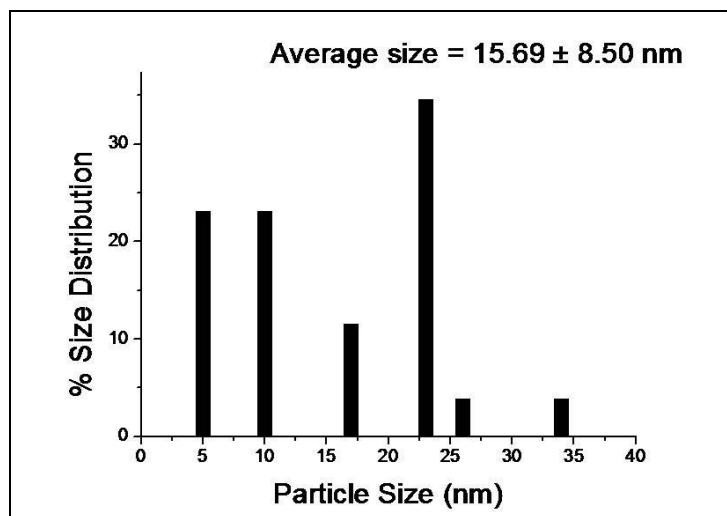


Figure 4.45 Particle size distribution of AuNPs in PNIPAm/PEI template synthesized at 45 °C, pH 7.0, stirring at 250 rpm for 2 hours. N/Au mole ratio = 28.5.

4.3.2.2 Temperature dependent formation of composite particles

The effect of temperature in the synthesis of the gold/polymeric composite particles can be observed in Table 4.1. The reaction temperatures are arranged in increasing pattern. However, the resulting gold nanoparticle size seems to have no particular correlation with the temperature. Results suggest that even at low temperature, such as 5 °C, gold nanoparticles were still able to form, indicating high chemical reactivity of the template in reducing gold salts.

Table 4.1 Synthesis temperature and its corresponding average gold nanoparticle size.

Synthesis Temperature (°C)	Ave. particle size (nm)
5	43.4±18.6
15	9.2±3.1
25	16.7±4.9
30	6.8±3.0
35	16.0±9.8
45	15.7±8.5

Based on the TEM images, it is obvious that the reaction temperature considerably affects the resulting composite particles.. The gold nanoparticles can be either located at the microgel shell or outside the microgel template. The main driving

force of this phenomenon can be related to the conformational changes of the microgel template when subjected to temperature.

To better compare the morphologies of particles obtained at different reaction temperature, representative TEM images from 5 to 45°C are summarized in Figure 4.46. At low temperature such as 5 °C, Au nanoparticles are visible, mostly outside the microgels. They are in high intensity of black dots. The Au nanoparticles appear to be aggregated due to lack of stabilizing agent. A similar phenomenon was observed with increasing reaction temperature to 15 °C. At this low temperature range, it is quite surprising that Au nanoparticles were formed. This is attributed to the efficient reduction of the gold ions in the microgel network. However, at low temperature, the core-shell microgels are at its fully swollen state owing to the hydrophilicity of the core and the shell regions of the microgel. At swollen state, the PEI shell layer behaves like a loose network where resulting Au nanoparticles could easily escape from the shell. Once detached from the shell, they tended to aggregate and form larger clusters due to their instability.

When the reaction temperature was raised to 25°C, most of Au nanoparticles generated were encapsulated by the microgel as shown in Figure 4.46c. At 30 °C, Au nanoparticles still can be observed surrounding the core-shell microgel structure, but few has started to show outside the microgel. This can be explained by the volume phase transition temperature (VPPT) of the microgel template. when approaching to VPPT of the microgel (~ 32 °C), composite particles start to shrink, leading to poorer encapsulation ability. As a result, formed Au nanoparticles would start to release from

the microgel template. Once the gold nanoparticles are released, they tend to aggregate and form larger particles. Further elevating the temperature to 35 and 45°C gave different effect. TEM images in Figure 4.46 e and f show that there are few Au nanoparticles within the microgel template. Most of them are outside with even bigger in size. When the solution temperature is above the VPTT of the microgel, the composite particle would considerably shrink, thus Au nanoparticles could be squeezed out of the microgel. Comparing those TEM images synthesized under different temperatures, it can be concluded that the 25 °C is the optimum temperature to synthesize Au Np/polymer composite particles.

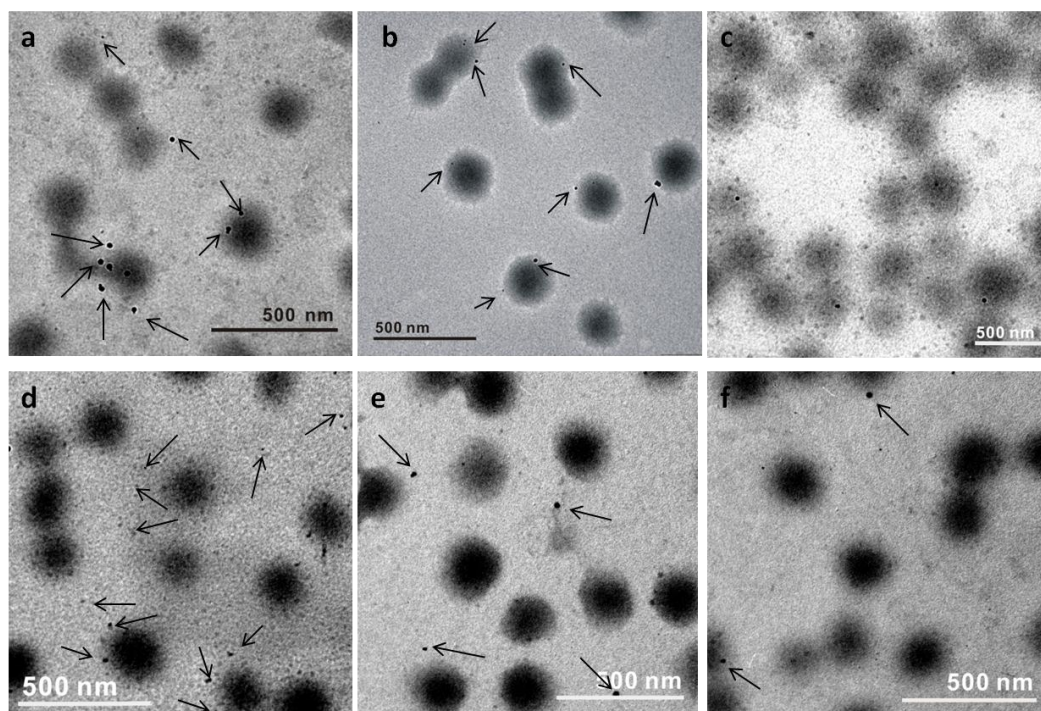


Figure 4.46 TEM Images of Au@PNIPAm/PEI in different synthesis temperature a) 5°C, b) 15°C, c) 25°C, d) 30°C, e) 35°C, f) 45°C conducted in pH 7.0, 250 rpm, 2 hours absorption with N/Au mole ratio = 28.5.

4.3.2.3 Comparison of kinetic of gold nanoparticles formation with microgels in different temperature

The temperature effect on chemical reactivity of PNIPAm/PEI microgel template was investigated through the kinetic studies. Kinetic curves of different temperature at the same pH are shown in Figure 4.47. Its inset graph is the Arrhenius plot of the highest observed reaction rate constants k in the fast nucleation stage measured at different temperatures. According to the Arrhenius Equation, the natural logarithm of reaction rate constant ($\ln k$) has a linear relationship with the negative reciprocal value of absolute temperature ($-T^{-1}$).

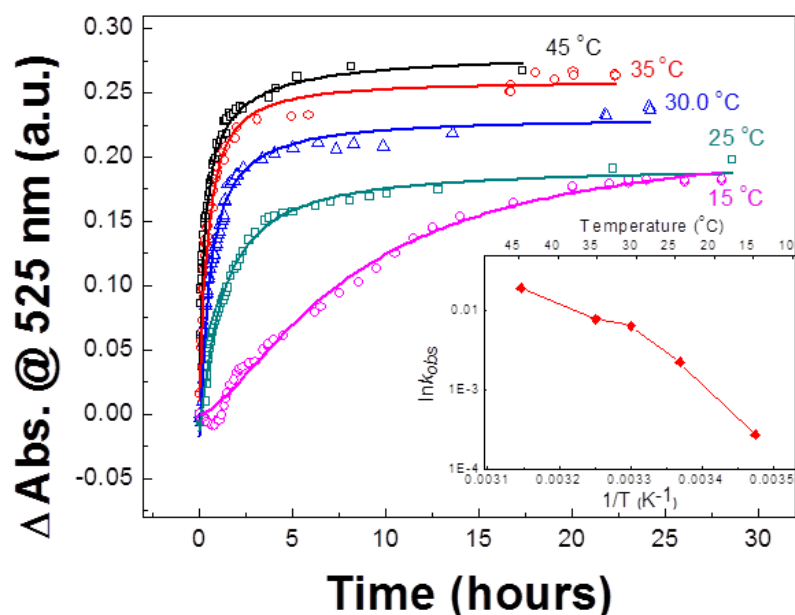


Figure 4.47 Kinetic comparison of gold nanoparticle formation in different temperature in the presence of microgel templates. Inset is the Arrhenius plot of the kinetic rate constants at different temperatures. (Conditions: [microgel] = 400 ppm; molar ratio of N/Au³⁺ = 28.5; pH 9.16, stirring rate of 200 rpm).

This figure shows that the kinetic rate of gold nanoparticle formation increases as temperature increases. However, based on the Arrhenius plot, there is an apparent turning point between 30 °C and 35°C. This could be due to the VPTT of the microgel template. At temperature above VPTT, the microgel template shrinks to a smaller size and become denser. A denser microgel template hindered the entry of gold chloride ions immensely. Since less gold chloride ions could react with the amino groups, the reduction reaction slowed down to some extent. The shrinkage of microgel template also resulted in the aggregation of formed gold nanoparticles within the composite particle shell.

In this experiment, the optimum temperature condition is not only based on the kinetic rates, but also the stability of the composite particles. Although in this experiment, the higher the temperature, the higher is the kinetic rate. However, at temperatures near or above VPTT, aggregation happens. Thus, it is safe to assume that the 25 °C reaction temperature is the optimum temperature for gold nanoparticle formation using PNIPAm/PEI template.

4.3.3 Effect of amino to gold salt ratio (N/Au)

One of the important factors to consider in synthesizing gold composite particle is the source of the gold ions and its concentration. HAuCl_4 and its hydrate form such as $\text{HAuCl}_4 \cdot 3\text{H}_2\text{O}$ are some common salts used in many experimental procedures. Gold salt dissociates in solution and becomes a precursor for gold nanoparticle formation. Concentration of the salt solution affects the formation of gold nanoparticle in terms of its size and shape, size distribution and stability in the colloidal system. In the study of Li *et al.*^[163], polydispersity and size distribution of gold nanoparticles produced through citrate reduction was dependent on the reactant concentration. Larger sizes of gold nanoparticles resulted from higher concentration of the reactants.

In this study, three different gold salt concentrations, expressed through amino to Au (N/Au) mole ratios were investigated to determine its effect on the synthesis of gold nanoparticles using the microgel template. Amino to gold (N/Au) mole ratio was used instead of the Au salt concentration as a variable factor. The ratio was necessary to indicate that the gold ions were reduced through the amine functionality of the microgel template. It is the amine, specifically the primary amines necessary for the reduction of gold ions to gold nanoparticles. The amino to gold ratios used in this study were 28.5, 14.30 and 9.50. This means that in all three ratios, excess amino were used. The higher the ratio, the higher is the amino content. The lower the ratio, the higher is the gold salt concentration. Other synthesis conditions such as pH, temperature and stirring rate were kept the same conditions.

4.3.3.1 Characterization of particle morphology using electron microscopies

An Au composite particle synthesized with a mole ratio of 28.5 is shown in Figure 4.48. This type of composite has been shown in the previous TEM images. In this figure, the microgel template is surrounded with Au nanoparticles. The average Au nanoparticle size is 17.40 nm with a narrow size standard deviation of 2.34 nm. All the Au nanoparticles produced were in spherical shape or spherical-like particles in general.

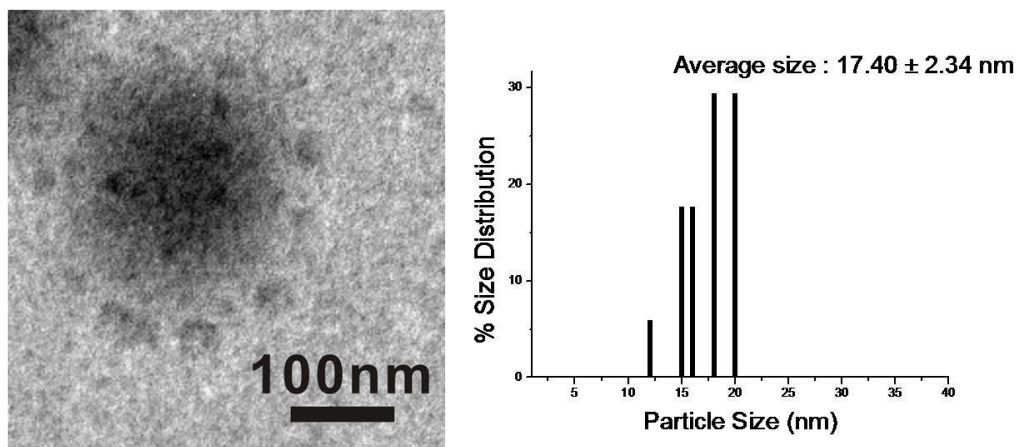


Figure 4.48 Image of the single composite particle synthesized at 25 °C, pH 5.6, stirring at 200 rpm for 24 hours. The N/Au mole ratio = 28.5.

Figure 4.49 shows TEM images of the Au composite particles with a mole ratio of 14.30. When the mole ratio was reduced, Au composite particles were reduced and kept them within its microgel template. As observed in this image, Au nanoparticles are well in tact within the perimeters of the PNIPAm/PEI template. Almost the same image can be observed with the image of 28.50 ratio. However, in this case, microgel template

has more Au nanoparticles attached. The microgels are denser with Au nanoparticles compared to the previous mole ratio. The spherical Au nanoparticles are sustained and maintained throughout the composite particles.

Aside from the denser microgel, the average size of the Au nanoparticles produced at this particular mole ratio of 14.30 resulted to a larger size of 21.40 nm (Figure 4.50). But then the standard deviation of 4.13 nm indicates a narrow size distribution. This also indicates that uniform Au nanoparticles were produced.

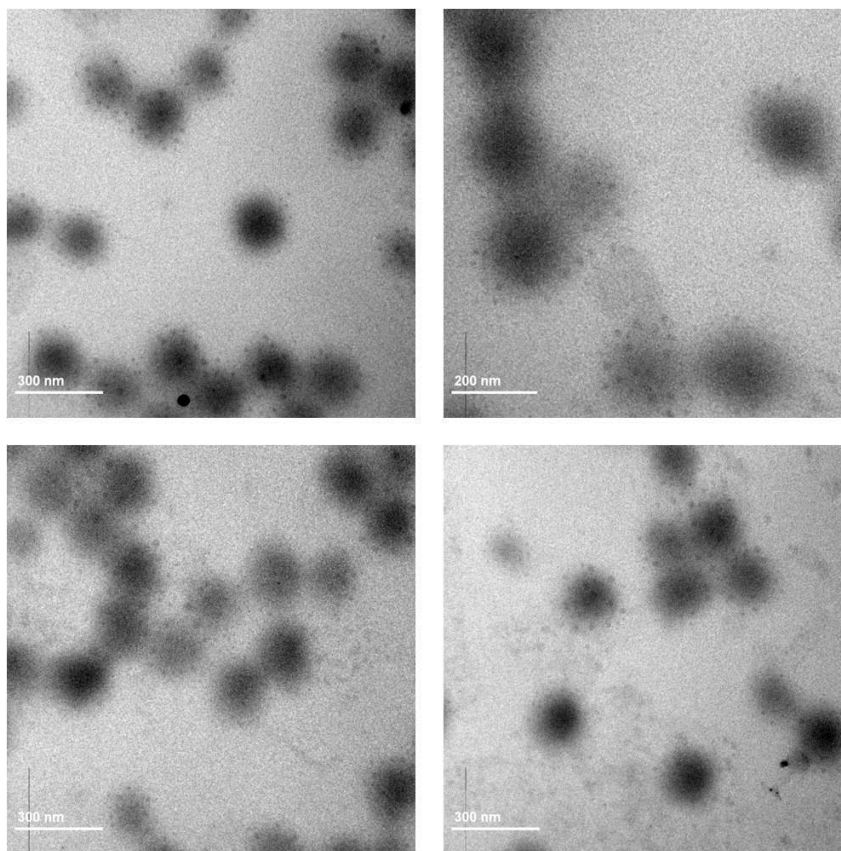


Figure 4.49 Composite particle synthesized at 25 °C, pH 5.6, stirring at 200 rpm with 24 hours reaction. N/Au mole ratio = 14.30.

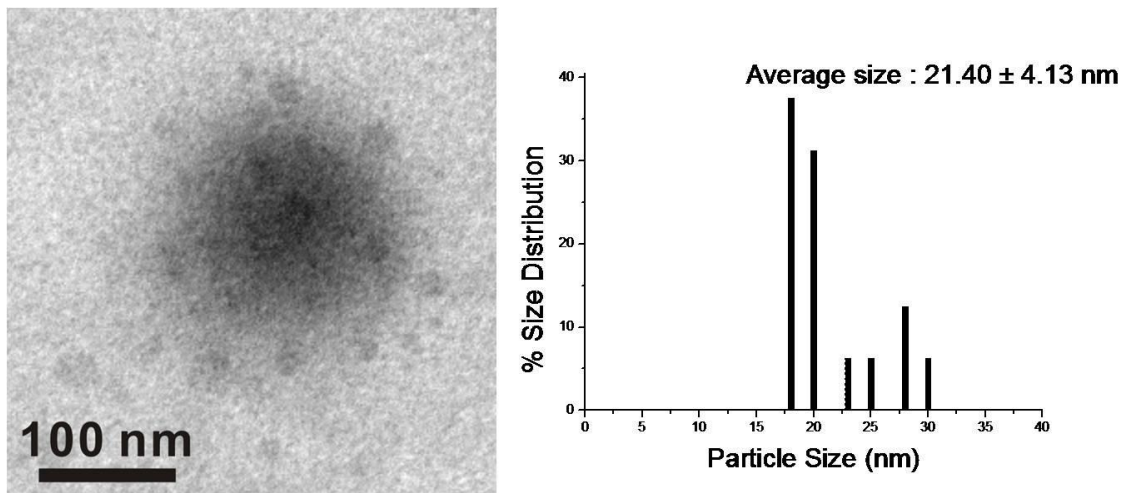


Figure 4.50 Single composite particle synthesized at 25°C, pH 5.6, 200 rpm 24 hours absorption with N/Au mole ratio = 14.30.

When the ratio was further reduced to 9.50, the result was significantly different from the previous two ratios. Figure 4.51 shows images of Au composite particles with mole ratio of N/Au= 9.50. In this image, both the Au nanoparticles and microgels are clearly revealed. The microgels are around 200 nm in diameter with spherical shape. The Au nanoparticles are in black colored specimen that randomly scattered in different locations. It is obvious that the Au nanoparticles are no longer inside the microgel templates in this case. Au nanoparticles have also evolved from the regular spherical to irregularly shaped spheres. It also showed different morphologies such as triangular, diamond shape and pentagonal. These gold nanoparticles have no special arrangement but randomly produced in the microgel template.

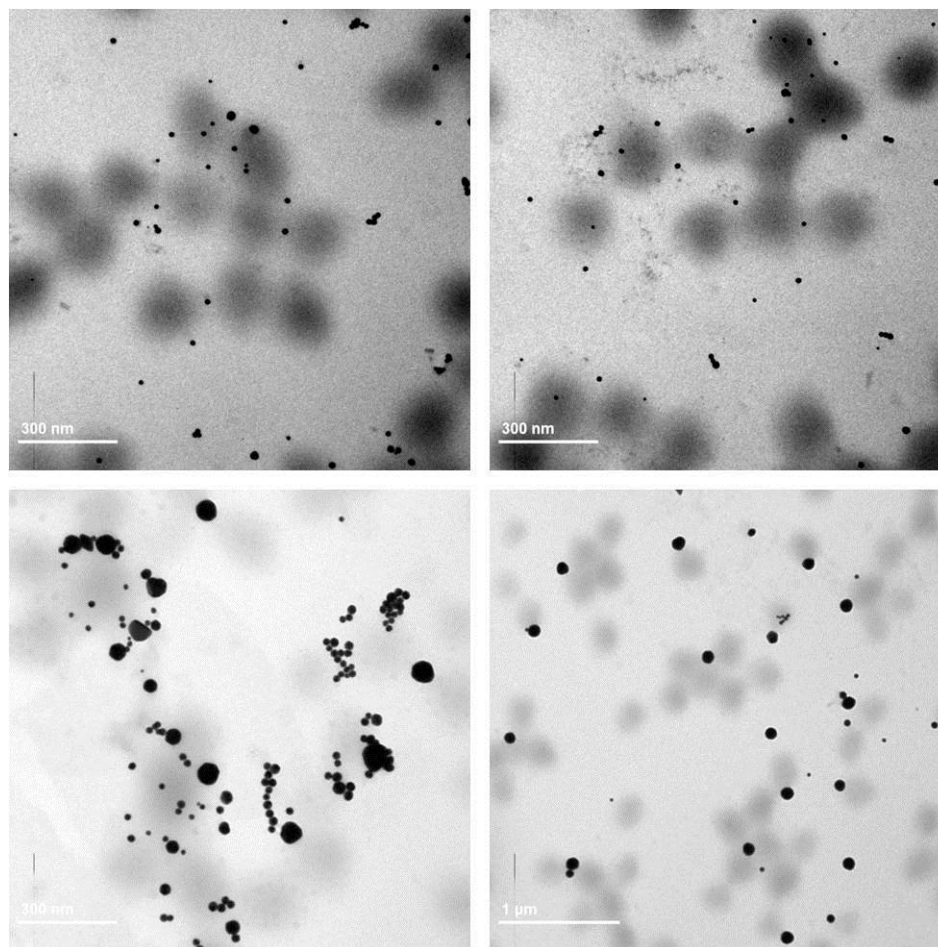


Figure 4.51 Morphology of gold nanoparticles synthesized with N/Au mole ratio = 9.50 (conditions: 25 °C, pH 5.6, stirring at 200 rpm for 24 hours).

Taking a closer look of the different morphologies of the Au nanoparticles produced in this condition (N/Au= 9.50) as shown in TEM images (Figure 4.52), spherical and spherical-like morphologies of Au nanoparticles are observed. Other well-defined morphologies also evolved, such as triangular, diamond and pentagonal shapes. Spherical Au nanoparticles produced in this condition has an average size of 30.50 nm, which is bigger than the ones produced at higher mole ratios.

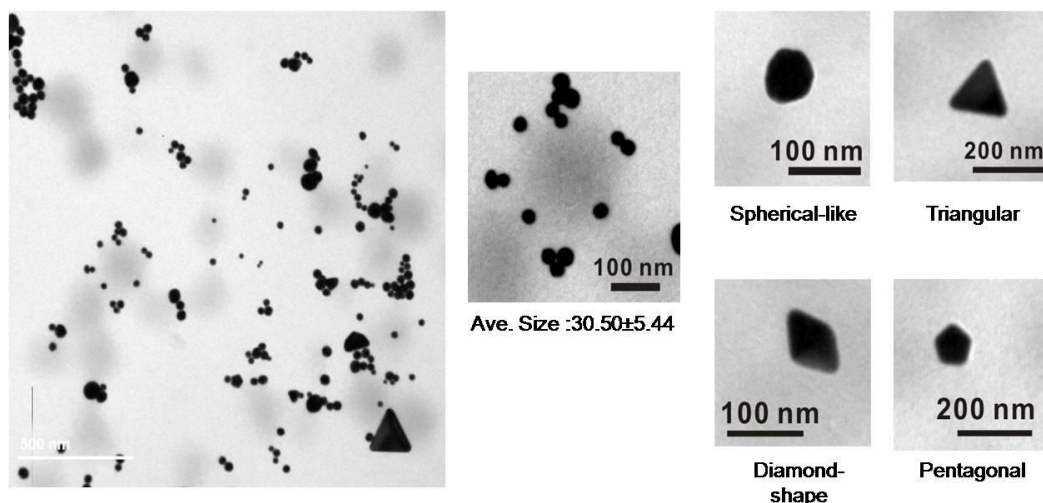


Figure 4.52 Composite particles and different shapes of Au nanoparticles synthesized with N/Au mole ratio = 9.50. Spherical Au nanoparticles has an average size of 30.50 nm (conditions: 25 °C, pH 5.60, stirring at 200 rpm for 24 hours).

4.3.3.2 N/Au dependent formation of composite particles

Figure 4.53 shows the Au composite particles synthesized in different nitrogen to gold mole ratios (N/Au ratio = 28.5, 14.3 and 9.5). The decreasing N/Au ratios mean an increasing gold salt loading. As observed in this figure, the decreasing mole ratios of amino to gold, increases the intensity of the color of the colloidal mixture. At N/Au ratio of 28.5, the color is light pink. When the ratio was reduced to 14.30, it turned to a darker pink color and became purple when reduced more to 9.50. Thus, the intensity of the color increases as the gold loading increases or the mole ratio decreases. When the ratio was further reduced below 9.50, the mixture became unstable and form precipitates (not

shown in the figure) after sometime. Thus, in this study, only three kinds of ratios were studied and believed to be stable gold composite colloidal systems.

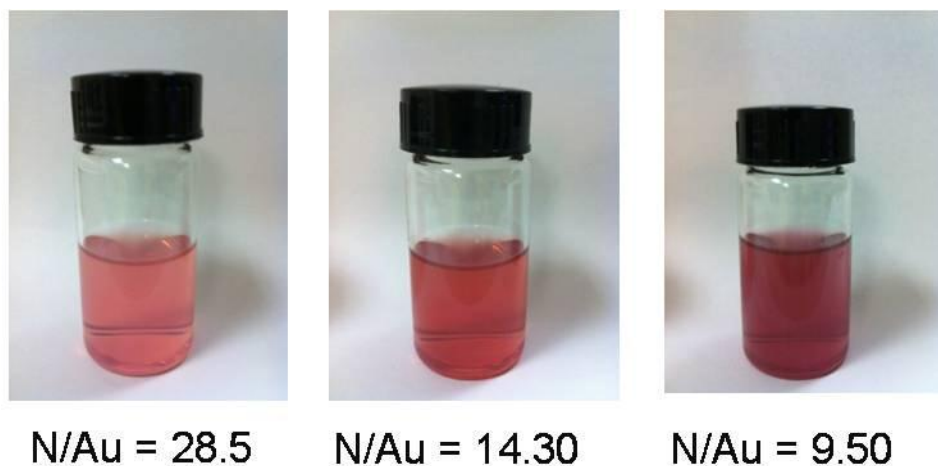


Figure 4.53 Comparison of Au/PNIPAm/PEI composite particles in different amino to gold mole ratios (N/Au). All samples were synthesized at room temperature, pH 5.6, 200 rpm, for 24 hours.

Figure 4.54 shows the UV-Vis spectra of the gold composite particles in different mole ratios of amino to gold salt. The composite particles in different ratios are in different colors and legends. The N/Au ratio of 28.5 and 14.30 exhibit the same absorption wavelength at 521 nm. However, when the ratio was further reduced to 9.50, a sudden shift of the absorbance to 532 nm was observed. The red-shift of the wavelength from 521 to 532 nm was caused by the increase in size and shape of the gold nanoparticles produced as evident with the TEM images.

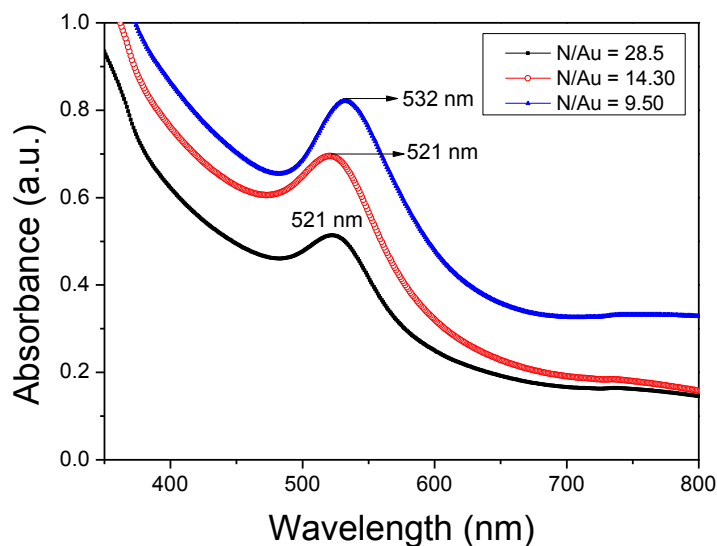


Figure 4.54 UV- Vis spectra of different N/Au mole ratios, black curve represents the 28.5 mole ratio, red curve represents 14.30 and blue represents the 9.50. All other synthetic conditions of the three mole ratios were the same.

4.3.3.3 Size and surface charge of composite particles

To verify the effect of the amino to gold mole ratios (N/Au) on the composite particles, its size and surface charge (*zeta*-potential) were measured corresponding to its different ratios. Three different ratios of N/Au were conducted (28.5, 14.30 and 9.50) and results are summarized in Table 4.2. It was found that both the particle size and the surface charge decrease with an increase of the gold ions added into the template. This is attributed to the increasing entry of gold ions into the template. As the negative gold ions enter the template, it is entrapped by the network-like structure of the shell through

electrostatic interaction. The reducing charge repulsion of the template results in shrinking of the whole composite particles. Thus, the more gold ions enter into the particle, the more is the decrease of the composite particle size. This effect was confirmed by the *zeta*-potential results. Increasing the amount of gold ions to the template decreases its *zeta*-potential. This is due to the higher consumption of the cationic charges on the template. The consumption of the cationic charges was a result of the electrostatic interaction with the anionic gold ions. The more anionic gold ions enter the template, the more it depletes the cationic charges of the composite particles. In this table, the decrease of the *zeta*—potential was significant when the amount of gold ions was doubled. However, a slight decrease follows when the amount of gold ions was tripled. This may indicate the saturation of the template with the gold ions. Furthermore, the small *zeta*-potential values means that the cationic surface charges of the templates have reached neutralization. The particles are mainly stabilized by the steric stabilization provided by the PNIPAm graft chains which co-existed with PEI in the shell.

Table 4.2 Particle size and *zeta*-potential profile of Au composite particles in different N/Au mole ratios with original template.

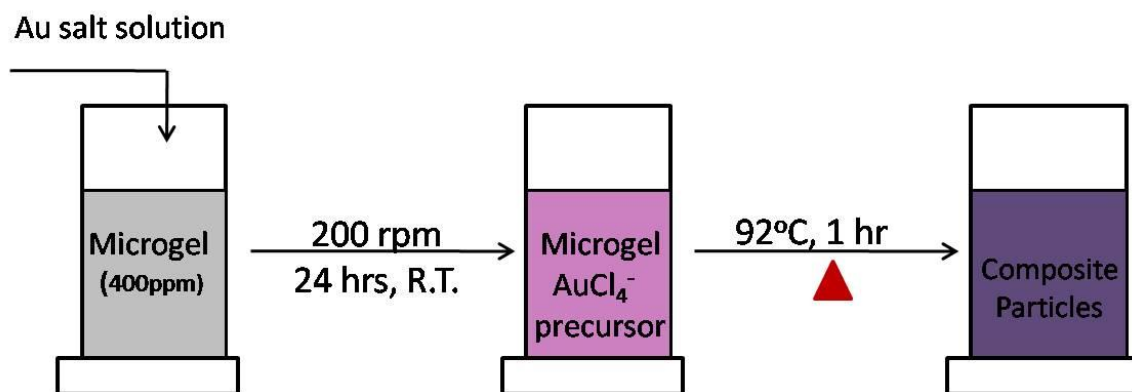
Conditions	Hydrodynamic size (nm)	Zeta-potential (mV)
Original template	348	34
N/Au = 28.50	284	15
N/Au = 14.30	271	-0.71
N/Au = 9.50	261	-1.22

4.3.4 Effect of heating on Au/PNIPAm/PEI composite particles

Based on the previous TEM images of the composite particles synthesized at room temperature (25 °C), it seems that these particles were not yet totally formed into full state gold nanoparticles. Instead, they are perceived to be precursor gold nanoparticles. Heating them at higher temperature will trigger the precursors to form fully grown gold nanoparticles and be more obvious in the TEM images.

This section will verify the effect of heating the composite particles at 60 °C and 92 °C. Scheme 4.2 displays the experimental procedure in the heating process of the composite particle. Here, the same protocol was used in the formation of Au composite particles by mixing the microgel (PNIPAm/PEI, 400 ppm) with the gold salt solution ($\text{HAuCl}_4 \cdot 3\text{H}_2\text{O}$, $6.59 \times 10^{-5}\text{M}$) for 24 hours at room temperature in a slow stirring rate (200 rpm). The amino to gold mole ratio was fixed at 28.5. Gold/polymer

complex or the precursor was synthesized first at 25 °C, followed by heating to 92 °C for an hour, then cooled to room temperature. Another heating experiment was carried out at a lower temperature (60°C) with reaction time of 60 minutes.



Scheme 4.2 Schematic procedure for the heating process of gold/polymer complex precursor to form fully grown gold composite particles.

4.3.4.1 Characterization of thermally treated gold composite particles using electron microscopies

Figure 4.55 shows the TEM image of the composite precursor material after the absorption of gold ions into the positively charged microgels. In this image, very small clusters of AuNPs are in black dots that are suspected to be precursors for nanoparticle formation, which are not fully grown nanoparticles. Microgels are in gray circles in the TEM image. Au clusters are located around the microgel template with the average size of 10.1 nm.

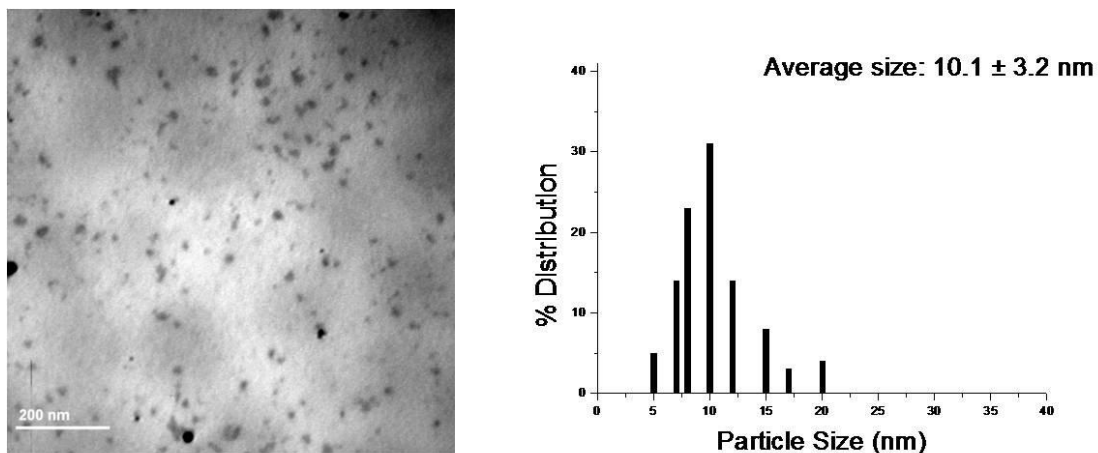


Figure 4.55 Size distribution of Au clusters synthesized by PNIPAm/PEI microgels with N/Au mole ratio of 28.5 (conditions: 25 °C, pH 5.6, stirring at 200 rpm, for 24 hours).

When the composite precursor was heated to 60 °C for one hour, the Au nano-clusters started to show up as more well-defined Au nanoparticles as seen in Figure 4.56. These Au clusters formed into brighter and more obvious spherical particles surrounding the microgel. It seems that particles started to come out as a bit more uncovered from the PEI shell network. This could also be a result of the growth of the original Au clusters into more well-defined Au nanoparticles. It can also be observed that Au cluster size has increased from 10.1 to 17.6 nm in diameter. The resulting fully grown Au nanoparticles here have also retained as single or individual particles. They didn't aggregate or form into larger clusters.

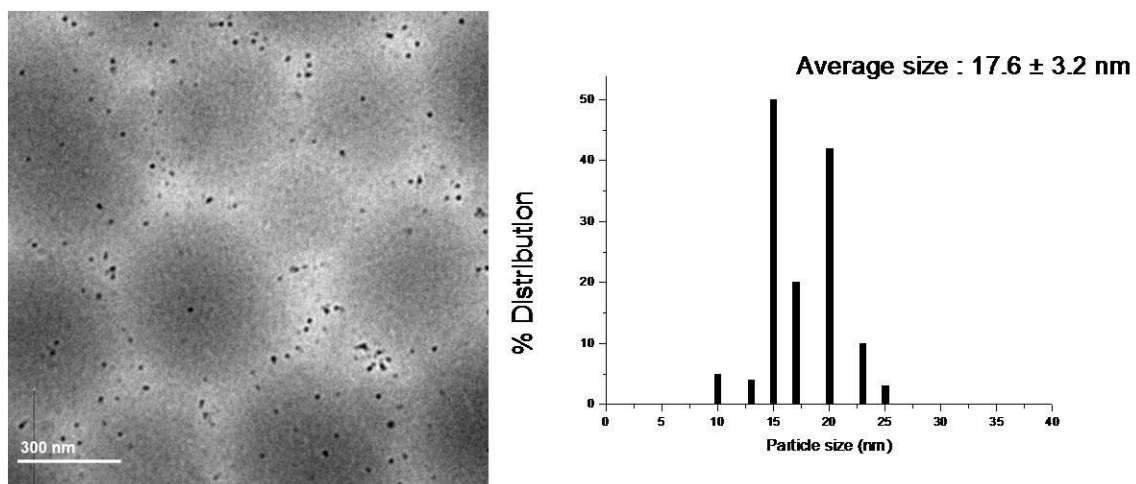


Figure 4.56 Post-treatment of Au/PNIPAm/PEI composite microgels at 60 °C for 1 hour (N/Au mole ratio of 28.5)

Figure 4.57 shows TEM images that demonstrate the effect of heating on the precursor particles to 92°C for one hour. In these images, both the microgel templates and the Au nanoclusters are evident. Microgels are the gray circular particles with an average size of ca. 200 nm in diameter while Au nanoclusters are the ones embedded within the microgel templates. Thus, the Au nanoclusters are blurry as they are like buried in the PEI shell network. However, those Au nanoparticles located outside the composite particles are seemingly darker in color and formed as aggregates. These aggregated particles are obviously bigger than those Au nanoparticles embedded in the templates. It is speculated that the formation of these bigger Au nanoparticles is triggered by the thermal energy provided during heating.

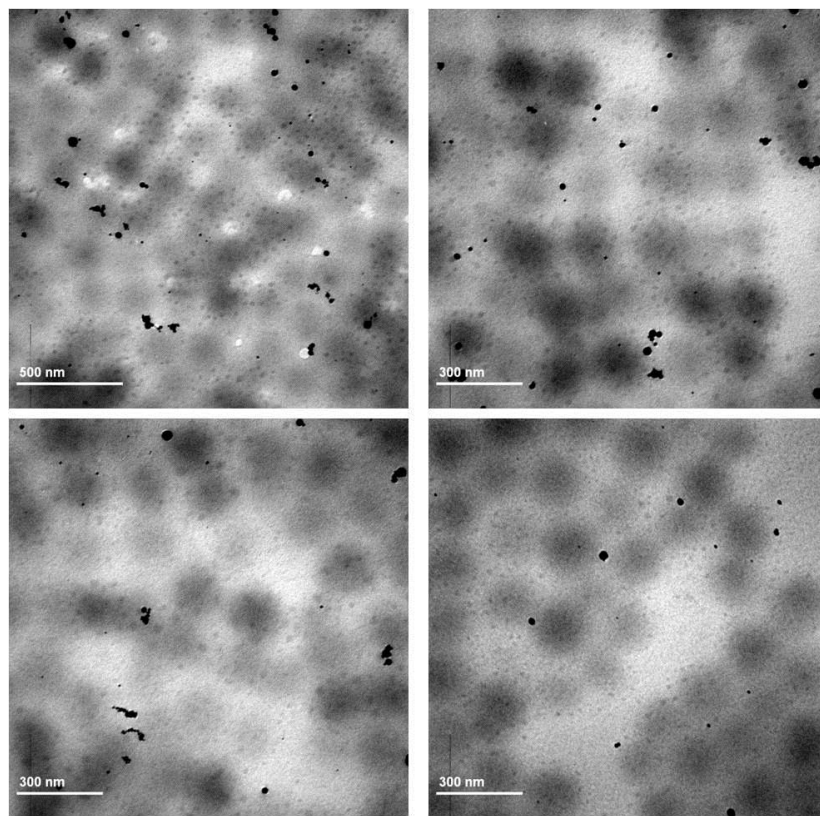


Figure 4.57 Post-treatment of Au/PNIPAm/PEI composite microgels at 92 °C for 1 hour (N/Au mole ratio of 28.5).

The effect of heating the precursor particle to a high temperature such as 60 and 92 °C leads to the growth of the Au nanoclusters embedded within the microgels forming larger particles. When the Au nanoparticles reach big enough size, the liable shell is no longer able to hold up the nanoparticles due to increasing kinetic energy, thus forcing out of the larger particles from the microgel template. Figure 4.58 shows the aggregated gold nanoparticles that are located outside of templates. These are fully grown Au nanoparticles having an average size of 24.7 nm.

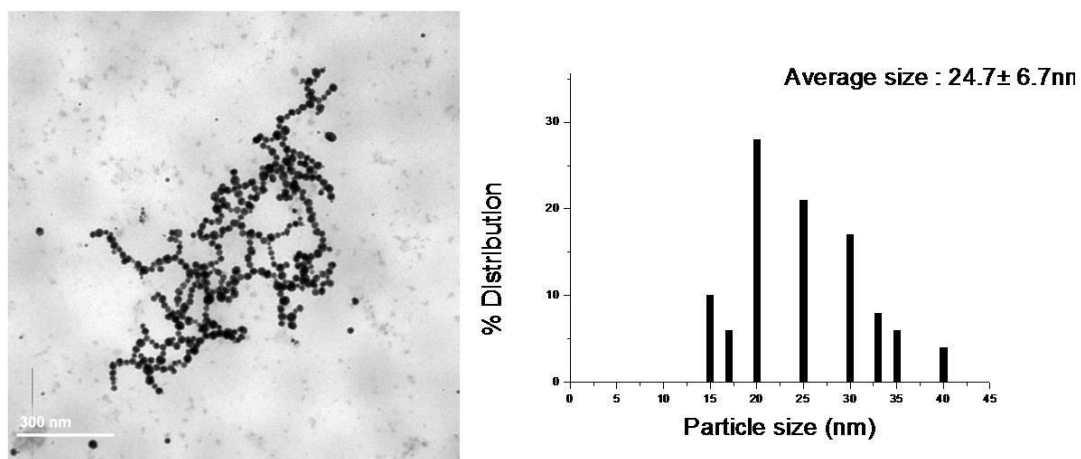


Figure 4.58 Post-treatment of Au/PNIPAm/PEI composite microgels at 92 °C for 1 hour (N/Au mole ratio of 28.5)

Another explanation for this phenomenon is that small Au nanoclusters are squeezed out from the microgel triggered by shrinking of the temperature-sensitive PNIPAm cores. As the Au nanoparticles are squeezed out from the template, they aggregate and form larger particles. In this condition, the perceived precursors are actually Au nanoparticles themselves covered in the PEI shell network.

4.3.4.2 Particle size and colloidal stability

In order to show the effect of the thermal treatment on the precursor composite particles, particle size and surface charge in terms of *zeta*-potential were measured with different conditions. These conditions are pure template (before reduction of gold ions), precursor composite particles and after heating the composite particles.

Figure 4.59 displays the effects of the three conditions mentioned above. The solid square points represent the particle size and the solid circles represent the *zeta*-potential. It is observed that both the particle size and *zeta*-potential values are in decreasing behavior starting from the pure template down to after the thermal treatment of the composite particles. There is a significant change in the particle size of the template after formation of gold nanoparticles. It has been established that the shrinking of the template after reduction of the gold ions to nanoparticles in the previous chapter. This was caused by the consumption of the cationic charges due to the electrostatic interaction between the positively template and the negative gold ions. Lessening the cationic charges means less polymer chain repulsion. Thus, this was evident with the reduced surface charge.

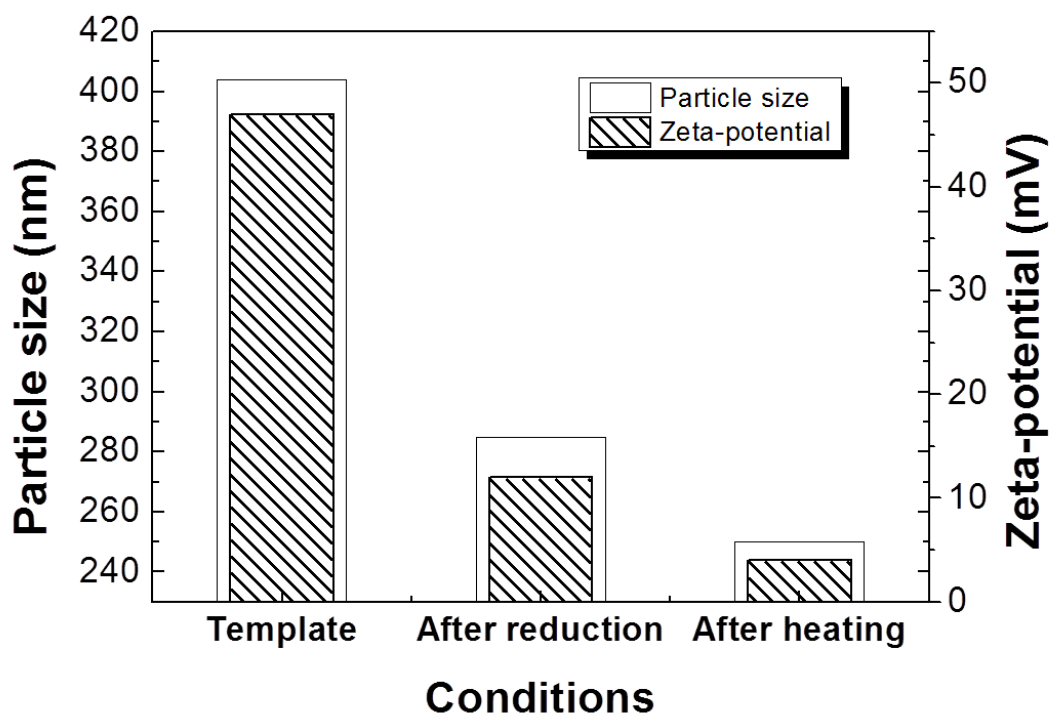


Figure 4.59 Particle size and *zeta*-potential profile at different conditions.

4.4 Conclusions

This study has demonstrated the effects of pH on the formation of the gold / PNIPAm/PEI composite particles. It was found that the formation of gold nanoparticles is dependent on the pH environment of the solution. The pH environment of the solution also affects the location of the gold nanoparticles within or outside the microgel template. This phenomenon was mainly caused by the pH sensitivity of the PEI shell of the microgel template. Due to its sensitivity, conformational changes of the template occur, thus affecting the formation of the gold nanoparticles and its final composite structure.

The effect of reaction temperature on the generation of the gold nanoparticles/polymeric composite particles was demonstrated in this chapter. The conformational changes of the microgel template brought by the temperature sensitive core have triggered the different formation of gold nanoparticles within the microgel. Based on this study, the optimum synthesis temperature is 25 °C.

The amino to gold ratio has an effect on the synthesis of gold composite particles using microgel as a template. For the N/Au ratios of 28.5 and 14.3, Au composite particles were uniformly produced with spherical morphologies and kept within the microgel templates. However, in the latter ratio, the Au nanoparticles are denser. It is speculated that saturation of the microgel template is reached. The increase of absorbance in the second ratio indicates the increase of the particle concentration and volume ^[164]. However, further saturating the microgel by reducing the ratio to 9.50

resulted in producing bigger and different morphologies of Au nanoparticles. The Au nanoparticles were also outside the microgel as well. It can be concluded from this study that the higher concentration of gold salt in the mixture results in saturation of the microgel capacity to reduce gold ions to nanoparticles. From this experiment, the mole ratio or the gold salt concentration dictates the resulting morphology of the Au nanoparticles produced and deposition in the microgel template. Saturation point was also determined. The same phenomenon was illustrated in the work of Sau *et al.* ^[165]. In this study, the gold nanoparticle morphology changed to bigger and higher order of morphology when the gold ions were increased.

The effect on the particle size and surface charges from pure template, Au/PNIPAm/PEI composite particle and after heating showed that both parameters decreased significantly. The decrease in size was due to the shrinking of the particles while the decrease of the cationic surface charge was a result of its consumption. The consumption of the cationic charges was a result of the interaction of the PEI and the gold ions. Lessening this charge lessened polymer repulsion and thus its surface charge.

Chapter 5

Synthesis of Bimetallic Au@Ag Using PNIPAm/PEI Core-Shell

Microgel Templates

There has been much interest in the synthesis of bimetallic nanoparticles in the past decade. This was due to the synergistic effects in combining two metals in one platform, leading to more efficient nano-catalysts with better performance compared to its monometallic counterpart. However, aside from the challenging task of finding suitable supports for controlling aggregation of metal nanoparticles, it also demands for innovative methods that can truly support greener synthesis in fabricating well-defined nanoparticle material.

Most currently, Au@Ag bimetallic nanoparticles were successfully synthesized and coalesced on the surface of an aminopropyl functionalized magnetic silica microspheres (MSM) (Figure 5.1a). The growth of Au@Ag nanoparticles on the surface of the MSM microsphere template was successfully controlled.^[166] However, one of the disadvantages of this process is its tedious multi-step synthesis. Xin *et al* recently also reported the synthesis of Au@Ag bimetallic nanoparticles in a template system (Figure 5.1b).^[167] In their work, Au@Ag nanoparticles were successfully synthesized in a polyelectrolyte-multilayers (PEMs) using poly(styrene sulfonate) PSS and poly(diallyldimethylammonium chloride) PDDA particles as support and using gold and silver salt solution. Counter ion exchange between the cations and anions of the PEMs and metals were used as a driving force in attracting metal ions into the template system.

Subsequent reduction of metal salts using NaBH_4 and ascorbic acid reducing system was carried out in a repeated cycle to improve the loading and the size of metal nanoparticles. Since the process uses a layer-by-layer approach, it is a tedious process which is difficult to be scale up.

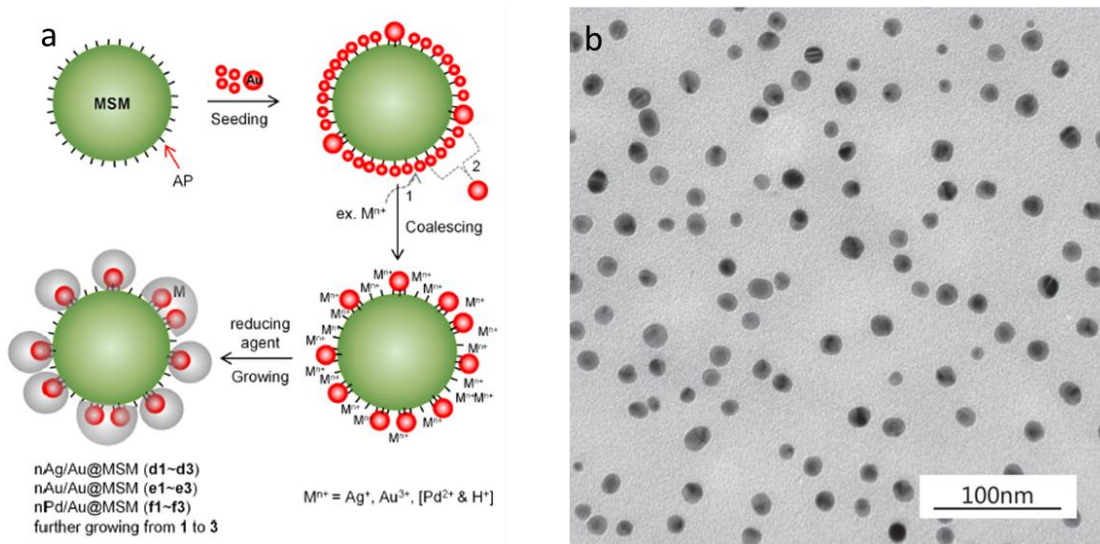


Figure 5.1 a) Au@Ag synthesized on the aminopropyl functionalized magnetic microspheres ^[177], b) TEM image of Au@Ag synthesized in polyelectrolyte-multilayers using poly(styrene sulfonate) and poly(diallyldimethyl ammonium chloride). ^[167]

Recently bimetallic nanoparticles have been controversial in its application on surface-enhanced Raman scattering and catalysis. ^[168] Researchers concluded that electromagnetic and chemical enhancement of the two metallic elements and target molecules constitute the increase of Raman scattering. Although phenomenal results have been published, further research is needed to fully understand its mechanism and

results. Another breakthrough is its catalytic enhancement brought about by its new bifunctional synergistic effects of the two metals in nanoscale. The important role of bimetallic catalyst is its quest for green and sustainable transformation of biomass-derived materials that pose challenges compared to those simple organic molecules. ^[169]

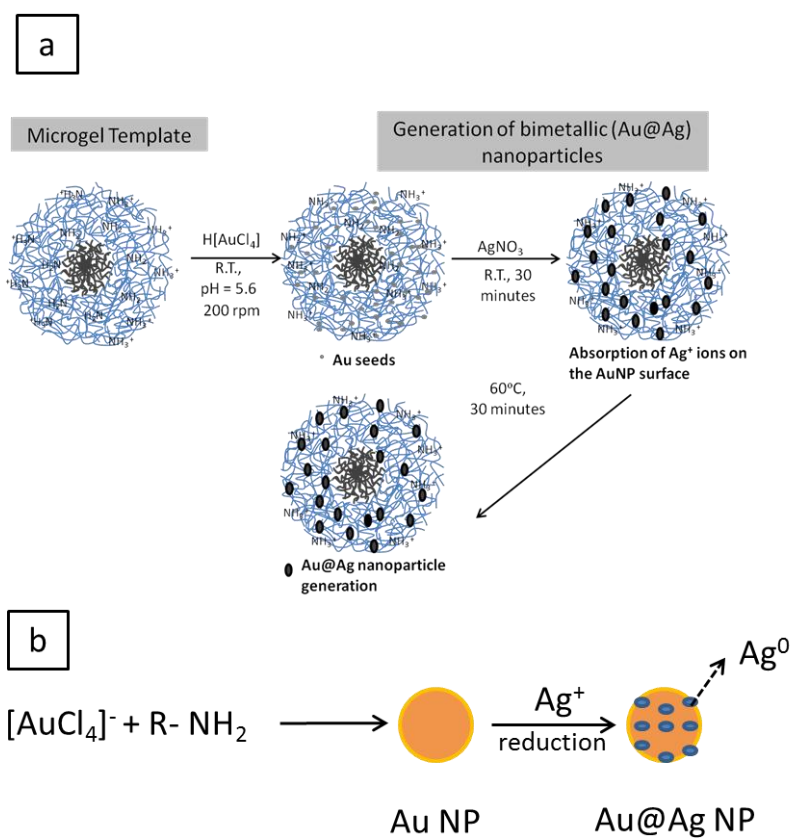
In this study, we use a core-shell particle colloidal template that is highly water-dispersible in water as a nanoreactor, stabilizer and immobilizer of metal nanoparticles. Due to its stimuli-responsive nature, the catalytic activity can be manipulated via conformational changes in response to temperature and pH environment.

5.1 Synthesis of Au@Ag bimetallic nanoparticles using core-shell microgel template

The strategic synthetic route of generating bimetallic nanoparticles in a microgel template is demonstrated in Scheme 5.1a. The synthesis of the Au@Ag bimetallic nanoparticles was carried out through successive reduction of Au and Ag metal ions in a polymeric soft template. First, the microgel template was synthesized through a graft copolymerization technique that results to the formation of amphiphilic core-shell particles with cationic charges. The core is mainly composed of the PNIPAm while the shell is composed of hyperbranched PEI. The PEI contains amine groups that are known to have reducing ability to generate metal nanoparticles. ^[170] Furthermore, PEI also has the ability to complex with metal-ions and metal nanoparticles through the chelating properties of the amino groups. ^[171, 172] Using this template, gold clusters were first generated on the shell layers of the templates. The gold nanoparticle acted as a

nucleation site for the bimetallic nanocrystals formation. Under slightly lower pH (e.g. 3.5), gold chloride ions (AuCl_4^-) were attracted into the template through electrostatic interaction between the positively charged polyelectrolyte microgel template and the negatively charged gold chloride ions. With the presence of the amine moieties in the shell, reduction was possible, resulting in the formation of gold metal nanoparticles. The formation of Au seeds was evident by the change of the solution color from turbid white to light pink, which occurred after 30 to 40 minutes of reaction at room temperature. These gold metal clusters were then used as seed nanoparticles for the successive reduction of the silver ions to silver nanoparticles. Upon change of the solution color, the ionization potential and electron affinity values of Au atom becomes higher than those of Ag atoms. This gives rise to the larger electronegativity value for Au. Therefore it is expected that significant charge transfer may occur from silver to gold atoms.^[173] Silver nitrate solution was used as source of silver ions, and was carried out at room temperature. With the presences of gold metal nanoparticles, silver metal ions (Ag^+) were reduced to silver nanoparticles through under-potential deposition mechanism^[174], wherein the reduced gold clusters act as seeds or active sites for further growth. In this mechanism, the metal with higher reduction potential reduces rapidly to form a core, while the second metal reduces at some later stage and deposits on the surface of the first metal. The reduction of silver ions to nanoparticles was possible through the noble metal induced reduction (NMIR) method.^[175] In this method, monometallic gold nanoparticles induced the reduction of the incoming silver ion to form the bimetallic nanoparticles. This was possible due to the fact that the second metal ion (Ag) has lower reduction potential than gold nanoparticles.^[176] This is illustrated in Scheme 5.1b

wherein gold nanoparticles reduced by the amine functional groups of microgel were used as seed for further reduction of silver ions to silver nanoparticles resulting to a bimetallic alloy nanoparticles. Further heating was also required to improve the crystallinity of the bimetallic nanoparticles and to make sure that HRTEM images would show clear picture of the metal nanoparticles. Heating or calcinations of the composite particles removes partially the template where the bimetallic nanoparticles reside. In this case the bimetallic nanoparticles are uncovered and exposed clearly from its template.



Scheme 5.1 a) Formation of bimetallic nanoparticles using gold/PNIPAm/PEI composite particles, b) Formation of Au@Ag nanoparticles using Au nanoparticle as seed.

5.2 Characterization of original template and composite particles

Pure template and composite particles Au/PNIPAm/PEI composite particles were characterized in terms of its particle size and colloidal stability using the same technique as discussed in Chapter 3. Morphologies were examined in TEM and high resolution TEM. Light absorbance of metallic nanoparticles was investigated through UV-vis spectroscopy and XPS was used to determine the surface chemical composition of the composite particles.

5.2.1 Particle size and colloidal stability

Particle sizes and their corresponding zeta-potential values of the original template (PNIPAm/PEI), the Au loaded template (Au/PNIPAm/PEI) and the Au@Ag loaded template (Au@Ag/PNIPAm/PEI) were studied and results are summarized in Table 5.1. The introduction of the Au metal ions into the PNIPAm/PEI template decreases both the particle size and the surface charge. Introduction of another metal ion (i.e. Ag ions) further decreases both the size and its surface charge density. These effects may be attribute to the presence of the Au ions into the template system which initially creates a contraction of the highly branched PEI shell. The incorporation of silver ions resulted into further entrapment of the bimetallic nanoparticles formed. On the other hand, even though the surface charge density has gone down to almost 5 mV, no precipitation was observed during the experiment. After several days, slight aggregation of the composite particles occurred. But it could be easily re-dispersed back to a stable

colloidal system. The presence of PEI graft chains present on the particle shell may contribute to the colloidal stability of the composite particle through providing steric stabilization.

Table 5.1 Particle size and *zeta*-potential profile of the original template (PNIPAm/PEI), Au/PNIPAm/PEI and Au @Ag composite particles.

Conditions	Hydrodynamic size (nm)	<i>Zeta</i> -potential (mV)
PNIPAm/PEI	384	34
Au/PNIPAm/PEI	284	15
Au@Ag/PNIPAm/PEI	270	5

5.2.2 Morphologies of the composite particles

Particle morphologies were investigated using transmission electron microscope (TEM JEOL 100 CX) operating at an accelerating voltage of 100 kV. The water-dispersed Au@Ag nanoparticles in microgel (10 μ L) were dropped onto a carbon-coated copper grid followed by air-drying at room temperature. High-resolution TEM (HRTEM) (JEOL, JEM-2010) images were also recorded at an accelerating voltage of 200 kV. No staining was conducted on all bimetallic composite TEM samples, while pure PNIPAM/PEI samples were stained with 2% phosphotungstic acid (PTA) for one minute and dried at room temperature.

The morphologies of the microgel template, the Au seeds and the bimetallic nanoparticles formed in the template are illustrated in Figure 5.2. The pure PNIPAm/PEI microgel template (Figure 5.2a) shows a core-shell structure, where the core has a darker contrast while the shell is in lighter contrast around the core. The microgels do not have a clear cut or obvious boundaries between its core and shells, indicating that some uncrosslinked PNIPAm grafted chains may co-exist with PEI on the particle shell. The shell containing amino groups is responsible in attracting gold metal ions and reducing them into gold seeds and formed in clusters (Figure 5.2b). The hydrodynamic diameter of the microgel template is at ca. 380 nm while the microgel with Au seeds is ca. 284 nm. The difference in their hydrodynamic sizes was due to the shrinkage of the template, which was caused by the absorption of metal ions into the PEI shell network during the interaction of the microgel template and the anionic metal ions. This indicates that the Au seeds are immobilized within the microgel template. Figure 5.2c-f illustrates the morphology of the bimetallic Au@Ag nanoparticles formed in the microgel template with the addition of the silver ions and subsequent heating. The hydrodynamic size of the bimetallic composite particles is ca. 270 nm while the Au@Ag bimetallic nanoparticles attached within the template is ca. 6.83 nm (Figure 5.3). The bimetallic nanoparticles are mostly attached around the microgel template where the gold nanoparticles originally formed.

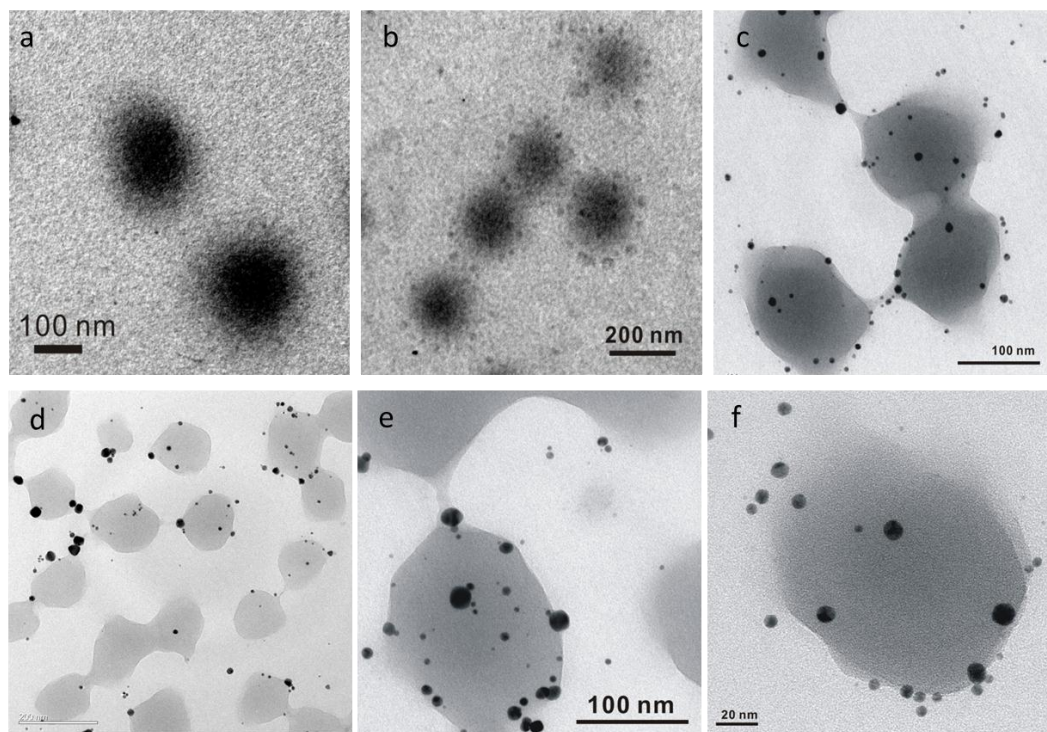


Figure 5.2 TEM images of a) PNIPAm/PEI template (Hydrodynamic ave. size: 380 ± 5.0 nm) , b) Au/PNIPAm/PEI seeds (Hydrodynamic ave. size: 284 ± 2.1 nm), c-f) Au@Ag/PNIPAm/PEI (Au/Ag = 0.50, Hydrodynamic ave. size: 270.6 ± 4.1 nm).

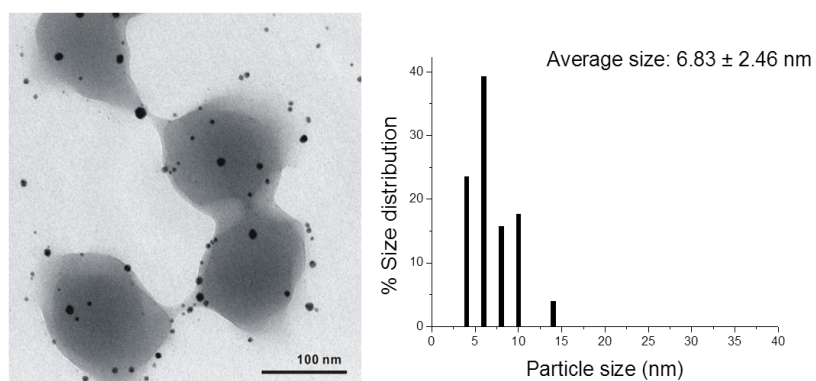


Figure 5.3 Au@Ag bimetallic nanoparticles found within the PNIPAm/PEI template. Particle size distribution on the right side.

High resolution TEM images were also obtained in order to have a closer look at the location of the bimetallic nanoparticles in the template. In Figure 5.4a, Au@Ag bimetallic nanoparticles are located within the shell layer of the template. These bimetallic nanoparticles come in different shades and darkness. Some parts of a single nanoparticle are darker than the surrounding areas. This indicates that the nanoparticles are composed of different metals with varying density of the shades. A magnified portion of this HRTEM in Figure 5.4a is shown in Figure 5.4b. Here, the bimetallic nanoparticles are seen to be located within the PEI-shell region rather than the PNIPAM core. Thus, the bimetallic nanoparticles are basically attached to the shell portion of the template.

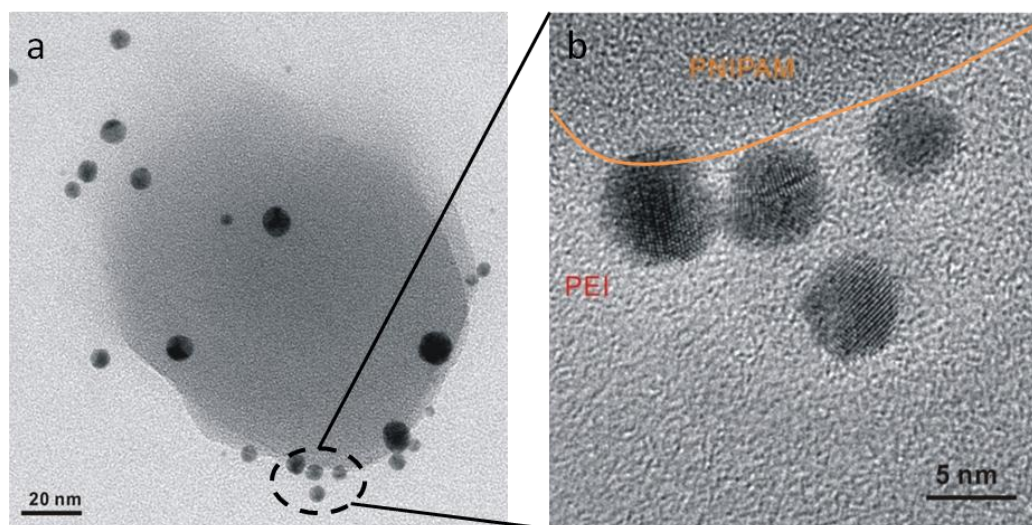


Figure 5.4 a) Single PNIPAm/PEI particle template with Au@Ag bimetallic nanoparticles, b) Localized Au@Ag bimetallic nanoparticles within the PNIPAM/PEI core-shell interface.

5.2.3 UV-vis spectroscopy

To investigate further the UV-vis absorbance of the bimetallic nanoparticles immobilized in the PNIPAm/PEI template, a UV-vis absorption study was conducted. Figure 5.5 illustrates the different absorbance of three different samples. First is the absorbance displayed by the pure silver nanoparticles in PNIPAm/PEI template (solid circles). Another one is by the pure gold nanoparticles in PNIPAm/PEI (solid squares) and the middle curve is the Au@Ag nanoparticles in the same template (hollow triangles). Silver nanoparticles immobilized in the microgel template do not show any absorbance in the spectra shown. Gold nanoparticles display sharp absorbance around 530 nm wavelength. When these gold nanoparticles were incorporated with silver nanoparticles, the original absorbance of pure gold nanoparticles was shifted to 520 nm.

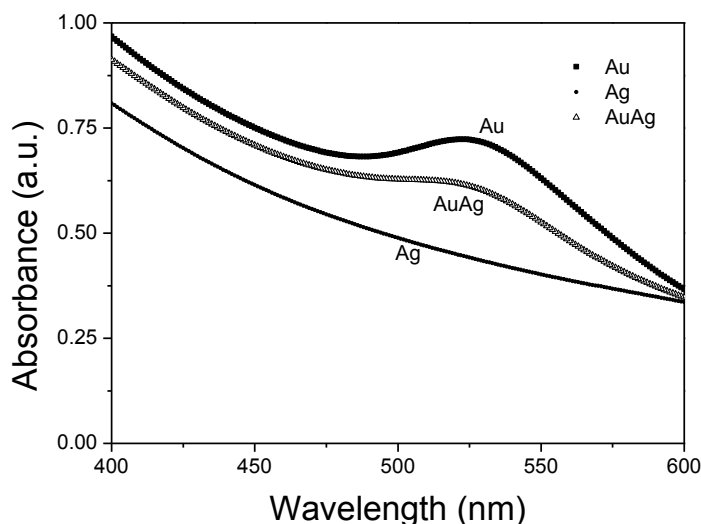


Figure 5.5 UV-vis spectra of Au/(PNIPAm/PEI), Au/(PNIPAm/PEI), Au@Ag/(PNIPAm/PEI) using the same metal ion concentration ($N/Au = N/Ag = N/AuAg = 14.09$ mole ratio). All composites were

219

synthesized at room temperature, pH 5.50, stirring at 200 rpm for 30 minutes absorption, followed by 30 minutes heating at 60°C.

To further verify the effects of the silver nanoparticles into the gold nanoparticles using the microgel template, a series of mixtures of different Au mole fractions in microgel were used to synthesize the bimetallic nanoparticles. Each mole ratio was then subjected to the UV-vis spectroscopy. Figure 5.6 shows the corresponding UV-vis spectra of different Au mole fractions charged into the microgel template. The numbers in fractions inside the box represents the mole fractions of Au/Ag in solution. Thus, 0 mean no Au salt solution was introduced, 0.5 means same moles of Au and Ag in solution is mixed and 1.0 means pure Au salt was added. There is an obvious change in the absorbance around 520 nm when the Au mole fraction reached 50%. This means that silver mole fraction is also 50%. Further increase of the Au mole fraction results in a shift of the absorbance to a higher wavelength.

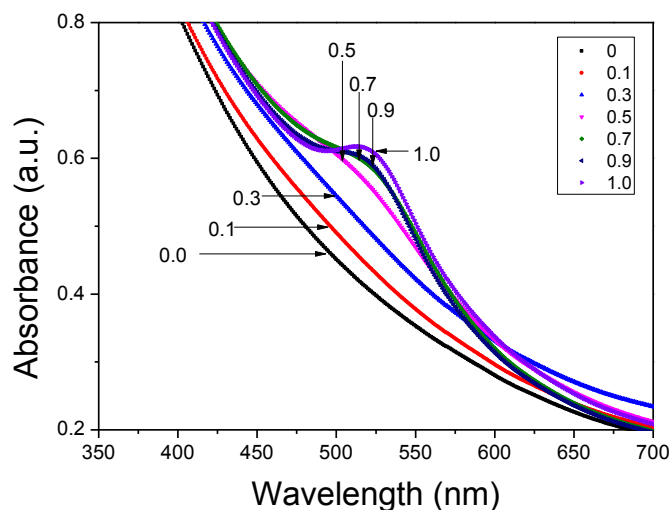


Figure 5.6 UV-vis spectra of nanoparticles in PNIPAm/PEI template in different Ag to Au mole fractions. Pure silver (0.0); 10% Au (0.1); 30% Au (0.3); 50% Au (0.5); 70% Au (0.7); 90% Au (0.9); Pure Au (1.0).

5.2.4 HRTEM and Crystallinity of Au@Ag nanoparticles

To further examine the crystallinity and the different lattice arrangement of the two metals involved, a high resolution TEM and a selective area electron diffraction (SAED) were performed (Figure 5.7b). The electron densities of two metals, gold and silver, are different in their lattice parameters which clearly demonstrate in Figure 5.7a. The Au domain has crystalline structure with the *d*-spacing of 0.237 nm while Ag domain has a lattice spacing of 0.205 nm. With this small difference of the lattice parameters, morphological structures can be ascertained to its specific arrangement. The SAED analysis of the bimetallic nanoparticles proves the co-existence of the crystalline orientations of Au and Ag in single nanoparticle.

SAED analysis showed concentric diffraction rings that indicate the polycrystalline nature of the nanoparticles. The lattice plane determined from the SAED pattern (Figure 5.7b) could be indexed as (111), (200), (220), and (311) reflections, and the corresponding *d*-spacings were revealed as 0.237 nm, 0.204 nm, 0.144 nm and 0.122 nm, respectively, (JCPDS card No: 04-0784) reveals that the single nanoparticles are face centered cubic (fcc) Au structure. The fringe spacing could be measured from the HRTEM image to be 0.237 ± 0.008 nm (Figure 5.7a) that matches the (111) plane of Au crystal lattice (JCPDS card No: 04-0784). Based on the highest intensity of the

diffraction ring indicates that (111) is the predominant crystallographic plane in the Au nanoparticles. The (111) facet is known to be more reactive because it has high atom packing density.

The lattice plane with Miller indices of (200) and (420) reflections, respectively were identified from weak diffraction rings in SAED pattern. The corresponding d -spacings were determined as 0.205 nm and 0.092 nm (JCPDS card No: 04-0783), indicating the face-centered cubic (fcc) structure of Ag. The fringe spacing could be measured from the HRTEM image to be 0.205 ± 0.006 nm (Figure 5.7a) corresponding to Ag (200), which is predominately the highest atomic packing density in fcc structure of Ag domain. The d -spacing of Ag(200) is very close to that of Au(200), a lattice mismatch less than 1 % (0.48 % between Au (200) and Ag(200)) might induce defect structure such lattice plane dislocation as well as stacking faults at atomic level observed from the single nanoparticle with two metallic species.

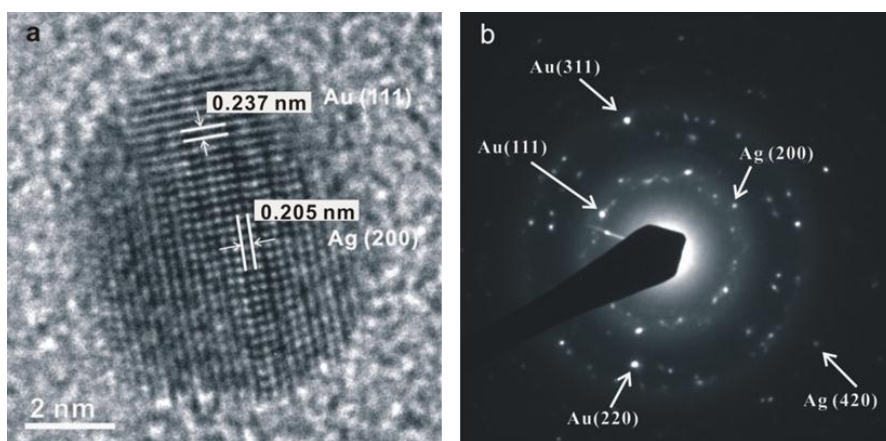


Figure 5.7(a) HRTEM images of a single Au@Ag nanocrystal with corresponding lattice parameters of Au and Ag, (b) SAED of bimetallic (Au@Ag) in PNIPAm/PEI template.

5.2.5 X-ray photoelectron spectroscopy (XPS)

The surface chemical compositions of the composite particles were characterized through XPS analysis. Figure 5.8 shows the XPS spectra of Au-Ag bimetallic nanoparticles @ PNIPAm-PEI microgel film (Au/Ag of 50/50 mol. ratio). Different peaks with their corresponding binding energies indicate the presence of the functional groups and metal nanoparticles. The XPS of a survey scan shows the peaks of C1s (284.9 eV), N1s (399.5 eV), O1s (531.2 eV) which represent functional groups of C-C bonded atoms from PEI and PNIPAm, amine coordinated with the metal nanoparticles and the C=O group from the PNIPAm component. The same spectrum contained two predominant peaks at 367.6 and 373.8 eV, which corresponded to Ag 3d_{5/2} and Ag 3d_{3/2} of metallic Ag⁰, respectively. ^[177] Two new peaks were also observed at binding energies of about 83.8 and 87.5 eV. These peaks were assigned to Au 4f_{7/2} and Au 4f_{5/2} of Au⁰, respectively. In addition to the signals of Au 4f, signals from elemental Ag were detected simultaneously, thereby implying the presence of both Au and Ag components in the shell region, which agreed with the HRTEM analysis.

It was also found out that at this depth of surface analysis, the presence of PNIPAm was evident. This also indicates that there is interpenetration between PNIPAm with the PEI shell. Thus there is no clear-cut distinction of the core and shell of the microgel template.

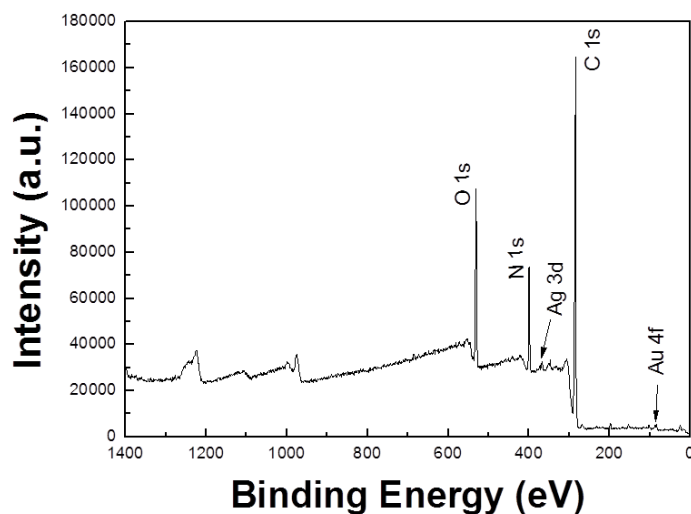


Figure 5.8 Survey scan of Au-Ag bimetallic nanoparticles @PNIPAm-PEI microgel film (Au/Ag of 50/50 mol. ratio).

A closer look at the binding energies of each metal nanoparticle (Figure 5.9) indicates the existence and the valency of each metal nanoparticle. The XPS survey scan suggests a zero valent state of both metal nanoparticles. Their peak positions were nearly the same as those from the vacuum evaporated neat gold and silver films. The differences between the $4f_{7/2}$ and $4f_{5/2}$ peaks for gold nanocrystal (3.6 eV) as well as between the $3d_{5/2}$ and $3d_{3/2}$ peaks for silver nanocrystal (~ 6.0 eV) were also exactly the same as the handbook values of zero valent gold and silver.^[178, 179] Each of the peak areas represents the atomic area of each metal distributed on the nanocrystal surface.

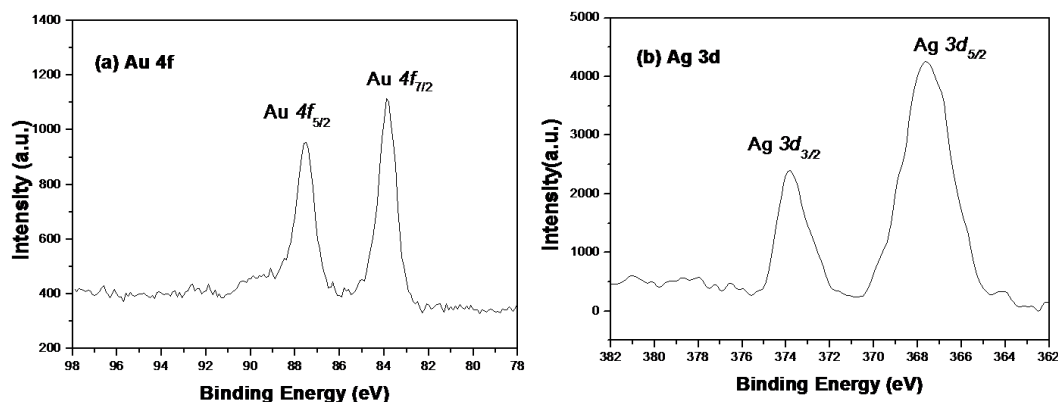


Figure 5.9 Survey scan of Au-Ag bimetallic nanoparticles@PNIPAm-PEI microgel film (Au/Ag of 50/50 mol. ratio).

Another set of bimetallic nanoparticles synthesized through the soft particle template is a higher gold/silver ion ratio (9:1). An XPS analysis was performed with convoluted peaks for each element (Figures 5.10, 5.11 and 5.12). All the XPS analyses for this set-up indicate the presence of all the elements concern (e.g. Au, Ag and the functional groups of the core and shell regions of the template). The binding energies on the two different ratios are summarized in Table 5.2.

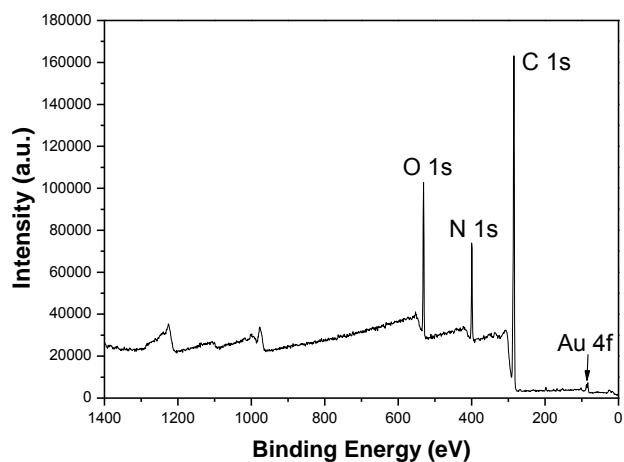


Figure 5.10 Survey scan of Au-Ag bimetallic nanoparticles@PNIPAm-PEI microgel film.(Au/Ag of 90/10 mol. ratio).

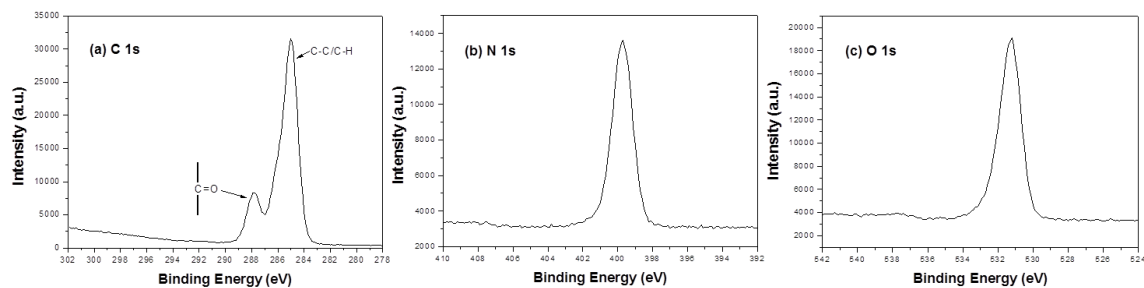


Figure 5.11XPS spectrum of (a) C 1s ; (b) N 1s and (c) O 1s of Au-Ag@PNIPAM-PEI microgel sample with Au/Ag of 90/10 mol. ratio).

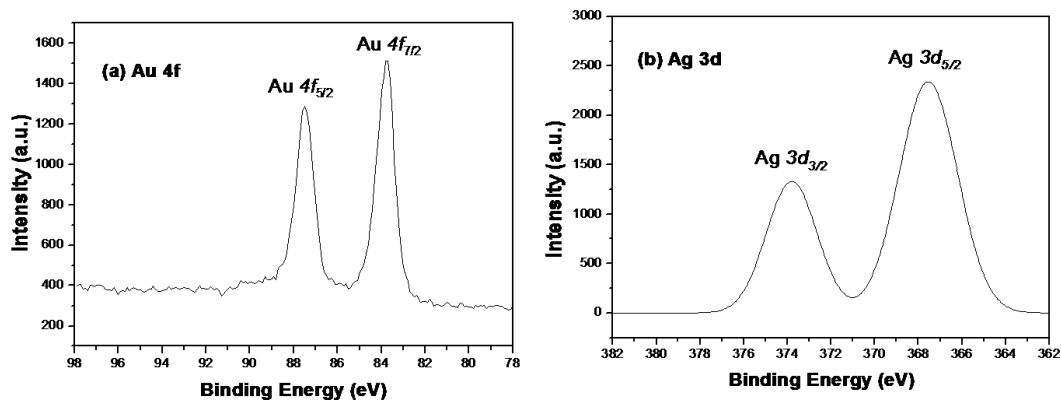


Figure 5.12 XPS spectrum of deconvoluted (a) Au4f and (b) Ag3d of Au-Ag@PNIPAm-PEI microgel sample with Au/Ag of 90/10 mole ratio).

Moreover, from Table 5.3, one can see that the surface composition of bimetallic Au-Ag@PNIPAm/PEI core-shell microgel samples changed in two different Au/Ag mole ratios from 1: 1 to 9: 1. When the Au/Ag ratio is 9/1, the surface Ag/Au atomic ratio was 1.23 as shown in Table 5.3 after reduction, implying a higher Au content. Calculation of the Ag/Au atomic ratio was performed by getting the ratio of the atomic areas on each metallic component. This provides more seed particles for Ag reduction, thus leading to the formation of the sparsely distributed metallic Ag phase to the Au seed particle surface. Compared to Au/Ag mole ratio of 1: 1, the higher surface Ag/Au atomic concentration ratio (1.48) revealed smaller aggregated seed Au particle area, thus higher surface density of Ag atoms distribution per Au seed particle unit area in terms of atomic concentration after reduction process results.

XPS spectra provide direct evidence of the presence of both Au and Ag in the surface layer of microgel particles. Furthermore, the atomic ratio of Au/Ag derived from XPS elemental peak area indicates the presence of different number of metallic Ag atoms (Ag atomic

concentration) on the surface of Au seed particles. We thus propose that deposition of Ag over Au seeds as nucleation platform results in alloying of Ag and Au with the microgel matrix.

Table 5.2 XPS Analysis results of Au and Ag peak positions (spin-orbit doublet) with two different Au/Ag mole ratios after reduction treatment.

Au:Ag mole ratio	Binding energy of Au 4f_{7/2} (eV)	Binding energy of Au 4f_{5/2} (eV)	Binding energy of Ag3d_{5/2} (eV)	Binding energy of Ag3d_{3/2} (eV)
1:1	83.8	87.5	367.6	373.8
9:1	83.9	87.6	367.6	373.8

Table 5.3 XPS Analysis results of Au/Ag surface atomic ratio with two different Au/Ag mole ratios after reduction treatment.

Au:Ag mole ratio	Peak area of Au 4f_{7/2}	Peak area of Ag3d_{5/2}	Ag/Au atomic ratio
1:1	49.4	73.1	1.48
9:1	54.4	66.9	1.23

5.3 Conclusion

The synthesis of bimetallic nanoparticles (Au@Ag) in a soft core-shell particle template, PNIPAm/PEI, was successfully demonstrated in this chapter. The strategy of successive reduction of metal ions in the sequence of Au and Ag was performed in order to create the gold in silver nanoparticles. The formation of the second metal nanoparticles was possible due to the underpotential difference between gold and silver ions. Thus, our studies prove that the gold nanoparticles can act as seeds for the successive reduction of the silver ions to generate bimetallic nanoparticles without the need to use additional toxic reducing and stabilizing agents.

Characterization of the bimetallic nanoparticles revealed the morphology and locations of the nanoparticles within the microgel template. The crystallinity and lattice parameters of the two metals proved the existence of both metals in the microgel template. Furthermore, a series of XPS analyses also showed the zero-valent gold and silver nanoparticles synthesized in this approach. Increasing the Au to Ag mole ratio showed a lower concentration of the silver nanoparticles based on the atomic ratios of Ag:Au nanoparticles. This reveals that the gold nanoparticles were used as a platform for the formation of the second metal, silver, giving bimetallic nanoparticles

Chapter 6

Catalytic Activities of Au/PNIPAm/PEI and Au@Ag/PNIPAm/PEI Composite Particles

One of the common uses of metal/polymeric composite particles is in the field of catalysis ^[190]. This type of application is due to the unique synergistic combination of polymeric template and metal nanoparticles. Polymeric templates with metal nanoparticles are a class of composite particles commonly referred to as polymer hybrids. Different forms of polymer hybrids have been incorporated in different catalytic applications. These hybrids come in different forms and types such as hybrid microspheres, hybrid dendrimers, yolk-shell polymer hybrids and the core-shell polymer hybrid. ^[180] These types of hybrids have been studied for their catalytic applications. Figure 6.1 is a summary of the different polymer hybrids which have catalytic applications adopted from the publication of Zahoor, *et al.* ^[180]. Hybrid microspheres can come in compact ^[181] and hollow ^[182] nanostructures. For example, silver containing microspheres were incorporated in poly(*N*-isopropylacrylamide) hollow particles and used in the catalytic degradation of *p*-nitrophenol. ^[182] Microspheres with platinum nanoparticles were reported to have electrocatalytic ability in the oxidation of methanol and benzyl alcohol. ^[183] Dendrimers with three dimensional, highly branched and non-crosslinked tree like polymeric material are also capable of incorporating metal nanoparticles on their periphery. For example, dendrimer encapsulated titania (TiO₂) supported with Pd-Au was used in the catalytic oxidation of carbon monoxide ^[184], while dendrimer encapsulated Pd-Pt was successful in the oxygen reduction reaction.

[185]. Another emerging type of hybrid polymer is the yolk-shell polymer. This type of hybrid depicts the structure of an egg, where the egg white is the shell and the egg yolk is the core. This type of particle is a modified core-shell structure wherein the core is etched, leaving a hollow space for metal nanoparticles. Au@silica yolk-shell hybrids showed efficient catalytic activity of orthonitroaniline [186] and *p*-nitrophenol (*p*-NP). [187] Most recently, core-shell polymer hybrids have shown promising potential in catalysis. This template type of hybrid is basically composed of a crosslinked central core and a loosely woven network like shell. Metal nanoparticles can be incorporated either in the core and/or in the shell depending on the framework design. Copper stabilized in poly(acrylonitrile-co-acrylic acid), synthesized in an oil-in-water miniemulsion system, was used in the degradation of *p*-nitrophenol, a toxic pollutant.[188] Silver in poly(styrene)- poly(ethylene glycol) methacrylate (PS-PEGMA) was also used in the same catalytic reaction.[189]

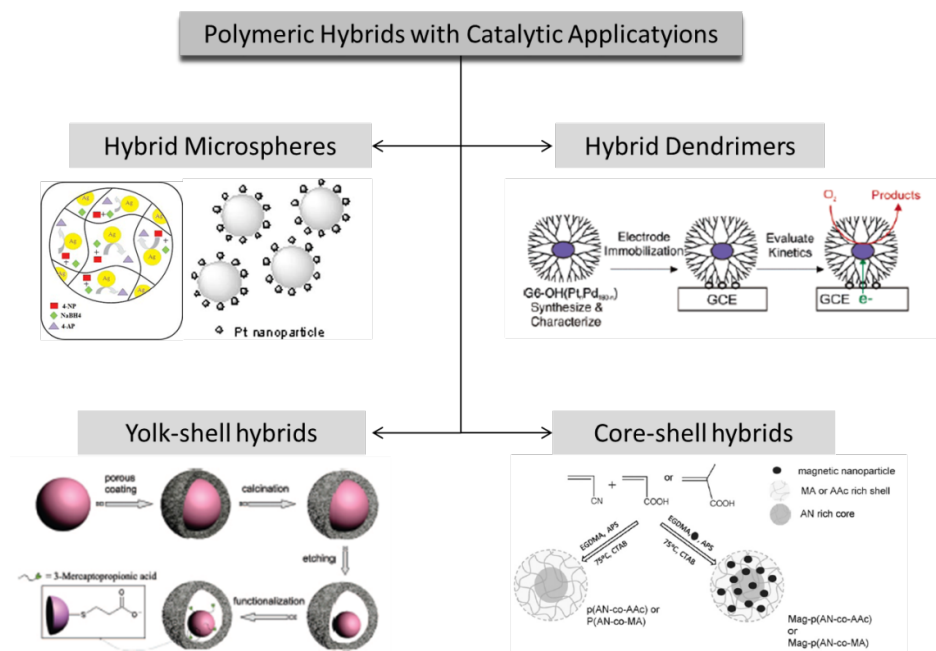


Figure 6.1 Different types of polymers hybrids with catalytic applications.[180]

In our study, dual-responsive microgel is used as a polymeric template for gold and silver nanoparticles. This type of hybrid can be classified as a core-shell polymer hybrid. The polymeric template is able to respond to certain stimulus such as pH and temperature, while the metal nanoparticles are known for its quantum size and plasmon effects which are a crucial in catalytic reactions. The combination of this type of hybrid particles gives the following advantages: 1) Catalytic activity of the metal nanoparticles immobilized in the microgel template could be easily altered through controlling the accessibility of the metal nanoparticles by adjusting the external conditions such as pH and temperature. 2) The steric effect of microgel's dimensional network structure prevents the aggregation of the metal nanoparticles immobilized within the template. 3) Metal nanoparticles and the microgel template could be easily recovered by simple manipulation of pH and temperature. The recovered catalysts can be reused because of their structure integrity.

The versatility of this type of hybrid makes it very much appealing to different applications especially in catalysis. In this study, two types of hybrid particles were explored in terms of its catalytic performance. One is with gold nanoparticles and the other is gold and silver nanoparticles. Both types of metal nanoparticles were immobilized within the microgel templates. As a catalyst, the same type of catalytic reaction was performed in both types of hybrids. Furthermore, the stimulus responsive nature of the microgel template was also examined with respect to their catalytic performance.

6.1 Catalytic activity of Au/PNIPAm/PEI composite particles

The catalytic activity of Au/(PNIPAm/PEI) composite particles was studied through a model reaction of reducing *p*-nitrophenol to *p*-aminophenol as shown below. The reaction was monitored by UV-vis spectroscopy and results are shown in Figure 6.2

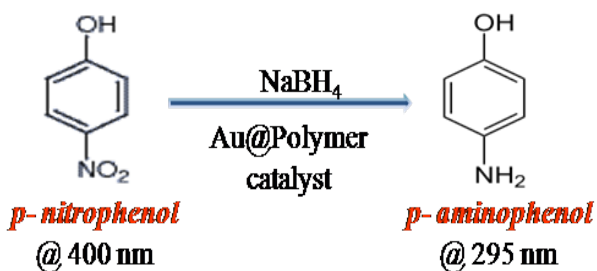


Figure 6.2 Catalytic reduction reaction of *p*-nitrophenol to *p*-aminophenol using Au/PNIPAm/PEI composite particles.

First, the reduction of *p*-nitrophenol was allowed to react in the absence of the Au/(PNIPAm/PEI) as catalyst. In this control experiment, the reactant, *p*-nitrophenol reacted with only a reducing agent, sodium borohydride to form *p*-aminophenol as the sole product. The change of absorbance at 400 nm was monitored in every two minute interval. As observed in this spectrum (Figure 6.3a), there is a minimal or insignificant change in the absorbance, indicating that the reduction rate of *p*-nitrophenol was very slow without any catalyst. In fact, the reaction mixture started to become clearly visible after 20 minutes when color changed from turbid white to light pink. This indicated that the disappearance and the transformation of the reactant to its product were slow. Though there was little reaction that occurred, the change of color was still visible

enough. This can be attributed to the sensitivity of few gold nanoparticles formed when absorbing UV-visible light. The rate of reaction constant was derived from the slope of the linear curve displayed in Figure 6.3b. The rate constant was estimated to be 5.4×10^{-3} using a first order model kinetics.

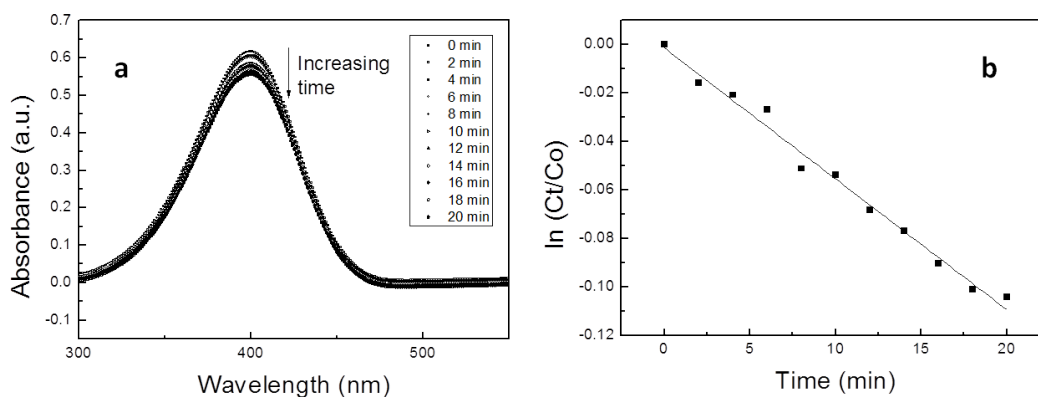


Figure 6.3 a) UV-vis spectra of the sodium borohydride reduction of *p*-nitrophenol to *p*-aminophenol in the absence of a gold-based catalyst, b) Plot of $\ln(C_t/C_0)$ as a function of time of the control experiment for reducing *p*-nitrophenol to *p*-aminophenol.

In comparison, the reduction rate of *p*-nitrophenol using the Au/PNIPAm/PEI composite particle as a catalyst was monitored through the reduction of the absorbance peak at 400 nm wavelength with the UV-vis spectroscopy. Figure 6.4 displays the UV-vis spectrum of the same catalytic reaction using Au/PNIPAm/PEI as a catalyst. The spectrum was obtained through monitoring the decrease of the peak intensity at 400 nm, which represents the absorbance of the reactant concentration. With the decrease of the

concentration of *p*-nitrophenol, the peaks at 295 nm, which represent the presence of *p*-aminophenol and a sole product in this reaction increase with reaction time. These results evidently indicate that the Au composite particles can considerably enhanced reduction rate of *p*-nitrophenol to *p*-aminophenol.

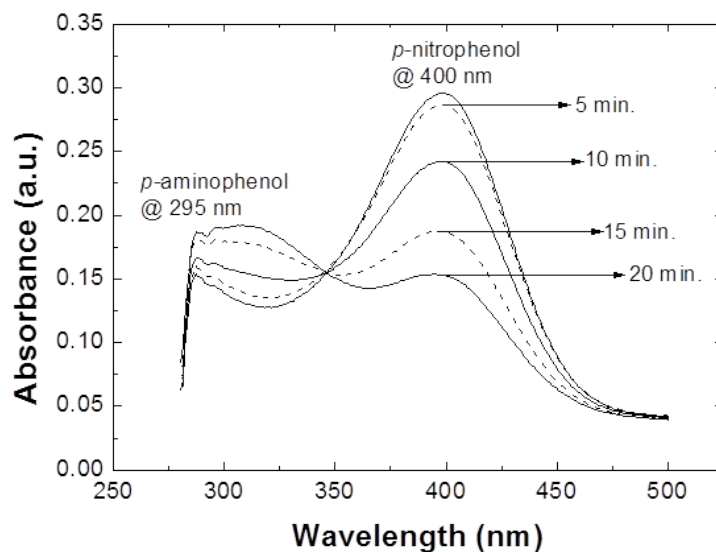


Figure 6.4 UV-vis spectroscopy profile for the reduction of *p*-nitrophenol to *p*-aminophenol using Au/ (PNIPAm/PEI) composite particle as catalyst.

To derive the catalytic rate of reaction of the gold nanoparticles in the microgel template, a catalytic model reaction was chosen. In this case, a pseudo first order kinetic reaction was chosen.

At an excess amount of the reducing agent, NaBH₄ (6.7:1 mole ratio of NaBH₄: *p*-nitrophenol), a pseudo first order kinetic model was used to determine the rate of reaction constant, *k*. This process is described by the following equation (1).

$$r = -\frac{d[A]}{dt} = k[A] \quad (1)$$

where r is the rate of disappearance of reactant A, p -nitrophenol. Equation (1) means that the reaction rate is proportional to the concentration of p -nitrophenol. We can follow the rate of p -nitrophenol reduction to p -aminophenol using a first-order integrated rate law, equation (2).

$$\ln A_{400,t} = -kt + \ln A_{400,t=0} \quad (2)$$

where t is the reaction elapsed time, A_{400} is the absorbance of p -nitrophenol at 400 nm at elapsed time t , and $A_{400, t=0}$ is the initial absorbance at 400 nm prior to addition of the catalyst. Since absorbance is proportional to the concentration of the p -nitrophenol, thus replacing, A_{400} to C_t and $A_{400, t=0}$ to C_0 in equation (2). Further solving the equation results to a linear equation [equation (3)]. Plotting $\ln (C_t/C_0)$ vs. *time* will give a slope of k (s^{-1} or min^{-1}), the rate constant.

$$\ln \left(\frac{C_t}{C_0} \right) = -kt \quad (3)$$

Figure 6.5 demonstrates a typical manner to solve for the rate constant carried out at specific temperature using the equations mentioned above. The linear curve in this figure has a high linearity of 99.2% indicating appropriateness of the model. The same method was carried out on different temperatures and pH conditions. A list of complete rate constants with its corresponding temperature is shown in a Table 6.1. This table shows a consistent high linearity of 98 – 99%. This justifies the use of a first order kinetics to be an appropriate model.

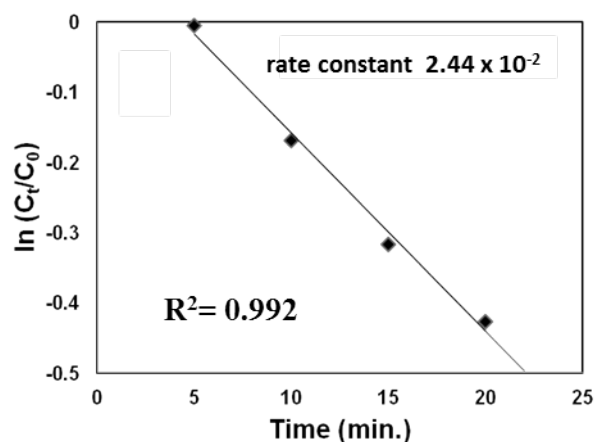


Figure 6.5 Plot of $\ln (C_t/C_0)$ as a function of time for the reaction catalyzed by Au PNIPAm/PEI (N/Au=28.20 mole ratio).

Table 6.1 Linearity of the reaction rate constant at different temperatures.

Temp. ($^{\circ}\text{C}$)	Rate Constant k , (s^{-1})	Rate Constant k , (min^{-1})	R^2
25	7.4×10^{-4}	4.3×10^{-2}	0.994
25	7.0×10^{-4}	4.2×10^{-2}	0.995
27	4.6×10^{-4}	2.8×10^{-2}	0.992
29	3.16×10^{-4}	1.9×10^{-2}	0.987
31	3.0×10^{-4}	1.8×10^{-2}	0.985
33	1.33×10^{-4}	0.8×10^{-2}	0.992

6.2 Effect of pH and temperature sensitivity of the microgel template on catalytic activity

The effect of temperature on the catalytic activity of the Au composite particles is demonstrated in Figure 6.6. At 25 °C, the catalytic activity was at the highest value while it decreased as temperature increased. The decrease in the catalytic activity can be explained by the accessibility of gold nanoparticle with the reacting species at different temperatures. The accessibility of the gold nanoparticles encapsulated within the template particle can be affected by the thermoreponsive property of the crosslinked PNIPAm maining located within the core region of the microgel template. At temperature above the phase transition temperature of the PNIPAm, the PNIPAm molecules become more hydrophobic which eventually shrinks the core region, leading to “drag in” the whole microgel system including the gold nanoparitcles immobilized in the PEI shells. This results in the convergence of the composite particles. Furthermore, the hydrogen bonding between the amide group of PNIPAm and the surrounding water molecules weakens as temperature increases. As a result, the gold nanoparticles embeded in the confined space of the particle shell may combine themselves to a larger aggregate, thus reducing the surface-area-to-volume ratio, and eventually the reactants become less available to proceed its reaction. Consequently, the whole system becomes more knitted, covering the catalyst surface area, resulting a densed composite shell network. In this situation, the reactants are less likely to penetrate through a densed polymer network into the surface of the gold nanocatalyst for the catalytic reaction to proceed. This phenomenon of increasing shell density that eventually covers the surface

catalyst gets more and more intense as the temperature increases, until most of the surface of the gold nanoparticles are covered and catalytic activity eventually ceases.

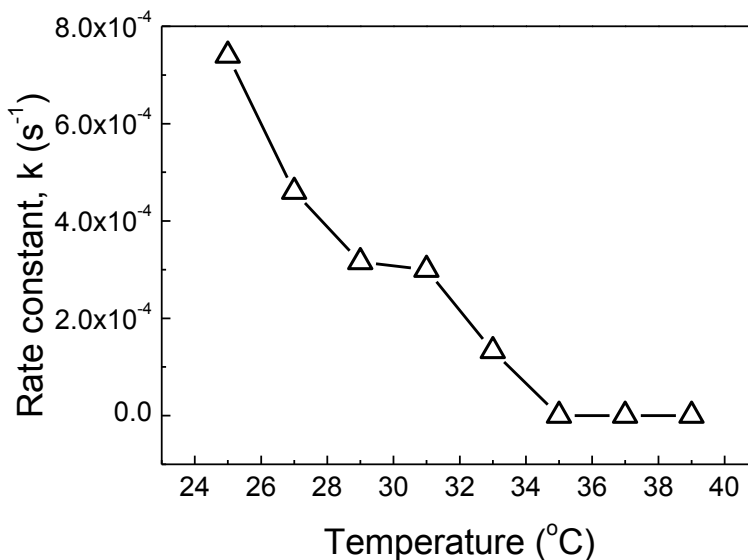


Figure 6.6 Effect of temperature on the catalytic activity of Au/ (PNIPAm/PEI) composite particle used as catalyst for reduction of *p*-nitrophenol to *p*-aminophenol at pH = 5.6.

The effect of solution pH on catalytic activity of the Au/(PNIPAm/PEI) was also systematically studied from pH 3 to 11. As demonstrated in Figure 6.7, the highest catalytic activity was at around pH 3 with a corresponding rate constant of $7.50 \times 10^{-3} s^{-1}$. This is almost 10 folds higher activity than at the neutral pH ($7.40 \times 10^{-4} s^{-1}$). The catalytic activity decreases abruptly with a slight change of pH condition. In this case, the sudden change of activity is evident in the pH range 3-3.5. Further increasing the solution pH to 7.5 has little effect on the catalytic activity. When increasing the pH to 11, its activity ceases. This phenomenon can be attributed to the pH responsiveness of

the PEI shell of the microgel, where the gold nanoparticles are also attached. As pH decreases, protonation of the amino groups occurs, resulting in the stretching of PEI network. This provides more exposure for the gold nanocatalyst to participate in the reaction. However, increasing the pH lead to deprotonation of the PEI shell. Thus the deprotonated PEI molecules become less extended in water medium, leading to shrinking of the composite particles. The change of particle size was evident by the particle size measurement. The original Au/(PNIPAm/PEI) size was ca. 600 nm (pH 3), it is 54% larger than the original size of the composite particles at neutral pH condition. Consequently, the shielding of gold nanoparticles by PEI network makes it difficult for the reacting species to diffuse into the catalytic surface of the gold nanoparticles. This proves that the particles allows with the in size as the pH decreases. During the shrinking and swelling of themicrogel template, the attached gold nanoparticles are also affected in terms of the nanoparticle surface availability necessary for reactants to use as playground for the reaction.

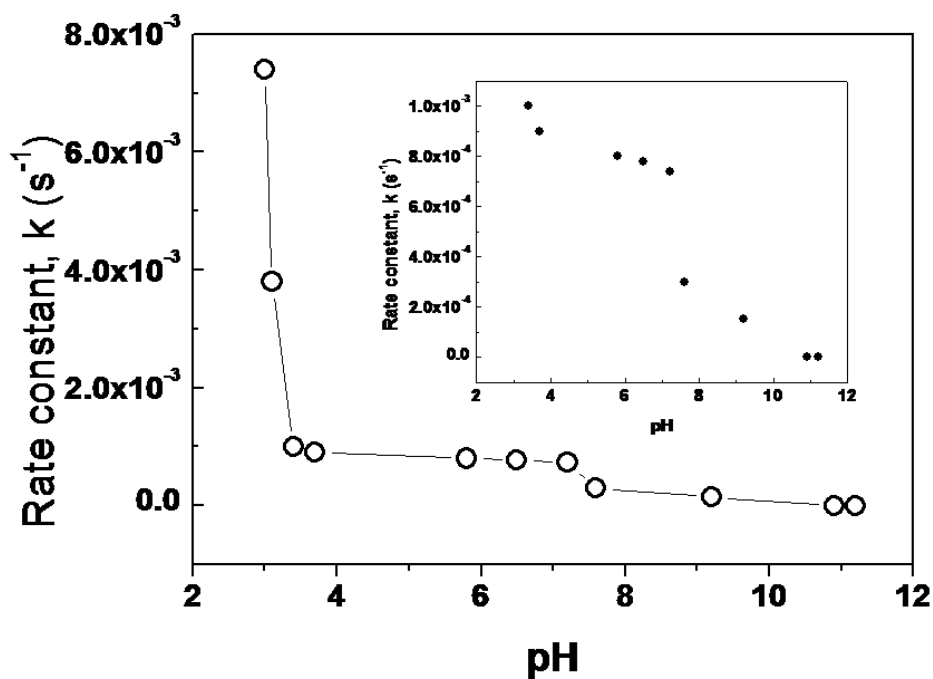


Figure 6.7 Effect of pH on the catalytic activity of Au/ (PNIPAm/PEI) composite particle used as catalyst for reduction of *p*-nitrophenol to *p*-aminophenol at room temperature.

The effects of both temperature and pH on the catalytic activities are basically rooted on the smart properties of the microgel template itself. The microgel template is composed of both temperature and pH sensitivities. The temperature sensitivity of the template comes from the PNIPAm core, while the pH sensitivity is due to the PEI shell. When solution temperature is below the VPTT of the microgel, the template is more swelling. Thus the gold nanoparticles are more accessible under this condition. However, when temperature is above the VPTT of the microgel, the PNIPAm core shrinks, resulting in contraction of the PEI shell. Thus a denser PEI shell hinders the accessibility of the gold catalyst, leading to lowering the reaction rate.

The pH-sensitive shell of the microgel template which is mainly composed of branched PEI. At different pH conditions, protonation degrees of branched PEI and charge density are very different. At low pH such as 3, its degree of protonation is 0.71 while it is 0.22 at pH 7. However, when at high pH such as 10, the degree of protonation is just 0.01. Clearly, increasing solution pH results in a lower degree of protonation, and thus leads to a denser and more compacted PEI shell. Results from Figure 6.7 indicate that there is a sharp change between pH 3 and 4. Thus the catalytic activity of the composite can be easily turned “on” and “off” by adjust the solution pH.

6.3 Catalytic activity of Au@Ag/PNIPAm/PEI composite particles

To demonstrate the catalytic activity of the Au@Ag microgel composites, a catalytic reduction of 4-nitrophenol by sodium borohydride was also chosen as a model system. The solution of 4-nitrophenol exhibited a typical absorption peak at around 320 nm under neutral or acidic condition. After the addition of NaBH₄, the nitrophenolate ions became the dominant species and reduced to aminophenol, which caused the absorption peak of the solution to shift to 400 nm as shown in the previous graph of Figure 6.3. The reduction of 4-nitrophenol by NaBH₄ could not proceed in the absence of a catalyst because the E_o value for the reduction of *p*-nitrophenol to *p*-aminophenol was -0.76 V and that of H₃BO₃/BH₄⁻ was -1.33 V versus the normal hydrogen electrode (NHE)^[203]. When the catalytic reaction had started, a new peak appeared at about 310 nm, which corresponded to the typical absorption peak of 4-aminophenol (4-AP). The reduction kinetics was monitored by performing a spectroscopic measurement based on the color changes in the reaction.^[190] From the UV/Vis spectra shown in Figure 6.8, it

took around 2 min. for Au@Ag microgel to complete the catalytic reaction. When comparing with reaction rates using monometallic Au catalyst, in which the catalytic reactions were completed in 15 min. and 3.5 min with amine to gold ratios of 28.2 and 14.09, respectively, the catalytic activity of the bimetallic catalyst was obviously higher than that of the monometallic catalyst using the same template.

A control experiment was also conducted by allowing the reaction to occur in the absence of a catalyst. After addition of sodium borohydride into the aqueous *p*-nitrophenol, the color did not change and the UV-vis spectrum has a strong absorption peak at 400 nm. The absorption intensity has no significant changes after 20 minutes as observed in Figure 6.3. This indicates that the reaction is difficult to proceed without a catalyst. Its corresponding pseudo first order linear relationship confirms that the kinetic rate constant which is estimated from its slope is $5.4 \times 10^{-3} \text{ s}^{-1}$. When monometallic gold nanoparticles (N/Au = 28.20 mole ratio) generated using a microgel template was used as a catalyst, the reaction proceeded approximately ten times faster ($2.44 \times 10^{-2} \text{ s}^{-1}$, Figure 6.4) than microgel template without immobilized catalysts. This indicates that gold nanoparticles immobilized on a microgel template can effectively catalyze the reaction. Moreover, when bimetallic (Au@Ag) nanoparticles were used as catalyst in this system, the reaction rate was significantly enhanced. Based on the UV-vis spectroscopy in Figure 6.8, the decrease of the absorption was faster than the monometallic gold nanoparticle system. This indicates that the incorporation of the silver nanoparticles was responsible for the significant increase of the reduction of the *p*-nitrophenol to *p*-aminophenol. The enhancement in catalytic activity can be attributed to

the synergistic effects and the flexible design between the two metal nanoparticles^{191,192}, wherein the electronic and geometrical properties of the synthesized bimetallic nanoparticles can positively affect the catalytic activity.¹⁹³ Others suggest that the increase in the number of low coordination number edge and corner sites are responsible for the high activity.^{194,195} Numerous surface science studies have also shown that the surface electronic structure can be modified by the interactions between the two kinds of atoms in the bimetallic alloy owing to ligand¹⁹⁶ and strain effects.¹⁹⁷

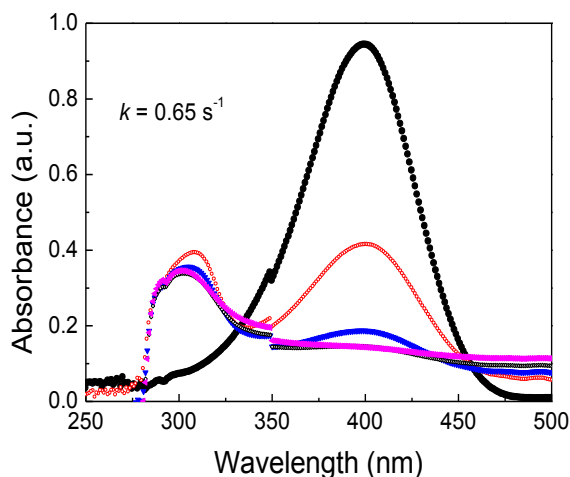


Figure 6.8 UV-vis spectroscopy profile for the reduction of *p*-nitrophenol to *p*-aminophenol using Au@Ag/ (PNIPAm/PEI) composite particle as catalyst. The different colored-curves refer to the different 30 second time intervals.

The ligand effect can be found for metal overlayers where a metal layer is deposited on top of another metal. This metal overlayers may lead to a combination of ligand and strain effects. The catalytic activity of a given metal can be varied substantially by deposition of another reduced metal ions, thus provides an elegant way

of controlling the reactivity of a given metal. Knowing how the d-band center (surface electronic structure) for a given metal changes when it is deposited on top of another metal lattice provides a good starting point for choosing interesting metal combinations.

The “strain effect” involves the average bond length of metal atoms on the supported template, which is typically different to those in the parent metals. Both effects result in changes in the width and average energy of the d-band center.¹⁹⁷ The distance between the center of the d-bands and the Fermi level (F_m) is an important factor in determining the catalytic activity of metallic catalysts and it plays a key role in electrochemical bond-breaking reactions. On the other hand, the interactions between Ag and Au, such as the partial charge transfer from Ag ($F_m = 4.26$ eV) to Au ($F_m = 5.10$ eV), may alter the adsorption energies of the reactants and intermediates¹⁹⁸, thereby leading to the improvement of catalytic activity. Therefore, the bimetallic atoms on the surface would intrinsically change the catalytic behavior (better than that of the monometallic Au nanocrystals) which was termed as “synergistic effects”.

6.4 Comparison of the catalytic activities between Au and Au@Ag in PNIPAm/PEI template

To give us a better picture of the comparison of the two different composite particles using monometallic and bimetallic nanoparticles, Figure 6.9 shows corresponding catalytic reaction rates by plotting $\ln(C_t/C_0)$ versus reaction time for the reduction of 4-NP. The plots of $\ln(C_t/C_0)$ versus time were all approximately linear.

The values of the kinetic rate constant of the Au/PNIPAm/PEI (N/Au=28.2 mole ratio), Au/PNIPAm/PEI (N/Au=14.09 mole ratio) and Au@Ag/PNIPAm/PEI (N/Au-Ag = 28.20; Au/Ag=1:1 mole ratio) estimated from their corresponding slopes were $2.44 \times 10^{-2} \text{ s}^{-1}$, $3.54 \times 10^{-1} \text{ s}^{-1}$ and $6.20 \times 10^{-1} \text{ s}^{-1}$, respectively. These results demonstrate that the increase or incorporation of different metal nanoparticles can significantly increase the reduction rate.

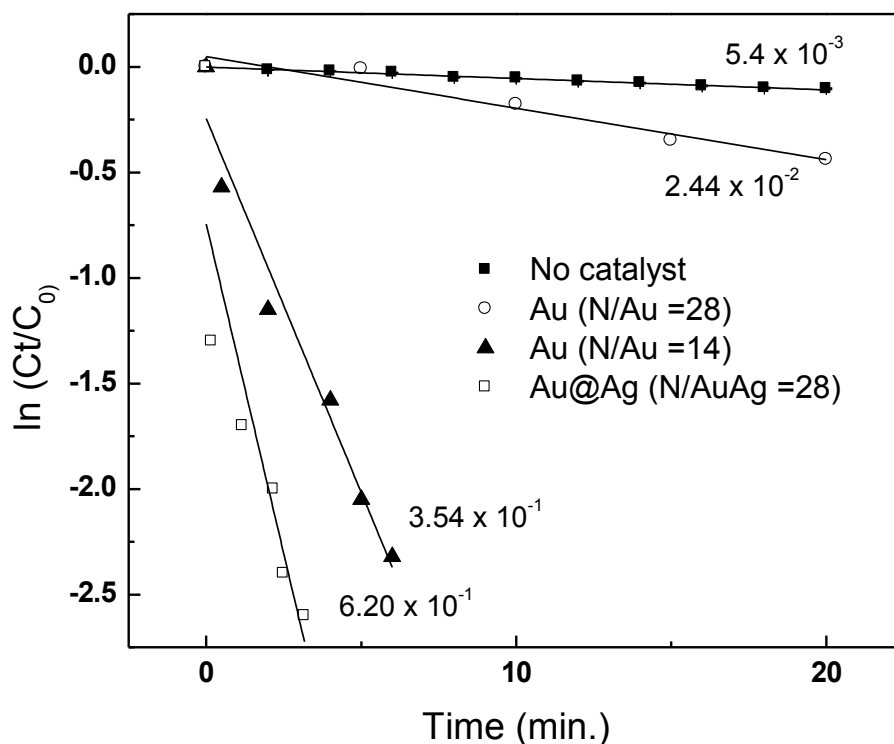


Figure 6.9 Plot of $\ln(C_t/C_0)$ as a function of time for the reaction catalyzed by Au/PNIPAm/PEI in different N/Au mole ratios and Au@Ag bimetallic nanoparticles in PNIPAm/PEI.

6.5 Conclusion

The application of the polymeric hybrids in catalysis was successfully demonstrated in this chapter. The catalytic model used in this study was the reduction of *p*-nitrophenol to *p*-aminophenol. Both monometallic (Au nanoparticles) and bimetallic (Au@Ag) nanoparticles synthesized and stabilized through the PNIPAm/PEI template showed catalytic activity compared to a system without a catalyst. The use of gold nanoparticles as catalyst increased almost 10 times the reduction reaction compared to a system without using any catalyst. When the silver nanoparticles were incorporated with the gold seeds and used as a catalyst, the catalytic activity increased by 10 times when comparing with the use of gold nanoparticles alone. This indicates that the inclusion of a different element at its zero-valent state causes a change in its metallic arrangement, resulting in producing active sites for catalytic reaction.

It was also shown in this chapter that due to the inert smart properties of the microgel template, the catalytic activity of gold nanoparticles can be altered or controlled. This was demonstrated when some control parameters such as pH or temperature is manipulated or controlled.

Chapter 7

Concluding Remarks and Future Study

This chapter sums up the conclusion and iterates the major findings and its significance and implications made. Finally, limitations of the research and recommendations will be further discussed.

8.1 Summary of the Major Findings

A comprehensive characterization of the metal/polymeric composite particles (e.g. AuNP in PNIPAm/PEI and Au@Ag in PNIPAm/PEI) in the discussion of this dissertation provides important insights into the relationships of different parameters affecting the synthesis and its aforementioned catalytic application. These parameters such as temperature and pH are relevant in the basic understanding of the synthesis of metal nanoparticles using a dual responsive microgel, referred here as poly(*N*-isopropylacrylamide/polyethyleneimine) (PNIPAm/PEI). Other important factors that affect its synthesis are metal precursor concentration and thermal heating process of the composite particles. The following results were obtained towards specific aims:

- 1) It was found that the formation of gold nanoparticles is dependent on the pH environment of the solution. The pH environment of the solution also affects the location of the gold nanoparticles within or outside the microgel template. This phenomenon was mainly caused by the pH sensitivity of the PEI shell of the microgel template. Due to its sensitivity, conformational changes of the template

occur, thus affecting the formation of the gold nanoparticles and its final composite structure. pH near neutral (i.e. pH 7.0-7.3) is necessary to strike a balance between the protonated and unprotonated amine groups in the template necessary to efficiently synthesize gold nanoparticles and its corresponding bimetallic nanoparticles.

- 2) Generally, all the temperature synthesis conditions were successful in the generation of gold nanoparticles using a microgel template. The effect of reaction temperature on the generation of the gold nanoparticles/polymeric composite particles was also investigated. The conformational changes of the microgel template brought by the temperature sensitive core, PNIPAm, have triggered the different formation of gold nanoparticles within the microgel. Based on this study, the optimum synthesis temperature is 25 °C.
- 3) The amino to gold ratio (N/Au) has an effect on the synthesis of gold composite particles using microgel as a template. For the N/Au ratios of 28.5 and 14.3, Au composite particles were uniformly produced with spherical morphologies and kept within the microgel templates. However, in the latter ratio, the Au nanoparticles are denser. It is speculated that saturation of the microgel template is reached. The increase of absorbance in the second ratio indicates the increase of the particle concentration and volume. Further saturating the microgel by reducing the ratio to 9.50 resulted in producing bigger and different morphologies of Au nanoparticles. The Au nanoparticles were also outside the microgel as well. It can be concluded from this study that the higher

concentration of gold salt in the mixture results in saturation of the microgel capacity to reduce gold ions to nanoparticles. From this experiment, the mole ratio or the gold salt concentration dictates the resulting morphology of the Au nanoparticles produced and deposition in the microgel template. Gold nanoparticle morphology changed to bigger and higher order of morphology when the gold ions were increased.

- 4) The effect of pH and temperature on the particle size and surface charges from pure template, Au/PNIPAm/PEI composite particle and after heating showed that both parameters decreased significantly. The decrease in size was due to the shrinking of the particles while the decrease of the cationic surface charge was a result of its consumption. The consumption of the cationic charges was a result of the interaction of the PEI and the gold ions. Lessening this charge lessened polymer repulsion and thus its surface charge.

The effect of heating the composite particles or the precursor to a high temperature such as 60 and 92°C can be explained in two ways. First is the growth of the Au nanoclusters embedded within the microgels forming larger particles. Second is the forcing out of the larger particles from the microgel template driven by the thermal energy, which is entropically driven phenomena. However, it is also speculated that this phenomenon simultaneously occurred during the rise of temperature in the heating process.

Another explanation for this phenomenon is that small Au nanoclusters are actually nanoparticles that were squeezed out from the microgel triggered by

temperature. As the Au nanoparticles are squeezed out from the template, they aggregate and form larger particles. In this condition, the perceived precursors are actually Au nanoparticles themselves covered in the PEI shell network that are quite impossible to observe. However, when Au nanoparticles are forced out from the microgel they can be more visible but consequently form larger size.

The synthesis of bimetallic nanoparticles (Au@Ag) in a soft core-shell particle template, PNIPAm/PEI, was successfully demonstrated in this study. The strategy of successive reduction of metal ions in the sequence of Au and Ag was performed in order to create the gold in silver nanoparticles. The formation of the second metal nanoparticles was possible due to the underpotential difference between gold and silver ions.

Through the catalytic activity of the reduction of *p*-nitrophenol to *p*-aminophenol indicates the performance of the catalyst using both the monometallic (AuNP) and bimetallic nanoparticles (Au@Ag) in the microgel template. However, since these metal nanoparticles are caged in a dual responsive carrier, they are also susceptible to changes in its activity as well. In summary the catalytic activity of the metal nanoparticles can be manipulated by both pH and temperature by:

- 1) As pH decreases, protonation of the amino groups occur, resulting in the stretching of PEI network. This phenomenon provides more exposure for the gold nanocatalyst to participate in the reaction and thus increases the catalytic activity. However, increasing the pH lead to deprotonation of the PEI shell which becomes less extended in water while the whole composite structure

shrinks. Consequently the shielding of gold nanoparticles by PEI network is difficult for the reacting species to diffuse into the catalytic surface of the gold nanoparticles. And so thus the activity decreases.

- 2) As temperature increases, PNIPAm becomes hydrophobic that eventually shrinks the core region, leading to “drag in” the whole microgel system including the gold nanoparticles immobilized in the PEI shells. This results in the convergence of the composite particles. Concurrently, the gold nanoparticles are able to combine themselves and reduced the surface-area-to-volume ratio, and eventually the reactants become less available to proceed its reaction, resulting to a denser composite shell network. In this situation, the reactants are less likely to penetrate through a denser polymer network into the surface of the gold nanocatalyst for the catalytic reaction to proceed. This phenomenon of increasing shell density that eventually covers the surface catalyst gets more and more intense as the temperature increases, until most of the surface of the gold nanoparticles are covered and catalytic activity eventually ceases.
- 3) Both monometallic (Au nanoparticles) and bimetallic (Au@Ag) nanoparticles synthesized and stabilized through the microgel PNIPAm/PEI template showed catalytic activity compared to a system without a catalyst. The use of gold nanoparticles as catalyst increased almost 10 times the reduction reaction compared to a system without using any catalyst. When the silver nanoparticles were incorporated with the gold seeds and used as a catalyst, an increase of its activity by 10 times more than the use of gold nanoparticles alone. This indicates

that the inclusion of a different element at its zero- valent state causes a change in its metallic arrangement resulting to produce active sites for catalytic reaction.

8.2 Significance and Implications of this Study

The primary motivation of this work is to create desirable metal/polymeric composite particles with potential applications using a core-shell platform as a template. Herein a microgel template which is both responsive to pH and temperature was used as a template for the synthesis of Au and Au@Ag metal nanoparticles. Although several microgel types have been used in the synthesis of these metal nanoparticles, only limited efforts have been paid in using a more environment-friendly approach and at the same time amenable for industrial scale.

Herein, a smart microgel template is used for the reduction of metal ions to its nanoparticles in water medium. Dilute amount of the template was used during reaction. In this process, reducing agents were not needed. A simple reduction process was conducted at ambient conditions, faster kinetics and minimal reactants used. As a result, economical and producing ready-to-use nanocomposite particles are amenable for industrialization. With such system, a green approach is created in a simple process.

The smart properties of the microgel template influence the chemical activity of the metal nanoparticle present within. This is very useful for tuning the catalytic activity of certain reactions or even its selectivity as well.

With such unique synthesis and properties, these composite particles are potential candidates that can be further functionalized as potential carriers of other molecules linked through the metal nanoparticles or through the microgel template.

8.3 Recommendation for Future Work

The synthetic capability of producing metal/polymeric composite particles using smart amphiphilic graft copolymer microgel template (i.e. Au/PNIPAm/PEI, Au@Ag/PNIPAm/PEI) in an environment-friendly approach has a strong potential for diverse applications in colloidal nanotechnology owing to its extremely simple procedure as well as its notable stability. Through its novelty, promising applications such as in biomedicine, catalysis and sensing if not far from possible. Gold nanoparticles have been mainly used in biomedical diagnostics and therapy while gold nanoparticles stabilized or use responsive polymers are good candidate for drug delivery and cancer therapy. This type of composite particles can also be useful in important catalytic reactions that can solve bigger issue of pollution and environmental problems. Furthermore, gold nanoparticles have been used in many sensing applications, while smart polymers with gold nanoparticles have been used in color tenability and sensing enhancements through metal nanoparticles' enhanced Raman Spectroscopy.

Future works aims to investigate further the scope of metal nanoparticle synthesis using PNIPAm/PEI with different molecular weights of the PEI shell. New

types of composites in terms of its structure and crystallinity can be created through various properties of the template shell. Another challenge is to investigate the control of the metal nanoparticle size and distribution. In this way, metal nanoparticles can be soon tailored in terms of its size for its corresponding applications. Further improvement is needed to create other types of bimetallic nanoparticles such as Au@Pt or Au@Pd. These two metal nanoparticles have different properties in terms of its cohesive energies, electronegativities and atomic radius. Having different metallic properties at nanoscale can lead to the creation of sophisticated structures and synergistic properties.

Strategies can be proposed including (1) the use of different molecular weights of PEI in the synthesis of the microgel template and in the reduction of the metal ions to nanoparticles. (2) Metal nanoparticles size control is important for different applications. This can be carried out by controlling the manner of introducing the metal salt precursor in such a way that nuclei are formed in a higher density and thus forming easily into nanoparticles rather into a bigger aggregate. Some studies introduce injection of the metal salt precursor rather than drop-wise. (3) To further study the reduction of bimetallic nanoparticles using a smart microgel, different types of noble metal should be paired with gold nanoparticles (e.g. Pt, Pd). These two particular metals have different properties compared to gold (e.g. cohesive energy, atomic radius, electronegativities) which will help in the understanding of creating bimetallic nanoparticles. The different properties of the metal nanoparticles are key factors in discovering other types of metal nanoparticle formation using a microgel template system.

Chapter 8

References

1. Li, D.; Cui, Y.; Wang, K.; Hem Q.; Yan, X.; Li, J. *Adv. Func. Mater.* **2007**, 17, 3134.
2. Li, D.; He, Q.; Li, J.; *Adv. Colloid, Interf. Sci.* **2009**, 149, 28.
3. Welsch, N.; Ballauff, M; Lu, Y. *Adv. Polym. Sci.* **2010**, 234, 129.
4. Li, D.; He, Q.; Cui, Y.; Wang, K.; Zhang, X.; Li, J. *Chem. Eur. J.* **2007**, 13, 2224.
5. Faraday, M. *Philos. Trans. R. Soc. London* **1857**, 147, 145.
6. Turkevich, J.; Stevenson, P.C.; Hillier, J. *Discuss. Faraday. Soc.* **1951**, 11, 55.
7. Brust, M.; Walker, M.; Bethell, D.; Schiffrin, D.J.; WHYman, R. *J. Chem. Soc. Chem. Commun.* **1994**, 801.
8. Frens, S.; *Nature: Phys. Sci.* **1973**, 241, 20.
9. Yonezawa, T.; Kunitake, T. *Colloids Surf. A.: Physicochem. Eng. Asp.* **1999**, 149, 193.
10. Hoshetler, M.J.; Templeton, A.C.; Murray, R.W. *Langmuir* **1999**, 15, 3782.
11. Tzhayik, O.; Sawant, P.; Efrima, S.; Kovalev, E.; Klug, J.T. *Langmuir* **2002**, 18, 3364.
12. Porter, L.A. Jr.; Ji, D.; Westcott, S.L.; Grape, M.; Czernuszewicz, R.S.; Halas, N.J.; Lee, T.R. *Langmuir* **1998**, 14, 7378.
13. Resch, R.; Baur, C.; Bugacor, A.; Koel, B.E.; Echtermach, P.M.; Madhukar, A.; Montoya, N.; Requicha, A.A.G.; Will, P. *J. Phys. Chem. B.* **1999**, 103, 3647.
14. Felidj, N.; Aubard, J.; Levi, G.; Krenn, J.R.; Hohenau, A.; Schider, G.; Leitner, A.; Aussenegger, F.R. *Appl. Phys. Lett.* **2003**, 82, 3095.

15. Balasubramanian, R.; Kim, B.; Tripp, S.L.; Wang, X.; Lieberman, M.; Wei, A.;
Langmuir **2002**, 18, 3676.
16. Weare, W.W.; Reed, S.M.; Warner, M.G.; Hutchison, J.E.; *J. Am. Chem. Soc.* **2000**,
122, 12890.
17. Heath, J.R.; Brandth, L.; Leff, D.V.; *Langmuir* **1996**, 12, 4723.
18. Selvakannan, P.R.; Mandal, S.; Phadtane, S.; Pasricha, R.; Sastry, M.; *Langmuir*
2003, 19, 3545.
19. Joo, S.-W.; Kim, W.-J.; Yoon, W.S.; Choi, I.S. *J. Raman. Spectrosc.* **2003**, 34, 271.
20. Li, G.; Lauer, M.; Schulz, A.; Boettcher, C.; Li, F.; Fuhrhop, J.-H. *Langmuir* **2003**,
19, 6483.
21. Cheng, W.; Dong, S.; Wang, E.; *Angew. Chem. Int. Ed.* **2003**, 42, 449.
22. Reetz, M.T.; Helbig, W. *J. Am. Chem. Soc. B* **1994**, 116, 7401.
23. Bakrania, S.D.; Rathore, G.K.; Wooldrige M. S. *J. Therm. Anal. Calorim.* **2009**, 95,
117.
24. Huang, W.-C.; Chen, Y.-C. *J. Nanopart. Res.* **2008**, 10, 697.
25. Okitsu, K.; Mizukoshi, Y.; Yamamoto, T.A.; Maeda, Y.; Nagata, Y. *Mater. Lett.*
2007, 61, 3429.
26. Amendola, V.; Polizzi, S.; Meneghetti, M. *J. Phys. Chem. B* **2006**, 110, 7232.
27. Seol, S.K.; Kim, D.; Jung, S.; Chang, W.S.; Kim, J.T. *J. Nanomater.* **2013**, 2013,
531760.
28. Das, S.K.; Marsili, E. *Rev. Environ. Biotechnol.* **2010**, 199.
29. Lengke, M.F.; Southam, G. *Geochimica et Cosmochimica Acta.* **2005**, 69, 3759.
30. Gericke, M.; Pinches, A. *Hydrometallurgy* **2006**, 83, 132.

31. Chauhan, A.; Zubair, S.; Tufail, S.; Sherwan, A.; Sajid, M.; Suri, C.R.; Azam, A.; Owais, M.. *Int. J. Nanomedicine* **2011**, 6, 2305.
32. Shukla, R.; Nune, S.K.; Chanda, N.; Katti, K.; Mekapothula, S.; Kulkarni, R.R.; Welshons, W.V.; Kannan, R.; Katti, K.V. *Small* **2008**, 4, 1425.
33. Song, J.Y.; Jang, H-K, Kim, B.S. *Process Biochem.* **2009**, 44, 1133-1138.
34. Irvani, S. *Green Chem.* **2011**, 13, 2638.
35. Gamex, G.; Dokken, K.; Herrera, I.; Parson, J.G.; Tiemann, K.J.; Gardea-Torresdey, J.L. *Proceedings of the 2000 Conference on Hazardous Waste Research*.
36. Gardea-Torresdey, J.L.; Parson,s J.G.; Gomez, E.; Videa, P.; Troiani, H.E.; Santiago, P.; Jose-Yacaman, M. *Nano Lett.* **2002**, 2, 397.
37. Huang, J.; Li, Q.; Sun, D.; Lu, Y.; Su, Y.; Yang, X.; wang, H.; Wang, Y. Shao, W.; He, N.; Hong, J.; Chen, C. *Nanotechnology* **2007**, 18, 105104.
38. Gardea-Tooresdey, J.L.; Tiemann, K.J.; Parsons, J.G.; Gamez, G.; Jose-Yacmann, .: *Adv. Environ. Res.* **2002**, 6, 313.
39. Ghodake, G.S.; Deshpande, N.G.; Lee, Y.P.; Jin, E. *Colloids Surf. B*, **2010**, 75, 584.
40. Chen, H.J.; Wang, Y.L.; Wang, Y.Z.; Dong, S.J.; Wang, E.K. *Polym.* **2006**, 47, 763
41. Sardar, R.; Park, J.W.; Shumaker-Parry, J.S.; *Langmuir* **2007**, 23, 11883.
42. Han, J.; Liu, Y.; Li, L.; Guo, R. *Langmuir* **2009**, 25, 11054.
43. Kuo, P.;L. Chen, C.C.; Jao, M.W. *J. Phys. Chem. B.* **2005**, 21, 4710.
44. Cai, L.J.; Wang, M.; Hu, Y.; Qian, D.J. Chen, M. *Nanotechnology* **2011**, 22, 285601.
45. Hoppe, C.E.; Lazzari, M.; Pardinias-Blanco, I.; Lopex- Quintela, M.A. *Langmuir* **2006**, 22, 7027.
46. Kundu, S.; Wang, K.; Liang, H. *J. Phys. Chem. C* **2009**, 113, 5157.

47. Wahio, I.; Xiong, Y.J.; Yin, Y.D. Xia, Y.N. *Adv. Mater.* **2006**, 18, 1745.
48. Huang, H.H.; Ni, X.P.; Loy, G.L.; Chew, C.H.; Tan, K. L. Loh, F. C.; Deng, J.F.;
Xu, G.Q. *Langmuir* **1996**, 12, 909.
49. Han, J.; Song, G.P.; Guo, R.; *Eur. Polym. J.* **2007**, 43, 4229.
50. Sun, X.P.; Dong, S.J.; Wang, E.K.; *Polym.* **2004**, 45, 2181.
51. Karg, M. Multifunctional inorganic/organic hybrid microgels. *Colloid. Polym. Sci.*
2012, 290, 673.
52. Shenhar, R.; Norsten, T.B.; Rotello, V.M. *Adv. Mater.* **2005**, 17, 657.
53. Li, D.; He, Q.; Cui, Y.; Li, J. *Chem. Mater.* **2007**, 19, 412.
54. Kim, J-H.; Boote, B.; Pham, J.A.; Hu, J.; Byun, H. *Nanotechnology* **2012**, 23, 275606.
55. Mantzaridis, C.; Pispas, S. *Macromol. Rapid Commun.* **2008**, 29, 1793.
56. Sakai, T.; Alexandridis, P. *J. Phys. Chem. B* **2005**, 109, 7766.
57. Hou, G.; Zhu, L.; Jiang, M. *Macromolecules* **2007**, 40, 2134.
58. Meristoudi, A.; Pispas, S. *Polymer* **2009**, 50, 2743.
59. Aslam, M.; Fu, L.; Su, M.; Vijayamohanan, K.; Dravid, V.P. *J. Mater. Chem. B* **2004**,
14, 1795.
60. Newman, J.D.S.; Blanchard, G.J. *Langmuir* **2006**, 22, 5882.
61. Zhou, Y.; Jiang, K.; Chen, Y.; Liu, S. *J. Polym. Sci., Part A: Polym. Chem.* **2008**, 46,
6518.
62. Lei, Z.; Wei, X.; Zhang, L.; Bi, S. *Colloids and Surfaces A: Physicochem. Eng.*
Aspects, **2008**, 317, 705.
63. Yabu, H.; Koike, K.; Motoyoshi, K.; Higuchi, T. Shimomura, M. *Macromol. Rapid*
Commun. **2010**, 31, 1267.

64. Werle, M. *Pharma. Res.* **2008**, 25, 500.
65. Umeda, Y.; Kojima, C.; Harada, A.; Hiromichi, H.; Kono, K. *Bioconjugate Chem.* **2010**, 21, 1559.
66. Scott, R.W.J.; Wilson, O.M.; Crooks, R.M. *J. Phys. Chem B* **2005**, 109, 692.
67. Myers, V.S.; Weir, M.G.; Carino, E.V.; Yancey, D.F.; Pande, S.; Crooks, R.M. *Chem. Sci.* **2011**, 2, 1632.
68. Daly, E.; Saunders, B.R. *Langmuir* **2000**, 16, 5546.
69. Hoare, T.; Pelton, R. *Langmuir* **2004**, 20, 2123.
70. Lopez-Leon, T.; Elaissari, A.; Ortega-Vinuesa, J.L. *Chem. Phys. Chem.* **2007**, 8, 148.
71. Molina, M.J.; Gomez-Anton, M. R.; Pierola, I.F.. *J. Phys. Chem. B* **2007**, 111, 12066.
72. Brugger, B.; Richtering, W. *Adv. Mat.* **2007**, 19, 2973.
73. Li, D.; He, Q.; Li, J. *Adv. Colloid Interface Sci.* **2009**, 149, 28.
74. Agrawal, M.; Gupta, S.; Stamm, M. *J. Mater. Chem.* **2011**, 21, 615.
75. Thomas, V.; Namdeo, M.; Mohan, Y.M.; Bajpai, S.K.; Bajpai, M. *J. Macromol. Sci., Pure Appl. Chem.* **2007**, 45, 107.
76. Karg, M.; Hellweg, T. *Curr. Opin. Colloid Interface Sci.* **2009**, 14, 438.
77. Suzuki, D.; Kawaguchi, H. *Langmuir* **2005**, 21, 12016.
78. Virtanen, J.; Tenhu, H. *Macromolecules* **2000**, 33, 5970.
79. Dong, Y.; Ma, Y.; Zhai, T.; Zeng, Y.; Fu, H.; Yao, J. *Nanotechnology* **2007**, 18, 455603.
80. Suzuki, D.; Kawaguchi, H. *Langmuir* **2006**, 22, 3818.

81. Karg, M. Pastoriza-Santos, I.; Perex-Juste, J.; Hellweg, T.; Liz-Marzan, L.M. *Small* **2007**, 7, 1222.
82. Liu, Y.; Feng, X.; Shen, J.; Zhu, J.-J.; Hou, W. *J. Phys. Chem. B* **2008**, 112, 9237.
83. Gorelikov, I.; Field, L.M. Kumacheva, E. *J. Am. Chem. Soc.* **2004**, 126, 15938.
84. Suzuki, D.; Kawaguchi, H. *Langmuir* **2005**, 23, 8175.
85. Schrunner, M.; Polzer, F.; Mei, Y.; Lu, Y. *Macromol. Chem. Phys.* **2007**, 208, 1542.
86. Lu, Y.; Mei, Y.; Walker, R. *Polymer*, **2006**, 47, 4985.
87. Yuan, J.; Wunder, S.; Warmuth, F.; Lu, Yan. *Polym.* **2012**, 53, 43.
88. Dykman L.; Khlebtsov, N. *Chem. Soc. Rev.* **2012**, 41, 2256.
89. Strong, L.E.; West, J.L. *WIREs Nanomed. Nanobiotechnol.* **2011**, 3, 307.
90. Sershen, S.R.; Westcott, S.L.; Halas, N.J.; West, J.L. *J. Biomed. Mater. Res. A* **2000**, 51, 293.
91. Sershen, S.R.; Halas, N.J.; West, J.L. *Ann Int Conf IEEE Eng Med Biol Proc* **2002**, 1, 490.
92. Lu, Yan.; Proch, S.; Schrunner, M.; Creschler, M.; Kempe, R.; Ballauff, M. *J. Mater. Chem.* **2009**, 19, 3995.
93. Suzuki, D.; Kawaguchi, H. *Langmuir* **2006**, 22, 3818.
94. Weiping, Lv.; Wany, Y.; Feng, W.; Qi, J.; Zhang, G.; Zhang, F.; Fan, X.. *J. Mater. Chem.* **2011**, 21, 6173.
95. Alexandridis, P. *Chem. Eng. Technol.* **2011**, 34, 15.
96. Li, W.; Jia, Q.X.; Wang, H-L. *Polymer* **2006**, 47, 23.
97. Ingert, D.; Pileni, M-P. *Adv. Funct. Mater.* **2001**, 11, 136.

98. Brust, M.; walker, M.; Bethell, D.; Schiffrin, D.J.; Whyman, R. *J. Chem. Soc. , Chem. Commun.* **1994**, 801.
99. Alvarez, M.M.; Khoury, J.T.; Schaaff, T.G.; Shafigullin, M.N.; Vezmar, I.; Whetten, R. L. *J. Phys. Chem. B.* **1997**, 101, 3706.
100. Nalawade, P.; Mukherjee, T.; Kapoor, S. *Advances in Nanoparticles* **2013**, 2, 78.
101. Meristoudi, A.; Pispas, S. *Polymer* **2009**, 50, 2743.
102. Zhang, N.; Xu, Yi-Jun. *Chem. Mater.* [dx.doi.org/10.1021/cm400750c](https://doi.org/10.1021/cm400750c)
103. Li, Y.; El-Sayed, M.A. *J.Phys. Chem. B.* **2001**, 105, 8938.
104. Ho, K.M.; Li, W.Y.; Wong, C.H.; Li,P. *Colloid. Polym. Sci.***2010**, 288, 1503.
105. Zhu, J. Tang, Law, L.P.; Fengm, M.; Ho, K.M.; Lee, DKL.; Harris, FW.; Li, P. *Bioconjug. Chem.* **2005**, 16, 139.
106. Feng, M.; Lee, D.; Li, P. *Int. J. Pharm.* **2006**, 311, 209.
107. Feng, M.; Li, P.*J. Biomed. Mater. Res.* **2007**, 80, 184.
108. Mao, X.; Huang, J. fai Leung, M.; Du, Z.; Ma, L.; Huang, Z.; Li, P.' Gu, L.*Appl. Biochem. Biotechnol.* **2006**, 135, 229.
109. Ho, KM.; Mao, X.; Gu, L.; Li, P. *Langmuir* **2008**, 24, 11036.
110. Ye, W.; Leung, M.F.; Xin, J.; Kwong, T.L.; Lee, DKL.; Li, P. *Polymer* **2005**, 46, 10538.
111. Chen, J.; Zeng, F.; Wu, S.; Su, J. Zhao, J.; Tong, Z.*Nanotechnology* **2009**, 20, 365502.
112. Mei, Y.; Sharma, G.; Lu, Y.; Ballauff, M.; Dreschler, M.; Irrgang, T.; Kempe, R. *Langmuir* **2005**, 21, 12229.
113. Lu, Y.; Mei, Y.; Drechsler, M.I Ballauff, M.*Angew. Chem. Int. Ed.* **2006**, 45, 813.

114. Lu, Y.; Proch, S.; Schrimmer, M.; Drechsler, M.; Kempe, R.; Ballauff, M. *J. Mater. Chem.* **2009**, 19, 3955.
115. Motornov, M.; Roiter, Y.; Tokarev, I.; Minko, S. *Prog. Polym. Sci.* **2010**, 35, 174.
116. Cho, E.C.; Lee, J.; Cho, K. *Macromolecules* **2003**, 36, 9929.
117. Guillem, V.M.; Aliño, S.F. *Gene Therapy and Molecular Biology* **2004**, 8, 369.
118. Geckeler, K.; Lange, G.; Eberhardt, H.; Bayer, E. *Pure Appl. Chem.* **1980**, 52, 1883.
119. Horn, D in Goethals (Ed.) *Polymeric Amines and Ammonium Salts*, Pergamon Press, Oxford, **1980**, 333.
120. Warshawsky, A. in Sherrington D.C. and Hodge, P. (Ed.) *Syntheses and Separation Using Eunctional Polymers*, Wiley, London, **1980**, 325.
121. Jager, M.; Schubert, S.; Ochrimenko, S.; Fischer, D.; Schubert, U.S. *Chem. Soc. Rev.* **2012**, 41, 4755.
122. Bolto, B.N. *Prog. Polym. Sci.* **1995**, 20, 987.
123. Ghoul, M.; Bacquet, M.; Morcellet, M. *Water Res.* **2003**, 37, 729.
124. Satyapal, S.; Filburn, T.; Trela, J.; Strange, J. *Energy Fuels* **2001**, 15, 250.
125. Cho, C-S. *ISRN Materials Science* **2012**, 798247.
126. Hoover, M.F.; Butler, G.B. *J. Polym. Sci. Symp.* **1974**, 45, 1.
127. Jere, D.; Jiang, H.L.; Arote, R. *Expert Opinion on Drug Delivery* **2009**, 6, 827.
128. Wu, C; Wang X. *Phys. Rev. Lett.* **1998**, 80, 4092.
129. Zhang, An-Q.; Cai, L-J.; Sui, L.; Qian, D-J.; Chen, M. *Polym. Rev.* **2013**, 53, 240.
130. Koka, C.M.; Rudin, A. *Makromol. Chem., Rapid Commun.* **1981**, 2, 655.

131. Demco, D.E.; Blumich, B. *Nuclear Magnetic Resonance, Encyclopedia of Polymer Science*, vol. 10, Wiley, New York, **2004**, 637.
132. Kinyanjui, J.M.; Hanks, J.; Hatchett, D.W.; Smith, A.; Josowicz, M. *J. Electrochem. Soc.* **2004**, 151, D113.
133. "Scanning Electron Microscope" *Wikipedia: The Free Encyclopedia*. Wikimedia Foundation, Inc. 22 July 2013. Web. 24 July 2013.
<http://www.thefullwiki.org/Scanning_Electron_Microscope>.
134. Atomic World. Retrieved 24 July 2013 from <http://www.hk-phy.org/atomic_world/tem/tem02_e.html>.
135. Atkins, P.W. *Physical Chemistry*, 7th Ed. W.H. Freeman, N.Y. **2002**.
136. Henry, D.; Eby, N.; Goodge, J.; Mogk, D. (2012 May 29). X-ray reflection in accordance with Bragg's Law. Retrieved 24 July 2013 from
<http://serc.carleton.edu/research_education/geochemsheets/BraggsLaw.html>
137. Yilmaz, E.; Suzer, S. *Appl. Surf. Sci.* **2010**, 256, 6630.
138. Basavaraja, C.; Kim, W.J.; Thinh, P.X.; Huh, D.S. *Bull. Korean Chem. Soc.* **2012**, 33, 449.
139. Švorčíka, V.; Chaloupka, A.; Záruba K.; Král V.; Bláhovác, O.; Macková, A.; Hnatowicz, V. *Nucl. Instrum. Meth. B* **2009**, 267, 2484.
140. Lala, N.L.; Deivraj, T.C.; Lee, J.Y. *Colloids and Surfaces A: Physicochem. Eng. Aspects* **2005**, 269, 119.
141. Perumal, S.; Hofmann, A.; Scholz, N.; Ruhl, E.; Graf, C. *Langmuir* **2011**, 27, 4456.
142. Keene, F.R. *Coord. Chem.* **1999**, 187, 121.

143. Sato, T.; Ruch, R. *Stabilization of colloidal dispersion by polymer adsorption*. Marcel Dekker Inc., New York, 1980.
144. Marchetti, B.; Joseph, Y.; Bertagnolli, H.J. *Nanopart. Res.* **2011**, 13, 3353.
145. Chen, C-C.; Kuo, P-L.; Cheng, Y-C. *Nanotechnology* **2009**, 20, 055603.
146. Liu, Y.; Fan, Y.; Yuan, Y.; Chen, Y.; Cheng, F.; Jiang, S-C.J. *Mater. Chem.* **2012**, 22, 21173.
147. Dey, P.; Blakey, I.; Thurecht, K.J.; Fredericks, P.M. *Langmuir* **2013**, 29, 525.
148. Takagishi, T.; Okuda, S.; Kuroki, N. Kozuka, H.J. *Polym. Sci.* **1985**, 23, 2109.
149. Horn, D.; E.J. Goethals (ED.), *Polymeric Amines and Ammonium Salts*, Pergamon Press, Oxford, **1980**, p. 333.
150. Warshawsky, A., in D.C. Sherrington, P. Hodge (Eds.), *Synthesis and Separations Using Functional Polymers*, Wiley, London, **1988**, p. 325.
151. Akamatsu, K.; Shimada, M.; Tsuruoka, T.; Nawafune, H.; Fujii, S.; Nakamura, Y. *Langmuir* **2010**, 26, 1254.
152. Ou, J.L.; Chang, C.P.; Ou, K.L.; tseng, C.C.; Ling, H.W.; ger, M.D. *Colloids and Surfaces A: Physicochem. Eng. Aspects* **2007**, 305, 36.
153. Haiss, W.; Thanh, N.T.K.; Aveyard, J.; Fernug, D.G. *Anal Chem.* **2007**, 79, 4215.
154. Buffat, P-A.; Flueli, M.; Spycher, R.; Stadelmann, P.; Borel, J.P. *Faraday Discuss.* **1991**, 92, 173.
155. Leff, D.V.; Brandt, L.; Heath, J.R. *Langmuir* **1996**, 12, 4723.
156. Yang, X.; Shi, M.; Zhou, R.; Chen, X.; Chen, H. *Nanoscale* **2011**, 3, 2596.
157. Zhang, F.; Srinivisan, M.P. *Langmuir* **2007**, 23, 10102.

158. Kumar, A.; Mandal, S.; Selvakannan, P.R.; Pasricha, R.; mandale, A.B.; Sastry, M.;
Langmuir **2003**, 16, 6277.
159. Manna, A.; Imae, T.; Aoi, K.; Okada, M.; Yogo, T. *Chem. Mater.* **2001**, 13, 1674.
160. Mohamed, M.B.; Wang, Z.L.; El-Sayed, M.A. *J.Phys.Chem.A* **1999**, 103, 10255.
161. Suh, J.; Lee, S.H.; Kim, S.M.; Hah, S.S. *Bioorg. Chem.* **1997**, 25, 221.
162. Gubicza, J.; Labar, J.L.; Quayuh, L.M.; Nam, N.H.; Luong, N.H. *Mat. Chem. Phys.*
2013, 138, 449.
163. Li, C.; Li, D.; Wan, G.; Xu, J.; Hou, W. *Nanoscale Res. Lett.* **2011**, 6, 440.
164. Young, J.K.; Lewinski, N.A.; Langsner, R.J.; Kennedy, L.C.; Satyanarayan, A.;
Nammalvar, V.; Lin, A.Y.; Drezek, R.A. *Nanoscale Res. Lett.* **2011**, 6, 428.
165. Sau, T.K.; Pal, A.; Jana, N.R.; Wang, Z.L.; Pal, T. *J. Nanopart. Res.* **2001**, 3, 257.
166. Park, H.H.; Woo, K. Ahn, J-P. *Nature Scientific Reports* **2013**, 3, 1497.
167. Zhang, X.; Su, Z. *Adv. Mater.* **2012**, 24, 4574.
168. Feng, L.; gao, G.; Huang, P.; Wang, K.; Wang, X.; Luo, T.; Zhang, C. *Nano
Biomed. Eng.* **2010**, 2, 258.
169. Sankar, M.; Dimitratos, N.; Miedziak, P.J.; Wells, P.P.; Kiely, C.J.; Hutchings,
G.J. *Chem. Soc. Rev.* **2012**, 41, 8099.
170. Tian, C.; Mai, B.; Wang, E.; Kuang, Z.; Song, Y.; Wang, C.; Li, S. *J. Phys. Chem.
C*, **2007**, 111, 3651.
171. Zelewsky, A.v.; Barbosa, L.; Schlaper, C.W. *Coord. Chem. Rev.* **1993**, 123, 229.
172. Kobayashi, S.; Hiroshi, K.; Tokunoh, M.; Saegusa, T. *Macromol.* **1987**, 20, 1496.
173. Mitric, R.; Burgel, C.; Burda, J.; Bonacic-Koutecky, V.; Fantucci, R. *Eur. Phys.
J.D.* **2003**, 24, 41.

174. Herrero, E.; Buller, L.J.; Abruna, H.D. *Chem. Rev.* **2001**, 101, 1897.
175. Wang, D.; Li, Y. *J. Am. Chem. Soc.* **2010**, 132, 6280.
176. Cheng, L-C.; Huang, J-H.; Chen, H. M.; Lai, T- C.; Yang, K-Y.; Liu, R-S.; Hsiao, M.; Chen, C-H.; Her, L-J.; Tsai, D.P.*J. Mater. Chem.* **2012**, 22, 224.
177. bin Saiman, M.I.; Brett, G.L.; Tiruvalam, R.; Forde, M.M.; Sharples, K.; Thetford, A.; Jenkins, R.L.; Dimitratos, N.; Lopez-Sanchez, J.A.; Murphy, D.M.; Bethell, D.; Willock, D.J. Taylor,S.H.; Knight, D.W.; Kiely, C.J.; Hutchings, G.J. *Angew. Chem. Int. Ed.* **2012**, 51, 5981.
178. Cuenya, B. R.; Baeck, S.H.; Jaramillo,T. F.; McFarland, E. W. *J. Am. Chem. Soc.* **2003**, 125, 12928-12934.
179. Shanmugam, S.; Viswanathan, B.; Varadarajan, T. K. *Nanoscale Res. Lett.* **2007**, 2, 175-183.
180. Zahoor, F.; Shanza, K. *Colloid Polym. Sci.* **2013**,
181. Khan, S.R.; Farooqi, ZH.; Ajimal M.; Siddiq, M.; Khan, M. *J. Disp. Sci. Technol.* **2012**, DOI:10.1080/01932691.2012.744690.
182. Xie, L.; Chen, M.; Wu, L. *J. Polym. Sci. Part A Polym. Chem.* **2009**, 47, 4919.
183. Yang, J.; Qiu, L.; Liu, B. Peng, Y.; Yan, F.; Shang, S. *J. Polym. Sci. Part A Polym Chem.* **2011**, 49, 4531.
184. Scott, R.W.; Sivadinarayana, C. Wilson O.M., Yan, Z.; Goodman, D.W. Crooks, R.M. *J. Am. Chem. Soc.* **2005**, 127, 1380.
185. Ye, H.; Crooks, R.M. *J. Am. Chem. Soc.* **2007**, 129, 3627.
186. Lee, J.; Park. J.C.; Bang, J.U.; Song, H. *Chem. Mater.* **2008**, 20, 5839.
187. Lee, J.; Park, J.C.; Song, H. *Adv. Mater.* **2008**, 20, 1523.

188. Sahiner, N.; Butun, S.; Ilgin, P. *Colloids Surf. A* **2011**, 386, 16.
189. Lu, Y.; Spyra, P.; Mei, Y.; Ballauff, M. Pich, A. *Macromol. Chem. Phys.* **2007**, 208, 254.
190. Zhao, C.; Nie, S.; Tang, M.; Sun, S. *Prog. Polym. Sci.* **2011**, 36, 1499.
191. Zhang, P.; Shao, C.; Zhang, Z.; Zhang, M.; Mu, J.; Guo, Z.; Liu, Y. *Nanoscale* **2011**, 3, 3357.
192. Hayakawa, K.; Yoshimura, T.; Esumi, K. *Langmuir* **2003**, 19, 5517.
193. Jiang, H.L.; Akita, T.; Ishida, T.; Haruta, M.; Xu, Q. *J. Am. Chem. Soc.* **2011**, 133, 1304.
194. bin Saiman, M.I.; Brett, G.L.; Tiruvalam, R.; Forde, M.M.; Sharples, K.; Thetford, A.; Jenkins, R.L.; Dimitratos, N.; Lopez-Sanchez, J.A.; Murphy, D.M.; Bethell, D.; Willock, D.J. Taylor, S.H.; Knight, D.W.; Kiely, C.J.; Hutchings, G.J. *Angew. Chem. Int. Ed.* **2012**, 51, 5981.
195. Edwards, J.K.; Solsona, B.E.; Landon, P.; Carley, A.F.; Herzing, A.; Kiely, J.; Hutchings, G.J. *J. Catal.* **2005**, 236, 69.
196. Kesavan, L.; Tiruvalam, R.; Ab Rahim, M.H.; bin Saiman, M.I.; Enache, D.I.; Jenkins, R.L.; Dimitratos, N.; Lopez-Sanchez, J.A.; Taylor, S.H.; Knight, D.W.; Kiely, C.J.; Hutchings, G.J. *Science*. **2011**, 331, 195.
197. Jirkovsky, J.S.; Panas, I.; Ahlberg, E.; Halasa, M.; Romani, S.; Schiffrin, D.J. *J. Am. Chem. Soc.* **2011**, 133, 19432.
198. Bligaard, T.; Norskov, J. K. *Electrochim. Acta* **2007**, 52, 5512.